CARDIFF UNIVERSITY
PRIFYSGOL CAERDYDD

Selective Oxidation of Methanol on Mixed Oxide Catalysts

Polina Yaseneva

School of Chemistry, Cardiff University
2011

ProQuest LLC
789 East Eisenhower Parkway
P.O. Box 1346
Ann Arbor, MI 48106-1346

DECLARATION

This work has not been submitted in substance for any other degree or award at this or any other university or place of learning, nor is being submitted concurrently in candidature for any degree or other award.

Signed ..... (candidate) Date 22.11.2011

STATEMENT 1

This thesis is being submitted in partial fulfillment of the requirements for the degree of .....PhD.....(insert MCh, MD, MPhil, PhD etc, as appropriate)

Signed ..... (candidate) Date 22.11.2011

STATEMENT 2

This thesis is the result of my own independent work/investigation, except where otherwise stated. Other sources are acknowledged by explicit references. The views expressed are my own.

Signed ..... (candidate) Date 22.11.2011

STATEMENT 3

I hereby give consent for my thesis, if accepted, to be available for photocopying and for inter-library loan, and for the title and summary to be made available to outside organisations.

Signed ..... (candidate) Date 22.11.2011

Abstract

In the present work selective oxidation of methanol over the model Mo/Fe_2O_3 and $Mo/Co(Zn)Fe_2O_4$ systems has been investigated. It was shown that pure iron oxide and cobalt ferrite combust methanol to carbon dioxide and water. When molybdenum is loaded on the surface of iron oxide and calcined at 500 °C, this leads to the formation of iron molybdate surface layer over Fe_2O_3 core, which significantly changes selectivity in methanol oxidation towards partial oxidation products. The neighbouring Fe-Mo and Mo-Mo pairs of iron molybdate layer are responsible for the formation of carbon monoxide and formaldehyde respectively.

According to XRD, Raman and XPS data, dosing of molybdenum onto the cobalt ferrite surface results in the formation of a mixed layer consisting of cobalt molybdate, iron molybdate and molybdena phases. Oxidation of methanol over $Mo/CoFe_2O_4$ results in the formation of a mixture of CO and CO_2 with small traces of formaldehyde. CO is produced on mixed Fe-Mo and Co-Mo sites at temperatures above 220 °C, whereas CO_2 is mainly produced at lower temperatures and low oxygen conversion due to oxidation of CO by highly reactive traces of pure cobalt ferrite or cobalt molybdate present on the surface.

Methanol oxidation was used as a model reaction to establish whether there is a relationship between catalytic activity and selectivity, and magnetic properties of catalysts. The catalytic behaviour of the pure and Mo impregnated $Zn_xCo_{1-x}Fe_2O_4$ systems in the vicinity of Curie point was studied. Curie temperature of the material and the nature of Curie transition were adjusted varying Zn content and sample calcination temperature.

Acknowledgements

It would not have been possible to complete this work without the help and support of many people. First of all, I am grateful to my supervisors Prof. Mike Bowker and Prof. Graham Hutchings who scientifically guided me throughout the years of my PhD and helped me with their advice. Special thanks must go to Cardiff University and ORSAS scheme for providing a funding and giving me a unique opportunity to study in Cardiff.

I would like to express my gratitude to Dr. D. Bavykin and Dr. A. Kulak from the University of Southampton for help with HR-TEM facilities and Dr. V. Sans (University of Warwick) for assisting with Raman spectroscopy experiments. I am also thankful to the group members who provided help and support in dealing with the equipment, and especially to Mirgul, who made a considerable contribution to this dissertation.

Thanks to my loving husband and mum and dad, who are always very supportive for my decisions and who are always there for me when I need help, which I needed a lot during these years. Thanks to my brother, who finally made his point and proved that he is more clever.

And finally, I am thankful to all my friends whom I met in Cardiff and who made this city a fantastic and very memorable place for me.

Glossary

AAS	Atomic Absorption Spectroscopy
AC	Alternating Current
AHM	Ammonium Heptamolybdate
BET	Brunauer, Emmett and Teller
CCD	Charge-Couple Device
DME	Dimethyl Ether
DMFC	Direct Methanol Fuel Cells
EDS	Energy Dispersive X-ray Spectroscopy
FWHM	Full-Width at Half Maximum
HRTEM	High Resolution Transmission Electron Microscopy
HTF	Heat Transfer Fluid
IPFR	Isothermal Pulse Flow Reaction
IR	Infrared
ML	Monolayer
MS	Mass Spectroscopy
MTBE	Methyl Tertiary Butyl Ether
PFR	Pulse Flow Reactor
SEM	Scanning Electron Microscopy
SP	Super Paramagnetism
STEM	Scanning Transmission Electron Microscopy
T_c	Curie Temperature
TEM	Transmission Electron Microscopy
TOF	Turnover Frequency
TPD	Temperature Programmed Desorption
TPPFR	Temperature Programmed Pulse Flow Reaction
UV	Ultraviolet
UHV	Ultra High Vacuum
VSM	Vibrating Sample Magnetometer
XRD	X-Ray Diffraction
XPS	X-Ray Photoelectron Spectroscopy

Table of Contents

List of Figures

List of Tables

Chapter 1. Literature review

1.1. Catalysis

Catalysis is a process whereby a chemical reaction rate is accelerated by the presence of a substance (catalyst) lowering the activation barrier for the reaction by formation of transition complexes stabilized by chemical bonds. In the catalytic process these bonds regroup in order to form products and the catalyst is released.

The phenomenon of catalysis was known already in 1552 when Valerio Cordus catalyzed the conversion of alcohol to ether by addition of sulphuric acid.[1] However, the term *catalysis* and the concept of controlling the rate of a chemical reaction was first introduced by Berzelius in 1836, who had continuously investigated and made parallels between the effect of sulphuric acid on ethanol, decomposition of hydrogen peroxide and the conversion of starch into sugar.[1-3]

Later, in 1877, George Lemoin had shown that the decomposition of hydriodic acid to hydrogen and iodine reached the same equilibrium point at 350 °C, irrespective of whether the reaction was carried out homogeneously and slowly in the gas phase or rapidly and heterogeneously in the presence of platinum. Bertholet in 1879 working on the acid-catalysed etherification of organic acids and hydrolysis of esters confirmed that catalysts do not influence the position of equilibrium, a key observation in our understanding of the nature of catalysis. [3]

The first catalytic industrial process was developed around 1875 and utilized platinum to oxidize SO_2 to SO_3. However, the most remarkable industrial processes were discovered in the XXth century: ammonia synthesis from H_2 and N_2 over Fe_3O_4 catalyst by Fritz Haber in 1905; methanol synthesis developed by BASF (1923) at high pressure over a ZnO-chromia catalyst; Fisher-Tropsch synthesis of fuels was commercialized in 1930 as an alternative to processing heavy oils.[2-4] The majority of industrial catalytic processes are heterogeneous.

However, homogeneously catalyzed processes assumed much more importance in recent years.

The very first industrial applications of catalysis were not based upon scientific principles of adsorption and equilibrium theories. These were developed in academia later, when in 1915 Langmuir published his adsorption theory, which was further developed to a kinetic theory by Hinshelwood in 1927.[5]

1.2. Selective oxidations

Among the important catalytic processes partial (selective) oxidation using air or oxygen are of great significance and are used to manufacture a variety of chemicals ranging from simple molecules to complex pharmaceuticals.[6-15] This industrial interest led to a huge increase in the amount of scientific publications devoted to catalytic selective oxidation during the second half of the XXth century.[13] However, despite decades of research the mechanisms of certain oxidations still remain poorly understood and improvement in the sustainability of these processes is needed.[7, 11-13]

There are three categories of effective oxidation catalysts as indicated by Satterfield:[2]

1. Transition metal oxides which possess high mobility of the surface and lattice oxygen which readily moves to and from the structure. Most of industrial catalysts of this type are mixed oxides containing two or more cations.
2. Metal on which oxygen is chemisorbed.
3. Metal oxides in which the active species is chemisorbed oxygen, as molecules or atoms. These may also provide a significant additional mechanism under some conditions with metal oxide catalysts that also contain interstitial oxygen as an active species.

For most oxidation catalysts the process occurs according to a redox mechanism, including two steps: reaction between catalysts in the oxidized form Cat-O and the reagent R, in which

the oxide becomes reduced, Cat-O + R = Cat + RO; and oxidation of the reduced catalyst by oxygen from gas phase, $2Cat + O_2 = 2Cat\text{-}O$. Under steady-state conditions, the rates of these reactions are the same. An example of this mechanism is given in Figure 1-1.

In 1954 Mars and Van-Krevelen developed a kinetic equation to explain the behaviour of the partial oxidation of aromatic hydrocarbons and sulphur dioxide over vanadium oxide catalysts of different formulations, based on the assumption that both chemisorbed and lattice oxygen are equally counted as the active species for the catalytic oxidation reaction.[2] This was later confirmed by many researchers, for instance, by Keulks and co-authors, who had shown the evidence of participation of lattice oxygen of bismuth molybdate in the oxidation of propylene to acrolein;[16-17] or by Pernicone who proposed participation of lattice oxygen of MoO_3 in methanol oxidation.[18-19]

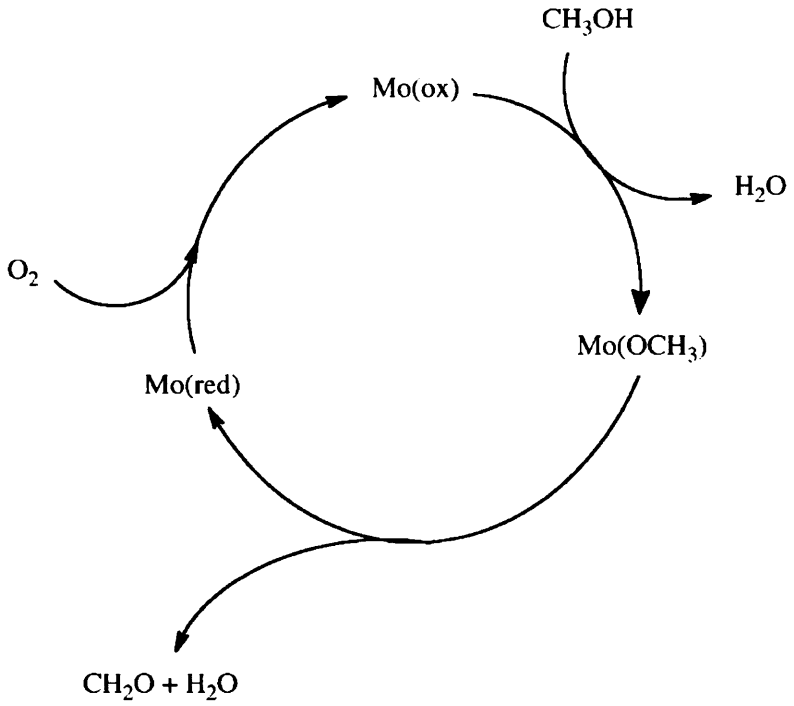

Figure 1-1. Schematic mechanism of methanol oxidation over molybdena catalyst.

1.3. Methanol oxidation

1.3.1. Methanol – uses and production

In this particular work we will focus on the selective oxidation of methanol. Methanol is a substance of high demand in industry as it is used as a feedstock for production of such substances as formaldehyde, methyl tertiary butyl ether (MTBE) and acetic acid (Table 1-1). The world demand for methanol is around 32 million tons per year.

Table 1-1. Major methanol derivatives uses.

Primary Derivative	Secondary Derivative	Tertiary Derivative	Quaternary Derivative
Acetic Acid	Vinyl Acetate Acetic Anhydride Terephthalic Acid	Polyvinyl Acetate Cellulose Acetate Polyesters	Polyvinyl Alcohol
Formaldehyde	Phenol Formaldehyde Resins Urea Formaldehyde Resins Melamine Resins Polyoxymethylene Polyols Butandieol Isoprene Paraformadehyde Hexamine	 Polyesters Rubber	
Methyl tetr-butyl Ether			
Methyl Methacrylate	Polymethylmethacrylate Methacrylate		
Methyl Chloride	Methylene chloride	Chloroform	
Methylamines	Caffeine Sevin Insecticides, herbicides, pesticides Water gel explosives Photographic developers Analgesics Antispasmodics		

Most of the industrial processes of methanol production are based on the ICI process, in which a high-pressure gas mixture of CO, CO_2 and H_2 is converted into the alcohol with 99

% efficiency over the catalyst containing copper, zinc oxide and alumina at temperatures between 250 and 300 °C.

Today, synthesis gas used in the process is made from steam-reformed methane:

$$CH_4 + H_2O = CO + 3H_2 \quad (1\text{-}1)$$

And the following reactions occur simultaneously during industrial synthesis:

$$CO + H_2O = CO_2 + H_2 \quad (1\text{-}2)$$

$$2H_2 + CO = CH_3OH \quad (1\text{-}3)$$

$$CO_2 + 3H_2 = CH_3OH + H_2O \quad (1\text{-}4)$$

From the mechanistic investigations it was postulated that CO_2 from CO/CO_2 mixture is the immediate precursor of methanol, while the role of CO is to keep the copper in a reduced state.[3, 20]

The emergence of carbon-capture technology from power stations in the last several years resulted in concentrated CO_2 becoming available as a cheap feedstock. The feasibility of direct synthesis of methanol from CO_2 and hydrogen has been demonstrated up to a pilot scale. The process itself is thermodynamically viable, but has low thermodynamic limit of conversion, which necessitates significant recycle and separation. Major cost contributions in the process are thus from gas recycle, separation of methanol and water, distillation of methanol from water and compression of reactants.[21-23]

Apart from a bulk chemical precursor, methanol is widely used as a solvent to dissolve organic compounds and as anti-freeze in pipelines. Methanol has also been used as an "alternative fuel." In Europe, methanol is used in the production of biodiesel, which can replace refinery-based diesel for use in transportation. And in China, methanol is used directly as a blending component of gasoline, driven by the need to extend the octane pool in that country, and also due to economic feasibility as high crude oil and gasoline prices have encouraged the use of less costly methanol. Methanol has also been considered for direct

combustion in combined cycle power generation facilities. And it is used as a fuel for direct methanol fuel cells (DMFC).

1.3.2. Methanol oxidation to formaldehyde

Formaldehyde production from methanol accounts for 40 % of the total methanol usage as formaldehyde is the most commercially important aldehyde. Urea-, phenol- and melamine-formaldehyde resins accounted for approximately 63% of world demand in 2009; other large applications include polyacetal resins, pentaerythritol, methylenebis (4-phenyl isocyanate), 1,4-butanediol and hexamethylenetetramine (Table 1-1).

Commercial formaldehyde production started in Germany in 1890, when methanol was oxidized by air over unsupported metallic copper at approximately atmospheric pressure and the product was rapidly quenched by solution in water. Around 1910 copper was replaced by silver as it gave higher yields of formaldehyde. Silver was supported on different inert materials, but it was not widely applied probably because the metallic silver is easily recyclable and can be regenerated at low cost. In 1930s the mixed oxide iron molybdate catalyst was developed and since the 1950s it has been used in industry for commercial formaldehyde production. Today the world's formaldehyde production industry uses both silver and mixed oxide catalysts equally. The difference is that iron molybdate catalyses the direct oxidation of methanol to formaldehyde (reaction 1-5); while the silver-catalyzed process is a combination of oxidation and dehydrogenation reactions (reactions 1-5 and 1-6).

Selective Oxidation:

$$CH_3OH + 1/2O_2 = CH_2O + H_2O \qquad (1\text{-}5)$$

$$\Delta H = -157 \text{ kJ mol}^{-1}$$

Dehydrogenation:

$CH_3OH = CH_2O + H_2$ (1-6)

$\Delta H = + 85 \text{ kJ mol}^{-1}$

Combustion:

$CH_3OH + 3/2O_2 = CO_2 + 2H_2O$ (1-7)

$\Delta H = -676 \text{ kJ mol}^{-1}$

Partial oxidation:

$CH_3OH + O_2 = CO + 2H_2O$ (1-8)

$\Delta H = -389 \text{ kJ mol}^{-1}$

In the silver-catalyzed process (1-5 and 1-6) the air/methanol mixtures fed to the reactor are always maintained rich in methanol, while for the oxide process (1-5) methanol lean mixtures are used. The thermodynamic data show that combustion pathway with the formation of total oxidation products CO_2 and water and oxidation to CO are thermodynamically favored (1-7, 1-8) compared to formaldehyde (1-5, 1-6). The addition of a catalyst makes it possible to obtain products of partial oxidation, as shown in Figure 1-2.

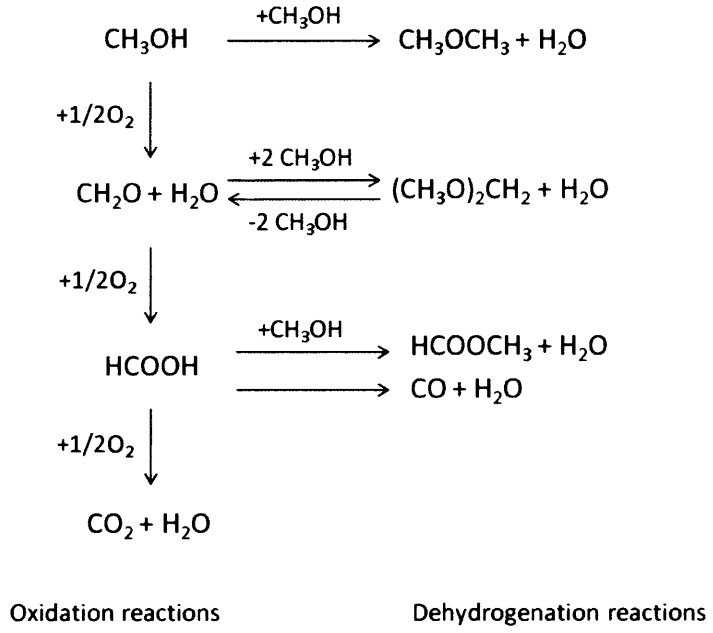

Figure 1-2. Oxidation and dehydration reactions of methanol.[24]

1.3.3. Industrial process

Figure 1-3 shows a simplified scheme of industrial Formox process for formaldehyde production. Formox has been continuously developing the process, technology and catalysts since 1959, when the first plant for formaldehyde production over an oxide catalyst was launched, and is now the world leader in this field.

Methanol is fed into a preheated vaporizer. The air from the atmosphere is run through a filter and compressed in a blower (B), before mixing with the recycled process gas to create a gas mixture with 10 mol % of oxygen. This mixture enters a vaporizer (V) where it is mixed and heated together with methanol and further passes to the pre-heater (H) right before entering the reactor at a temperature 85 °C and a pressure 1.4 bar. The reactor (R) contains tubes filled with a metal oxide catalyst. Methanol reacts with oxygen at 250-400 °C to produce formaldehyde. The heat of reaction is removed by a heat transfer fluid (HTF) and then transferred to steam in the condenser (C). This steam can be further used for electricity cogeneration or for heating purposes, thus increasing the overall energy efficiency of the

process. The process gas then passes to absorber (A), where formaldehyde is absorbed into process water. The flow of the process water is adjusted so that the desired concentration of 37 % formalin solution is obtained. Cooling water is used to remove the heat of absorption, which promotes further absorption.

The yield from this process is around 92 % of formaldehyde and the minor by-products are CO, dimethyl ether (DME), a limited amount of CO_2 and formic acid.

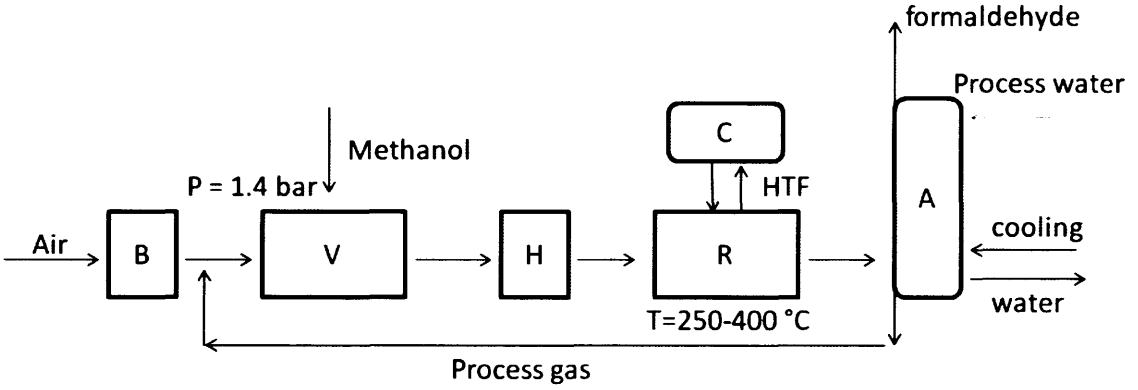

Figure 1-3. A simplified scheme of industrial formaldehyde production process.

In industry an iron molybdate catalyst with an excess of molybdena is usually prepared by co-precipitation from iron chloride ($FeCl_3$) and ammonium heptamolybdate at pH 2 under stirring. After that the catalyst is washed, dried and calcined at 420 °C.[25-26] Different preparation conditions affect catalyst activity. Thus, Pernicone postulated that the catalyst activity depends on the pH of the final solution after precipitation, as the surface area of catalysts depends on the concentration of ammonium heptamolybdate solution.[25] A number of authors related catalyst activity to the Mo/Fe atomic ratio, which is agreed to be higher than stoichiometric.[27-29] This excess is needed to compensate sublimation of Mo occurring particularly in the reactor hot spots according to the following reactions:

$$CH_3OH + Fe_2(MoO_4)_3 = 2\ (\beta\text{-}FeMoO_4) + MoO_3 + HCOH + H_2O \qquad (1\text{-}9)$$

$$2\ (\beta\text{-}FeMoO_4) + MoO_3 + \tfrac{1}{2}\ O_2 = Fe_2(MoO_4)_3 \qquad (1\text{-}10)$$

$$2\ (\beta\text{-}FeMoO_4) + 1/2\ O_2 = Fe_2O_3 + 2MoO_3 \qquad (1\text{-}11)$$

Pernicone pointed out several advantages of methanol oxidation over oxide catalysts:[25]

(a) higher yield, which allows production of low-methanol solutions;

(b) higher resistance to poisoning, so that no special precaution needs to be taken for air purification;

(c) longer life of the catalyst;

(d) less fire or explosion hazards in the plant, owing to the low methanol concentration.

1.3.4. Reactivity of iron molybdate in the methanol oxidation

As it was mentioned above the industrial iron molybdate always contains an excess of molybdena present in the catalyst as a separate phase. Though it was reported many times that the presence of a slight molybdenum excess in $Fe_2(MoO_4)_3$ catalyst enhances the resulting catalytic performance during the oxidation of methanol, some authors attribute the catalytic activity only to stoichiometric iron molybdate.

In 1965 Boreskov *et al.* assigned the active phase to stoichiometric $Fe_2(MoO_4)_3$. The fact that the most active catalyst had Mo/Fe=1.7 atomic ratio they explained that a slight excess of MoO_3 is needed to totally convert iron oxide to iron molybdate.[30] Alessandrini also attributed the active phase to iron molybdate (Mo/Fe=1.5) as the excess of molybdena had no influence on specific activity. However, it was pointed out that an excess of MoO_3 provides higher surface area and coherence of the sample.[27] Fagherazzi and Pernicone suggested the active phase of the catalyst is iron molybdate with excess of Mo.[28] Based on the X-ray diffraction (XRD) studies they had a suggestion that Mo^{6+} ions replace some Fe^{3+} ions in the crystalline structure and the resulting charge difference is compensated by the incorporation

of O^{2-} in the lattice. Sun-Kou *et al.* showed that catalysts with an excess of Mo have higher activity than the stoichiometric samples. However, they emphasised the influence of the preparation method on the activity.[29] Trifiro *et al.* identified three reasons for the need of Mo excess in iron molybdate catalyst:[31] (i) to improve the mechanical properties of the catalyst, (ii) to dope the $Fe_2(MoO_4)_3$ in order to reach a Mo/Fe ratio greater than 1.5 in the active phase, (iii) to allow the re-oxidation process of β-$FeMoO_4$ to $Fe_2(MoO_4)_3$ by supplying in situ the MoO_3 involved in the reaction (reaction 1-10).

On the contrary, Soares *et al.* showed that activities of iron molybdate catalysts, if normalised to a unit surface area, for the stoichiometric sample and the one with Mo/Fe=3 atomic ratio, are identical.[32] They concluded that under the reaction conditions the iron molybdate surface is stoichiometric due to the sublimation of excess Mo. It was also showed that Mo excess increases H_2CO selectivity due to difference in acidity of this sample and that it seemed to increase surface reoxidability. In a recent publication Routray *et al.*[33] stated that catalytic activity and turnover frequency (TOF) values of bulk $Fe_2(MoO_4)_3$, with or without the presence of excess of molybdena, are almost the same. The only difference observed was the increase in formaldehyde selectivity for the catalyst with excess molybdena, which was explained by the authors as a consequence of the excess MoO_3 supplying surface MoO_x species that cover up exposed FeO_x sites responsible for the formation of by-products.[33]

The influence of composition and of calcination temperature of iron molybdates (Mo/Fe = 1.1-2.2) was studied by Popov *et al.*[34-35] It was found that regarding the composition, the maximum selectivity is observed over samples with 1.6 and 1.9 Mo to Fe ratio. For the stoichiometric sample calcined at different temperatures (300-500 °C) the maximum activity was attained over the 400 °C sample. Activity was attributed to the formation of the crystallized phase; while at low calcination temperatures the samples were amorphous. Calcination at higher temperatures also resulted in high activity and selectivity;

however it was lower than that observed for the catalyst calcined at 400 °C. The same authors studied the effect of mechanical treatment on iron molybdate. Mechanical treatment led to the formation of amorphous iron molybdate samples, which crystallized upon exposure to oxidising conditions. Thus, the authors concluded that the crystalline state of the catalyst is active in methanol oxidation.[36] Morphological study of the stoichiometric and the Mo-rich iron molybdates was performed by Soares *et al.*[32] The catalysts with stoichiometric composition displayed ordered *lamellae* morphology, whereas catalysts with Mo excess showed a sponge-like morphology. Del Arco *et al.* performed scanning electron microscopy (SEM) studies of iron molybdates and showed that $Fe_2(MoO_4)_3$ appears as sponge-like crystals, while MoO_3 was present as stick-like crystals.[37-38]

Wachs *et al.*[39-41] conducted a detailed study on the quantitative determination of surface active sites and turnover frequencies for methanol oxidation over bulk molybdates and supported monolayer samples. It was postulated that the product distribution in methanol oxidation depends on the redox and/or acid-base nature of the surface active sites as they yield formaldehyde, DME or CO_2 respectively. Thus, iron molybdate and molybdena catalyze the oxidation of methanol towards formaldehyde and DME either due to the presence of surface redox and acid sites respectively.[39] It was shown that methanol chemisorption on iron molybdate (stoichiometric and with excess of Mo) produces both intact surface CH_3OH_{ads} and $-OCH_3$ species, which are assigned to Lewis acid sites and less acidic or basic surface sites respectively, and both form HCOH as a reaction product. The TOF values for bulk iron molybdate and the supported system (MoO_3/Fe_2O_3) turned out to be similar. The correlation of TOF to ligand cation electronegativity in both the supported and the bulk systems strongly suggests that the ligand effect originates from the same source in each system.[41] It was explained by suggesting a possible formation of "monolayer" of surface molybdenum oxide species (MoO_x) on the bulk iron molybdate. According to Routray *et al.*[33] this monolayer

represents the catalytic active sites, and excess of Mo in bulk $Fe_2(MoO_4)_3$ replenishes this monolayer. Low activity of molybdena was explained by the low number of redox sites since only the edge planes of its platelet morphology are active. Bulk iron molybdate transforms the anisotropic morphology of MoO_3 to the isotropic morphology where all the exposed planes are catalytically active.[33] This supports the previously reported idea of Chowdhry *et al.*[42] that the reason for lower activity of MoO_3 in methanol oxidation is the surface structural differences with iron molybdate.

The selectivity towards formaldehyde over iron molybdate catalyst increases with the increasing temperature until the high conversion is reached and by-products (mainly CO) start to form as a secondary oxidation products.[43] Although CO is usually formed from formaldehyde, direct oxidation of methanol to CO was observed at high temperatures.[44]

Most of the authors proposed the Mars van Krevelen mechanism for the oxidation of methanol over iron molybdate.[2, 19, 25, 33, 43, 45-47] This mechanism is supported by kinetic studies and experimental works indicating rapid diffusion of bulk oxygen to the catalyst surface.[47-49] However, there are reports referring to the Langmuir-Hinshelwood mechanism. For instance, Deshmukh *et al.*[50] studied oxidation of methanol in a differentially operated reactor at the temperatures 230-260 °C over commercial Fe-Mo-O catalyst and described the kinetics of formaldehyde formation with Langmuir-Hinshelwood kinetics, assuming two different metal oxides, one containing absorbed oxygenates and the other one containing lattice oxygen. The presence of water vapor inhibited formaldehyde formation significantly, especially at lower water partial pressures.[50] O`Brien *et al.*[51] combining in situ wide angle X-ray scattering with on-line mass spectroscopy showed that for redox surface MoO_3 species both Mars van Krevelen and Langmuir-Hinshelwood types of mechanism can operate.

Numerous suggestions have been made about the rate-limiting step in the oxidation of methanol to formaldehyde over iron molybdate. The situation was clarified when Machiels *et*

al.[52], studying kinetic isotopic effects over MoO_3 and iron molybdate with different Mo/Fe ratio, showed that for all samples hydrogen abstraction from the methyl group is the rate-limiting step. In the same work they pointed out that water inhibits the reaction rate due to competitive adsorption. In a more recent publication it was shown that site blockage by adsorbed water at temperatures below 200 °C may be an additional factor contributing to product inhibition, whereas at temperatures > 300 °C it does not appear to be significant. The true activation energy was calculated to be 98 kJ mol^{-1}.[53] Oayma *et al.*[54] reported C-H bond cleavage as the rate limiting step for oxidation of methanol over supported MoO_3 and that electron transfer to the metal centre accompanying the bond scission is the critical step.

Recently several publications were dedicated to the optimization of conditions for methanol oxidation to formaldehyde. Thus the oxidation of methanol over supported iron molybdate catalyst was studied under a variety of different conditions (e.g. Mo/Fe ratio, different temperatures, different space times).[55] Reaction kinetics was studied over the silica supported iron molybdate with Mo/Fe ratio = 5 as it favoured formaldehyde formation and the surface reaction controlling model was found to be the most suitable reaction mechanism.[55] Ivanov et al in their optimization studies showed that the oxygen concentration in the feed mixture has to be equal to or higher than the methanol concentration and water concentration in the range of 2.0–3.0% does favour the selectivity of the process. The increase of methanol concentration in the gas mixture fed in the reactor leads to a dramatic change both of the temperature profile of the catalyst layer and the distribution of the reaction products.[56]

1.3.5. Catalyst deactivation

Though industrial Fe-Mo-O catalysts for methanol oxidation to formaldehyde have high activity and selectivity, they have a rather short lifetime (under 2 years) and need to be replaced. The main reason for the catalyst deactivation proposed by many authors is the loss

of MoO_3 by volatilisation.[57-59] The volatile species are formed by the reduction of iron molybdate by reacting methanol in the redox catalytic process (reaction 1-9).[43, 51, 60] Pernicone *et al.*[61] performed catalytic tests simulating catalyst deactivation processes, in the industrial plant. They reported that deactivation is related to the volatilisation of molybdena and with consequent formation of iron oxide. Using x-ray photoelectron spectroscopy (XPS) they found that in the hot-spots the catalyst surface composition was Mo/Fe=1, which was evidence of the presence of $Fe_2(MoO_4)_3 - 1/2Fe_2O_3$. Volatile MoO_3 can crystallize as a fibre-like material in the voids of the catalytic bed increasing the pressure drop through it. Mechanical resistance of the catalyst degrades due to the loss of MoO_3. Simultaneously with MoO_3 sublimation by thermal effect, the loss of Mo can occur in the form of Mo-MeOH.[59] The volatilisation of Mo in this form is proportional to the methanol concentration and increases with temperature. Molybdenum can also sublimate as Mo-water volatile compounds.[62] Studying the kinetics of deactivation of the supported iron molybdate catalyst in the presence of water Jianhong *et al.*[63] proposed the following mechanism (for temperatures 547-700 °C):

$$MoO_4^{2-} + 2H_2O \leftrightarrow MoO_2(OH)_2 + 2OH^- \quad (1\text{-}12)$$

$$MoO_2(OH)_2 \leftrightarrow MoO_3 + H_2O \quad (1\text{-}13)$$

This mechanism is similar to the one proposed by Zhang *et al.* for Bi-Mo oxides supported on silica.[64] Ivanov *et al.* also referred to this mechanism in their investigation of the deactivation of industrial iron molybdate catalyst.[65]

Andersson *et al.*[57] showed that during the Formox process volatilisation of Mo occurs from the mixed layer and inert rings. This molybdenum later forms needle-like MoO_3 crystals in the pure layer. A patent by Wachs *et al.* offered to regenerate deactivated industrial iron

molybdate catalyst by moving the MoO_3 formed around with methanol in nitrogen stream flowing in the opposite direction to that normally used within the industrial conditions.[66]

1.4. Alternative catalysts

1.4.1. Silver catalyst

As was mentioned above, another important industrial process for formaldehyde production is a silver-based process. The commercial industrial silver catalysts are unsupported and made of very high purity metal (99.999 %). Usually these catalysts have the shape of needles, wires or gauzes.[67] The advantages of this technology are: relatively low investment cost, high yield and simplicity of process operation.

The particular property of silver is its ability to accommodate different active oxygen species. In the literature one can usually find descriptions of three different types of chemisorbed oxygen, denoted as O_α, O_β and O_γ. [68-71] Molecular oxygen adsorbs and dissociates on (110) and (111) surfaces of Ag giving rise to the formation of two surface oxygen species (O_α and O_γ), distinguished by their bonding with silver (Ag-O-Ag and Ag=O respectively). The O_β corresponds to oxygen dissolved in the silver lattice. The selectivity to formaldehyde during methanol oxidation is largely controlled by the surface populations of the O_α and O_γ oxygen species as reactive oxygen (O_α) mainly catalyses the production of HCOOH, CO_2, $HCOOCH_3$, CH_2O; while O_γ benefits selective oxidation to formaldehyde. O_γ oxygen species exist only at temperatures above 630 °C. Thus, the O_γ/O_α ratio and, consequently, methanol conversion and formaldehyde yield increase significantly with temperature. Bulk oxygen cannot participate directly in the oxidation process, however it segregates from the bulk to the surface and forms strongly bound O_γ oxygen species.

During the activation of silver under the industrial conditions (650 °C), the catalyst undergoes significant restructuring. Millar using scanning electron microscopy (SEM)

observed the appearance of "pinholes" close to the initial surface defects, which spread gradually from defect regions to the entire silver surface.[72] Restructuring modifies the oxygen chemisorption properties of the catalyst and promotes formation of O_γ oxygen, selectively oxidizing methanol and increasing formaldehyde yield.[68, 70, 72]

Morphological properties of the silver catalysts from different suppliers vary enormously (shape, surface area, nature of crystallographic planes exposed, defects density), which affect the catalyst start-up performance in formaldehyde production.

In order to prolong silver catalyst lifetime attempts had been made to make supported silver catalysts. Dai *et al.* prepared Ag/SiO_2 and $Ag/SiO_2/Al_2O_3$ catalysts which showed excellent activity and selectivity in methanol oxidation with formaldehyde yield >90 %. [73-74] Pestryakov *et al.* have shown that addition of Zr and Ce oxides to a silver catalyst improves its performance; whilst La, Pr and Sm oxides have lowered the yield of formaldehyde.[75] However, despite of these investigations none of these catalysts was commercialized.

1.4.2. Promoted Mo-Fe-O catalyst

Promotion or doping is widely used in catalysis to either attenuate catalytic activity or to improve catalyst stability. Thus, the effects of addition of different promoters to iron molybdate catalyst have been presented in the literature.

Sanchez *et al.* showed a promotional effect of chromium addition to iron molybdate catalyst. [76] They reported that addition of even small amounts of Cr leads to an increase in surface area and formaldehyde yield compared to the unpromoted catalyst. Del Arco *et al.* investigated the role of chromium and showed that in the promoted catalyst molybdena appeared to be plate-shaped instead of sticks, revealing that Cr affects MoO_3 topology.[38] It is reported that chromium increases the mobility of the oxygen ions bound to molybdenum

through a change in coordination, stereochemistry or oxidation state of molybdenum. Cr doped iron molybdate has an improved stability and can be used for a longer time.[77]

Popov *et al.* studied the effect of sodium addition to the iron molybdate catalyst on catalytic activity and reported that impregnation of iron molybdate with 0.4 wt. % Na leads to a decrease in activity by a factor of 10-12.[78] Later Ivanov *et al.* studied the addition of Na to Mo-Fe-Cr-O sample and showed that it did not have a negative influence on the properties of the catalyst.[79]

Another doping element studied by Ivanov *et al.* is tungsten. Using $FeCl_3$ and a mixture of ammonium heptamolybdate and Na_2WO_4 they obtained solid solutions of $Fe_2(Mo_xW_{1-x}O_4)_3$ and $Mo_xW_{1-x}O_3$ via co-precipitation.[80] The sample with 5 wt% of WO_3 showed higher activity in methanol oxidation at 350 °C than the pure iron molybdate with conversion of 97 % and selectivity towards formaldehyde 96.3 %.

1.4.3. Supported Iron Molybdate catalyst

Due to the high exothermicity of the methanol oxidation reaction (reaction 1-5), the formation of hot-spots in the catalyst bed is a common problem, leading to catalyst deactivation by molybdena sublimation.[32, 61] It was proposed to use fluidized bed reactors instead of fixed bed reactors for the oxidation of methanol as it would minimize hot-spots in the catalytic bed.[81] The other advantages mentioned were the decrease of explosion risk, handling of the catalyst deactivation without interrupting the operation and an increase in production capacity.

However iron molybdate itself has a low mechanical strength and cannot be used in a fluidized reactor unsupported. Therefore studies of Mo-Fe-O supported on materials with high mechanical resistance (Al_2O_3, SiO_2) can be found in the literature.[82-88] It was reported that supported iron molybdates are much less active than unsupported due to the interaction between supports and Mo-Fe-O mixed oxide.

It was shown that the increase of surface area of a support has a negative effect on the catalytic activity of supported iron molybdate. Thus Carbucicchio *et al.*[83] studied methanol oxidation as a function of temperature over silica-supported iron molybdates with different surface areas. They reported that by increasing the surface area both, activity and selectivity remain practically constant up to 40 m^2/g and after that the values decrease rapidly. For the alumina-supported iron molybdates this effect was more pronounced as the increase of surface area from 5 to 125 m^2/g drastically changed both activity and selectivity.[84] Basically, when iron molybdate was supported onto high-surface alumina no formaldehyde was detected among the products. Dehydrogenation of methanol on alumina species gave rise to significant DME production. In the investigation of Raman spectra of silica and alumina supported iron molybdates Hill and Wilson have shown that samples with 5.2 wt.% loading of iron molybdate have no Raman bands corresponding to either iron molybdate or molybdena in their spectra.[86] This result was taken as an indication of significant catalyst-support interaction. They also compared Raman spectra of supported iron molybdate with the same loading onto SiO_2 and Al_2O_3 and concluded that catalyst-support interaction is stronger for the alumina supported system. Carbucicchio[82] reported the formation of Fe-Mo-SiO_2 and Fe-Mo-Al_2O_3 or Fe-$Al_2(MoO_4)_3$ when silica and alumina were used as supports for iron molybdate. Castelo-Dias *et al.* studied SiC, SiO_2 and TiO_2 as support materials for iron molybdate and concluded that the Mo-Fe-O phase reacts with the support material and that this interaction depends on the surface area of the material with a stronger effect for higher surface areas.[89]

Recently Soares *et al.* reported new Mo-Fe-P-O supported catalyst for fluidized bed reactors.[85] The presence of heteropolymolybdates containing phosphorus in these samples was suggested as an explanation of pronounced catalytic behavior (for temperatures lower than 400 °C this sample presented higher formaldehyde yield than the unsupported industrial

catalyst). The absence of MoO_3 needles (easily sublimated) in SEM micrographs of the post reaction sample was suggested as an indication of a different reaction mechanism.

1.4.4. Other catalysts

In the area of alternative catalysts for methanol oxidation a significant number of studies were reported on vanadia-based catalysts including pure vanadia, mixed oxides and supported catalysts.[39, 90-98] Malinski *et al.* had shown that V_2O_5/NiO (Fe_2O_3, Co_3O_4) systems are selective towards formaldehyde and the catalysts with the atomic ratio V:Me = 1 having the highest conversion of methanol to formaldehyde. However, addition of vanadia to metal oxides decreases conversion compared to pure oxides.[96] Briand *et al.* compared product distribution in methanol oxidation for a variety of different vanadates (Ni, Fe, Co, Mg, Cr, Al, Cu etc.) with pure metal oxides.[39] They have shown that the surface of bulk metal vanadates is composed of vanadium oxide species VO_x which are highly selective towards formaldehyde at low and high methanol conversions. Comparing activity results in methanol oxidation at 300 °C, it was shown that iron vanadate is more active and selective towards formaldehyde (conversion 94 and selectivity 95 %) than industrial iron molybdate (conversion and selectivity 91 and 94.8 % respectively). Haggblad *et al.* studied $Fe_{1-x}VAl_xO_4$ systems and have shown that compared to the industrial iron molybdate catalyst the vanadates were more active per unit surface area and less selective to formaldehyde at high methanol conversions (~90% vs 93%). Substituting Al for Fe gave a slightly improved activity but had no notable effect on the selectivity to formaldehyde.[93] Isaguliants and Belomestnykh reported V-Mg-O catalyst showing 94 % formaldehyde yield at the selectivity of 97 % at 450 °C under optimised reaction conditions.[94]

Characterization of vanadate surface species by multiple techniques had demonstrated that at low coverage the active site is VO_4 consisting of a single V=O (mono-oxo) bond and

three V-O-M bonds (M=V or support cation), irrespective of support composition. Both, the isolated and polymerized VO_4 species exist on the surface and the degree of polymerisation increases with the increase of coverage. Though the structure of surface vanadia species is the same on different supports, the nature of the support plays an important role in determining catalytic activity, which still has not been understood.[98-99]

There are several reports regarding Sb-containing systems as effective catalysts for methanol oxidation. For instance, a high performance of a mechanical mixture of Sb_2O_4 and MoO_3 with formaldehyde yield of 93.5 % at 450 °C was observed by Castillo.[100]

An interesting study was performed by Liu and Iglesia[101] showing activity of RuO_2 domains supported on common metal oxides (SnO_2, ZrO_2, TiO_2, Al_2O_3, SiO_2) in low temperature (27-127 °C) oxidation of methanol. The products observed were formaldehyde (< 25 % selectivity), methyl formate (<83 % selectivity), dimethoxy methane (< 67 % selectivity) and CO_x (< 16 % selectivity). Depending on the support the product distribution varied significantly.

1.5. Previous studies in Bowker group

Significant research into selective oxidation of methanol to formaldehyde over iron molybdate catalysts has been carried out in the Bowker group over several years.[102-109] Starting from a comparison of catalytic properties of an industrial iron molybdate catalyst with single oxides, the research later moved to more in-depth studies. The effects of variation of different parameters such as synthesis methods, catalyst composition (Mo/Fe ratio) and reaction conditions (space velocity) on the catalyst activity were investigated.[109] Other aspects of investigations concerned the synergy effect in MoO_3-$Fe_2(MoO_4)_3$ catalyst,[108] the role of different oxygen types in iron molybdate,[104] molybdenum surface segregation in iron molybdate[107] and reduction processes in iron molybdate.[102, 105] To characterize the catalytic

properties of iron molybdate catalysts a pulse flow reactor (PFR) and temperature programmed desorption (TPD) techniques were used. Structural, compositional and morphological properties of the samples were characterized by such methods as XPS, XRD, Raman, BET, TEM.

In the early paper Bowker *et al.*[103] reported on the methanol oxidation over industrial iron molybdate and single oxides. Using TPD it was shown that desorption of formaldehyde is only observed over MoO_3 as the product of decomposition of the surface methoxy species, while quite opposite, on the iron oxide desorption of only the combustion products CO_2 and H_2 was observed. The industrial catalyst was shown to be more active than molybdena with conversion beginning at 150 °C versus 270 °C for MoO_3. Its selectivity stayed 100 % in the temperature range ~170-220 °C. In this work the energy profile for the reaction was proposed with the energy barrier of 132 kJ mol^{-1} in the rate-limiting step of hydrogen abstraction from methoxy.

Varying the Mo/Fe ratio in iron molybdates from 0.2:1 to 4:1, it was shown that catalysts with Mo/Fe ratio 1.5 or lower lose selectivity at high conversions and produce CO (intermediate ratios) or CO_2 (low ratios), while the catalysts with Mo/Fe ratio above stoichiometric kept formaldehyde selectivity above 90 % even at 90 % conversion. Better activity of iron molybdate compared to molybdena was explained by: (i) more favourable morphology of MoO_3 layer due to the underlaying ferric molybdate, (ii) higher surface area of iron molybdate, (iii) higher oxygen mobility due to the presence of Fe in the lattice.[106]

Using scanning transmission electron microscopy (STEM) it was shown that molybdenum segregates on the surface of $Fe_2(MoO_4)_3$ forming a complete cover by MoO_3. Therefore, iron molybdate samples even with low Mo content show high activity and selectivity toward formaldehyde in the oxidation of methanol.[107]

The role of different oxygen types (surface and lattice) was discussed[104] and a modified Mars van Krevelen mechanism including oxygen from the bulk was suggested:

$$H\text{-}R\text{-}H + M\text{-}O_s = H\text{-}R\text{-}M\text{-}OH_s \quad (1\text{-}14)$$

$$H\text{-}R\text{-}M\text{-}OH_s = R_g + H_2O + V_s + M \quad (1\text{-}15)$$

$$V_s + O_b \leftrightarrow O_s + V_b \quad (1\text{-}16)$$

It was also suggested that both terminal and bridging oxygen sites are involved in dehydrogenation of methanol.

In a study of the synergy effect in MoO_3-$Fe_2(MoO_4)_3$ system[108] it was shown that the best performing catalyst is a mixture of crystalline phases MoO_3 and $Fe_2(MoO_4)_3$. Based on the results of surface analysis by SEM, XPS, HRTEM and STEM-EDS methods, it was reported that iron molybdate served as a support for the active structure in the oxidation of methanol, the latter being an amorphous surface layer with a higher Mo/Fe ratio compared to the bulk and with Mo in octahedral coordination.

In order to investigate the process of iron molybdate reduction, methanol was pulsed over an iron molybdate catalyst under anaerobic conditions.[105] It was shown that the catalyst is efficient and selective to formaldehyde even without oxygen in the gas-phase (> 90 % selectivity at ~90 % conversion at 340 °C), which is indicative of participation of the surface and the lattice oxygen in the process. When lattice oxygen is removed the bulk iron molybdate and molybdena convert to MoO_2, Mo_4O_{11} and α-$FeMoO_4$ leading to a decrease in formaldehyde selectivity and production of CO and CO_2. A detailed study of the comparative activity of MoO_3 and MoO_2 oxides in the oxidation of methanol proved that the oxidation state of molybdenum is crucial for the selectivity towards formaldehyde and must be the highest (+6) during the reaction.[102]

Model monolayer MoO_3-Fe_2O_3 systems with different molybdenum loading were studied and it was shown that the addition of very small amounts of Mo to iron oxide changes its catalytic properties drastically.[109] Thus, addition of 0.6 monolayer of MoO_3 resulted in significant suppression of CO_2 formation and production of formaldehyde and CO especially at lower temperatures (55 % and 43 % selectivity respectively at 30 % conversion and reaction temperature 180 °C). However at higher molybdenum loadings the product distribution seemed to be not so much dependent on the catalyst composition.

1.6. Nanomagnetism and catalysis

In the last years nanomagnetism became a very popular scientific field.[110-112] Nanomagnetism is the discipline dealing with magnetic phenomena specific to structures having dimensions in the submicron range. As a subfield of nanoscience, nanomagnetism shares many of the same basic principles, such as geometric confinement, physical proximity, and chemical self-organization.[110] The atomic exchange interaction that defines ferromagnetism is typically on the length scale of 10 nm for most materials. Competition between the exchange interaction and magnetic anisotropy leads to domain formation, with a domain wall width also in the nanometer region. When the dimensions of the materials become comparable to these length scales, new properties begin to emerge, such as enhanced magnetic moments, exchange-coupled dynamics, quantization of spin waves and giant magnetoresistance. These new properties lead to potential applications in different scientific fields and especially in catalysis. Research and applications of these unique features of magnetic nanostructures start with the material synthesis and fabrication.[112] A significant body of literature has been dedicated to the problem of nanoparticles synthesis. We will focus on the synthesis of Fe-Co-based systems, as they are used in the present study as magnetic systems.

The synthesis and magnetic structure characterization of metastable spinel nanoferrites have been investigated with much interest and a lot of attention has been focused on the preparation and characterization of superparamagnetic metal oxide nanoparticles of spinel ferrites, $CoFe_2O_4$.[113-117] The rich crystal chemistry of spinel ferrite systems offers excellent opportunities for understanding and fine-tuning the superparamagnetic properties of nanoscale by chemical manipulations.[118]

Cobalt ferrite, with a partially inverse spinel structure, is one of the most abundant magnetic materials. As a conventional magnetic material, with a Curie Temperature (T_c) about 520 °C, $CoFe_2O_4$ is well known to have large multiaxial magnetic anisotropy ($K=2*10^6$ *erg/cc)*, moderate magnetization saturation, remarkable chemical stability and mechanical hardness.[118] The cubic anisotropy of cobalt ferrite leads to a more complex system of energy barriers. In a system where K is greater than zero there are six easy directions along the cube edges of the crystal, four hard directions across the body diagonals and twelve saddle points across the face diagonals. The magnetization process will therefore differ from those of a system of particles with uniaxial anisotropy. Due to the presence of six easy directions there is a greater probability that the randomly aligned particles will have an easy direction close to any direction in which field is applied.[119]

The magnetic characteristics of ferrite particles depend critically on their size and shape. There is a critical size, d_{SD}, below which it remains a single domain. There also exists a characteristic size of the particle, d_{Sp}, below which the material becomes superparamagnetic (SP) at the temperature of operation, i.e., no hysteresis, zero coercivity and zero remanence at the temperature of operation. Size reduction in magnetic materials resulting in the formation of single-domain particles also gives rise to the phenomenon of superparamagnetism. Briefly, superparamagnetism occurs when thermal fluctuations or an applied field can easily move the magnetic moments of the nanoparticles away from the easy axis, the preferred

crystallographic axes for the magnetic moment to point along. Each particle behaves like a paramagnetic atom, but with a giant magnetic moment, as there is still a well-defined magnetic order in each nanoparticle.[118, 120]

Investigation of $CoFe_2O_4$ particle size dependence on annealing temperature has been carried out.[121] The samples prepared by co-precipitation method were calcined at 100, 300, 500, 700 and 900 °C. The $CoFe_2O_4$ particle size (as was determined by XRD and TEM methods) varied from 4-10 nm for the samples calcined at 100°C to 100 nm for samples calcined at 900°C. Magnetic characterization of these samples has shown the absence of saturation and coercivity in the B-H curve of samples annealed at 100°C, that indicates the superparamagnetic nature of the particles which relax back their spins by rotation on the removal of an applied magnetic field, so as to give a zero net magnetic moment. SP occurs when the material is composed of very small particles (4-12 nm). Also, it was shown that coercivity goes from 0 for 100°C calcined samples through the maximum for the 700 °C calcined samples. And it was explained on the basics of the domain structure and particle size: the initial increase in coercivity is due to the increase in particle size from the SP size range (4-12 nm) to the single domain size (35-40nm), which then decreases on further annealing due to the formation of multi-domains (growth) after the single-domain size limit of the $CoFe_2O_4$ nano-particles.[121]

Previous investigations have shown that the use of magnetic materials in catalysis has a certain effect on reaction *e.g.* the change of activation energy in the vicinity of the Curie point of the material (see Chapter 4 for more details). However, the observed effects were not proved and explained sufficiently. Development of magnetic materials with tunable characteristics could give us an interesting possibility of discovering new relationship between different scientific fields.

1.7. Research objectives

The main objective of this thesis was to study methanol oxidation over mixed oxides catalysts. It is divided into two parts of investigation with their own sub tasks. The first part is concerned with the behavior of monolayer oxide systems of molybdenum over iron oxide and cobalt ferrite in the oxidation of methanol. The effect of the amount of molybdenum loaded onto the Fe_2O_3 and $CoFe_2O_4$ supports on the structural and morphological properties of the samples, and on the catalytic activity and products distribution in methanol oxidation are studied. The second part is concerned with the establishment of the relationship between the magnetic properties and catalytic behaviour of magnetic Zn-doped $Mo/CoFe_2O_4$ systems using oxidation of methanol as a model reaction. Structural and physical properties of Zn-doped systems compared to pure cobalt ferrite are presented as well. Catalytic activity of all samples in oxidation of methanol is studied using the fixed bed pulse flow reactor via temperature programmed pulse flow reaction (TPPFR), isothermal experiments and temperature programmed desorption (TPD). To characterize structure and morphology, surface composition and magnetic properties of investigated samples such techniques as Raman spectroscopy, XRD, TEM, XPS and magnetic susceptibility measurement were used.

The first results chapter deals with monolayer Mo/Fe_2O_3 ($CoFe_2O_4$) systems, their structural properties and activity in methanol oxidation. The dependence of the catalyst activity and selectivity on the molybdenum loading is shown. As the differences in catalytic behaviour arise from the differences in phase composition of the investigated catalysts, the suggested compositional models of both iron oxide and cobalt ferrite based systems are presented in accordance with Raman spectroscopy, XRD and XPS data.

The aim of the second results chapter is to investigate whether there is any correlation between catalytic performance and magnetic properties of materials, particularly the changes in activity of the catalyst in the vicinity of the Curie transition are studied. Oxidation of

methanol is used as a model reaction, and Mo loaded Zn-doped cobalt ferrite systems are used as the catalysts. Detailed characterisation of Zn-doped cobalt ferrites and engineering of the samples with the desired Curie temperature by varying Zn content and calcination temperature are described in this chapter. Investigations of the relationship between activity and ferromagnetic transition are studied using TPPFR and isothermal experiments with and without the presence of magnetic field.

A final concluding chapter summarises all the discussed data and relates this to the aims of the research. A possible development of this work in the future is included in this chapter.

1.8. References

1. Lindström, B.; Pettersson, L. J., *CATTECH* **2003,** *7*, 130-138.
2. Satterfield, C. N., *Heterogeneous catalysis in Practice*. McGraw-Hill, Inc.: 1980.
3. J.M. Thomas, W. J. T., *Principles and Practice of Heterogeneous Catalysis*. VCH: Weinheim; New York; Basel; Cambridge; Tokyo, 1997.
4. Armor, J. N., *Catalysis Today* **2011,** *163*, 3-9.
5. Langmuir, I., *Phys. Rev* **1915,** *6*, 79.
6. Arends, I. W. C. E.; Sheldon, R. A., *Applied Catalysis A: General* **2001,** *212*, 175-187.
7. Buijs, W., *Topics in Catalysis* **2003,** *24*, 73-78.
8. Cavani, F., *Catalysis Today* **2010,** *157*, 8-15.
9. Cavani, F.; Ballarini, N.; Cericola, A., *Catalysis Today* **2007,** *127*, 113-131.
10. Cavani, F.; Ballarini, N.; Luciani, S., *Topics in Catalysis* **2009,** *52*, 935-947.
11. Centi, G.; Trifiro, F., *Applied Catalysis* **1984,** *12*, 1-21.
12. Dubois, J.-L., *Catalysis Today* **2005,** *99*, 5-14.
13. Hermans, I.; Spier, E.; Neuenschwander, U.; Turrà, N.; Baiker, A., *Topics in Catalysis* **2009,** *52*, 1162-1174.
14. Panov, G. I.; Dubkov, K. A.; Starokon, E. V., *Catalysis Today* **2006,** *117*, 148-155.
15. Rafelt, J. S.; Clark, J. H., *Catalysis Today* **2000,** *57*, 33-44.
16. Keulks, G. W., *Journal of Catalysis* **1970,** *19*, 232-235.
17. Wragg, R. D.; Ashmore, P. G.; Hockey, J. A., *Journal of Catalysis* **1971,** *22*, 49-53.
18. Liberti, G.; Pernicone, N.; Soattini, S., *Journal of Catalysis* **1972,** *27*, 52-55.
19. Pernicone, N.; Lazzerin, F.; Liberti, G.; Lanzavecchia, G., *Journal of Catalysis* **1969,** *14*, 391-393.
20. Waugh, K. C., *Catalysis Today* **1992,** *15*, 51-75.
21. Olah, G. A., *Angewandte Chemie-International Edition* **2005,** *44*, 2636-2639.
22. Olah, G. A.; Goeppert, A.; Prakash, G. K. S., *Journal of Organic Chemistry* **2009,** *74*, 487-498.
23. Ushikoshi, K.; Mori, K.; Kubota, T.; Watanabe, T.; Saito, M., *Appl. Organometal. Chem.* **2000,** *14*, 819-825.

24. Tatibouët, J. M., *Applied Catalysis A: General* **1997,** *148*, 213-252.
25. Pernicone, N., *Journal of the Less Common Metals 36*, 289-297.
26. Trifirò, F.; Notarbartolo, S.; Pasquon, I., *Journal of Catalysis* **1971,** *22*, 324-332.
27. Alessandrini, G.; Cairati, L.; Forzatti, P.; Villa, P. L.; Trifirò, F., *Journal of the Less Common Metals* **1977,** *54*, 373-386.
28. Fagherazzi, G.; Pernicone, N., *Journal of Catalysis* **1970,** *16*, 321-325.
29. Sun-Kou, M. R.; Mendioroz, S.; Fierro, J. L. G.; Palacios, J. M.; Guerrero-Ruiz, A., *Journal of Materials Science* **1995,** *30*, 496-503.
30. G.K. Boreskov, G. D. K., L.M. Kefeli, L.M. Plyasova, L.G. Karakchiev, V.N. Mastikhin, V.I. Popov, V.A. Dzisko, D.V. Tarasova, *Kinet. Catal.* **1965,** *7*, 125.
31. Trifirò, F.; Carbucicchio, M.; Villa, P. L., *Hyperfine Interactions* **1998,** *111*, 17-22.
32. Soares, A. P. V.; Farinha Portela, M.; Kiennemann, A.; Hilaire, L.; Millet, J. M. M., *Applied Catalysis A: General* **2001,** *206*, 221-229.
33. Routray, K.; Zhou, W.; Kiely, C. J.; Gruenert, W.; Wachs, I. E., *J. Catal.* **2010,** *275*, 84-98.
34. Popov, B. I.; Pashis, A. V.; Shkuratova, L. N., *Reaction Kinetics and Catalysis Letters* **1986,** *30*, 129-135.
35. Popov, B. I.; Smokorokhova, N. G., *Reaction Kinetics and Catalysis Letters* **1982,** *18*, 107-110.
36. Popov, B. I.; Shkuratova, L. N.; Kuznetsov, V. I.; Pavlyukin, Y. T., *Reaction Kinetics and Catalysis Letters* **1984,** *25*, 255-259.
37. Del Arco, M.; Martin, C.; Rives, V.; Estevez, A.; Marquez, M.; Tena, A., *Journal of Materials Science* **1989,** *24*, 3750-3755.
38. Del Arco, M.; Martin, C.; Rives, V.; Estevez, A. M.; Marquez, M. C.; Tena, A. F., *Materials Chemistry and Physics* **1989,** *23*, 517-528.
39. Briand, L. E.; Jehng, J.-M.; Cornaglia, L.; Hirt, A. M.; Wachs, I. E., *Catalysis Today* **2003,** *78*, 257-268.
40. Burcham, L. J.; Briand, L. E.; Wachs, I. E., *Langmuir* **2001,** *17*, 6164-6174.
41. Burcham, L. J.; Briand, L. E.; Wachs, I. E., *Langmuir* **2001,** *17*, 6175-6184.
42. Chowdhry, U.; Ferretti, A.; Firment, L. E.; Machiels, C. J.; Ohuchi, F.; Sleight, A. W.; Staley, R. H., *Appl. Surf. Sci.* **1984,** *19*, 360-72.
43. Soares, A. P. V.; Portela, M. F., *Catal. Rev. - Sci. Eng.* **2005,** *47*, 125-174.
44. Soares, A. P. V.; Portela, M. F.; Kiennemann, A., *Stud. Surf. Sci. Catal.* **2001,** *133*, 489-494.
45. Tatiboueet, J. M., *Appl. Catal., A* **1997,** *148*, 213-252.
46. Edwards, J.; Nicolaidis, J.; Cutlip, M. B.; Bennett, C. O., *Journal of Catalysis* **1977,** *50*, 24-34.
47. Farneth, W. E.; Ohuchi, F.; Staley, R. H.; Chowdhry, U.; Sleight, A. W., *J. Phys. Chem.* **1985,** *89*, 2493-7.
48. Carbucicchio, M.; Trifirò, F., *Journal of Catalysis* **1976,** *45*, 77-85.
49. Nováková, J.; Jíru, P., *Journal of Catalysis* **1972,** *27*, 155-156.
50. Deshmukh, S. A. R. K.; Annaland, M. v. S.; Kuipers, J. A. M., *Applied Catalysis A: General* **2005,** *289*, 240-255.
51. O'Brien, M.; Beale, A.; Jacques, S.; Weckhuysen, B., *Topics in Catalysis* **2009,** *52*, 1400-1409.
52. Machiels, C. J.; Sleight, A. W., *Journal of Catalysis* **1982,** *76*, 238-239.
53. Holstein, W. L.; Machiels, C. J., *Journal of Catalysis* **1996,** *162*, 118-124.
54. Oyama, S. T.; Radhakrishnan, R.; Seman, M.; Kondo, J. N.; Domen, K.; Asakura, K., *J. Phys. Chem. B* **2003,** *107*, 1845-1852.

55. Ulukardesler, A. H.; Atalay, S.; Atalay, F. S., *Chemical Engineering & Technology* **2010,** *33*, 167-176.
56. Ivanov, K.; Dimitrov, D.; Boyanov, B., *Chemical Engineering Journal* **2009,** *154*, 189-195.
57. Andersson, A.; Hernelind, M.; Augustsson, O., *Catalysis Today* **2006,** *112*, 40-44.
58. Soares, A. P. V.; Portela, M. F.; Kiennemann, A.; Hilaire, L., *Chemical Engineering Science* **2003,** *58*, 1315-1322.
59. Popov, B. I., *Kinetika i Kataliz* **1976,** *17*, 322.
60. Burriesci, N.; Garbassi, F.; Petrera, M.; Petrini, G.; Pernicone, N., *Stud. Surf. Sci. Catal.* **1980,** *6*, 115-26.
61. Pernicone, N., *Catalysis Today* **1991,** *11*, 85-91.
62. Leyrer, J.; Mey, D.; Knözinger, H., *Journal of Catalysis* **1990,** *124*, 349-356.
63. Jianhong, *J. Molec Catal (China)* **1995,** *9*, 471.
64. Zhang, L.; Liu, D.; Yang, B.; Zhao, J., *Applied Catalysis A: General* **1994,** *117*, 163-171.
65. Ivanov, K. I.; Dimitrov, D. Y., *Catalysis Today* **2010,** *154*, 250-255.
66. Wachs, I. E.; Briand, L. E. In-situ regeneration of iron-molybdate catalysts for methanol oxidation to formaldehyde. WO9952630A1, 1999.
67. Wachs, I. E., *Surface Science* **2003,** *544*, 1-4.
68. Nagy, A.; Mestl, G.; Rühle, T.; Weinberg, G.; Schlögl, R., *Journal of Catalysis* **1998,** *179*, 548-559.
69. Qian, M.; Liauw, M. A.; Emig, G., *Applied Catalysis A: General* **2003,** *238*, 211-222.
70. Waterhouse, G. I. N.; Bowmaker, G. A.; Metson, J. B., *Applied Catalysis A: General* **2004,** *266*, 257-273.
71. Deng, J.; Xu, X.; Wang, J.; Liao, Y.; Hong, B., *Catalysis Letters* **1995,** *32*, 159-170.
72. Millar, G. J.; Nelson, M. L.; Uwins, P. J. R., *Journal of Catalysis* **1997,** *169*, 143-156.
73. Cao, Y.; Dai, W.-L.; Deng, J.-F., *Applied Catalysis A: General* **1997,** *158*, L27-L34.
74. Dai, W. L.; Li, J. L.; Cao, Y.; Liu, Q.; Deng, J. F., *Catalysis Letters* **2000,** *64*, 37-40.
75. Pestryakov, A. N., *Catalysis Today* **1996,** *28*, 239-244.
76. Estévez Sánchez, A.; Fernández Tena, A.; Márquez Moreno, M., *Reaction Kinetics and Catalysis Letters* **1989,** *38*, 193-198.
77. Klissurski, D.; Rives, V.; Pesheva, Y.; Mitov, I.; Abadzhjieva, N., *Catalysis Letters* **1993,** *18*, 265-271.
78. Popov, B. I.; Shkuratova, L. N.; Skorokhova, N. G., *Reaction Kinetics and Catalysis Letters* **1975,** *3*, 463-469.
79. Ivanov, K.; Krustev, S.; Litcheva, P., *Journal of Alloys and Compounds* **1998,** *279*, 132-135.
80. Ivanov, K.; Mitov, I.; Krustev, S., *Journal of Alloys and Compounds* **2000,** *309*, 57-60.
81. Cairati, L.; Di, F. L.; Forzatti, P.; Pasquon, I.; Trifiro, F., *Ind. Eng. Chem. Process Des. Dev.* **1980,** *19*, 561-5.
82. Carbucicchio, M., *The Journal of Chemical Physics* **1979,** *70*, 784-787.
83. Carbucicchio, M.; Trifirò, F., *Journal of Catalysis* **1980,** *62*, 13-18.
84. Carbucicchio, M.; Trifirò, F.; Vaccari, A., *Journal of Catalysis* **1982,** *75*, 207-218.
85. Dias, A. P. S.; Rozanov, V. V.; Waerenborgh, J. C. B.; Portela, M. F., *Applied Catalysis A: General* **2008,** *345*, 185-194.
86. Hill, C. G.; Wilson, J. H., *Journal of Molecular Catalysis* **1991,** *67*, 57-77.
87. Wilson, J. H.; Hill, C. G.; Dumesic, J. A., *Journal of Molecular Catalysis* **1990,** *61*, 333-352.
88. Forzatti, P., *Reaction Kinetics and Catalysis Letters* **1982,** *20*, 213-218.

89. M. Castelo-Dias, B. F. O. C., R.M. Quinta-Ferreira, *Hyperfine Interactions* **2001,** *136*, 9.
90. Deo, G.; Wachs, I. E., *Journal of Catalysis* **1994,** *146*, 323-334.
91. Forzatti, P.; Tronconi, E.; Elmi, A. S.; Busca, G., *Applied Catalysis A: General* **1997,** *157*, 387-408.
92. Häggblad, R.; Massa, M.; Andersson, A., *Journal of Catalysis* **2009,** *266*, 218-227.
93. Häggblad, R.; Wagner, J. B.; Hansen, S.; Andersson, A., *Journal of Catalysis* **2008,** *258*, 345-355.
94. Isaguliants, G. V.; Belomestnykh, I. P., *Catalysis Today* **2005,** *100*, 441-445.
95. Kim, T.; Wachs, I. E., *Journal of Catalysis* **2008,** *255*, 197-205.
96. Malinski, R.; Akimoto, M.; Echigoya, E., *Journal of Catalysis* **1976,** *44*, 101-106.
97. Vuurman, M. A.; Wachs, I. E., *Journal of Molecular Catalysis* **1992,** *77*, 29-39.
98. Burcham, L. J.; Wachs, I. E., *Catalysis Today* **1999,** *49*, 467-484.
99. Bronkema, J. L.; Bell, A. T., *The Journal of Physical Chemistry C* **2008,** *112*, 6404-6412.
100. Castillo, R.; Dewaele, K.; Ruiz, P.; Delmon, B., *Applied Catalysis A: General* **1997,** *153*, L1-L8.
101. Liu, H.; Iglesia, E., *The Journal of Physical Chemistry B* **2004,** *109*, 2155-2163.
102. Bowker, M.; Carley, A. F.; House, M., *Catal. Lett.* **2008,** *120*, 34-39.
103. Bowker, M.; Holroyd, R.; Elliott, A.; Morrall, P.; Alouche, A.; Entwistle, C.; Toerncrona, A., *Catal. Lett.* **2002,** *83*, 165-176.
104. Bowker, M.; Holroyd, R.; House, M.; Bracey, R.; Bamroongwongdee, C.; Shannon, M.; Carley, A., *Top. Catal.* **2008,** *48*, 158-165.
105. House, M. P.; Carley, A. F.; Bowker, M., *J. Catal.* **2007,** *252*, 88-96.
106. House, M. P.; Carley, A. F.; Echeverria-Valda, R.; Bowker, M., *J. Phys. Chem. C* **2008,** *112*, 4333-4341.
107. House, M. P.; Shannon, M. D.; Bowker, M., *Catal. Lett.* **2008,** *122*, 210-213.
108. Soederhjelm, E.; House, M. P.; Cruise, N.; Holmberg, J.; Bowker, M.; Bovin, J.-O.; Andersson, A., *Top. Catal.* **2008,** *50*, 145-155.
109. House, M. The selective oxidation of methanol over iron molybdate catalysts. Cardiff University, Cardiff, **2006**.
110. Bader, S. D., *Rev. Mod. Phys.* **2006,** *78*, 1-15.
111. Bader, S. D.; Buchanan, K. S.; Chung, S. H.; Guslienko, K. Y.; Hoffmann, A.; Ji, Y.; Novosad, V., *Superlattices Microstruct.* **2007,** *41*, 72-80.
112. Lin, X.-M.; Samia, A. C. S., *J. Magn. Magn. Mater.* **2006,** *305*, 100-109.
113. Chen, Z.; Gao, L., *Mater. Sci. Eng., B* **2007,** *141*, 82-86.
114. Gul, I. H.; Maqsood, A.; Naeem, M.; Ashiq, M. N., *J. Alloys Compd.* **2010,** *507*, 201-206.
115. Maaz, K.; Mumtaz, A.; Hasanain, S. K.; Ceylan, A., *J. Magn. Magn. Mater.* **2007,** *308*, 289-295.
116. Mueller, R.; Schueppel, W., *J. Magn. Magn. Mater.* **1996,** *155*, 110-112.
117. Vaidyanathan, G.; Sendhilnathan, S.; Arulmurugan, R., *J. Magn. Magn. Mater.* **2007,** *313*, 293-299.
118. Mathew, D. S.; Juang, R.-S., *Chem. Eng. J. (Amsterdam, Neth.)* **2007,** *129*, 51-65.
119. Virden, A.; Wells, S.; O'Grady, K., *J. Magn. Magn. Mater.* **2007,** *316*, e768-e771.
120. O'Handley, R., *Modern magnetic materials: priciples and applications*. Jon Wiley & Sons, inc. : Canada, **2000**.
121. Kumar, V.; Rana, A.; Yadav, M. S.; Pant, R. P., *J. Magn. Magn. Mater.* **2008,** *320*, 1729-1734.

Chapter 2. Experimental

2.1. Introduction

In this chapter the preparation of catalysts and characterization techniques are described. The first section is dedicated to the preparation of the catalytic materials that were tested for their activity and selectivity. Then, the pulse flow reactor, its principles and modes of operation are described. Synthesized catalysts were characterized by X-ray Diffraction (XRD), Raman Spectroscopy, low temperature nitrogen adsorption (BET method), X-ray Photoelectron Spectroscopy (XPS), Transmission Electronic Microscopy (TEM) and Magnetic Susceptibility, which are also described in this chapter.

2.2. Catalyst preparation

Catalysts for the present study were prepared by a number of methods as described below. Prior to each activity test the samples were pressed within a pellet die, crushed and sieved to produce a fraction of 650-800 μm particles in diameter.

2.2.1. Single oxides

A sample of iron oxide was prepared by dropwise addition of 50 ml iron nitrate solution to a dilute solution of 100 ml nitric acid (~pH 2, HNO_3) while stirring at 60 °C. Water was then evaporated from the sample at 90 °C before drying overnight at 120 °C and calcination in air at 500 °C for 48 hours. Cobalt oxide (Co_3O_4) provided by Dr Stuart Taylor and commercial molybdena (BDH, 99,5%) were tested for the comparison with more complex systems.

2.2.2. Iron molybdate

Co-precipitation was used to synthesize $Fe_2(MoO_4)_3$ (Fe:Mo=1:1.5) catalyst. 4.48 g of $(NH_4)_6Mo_7O_{24}*4H_2O$ was dissolved in 100 ml of deionised water before being acidified to

pH~2 using HNO_3. To this a solution of $Fe(NO_3)_3*9H_2O$ (6.38 g in 50 ml of water) was added dropwise while stirring at 60 °C. A canary yellow precipitate was formed, which was evaporated to near dryness at 90 °C. The resulting solid was dried at 120 °C overnight and calcined in air at 500 °C for 48 h.

2.2.3. Cobalt molybdate

$CoMoO_4$ was synthesized by the co-precipitation technique. To obtain 5 g of cobalt molybdate 0.5 M solution of ammonium heptamolybdate (46.5 ml) was added dropwise to the solution of 0.5 M cobalt nitrate (46.5 ml) under stirring at 80 °C. During the synthesis the pH was kept 6 by adding 1 M NH_4OH solution. After precipitation the sample was aged for 1 hour at 80 °C and 2 hours at room temperature under stirring. The precipitate of grey colour was formed. Then it was filtered, washed with distilled water, dried at 100 °C overnight and calcined in air at 500 °C for 4 hours.

2.2.4. Cobalt ferrite

To synthesize a single-phase $CoFe_2O_4$ sample two methods were used: co-precipitation and a combustion method.

Co-precipitation: to obtain 5 g of cobalt ferrite to the mixed solution of 42.6 ml of 0.5M Co^{2+} and 85.2 ml of 0.5M Fe^{3+} nitrates a 1 M solution of NH_4OH (116 ml) was added dropwise while stirring at 60 °C until pH=9. The obtained precipitate (dark red colour) was maintained at 85 °C for 3 hours. After that the precipitate was washed with distilled water, dried at 100 °C overnight and calcined on air at 500 °C for 6 hours. Another sample was prepared by adding to the mixture of 0.5 M cobalt nitrate and iron nitrate solutions a 1 M Na_2CO_3 solution while stirring at 60 °C until pH=10 was attained. The obtained precipitate was kept under stirring at room temperature for one hour. Then it was washed with distilled

water until no Na^+ ions were detected in the filtrate by atomic absorption spectroscopy (AAS), dried at 120 °C overnight and calcined in air at 500 °C for 4 hours.

A urea-nitrate combustion method[1] also was used to prepare cobalt ferrite. To the mixture of 20 ml of 0.5M cobalt and 40 ml of 0.5 M iron nitrate solutions 15 ml of urea was added. The obtained solution was heated until a viscous gel formed. After that the sample was placed into oven preheated to 400 °C, and an auto-ignition reaction occurred, producing a black powder.

2.2.5. Zn-substituted cobalt ferrites

Zn-substituted $Zn_xCo_{1-x}Fe_2O_4$ samples, where x ranges from 0.1 to 0.5 (denoted as Zn_xCF), were prepared the same way *via* the co-precipitation method. To obtain 6g of sample to the mixture of 0.5 M zinc, cobalt and iron nitrate solutions (Table 2-1) 1 M Na_2CO_3 solution was added while stirring at 60 °C until pH=10 was attained. The precipitate was then maintained in solution while stirring at room temperature for one hour. Then it was washed with distilled water until no Na^+ ions were detected in the filtrate by AAS, dried at 120 °C overnight and calcined in air at 500 °C for 4 hours. A series of samples calcined at high temperatures was produced by additional calcination of obtained samples at 600 °C, 700 °C, 800 °C, 900 °C or 1000 °C for 1 hour.

Table 2-1. Volumes of Zn^{2+}, Co^{2+} and Fe^{3+} nitrate solutions used in the synthesis of $Zn_xCo_{1-x}Fe_2O_4$ samples.

Sample	$V_{Zn\ nitrate}$, ml	$V_{Fe\ nitrate}$, ml	$V_{Co\ nitrate}$, ml
$Zn_{0.1}CF$	5.1	101.9	45.9
$Zn_{0.2}CF$	10.2	101.8	40.7
$Zn_{0.3}CF$	15.2	101.5	35.5
$Zn_{0.4}CF$	20.2	101.2	30.4
$Zn_{0.5}CF$	25.2	100.9	25.2

2.2.6. Molybdenum impregnated monolayer samples

Mo/Fe_2O_3, $Mo/CoFe_2O_4$ and $Mo/Zn_xCo_{1-x}Fe_2O_4$ with different amount of monolayers (from 1 to 9) catalysts were prepared by the incipient wetness impregnation method. Normally 1 g of a sample was impregnated with $(NH_4)_6Mo_7O_{24}$ solution of different concentrations (from 25 to 1990 g L^{-1}).

In calculating the loading of Mo to add on the iron oxide, it was assumed that a surface of Fe_2O_3 contains 10^{19} surface sites m^2, with a total of 5/12 of these being metal cations as it was thought a $Fe_2(MoO_4)_3$ layer may form. The catalysts were made by the incipient wetness impregnation onto a synthesised Fe_2O_3 with a surface area of 12 m^2/g. Ammonium heptamolybdate (AHM) was made into an aqueous solution and added to iron oxide until the pores of the support were full. The material was then dried overnight at 120 °C. Calcination of the material was carried *in-situ* in 10 % O_2/He gas flow after loading to the reactor at 400 °C for 30 minutes. Catalysts were made with 1, 3, 6, 7 and 8 monolayers (ML) coverage.

Calculating the loading of Mo to add on the surface of cobalt ferrite similar considerations were used. Though instead of iron molybdate, molybdena was assumed to form as a surface layer. Catalysts were made with 2, 6 and 9 monolayers coverage, dried at 120 °C overnight and calcined *in-situ* in 10 % O_2/He gas flow at 400 °C for 30 minutes.

A number of samples for XRD and Raman spectroscopy studies were prepared by calcination of monolayer samples at 300 °C, 400 °C and 500 °C for 1 hour.

2.3. Catalyst testing: pulse flow reactor

2.3.1. Overview

To measure the activity of the prepared catalysts in methanol oxidation the home-built pulse flow microreactor (PFR) was used. In the past this reactor was used by other group members:

Jorge Soares to study CO oxidation,[2] Peter Stone to study propene oxidation/ammoxiation and NO_x storage and reduction catalysts,[3] and Matthew House to study oxidation of methanol.[4] The data obtained using PFR gives us chemical conversions, kinetic and mechanistic information. The main advantages of PFR are:

(i) small reactants pulses do not poison the surface quickly, the surface is in a transient state, since after every pulse the surface species composition returns to the initial state, unless irreversible sorption or catalyst poisoning take place,

(ii) a large amount of data is collected during a short period of time (1-2 hour experiment); each pulse contains kinetic data corresponding to different surface coverage, any decrease in activity due to reversible or irreversible changes are quickly picked up by the concentration response in the mass spectrometer, it is easy to identify reversible and irreversible changes to the catalyst by performing pulse experiments with different feed composition and different temperatures.

The transient nature of the PFR technique is an advantage over other more common techniques that analyze products at the steady state of the reaction (*e.g.* plug flow reactor with continuous reactant feed). A schematic diagram of the rig and labeled photographs of its parts are shown in Figure 2-1, Figure 2-2 and Figure 2-3 respectively.

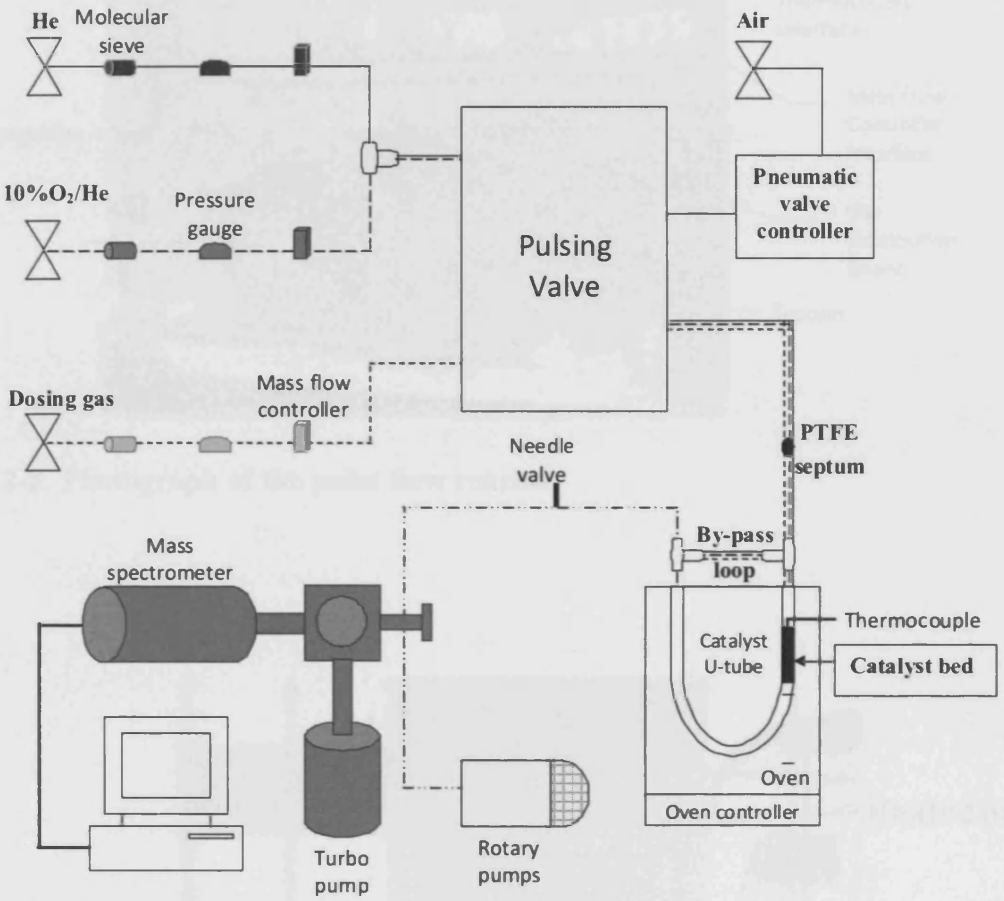

Figure 2-1. Schematic diagram of the pulse flow microreactor setup used in this study.

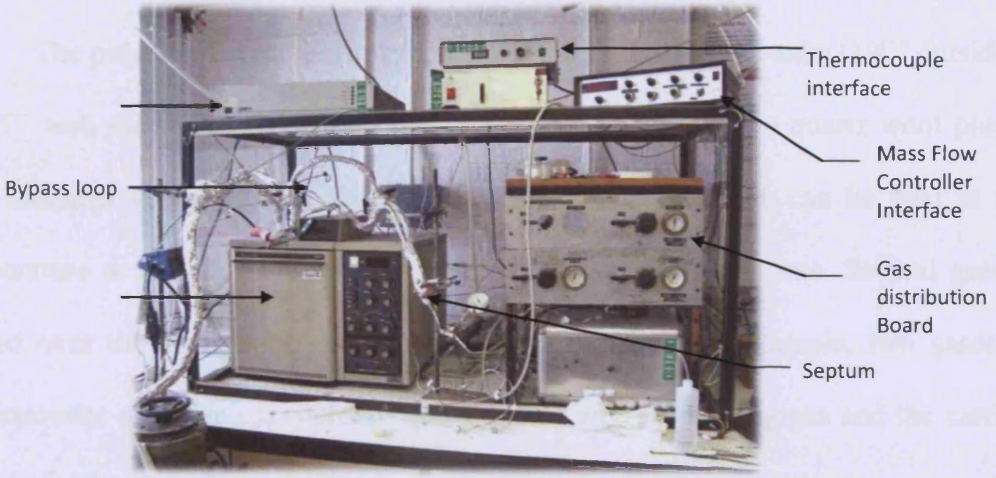

Figure 2-2. Photograph of the pulse flow reactor.

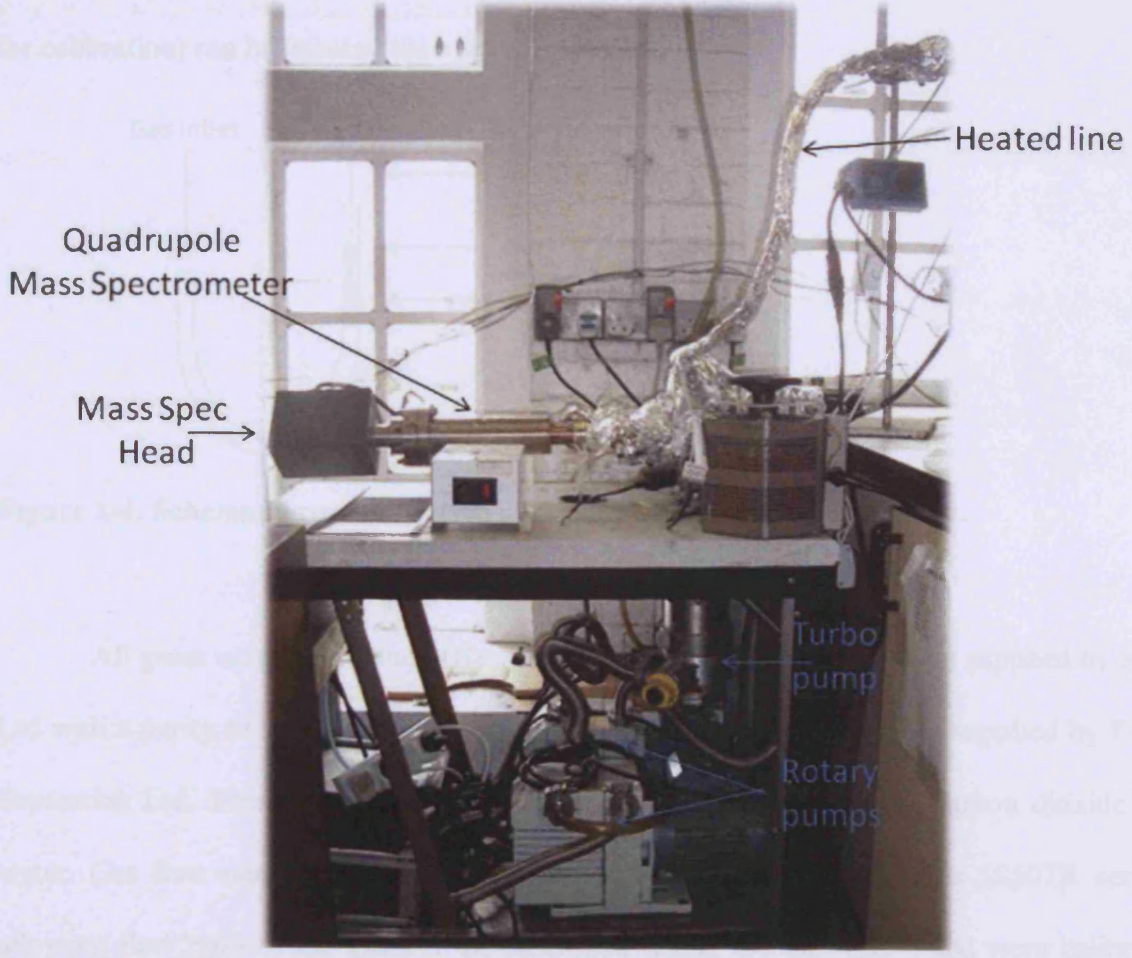

Figure 2-3. Photograph of the mass spectrometer trolley of the pulse flow reactor.

The pulse flow microreactor consists of a stainless steel U-tube (1/4'' outside diameter, 0.065'' wall thickness) containing the catalyst held between two quartz wool plugs (Figure 2-4) mounted vertically in a Phillips PU 4500 GC oven which can be held at a constant temperature or ramped between two temperatures at a constant rate. Several gases may be passed over the catalyst bed in different combinations. For example, two gases can flow continuously: a carrier gas (helium) and a dosing gas. The dosing gas and the carrier gas are joined together by a T-piece, which allows for intimate mixing of the two gases. A third gas can be introduced by means of a pneumatic sampling valve. The valve is controlled by a computer, which allows the user to set timing of the gas pulses. Further liquids or gases (in this study primarily methanol (Fisher, Laboratory grade methanol, >99.5 %), but also others for calibration) can be injected *via* a septum assembly.

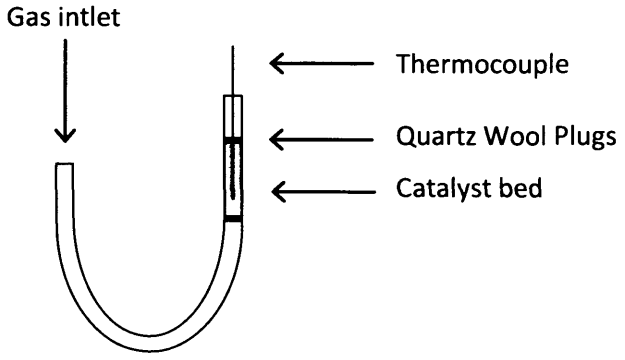

Figure 2-4. Schematic representation of a loaded U-tube for catalyst test.

All gases used in this study (He, 10 %O_2/He, CO, CO_2, H_2, O_2) were supplied by BOC Ltd with a purity of 99.5 % or greater and were passed through Puritubes supplied by Phase Separation Ltd. These were filled with 5 Å molecular sieve to remove carbon dioxide and water. Gas flow rates were controlled by mass flow controllers (Brookes 5850TR series), allowing flow rates of the gases to be controlled within 0.1 cm^3 min^{-1}, and were calibrated using a bubble flow meter both before the catalyst bed and on the exit of the capillary line

rotary pump (with the ultra high vacuum (UHV) chamber kept shut). After flowing over the catalyst bed, the reactants and products flow down a heated capillary line, with the temperature controlled by means of a variable resistor. The flow of gas to the capillary line was controlled by a needle valve, with most of the gas then vented by a Leybold Heraeus Trivac rotary pump, allowing a small fraction to be bled into the UHV chamber containing the mass spectrometer.

The mass spectrometer assembly consists of a high vacuum chamber, pumped by a Leybold 151 turbo molecular pump and backed by an Edwards 5 rotary pump. The mass spectrometer was a Hiden Analytical quadrupole Hal 201, which is computer controlled and allows for real time displaying of the results. The mass spectrometer was used with an emission of 1000 μA, a cage potential of 3 V, and a multiplier potential of 850 V. To account for sensitivity drift within the mass spectrometer, pulses of methanol were passed through the bypass before each run. It usually took around 24 second after the actual injection for reactants and products to reach mass spec chamber and being detected.

To accurately measure the temperature a thermocouple was inserted into the catalyst bed (Figure 2-4); its output was also recorded by the data acquisition computer.

2.3.2. Mass spectrometry (MS)

The main principle of mass spectroscopy is ionizing of chemical compounds to generate charged molecules or molecular fragments, accelerating the positive ions in an electric field and separating of the ions with different mass-to-charge ratio (m/z) based on the details of motion of the ions as they transit through a three-dimensional electromagnetic field.

Quadrupole analyzers are made up of four rods with circular or hyperbolic section (Figure 2-5). The rods must be perfectly parallel. A positive ion entering the space between

the rods will be drawn towards a negative rod. If the potential changes sign before an ion discharges itself on this rod, the ion will change direction.

Ions travelling along the z-axis are subjected to the influence of a total electric field made up of a quadrupolar alternative field superimposed on a constant field, resulting from the application of the potentials upon the rods: $\Phi_0 = +(U\text{-}V \cos wt)$ and $-\Phi_0 = -(U\text{-}V \cos wt)$.

In this equation Φ_0 represents the potential applied to the rods, w is the angular frequency, U is the direct potential and V is the "zero to peak" amplitude of the RF voltage.[5]

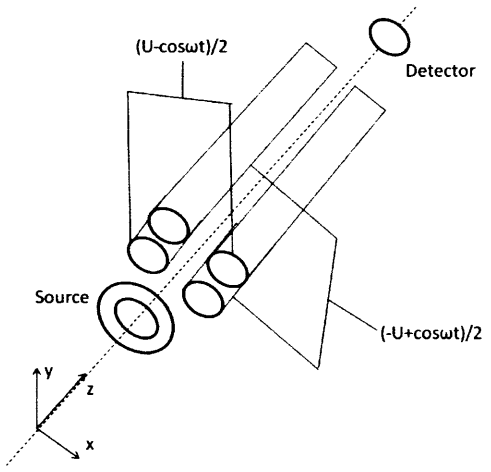

Figure 2-5. Schematic representation of basic components of a quadrupole mass spectrometer.

Once ions have escaped from the separation system they move to the ion trap, which in our case is secondary electron multiplier. It is possible with this method to detect several gases in real time.

Since each molecule has its own fragmentation spectrum, care must be taken on the choice of the masses to analyse and on the interpretation of the spectra. Table 2-2 shows the literature values for the mass spectrometer cracking patterns of the major molecules used or expected to arise in this study, recorded on a magnetic sector mass spectrometer.[6] However

these values are just semiquantative as for the quadrupole mass spectrometer the cracking patterns may be somewhat different, and calibration of the MS is needed prior to the experiment. The main masses being analyzed in this work were the following: CH_3OH (31), CH_2O (30), O_2 (32), CH_3OCH_3 (45), H_2O (18), CO (28), CO_2 (44) and H_2 (2) which correspond to the molecular masses of the respective gases. But we should consider one correction – the filament itself acts as a catalyst and gives some extra amount of several masses in the cracking pattern of methanol.

Table 2-2. Cracking patterns of molecules of interest.[6]

Compound	**Cracking Fractions**
Hydrogen	2 (1000), 1 (21)
Water	18 (1000) 17 (211), 16 (09), 19 (05) 20 (03)
Carbon Monoxide	28 (1000) 12 (47), 16 (17), 29 (12), 14 (08), 30 (02), 13 (01)
Formaldehyde	29 (1000), 30 (660), 28 (330), 31 (30), 15 (06), 27 (03)
Methanol	31 (1000), 32 (717), 29 (421), 28 (90), 30 (78), 33 (11), 27 (05)
Oxygen	32 (1000), 16 (36)
Carbon Dioxide	44 (1000), 16 (94), 28 (82), 12 (67)
Dimethyl ether	45 (1000), 29 (390), 15 (240), 31 (30), 43 (10), 30 (10), 28 (09),44 (06), 42 (03), 27 (02)

Figure 2-6 shows a comparison of tabled and experimental values for methanol cracking masses. A significant difference in intensities of the same masses is observed. Also, the hot filament may act as a catalyst itself. For example, in Figure 2-6 we can observe the formation of mass 44 during the pulsing of methanol over the by-pass into a O_2/He flow,

which does not appear in the cracking pattern of methanol. This is due to oxidation of methanol on the filament.

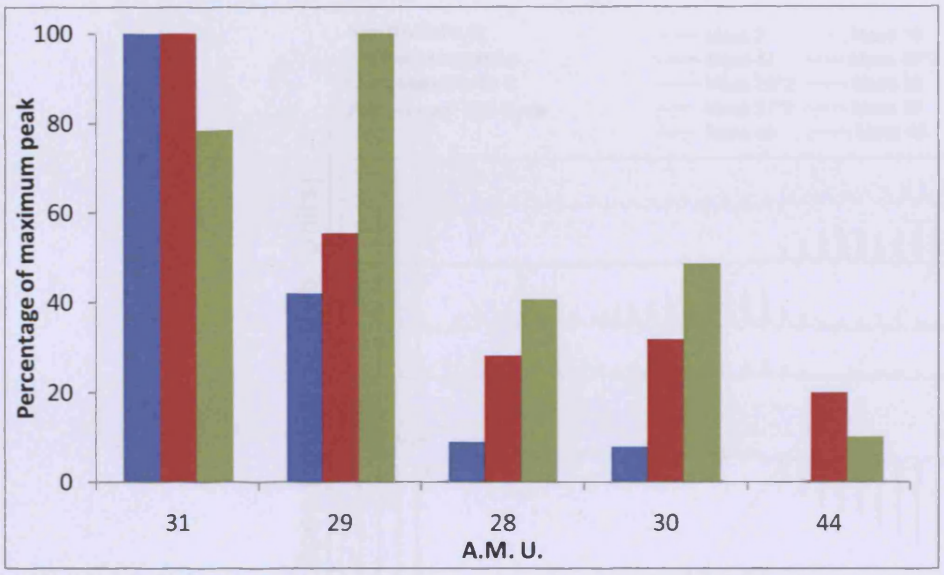

Figure 2-6. Comparison of methanol cracking masses taken from literature (blue) and obtained in present study in aerobic conditions (red) and anaerobic conditions (green).

2.3.3. Modes of operation

2.3.3.1. Temperature Programmed Pulse Flow Reaction

This mode of an experiment is used to obtain information about the products evolution during reaction at different temperatures in a single experiment. A known volume of the initial compound (in our case methanol) is periodically (every 2 minutes) injected into the gas flow of 10% O_2/He (30 mL min^{-1}) while the temperature is kept constant for a period of time, then linearly ramped (8 °C min^{-1}) up to 400 °C and dwelled again at high temperature. Figure 2-7 shows an example of raw data for methanol oxidation over the 9 ML $Mo/CoFe_2O_4$ catalyst. The first five injections starting from zero time are made over the by-pass to determine the mass spectrometer sensitivity. Starting from 10 minutes the injections are made over the catalyst bed at room temperature until the catalyst surface is saturated with methanol. The intensity of the methanol mass spec signal after the catalyst bed is much lower than after the

by-pass because the volumetric flow rate changes due to the higher pressure drop over the catalyst bed.

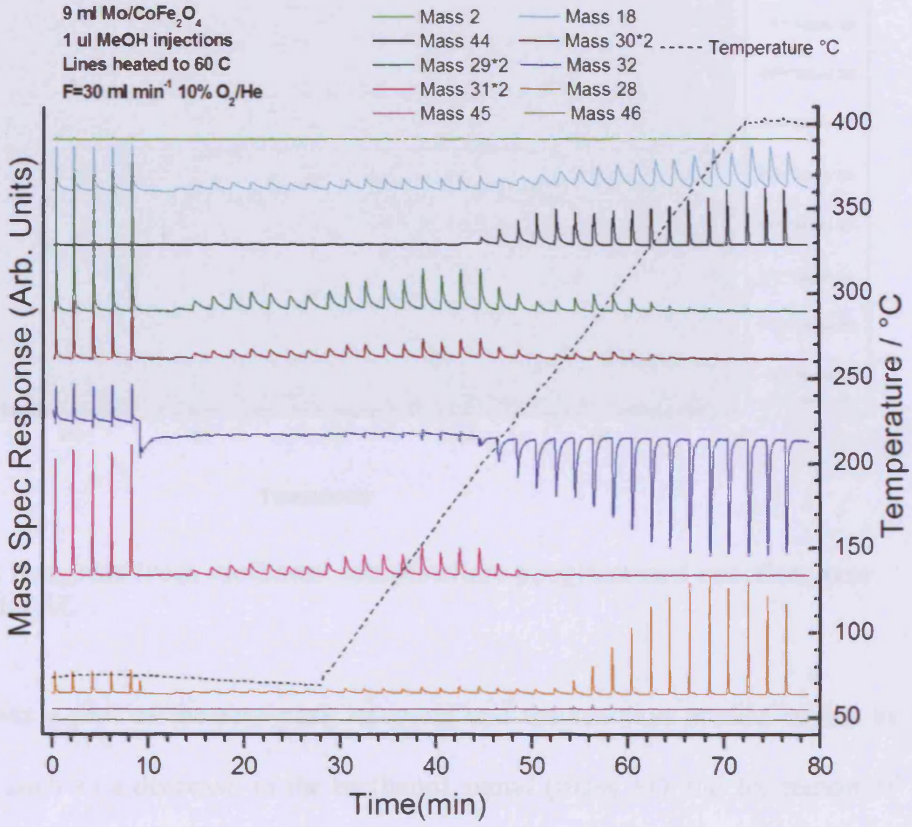

Figure 2-7. Raw data of TPPFR for methanol oxidation over the 9 $Mo/CoFe_2O_4$ catalyst.

Usually, during several first pulses no mass spectrometer response is observed. This is because methanol is fully adsorbed on the catalyst surface. Then, the signal begins to increase to some constant level with every following pulse. Once plateau is reached and all pulses have the same intensity, the temperature ramp starts and the main methanol mass 31 gradually drops to zero indicating the complete conversion of methanol. Integration of the area under the peaks allows the calculation of conversion at a given temperature.

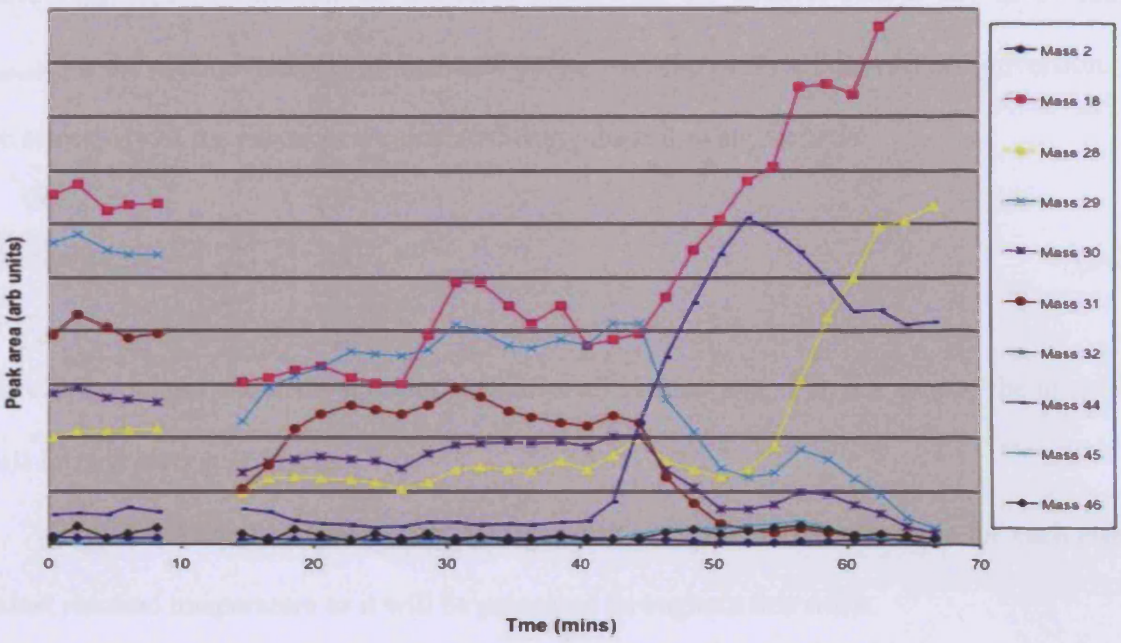

Figure 2-8. Raw peak integrals from methanol temperature programmed reaction over the 9 Mo/$CoFe_2O_4$ catalyst.

Figure 2-8 shows a plot of the raw peak integrals and the reaction profile begins to take shape as features such as a decrease in the methanol signal (mass 31) and formation of the product formaldehyde (mass 44 and mass 28) begin to be quantified.

From the raw data, the contributions of each compound to each mass line can be removed. As can be seen from the first pulses over the by-pass, methanol contributes to other mass traces. By calibration this contribution can be estimated and removed. As an example for CO, we must subtract methanol, formaldehyde and carbon dioxide contributions in the integral of mass 28 and then the residual integral is the correct response of the carbon monoxide in the mass spectrometer. Then, the subtracted integrals are adjusted for sensitivity of the mass spectrometer to each compound. Once this has been done an accurate measure of the composition of each pulse is known and from this methanol conversion can be calculated:

$$\text{Conversion (\%)} = 100 - \left(\frac{Xmethobs}{Xunreacted} \right) * 100 \qquad (2\text{-}1)$$

where $X_{meth\ obs}$ is the integral of methanol pulse over the catalyst bed at any given time, $X_{unreacted}$ is the average integral of methanol pulses over the catalyst bed with no conversion.

The selectivity of the products is calculated using the following formula:

$$\text{Selectivity (\%)} = \left(\frac{Si}{\sum_i Si} \right) * 100 \qquad (2\text{-}2)$$

where S_i is integral under the product peak after all subtractions, ΣS_i is a sum of the integrals of all formed carbon products.

Figure 2-9 shows a typical plot of calculated conversion and selectivity for each pulse against reaction temperature as it will be presented throughout this work.

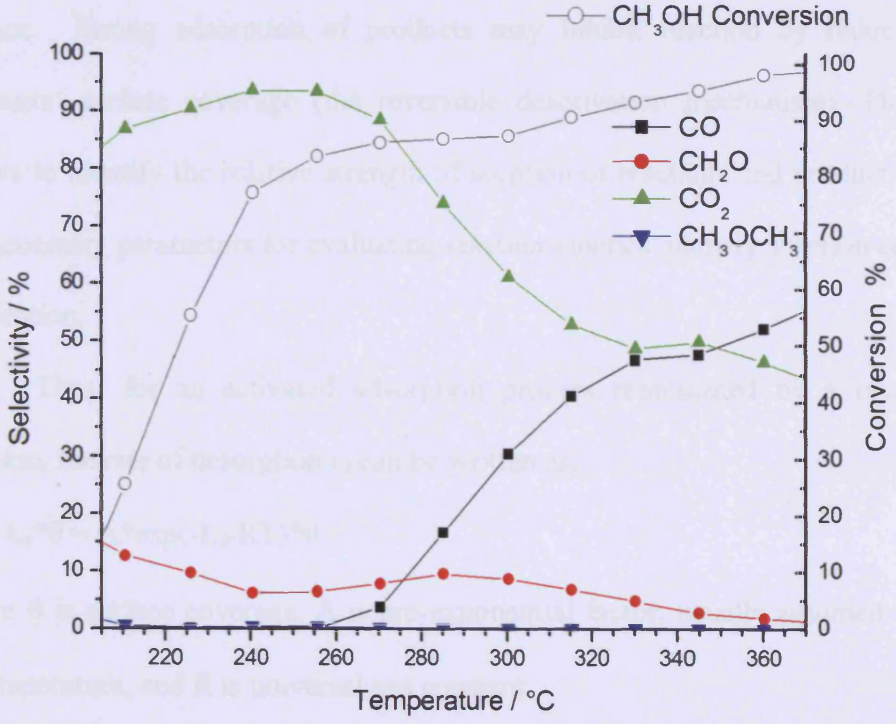

Figure 2-9. Conversion and selectivity for methanol oxidation over the 9 Mo/ $CoFe_2O_4$ catalyst.

2.3.3.2. Isothermal reaction mode

The isothermal reaction is a mode of operation when the known volume of initial compound (in our case methanol) is periodically (every 2 minutes) injected into gas (30 mL min^{-1})

flowing through the catalyst bed while the temperature is kept constant. This technique allows one to examine catalyst stability and changes in the product distribution over time.

2.3.3.3. Temperature Programmed Desorption

This mode of operation provides important information about surface coverage, reaction kinetics, mechanism and the nature of adsorption centers. The main principle of this method is saturation of a catalyst with an adsorbed reactant at a temperature where physical adsorption is prevalent and no reaction occurs (thus a maximum adsorption of a compound is achieved), followed by a linear ramp of temperature. According to the Langmuir – Hinshelwood reaction kinetic model[7] a reaction is assumed to occur between adsorbed species on the catalyst surface. Strong adsorption of products may inhibit reaction by reducing the adsorbed reactants' surface coverage (the reversible deactivation mechanism). The TPD technique allows to identify the relative strength of sorption of reactants and products and, thus, obtain the necessary parameters for evaluating reaction kinetics, namely sorption constants and heats of sorption.

Thus, for an activated adsorption process represented by a reversible first-order reaction, the rate of desorption r_d can be written as:

$$-r_d = k_d*\theta = A*\exp(-E_d/RT)*\theta \qquad (2\text{-}3)$$

where θ is surface coverage, A is pre-exponential factor, usually assumed to be independent of temperature, and R is universal gas constant.

At low temperatures, the coverage remains approximately constant so an Arrhenius plot of ln(rate) *vs.* 1/T can yield a value for E_d from the slope and hence the pre-exponential factor (A) can be derived. However, in most cases the processes are more complicated due to the changes in θ, hence an alternative equation can be used to identify the desorption energies for a particular species, by simply using the temperature of maximum desorption rate (T_p).

For a first order process Redhead has shown that the Arrhenius equation can be solved to obtain:[8]

$$\left(\frac{E_d}{RT_p^2}\right) = \frac{A}{\beta}\exp\left(\frac{-E_d}{RT_p}\right) \qquad (2\text{-}4)$$

where T_p is the temperature at which peak desorption occurs for a specific adsorbate, ß is the heating rate and A is usually assumed to be 10^{13} s^{-1}.

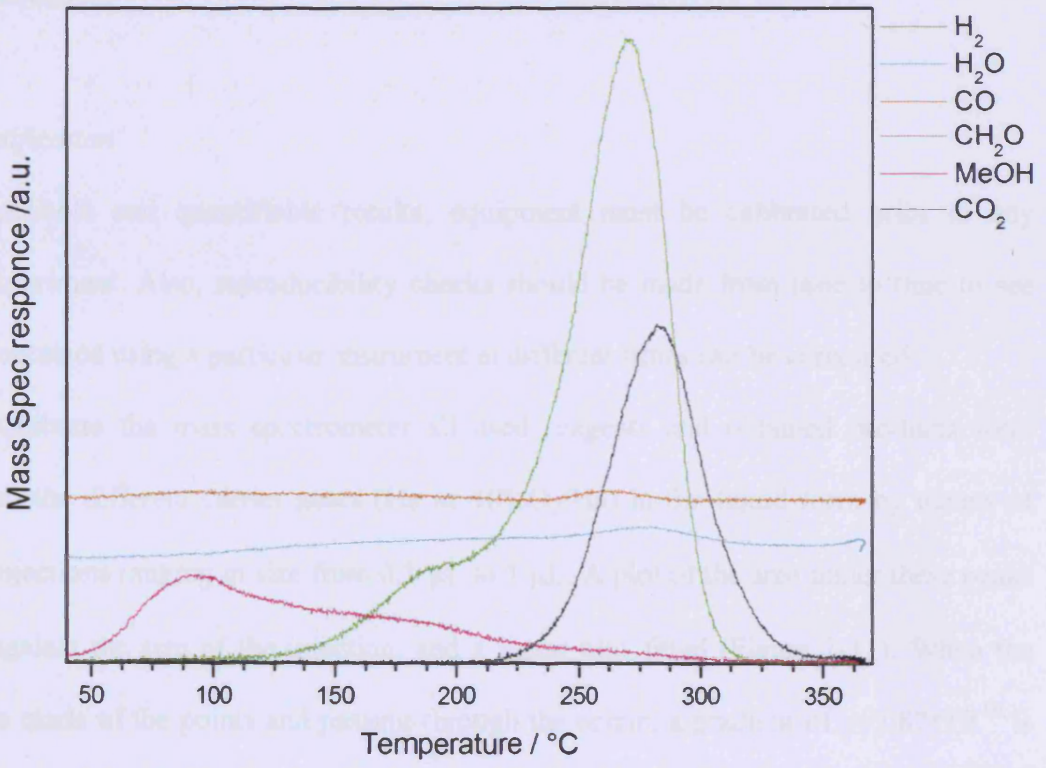

Figure 2-10. TPD of $CoFe_2O_4$ saturated with methanol at room temperature.

The raw data of the typical TPD experiment is processed to remove the cracking patterns of the molecules from each other, the effect of the filament and the sensitivity of the mass spectrometer and shown with only the molecules observed (see Figure 2-10).

The uptake of an adsorbate onto the surface can be measured by determining where the saturation breakthrough occurs. For more accurate determination the injections of very small volume (0.1 μL) of liquid can be made. Thus for a certain period of time we do not see any mass spectrometer response. When the surface is fully covered (saturated) with the pulsed compound, the breakthrough is observed in mass spectrometer signal, the signal eventually reaching an integral corresponding to the input injection. By calculating the methanol area expected and that observed by integration under peaks, the amount of reagent adsorbed on the surface is calculated.

2.3.4. Quantification

To obtain reliable and quantifiable results, equipment must be calibrated prior to any scientific experiment. Also, reproducibility checks should be made from time to time to see that results obtained using a particular instrument at different times can be compared.

To calibrate the mass spectrometer all used reagents and obtained products were introduced to the different carrier gases (He or 10%O_2/He) in the liquid form by means of series of 5 injections ranging in size from 0.1 μL to 1 μL. A plot of the area under these peaks was made against the size of the injection, and a linear plot fitted (Figure 2-11). When the linear plot is made of the points and passing through the origin, a gradient of $y=2.87*10^{-10}$ is obtained with an R^2 value of 0.998.

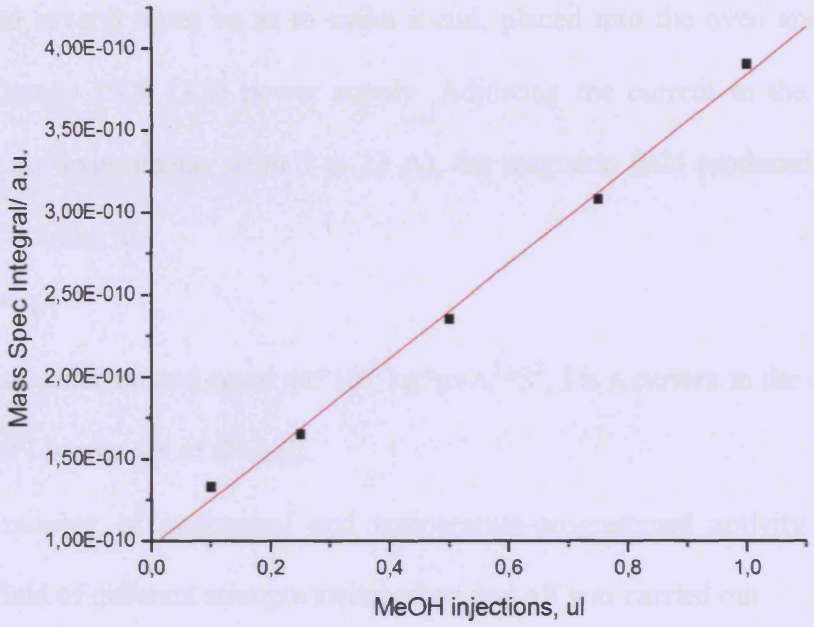

Figure 2-11. Calibration of mass 31 (methanol) in 10% O_2/He flow.

To check if the stainless steel U-tube is not active itself, a blank experiment with quartz wool normally used to hold the catalyst bed in place was carried out in a flow of 10 %O_2/He so that the influence of these components on the product concentration response could be evaluated and removed from the data obtained with a loaded catalyst if needed. The tube generally did not show significant activity; ~ 4 % conversion was observed at 400 °C with formation of CO_2.

To control the reproducibility of the reactor three separate batches of catalysts were tested at different times throughout three years of this study.

2.3.5. TPPFR experiments in a presence of magnetic field

Figure 2-12 shows a photograph of set-up constructed in order to perform catalytic experiments in the presence of a magnetic field. Stainless steel U-tube was replaced by the quartz tube the same shape, which is inert to magnetic field. The catalyst was placed into this

tube between two quart wool plugs. A thermostable copper cord was wrapped around the catalyst bed several times so as to make a coil, placed into the oven and connected to the Thorlby Thanda TSX 1820 power supply. Adjusting the current in the cord using power supply (in our experiments from 5 to 13 A), the magnetic field produced in the coil can be changed according to:

$$B = \mu_0 * I * N/l \qquad (2\text{-}5)$$

where μ_0 is a constant and equal $4\pi*10^{-7}$ kg*m/A^2*S^2, I is a current in the coil, N is a number of turns and l is a length of the coil.

A number of isothermal and temperature-programmed activity experiments with magnetic field of different strength switched on and off was carried out.

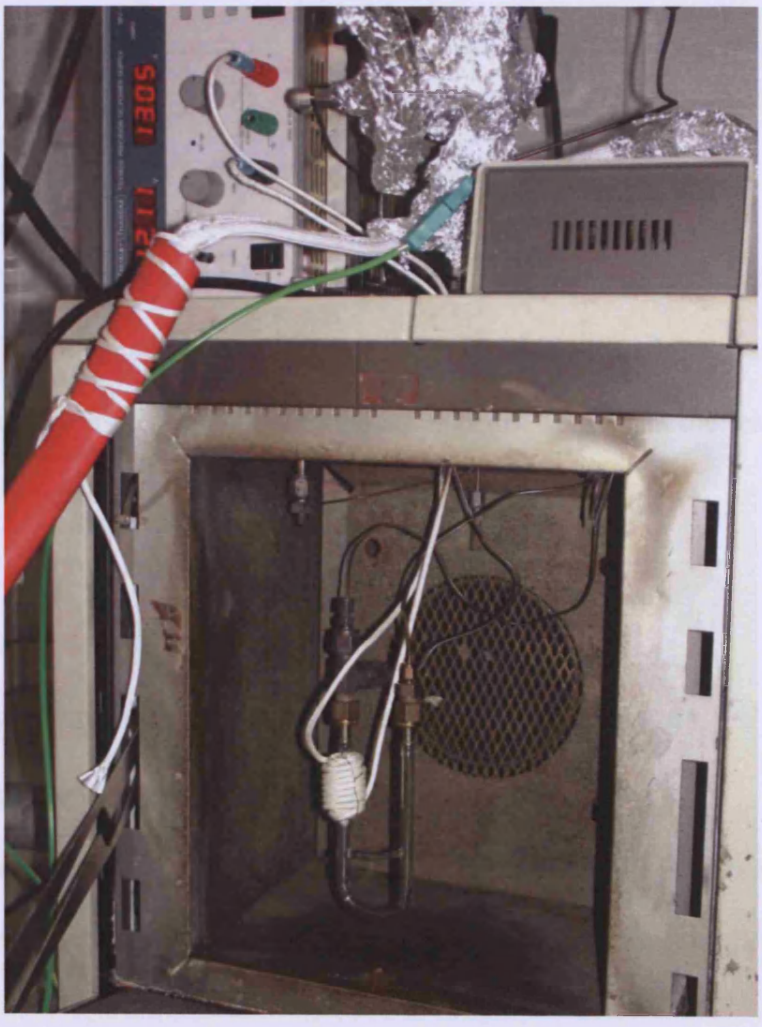

Figure 2-12. A photograph of set up for experiment with magnetic field.

2.4. X-ray Diffraction

2.4.1. Theory

X-ray powder diffraction is a technique used to determine crystalline structure and crystallite size of powdered compounds.

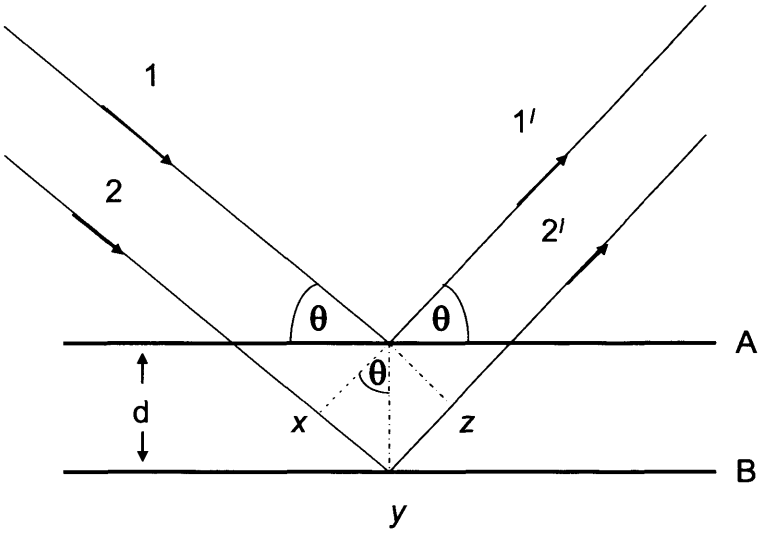

Figure 2-13. Derivation of Bragg's law for X-ray diffraction.

In this method, developed by William Bragg, crystals are regarded as build up in layers or planes which act as semi-transparent mirrors. Some of the X-rays are reflected off a plane with the angle of reflection equal to the angle of incidence, but the rest are transmitted to be subsequently reflected by succeeding planes.

Figure 2-13 shows derivation of Braggs's law:

$$2d \sin\theta = n\lambda \qquad (2\text{-}6)$$

where d is perpendicular distance between pairs of adjacent planes, θ is the angle of incidence, Bragg's angle, λ is X-ray wavelength.

Two x-ray beams are reflected from adjacent planes, A and B, within the crystal and we wish to know under which conditions the reflected beams 1'and 2' are in phase. Beam 22'

has to travel the extra distance *xyz* as compared to beam 11', and for 1' and 2' to be in phase distance *xyz* must equal to a whole number of wavelengths:

$$xy = yz = d\sin\theta, \text{ thus } xyz = 2d\sin\theta = n\lambda$$

when Bragg's law is satisfied, the reflected beams are in phase and interfere constructively. At angles of incidence other than the Bragg angle, reflected beams are out of phase and destructive interference or cancellation occurs.[9]

The principle of an XRD experiment is shown in Figure 2-14. A monochromatic beam of X-rays strikes a finely powdered sample that has crystals randomly arranged in every possible orientation. In such a powder sample, the various lattice planes are also present in every possible orientation. For each set of planes, therefore, at least some crystals must be oriented in the Bragg angle to the incident beam and thus diffraction occurs from this crystals and planes. The diffracted beams are then collected by a detector connected to a chart recorder (diffractometer).

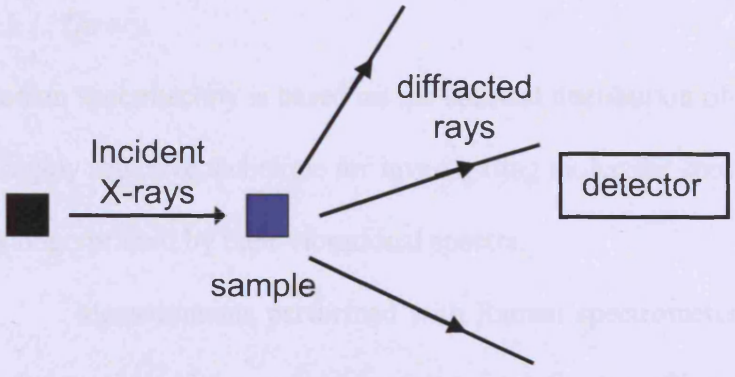

Figure 2-14. X-ray diffraction experiment.

2.4.2. Experimental

In this work XRD was used to investigate phase composition of samples before the reaction and detect compositional changes after the reaction. The X-ray powder diffraction patterns were obtained using a Chiller 59 fitted with a hemispherical analyser. The conditions

employed were Cu K_α radiation (λ=1.540598 Å) with a voltage of 40 kV and a current of 40 mA. During the experiment sample was rotated. The machine was calibrated periodically using silicon which has a well-known, well-defined and strong diffraction pattern.

The particle sizes were measured from the X-ray line broadening analysis using Debye- Scherrer equation:

$$D_{XRD} = 0.89\,\lambda / \beta \cos\theta \qquad (2\text{-}7)$$

Where λ is a wavelength of X-ray used in Å, β is full-width at half maximum (FWHM) in radians in the 2θ scale, θ is the Braggs angle.

In situ XRD experiments in O_2/He flow at the elevated temperature was performed using in-situ cell. The flow rate was adjusted to 20 ml/min and the speed of acquisition was ~ 0.6 °θ/min. The patterns were recorded at the temperatures 25-450 °C and the step time was 10 minutes. The temperature was controlled by thermocouple inserted into the cell.

2.5. Raman spectroscopy

2.5.1. Theory

Raman spectroscopy is based on the spectral distribution of inelastically scattered light and is a highly selective technique for investigating molecular species in all phases of matter, as they as fingerprinted by their vibrational spectra.

Measurements performed with Raman spectrometers are mainly based on excitation and detection of the normal (spontaneous) Raman effect. The effect is inelastic scattering process, observed in near ultraviolet (UV) visible to near infrared (IR) spectral region, which involves the interaction of a monochromatic beam of light (of frequency ν) with the molecules of the sample (Figure 2-15).

This interaction produces scattered radiation at different frequencies ($\nu+\nu_i$ *anti-Stokes* and $\nu-\nu_i$ *Stokes,* where ν_i represents a vibration frequency of the molecule). These frequency

shifts (from the exciting line) are identified with the frequencies of atom oscillations in polyatomic structures contained in the sample. In the case of Stokes lines, the molecule at $v=0$ is excited to the $v=1$ state by scattering light of frequency $v-v_i$. Anti-Stokes lines arise when a molecule initially in the $v=1$ state scatters radiation of frequency $v+v_1$ and reverts to the $v=0$ state. Since the population of molecules is larger at $v=0$ than at $v=1$, the Stokes lines are always stronger than the Anti-Stokes lines. Thus, it is customary to measure Stokes lines in Raman spectroscopy.[10-11]

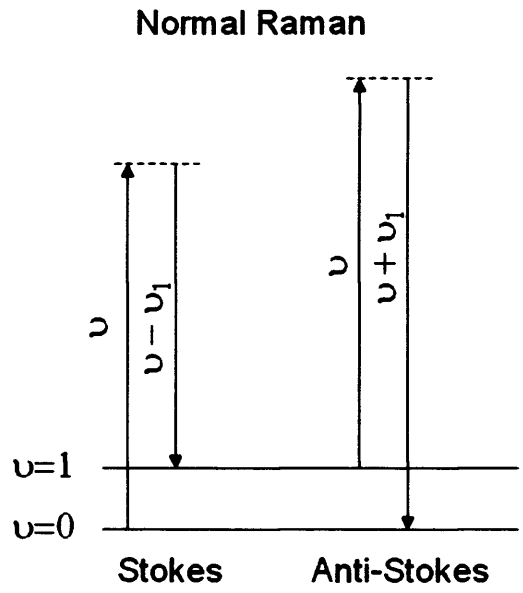

Figure 2-15. Mechanism of Raman scattering.

2.5.2. Experimental

Raman spectra were obtained using a commercial spectrometer (Horiba Jobin-Yvon LabRAM HR) equipped with a charge-couple device (CCD) detector. The 532 nm line from an argon ion laser was used to illuminate the samples at 5 mW power. Prior to each experiment the spectrometer was calibrated using silicon, which has strong Raman band at 520 cm^{-1}.

2.6. Specific surface area analysis using BET model

2.6.1. Theory

An adsorption isotherm represents the quantity of the adsorbate which can be accommodated on the surface of the solid as the function of pressure of adsorbate at constant temperature.

In 1938 Brunauer, Emmett and Teller extended the Langmuir monolayer adsorption mechanism to multilayer adsorption. The state of surface coverage, when equilibrium is reached at any given pressure, may be presented as a variable numbers of molecules being adsorbed on any one site. Within each layer dynamic equilibrium is assumed to prevail; in layer i, for example, the number of molecules evaporating per second is equated to the number of molecules condensing per second on the layer immediately below.

The BET equation describing this physical model is:

$$\left(\frac{V}{V_{mon}}\right) = \frac{C\left(\frac{P}{P_0}\right)}{(1-\frac{P}{P_0})(1+(C-1)\frac{P}{P_0})} \qquad (2\text{-}8)$$

where V is the total volume of the adsorbed material in cm^{-3}, V_{mon} is the volume corresponding to monolayer coverage in cm^{-3}, P is the equilibrium pressure for a particular surface coverage, P_0 is the vapour pressure above a layer of adsorbate that is more than one molecule thick and which resembles a pure bulk liquid, and C is a constant which is large when the enthalpy of desorption from a monolayer is large when compared with the enthalpy of vaporization of the liquid adsorbate.[12]

The constant C is equal to relative lifetimes of molecules in the first and higher layers. Since all the layers beyond the first one are supposed to have the same evaporation-condensation properties as the bulk liquid, C is also equal to the relative lifetimes of molecules in the first layer and in the bulk liquid respectively.

$$C = \exp(\Delta_{ads}H^{\Theta} - \Delta_{liq}H^{\Theta})/RT \quad (2\text{-}9)$$

where $\Delta_{ads}H^{\Theta}$ is the enthalpy of adsorption, $\Delta_{liq}H^{\Theta}$ is the enthalpy of liquefaction, R is the gas constant and T is temperature.

The BET isotherm can be used to calculate the area associated with a monolayer of gas adsorbed onto the adsorbate surface, and therefore determine specific surface area of a given sample. When nitrogen is adsorbed onto the surface at 77 K, the technique can be used to provide highly accurate surface areas. Surface area is determined from several points of the nitrogen adsorption at relative pressures below P/P_0=0.35. Hence, in this work five points of the isotherm were measured (Figure 2-16). If a whole isotherm is measured, the total surface area can be divided into subgroups, each being associated with a particular pore size, allowing pore density distribution information to be calculated using isotherm models specific to each group.

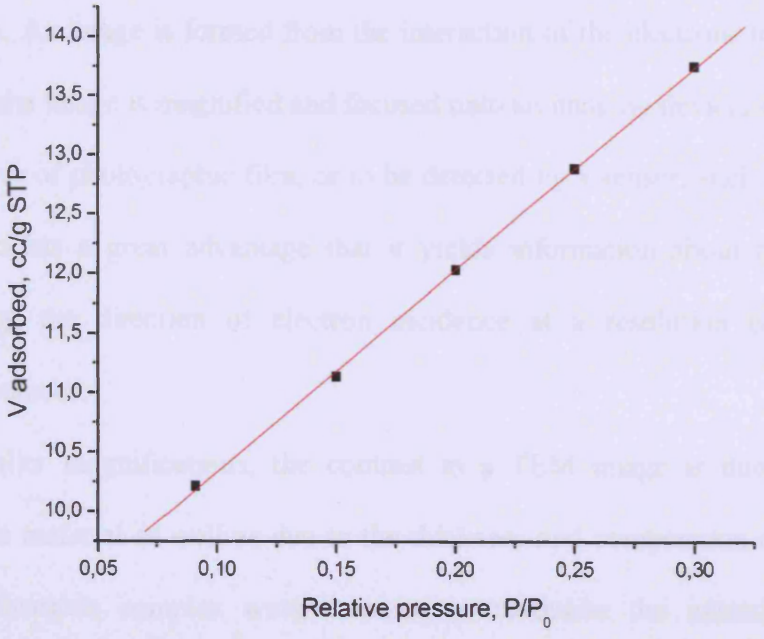

Figure 2-16. Part of BET isotherm of the 6 Mo/$CoFe_2O_4$ sample used for surface area calculations.

2.6.2. Experimental

A Micromeretics Gemini 2360 was used in a static volumetric method, in which between 0.5 and 2.5 g of catalyst was weighed and placed in a sample tube holder, before being heated to 150 °C under vacuum for 1 hour to remove water from the surface. The sample tube and a blank reference tube were then connected to the machine. The sample and the reference tube were cooled using liquid nitrogen and the pressure to achieve equilibrium was measured upon admission of nitrogen gas at pre-determined pressure points. The analyser collected five points at different pressures before calculating the surface area in $m^2 g^{-1}$.

2.7. High resolution transmission electron microscopy (HR-TEM)

2.7.1. Theory

High resolution transmission electron microscopy is a microscopy technique whereby a beam of electrons is transmitted through an ultra thin specimen, interacting with the specimen as it passes through. An image is formed from the interaction of the electrons transmitted through the specimen; the image is magnified and focused onto an imaging device, such as fluorescent screen in a layer of photographic film, or to be detected by a sensor, such as a CCD camera. This technique has a great advantage that it yields information about the bulk structure, projected along the direction of electron incidence at a resolution comparable to the interatomic distances.

At smaller magnifications, the contrast in a TEM image is due to absorption of electrons in the material as well as due to the thickness and composition of the material. At lighter magnifications complex wave interactions modulate the intensity of the image, requiring expert analysis of the obtained images. Alternate modes of use allow for the TEM to observe modulations in chemical identity, crystal orientation, electronic structure and sample-induced electron phase shift as well as the regular absorption-based imaging.

A modern transmission electron microscope can be schematically represented as a three-lens system: an objective lens, an intermediate lens and a projector lens (Figure 2-17). The system allows easy switching from the high-magnification imaging mode to the selected area diffraction mode. The image resolution of the system is to a large extent determined by the characteristics of the objective lens, in particular by its spherical aberration constant.

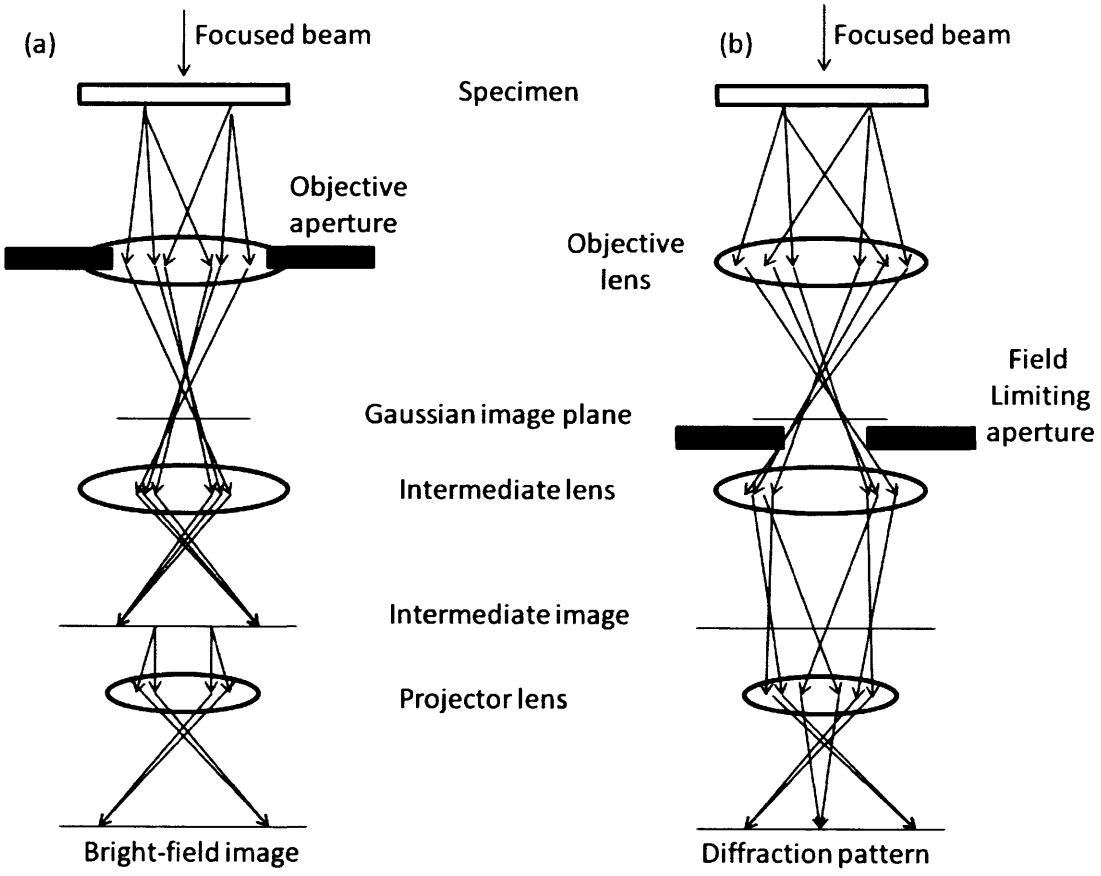

Figure 2-17. Ray paths in a reference transmission electron microscope (a) High resolution high magnification imaging mode. (b) Selected area diffraction mode. Adapted from ref 11.

High resolution, high magnification imaging mode. The electron beam produced by an electron source is collimated by the condenser lens system and scattered by the specimen. An image is formed in the image plane of the objective lens. The selective apparatus allows us to select one area of the image which is then magnified by the intermediate lens. The

intermediate lens is focused on the image plane of the objective lens and an intermediate image is formed in the image plane of the intermediate lens. This image is the object for the projector lens which forms a final image on a fluorescent screen or on the entrance plane of a recording device.

In the modern microscopes a sharp LaB_6 single crystal mounted on a V-shaped tungsten heating filament is often used as an electron source because of its small work function. It emits electrons at a lower temperature than tungsten and the thermal energy distribution of the electrons is narrow (~0.5 eV) because of the use of cold field emission guns, thus leading to a lower chromatic aberration. Such guns consist of a very fine point, placed on the pointed filament, which emits electrons by tunnelling. A sufficiently strong electric field is required (10^6 V cm^{-1}) in the vicinity of the field point to cause a sufficiently strong tunnelling current density.

To accelerate the electrons emitted by the source and to form the collimated beam, a large negative voltage must be applied to the emitter, keeping the anode grounded. The incident beam is finally shaped into a parallel beam by the system of condenser lenses and by apertures. Typically, the angular spread may be made as small as 10^{-4} rad.

Clean high vacuum (10^{-8} torr) is essential in TEM to provide stability and avoid contamination of the specimen by a carbon film resulting from the cracking of organic molecules present in the residual gas.

Usually images are made visible on a fluorescent screen and viewed by means of binoculars. For high-resolution work many advantages are offered if the electron microscope is equipped with an image-intensifying camera mounted below the photographic plate holder. This facilitates observation of the high-resolution images and adjustment of the microscope.

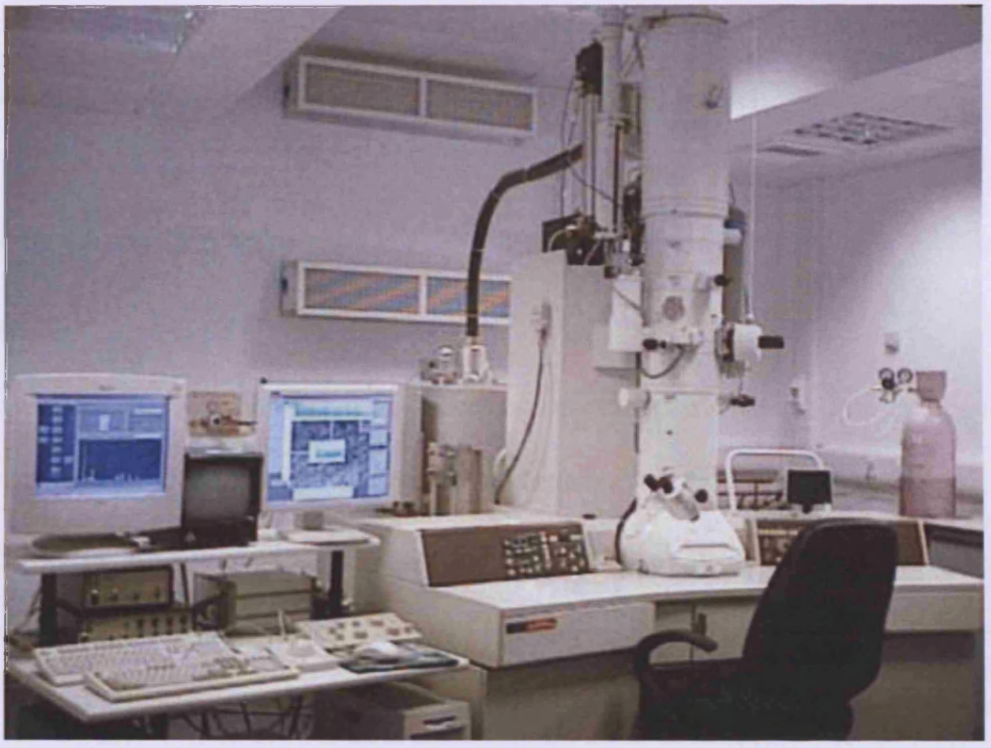

Figure 2-18. TEM at the University of Southampton, used in this study.

Before starting the high-resolution work, it is necessary to determine the most important optical parameters of the instrument for later use in imaging simulation and reconstruction. For very high resolution (below 0.2 nm) the standard correction procedure for the aberrations is insufficient, and methods have been developed for automatic alignment. Furthermore, the spherical aberration constant depends on the position of the specimen in the objective lens. For this purpose the microscope should be equipped with a CCD camera and on-line image-processing capabilities.[11]

2.7.2. Experimental

Transmission electron microscopy (HR-TEM) images were obtained using a JEOL 3010 TEM (Figure 2-18), with accelerating voltage 100 to 300 kV, resolution 0.21 nm, magnification to 1,500,000, high tilt polepieces and energy dispersive X-ray monoanalysis. The requirements for the specimen are that the specimen should be sufficiently thin, that is less than about 10 nm. The powder sample was "dry" deposited onto a copper grid covered

with a perforated carbon film. The experiments were carried out with the help of Dr. Dmitrii Bavykin and Dr. Alexander Kulak in the University of Southampton.

2.8. X-ray photoelectron spectroscopy (XPS)

2.8.1. Theory

Surface analysis by X-ray Photoelectron spectroscopy is accomplished by irradiating a sample with monoenergetic x-rays and analyzing the energy of the detected electrons. Mg Kα (1253.6 eV) or Al Kα (1486.6 eV) x-rays are usually used. These photons have limited penetrating power in a solid on the order of 1-10 micrometers. They interact with atoms in the surface region, causing electrons to be emitted by photoelectric effect. The emitted electrons have measured kinetic energies given by:

$$KE = h\nu - BE - \phi \qquad (2\text{-}10)$$

where hν is the energy of the photon, BE is the binding energy of the atomic orbital from which the electron originates, and ϕ is the spectrometer work function.

The binding energy may be regarded as the energy difference between the initial and the final states after the electron has left the atom. Because there are different possible final states of ions from each type of atom, there is a corresponding variety of kinetic energies of the emitted electrons. Moreover there is a different probability or cross-section for each final state.

Because each element has a unique set of binding energies, XPS can be used to identify and determine concentrations of the elements on the surface. Variations in the elemental binding energies (the chemical shifts) arise from differences in the chemical potentials and polarizability of compounds. These chemical shifts can be used to identify the chemical state of the materials being analyzed.

In addition to photoelectrons emitted in the photoelectric process, Auger electrons can be emitted because of relaxation of the excited ions remaining after photoemission (Figure 2-19). This Auger electron emission occurs roughly 10^{-14} seconds after the photoelectric event. The competing emission of a fluorescent x-ray photon is a minor process in this energy range. In the Auger process an outer electron falls into the inner orbital vacancy and a second electron is simultaneously emitted, carrying off the excess energy. The Auger electron possesses kinetic energy equal to the difference between the energy of the initial ion and doubly charged final ion. Thus, photoionization normally leads to two emitted electrons – a photoelectron and an Auger electron. The sum of the kinetic energies of the electron emitted cannot exceed the energy of the ionizing photons. Probabilities of electron interaction with matter far exceed those of photons, so while the pathlength of the photons is of the order of micrometers, that of the electrons is of the order of tens of angstroms. Thus, while ionization occurs to a depth of a few micrometers, only those electrons that originate within tens of angstroms below the solid surface can leave the surface without energy loss. These electrons produce the peaks in the spectra and are the most useful. The electrons that undergo inelastic loss possesses before emerging from the background.

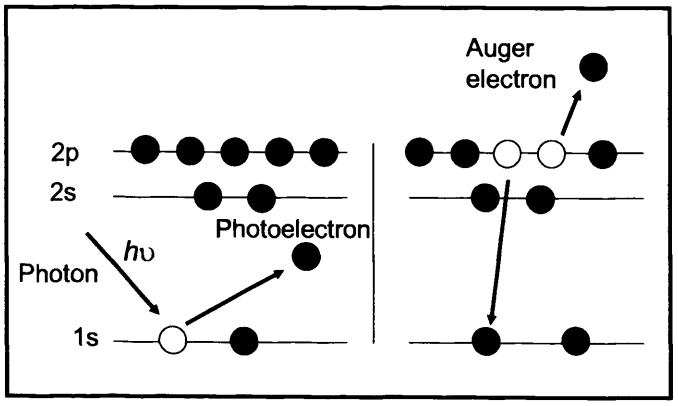

Figure 2-19. Principles of XPS.

The electrons leaving the sample are detected by an electron spectrometer according to their kinetic energy. The analyzer is usually operated as an energy window, referred to as the

pass energy, accepting only those electrons having energy within the range of this window. To maintain a constant energy resolution the pass energy is fixed. Incoming electrons are adjusted to the pass energy before entering the energy analyzer. This retardation voltage may be varied from zero up to and beyond the photon energy. Electrons are detected as discrete events, and the number of electrons for a given detection time and energy is stored and displayed.[13]

X-ray sources make use of the characteristic emission lines from a target (anode) when it is bombarded with high energy electrons. The choice of source for XPS work is based upon the width of the emission line (>1.0 eV) and the x-ray energy, which determines the deepest core energy level from which an electron can be emitted. The discrete X-ray lines produced are superimposed on a continuum which is termed Bremsstrahlung. The continuum is formed when the high speed electrons are slowed rapidly by multiple collisions within the anode material. Use of a thin aluminium foil in XPS removes low energy secondary electrons.

2.8.2. Experimental

A Kratos *AXIS (Ultra-DLD)* (located at Cardiff University) fitted with a monochromated Al Ka radiation source and a refocusing lens to give high resolution XPS was used to obtain XPS spectra. The survey scans were acquired with a pass energy of 160 eV in a single sweep with a step of 0.5 eV. Region scans were acquired with a pass energy of 40 eV, in 5 to 10 sweeps in steps of 0.1 eV. Calibration was done using carbon C 1s peak. Obtained spectra were analyzed using Casa XPS software. The XPS experiments were carried out by David Morgan in the Cardiff University.

2.9. Magnetic Susceptibility Measurement

2.9.1. Principles

In electromagnetism the magnetic susceptibility is the degree of magnetization of a material in response to an applied magnetic field. The magnetic state of a specimen is generally described by the following equation:

$$B=\mu_0(H+M) \quad (2\text{-}11)$$

where B is a flux density of the specimen in Tesla, μ_0 is the permeability of free space, which is a constant in units N A^{-2}, H is the applied field strength in A m^{-1}, M is magnetization of the specimen in A m^{-1}.

Dividing the equation by H we obtain:

$$\mu = \mu_0 + \mu_0\chi \quad (2\text{-}12)$$

Where μ is the permeability of the specimen in N A^{-2}, χ is the volume magnetic susceptibility of the specimen (dimensionless).

Rewriting, we obtain:

$$\mu_0\chi = \mu - \mu_0 \quad (2\text{-}13)$$

The meter to which the sensor is connected digitises the μ_0 and μ dependant frequency values with a resolution of better than one part in a million and computes the value of magnetic susceptibility.

2.9.2. Experimental

The alternating (AC) susceptibility and the Curie temperature of samples of interest were measured using the temperature-programmable MS2 Magnetic Susceptibility System (Bartington Instruments) (see image in Figure 2-20) which consists of MS2WFP power

supply, MS2 susceptibility meter, MS2W sensor and MS2WF furnace (maximum operating temperature is 850 °C).

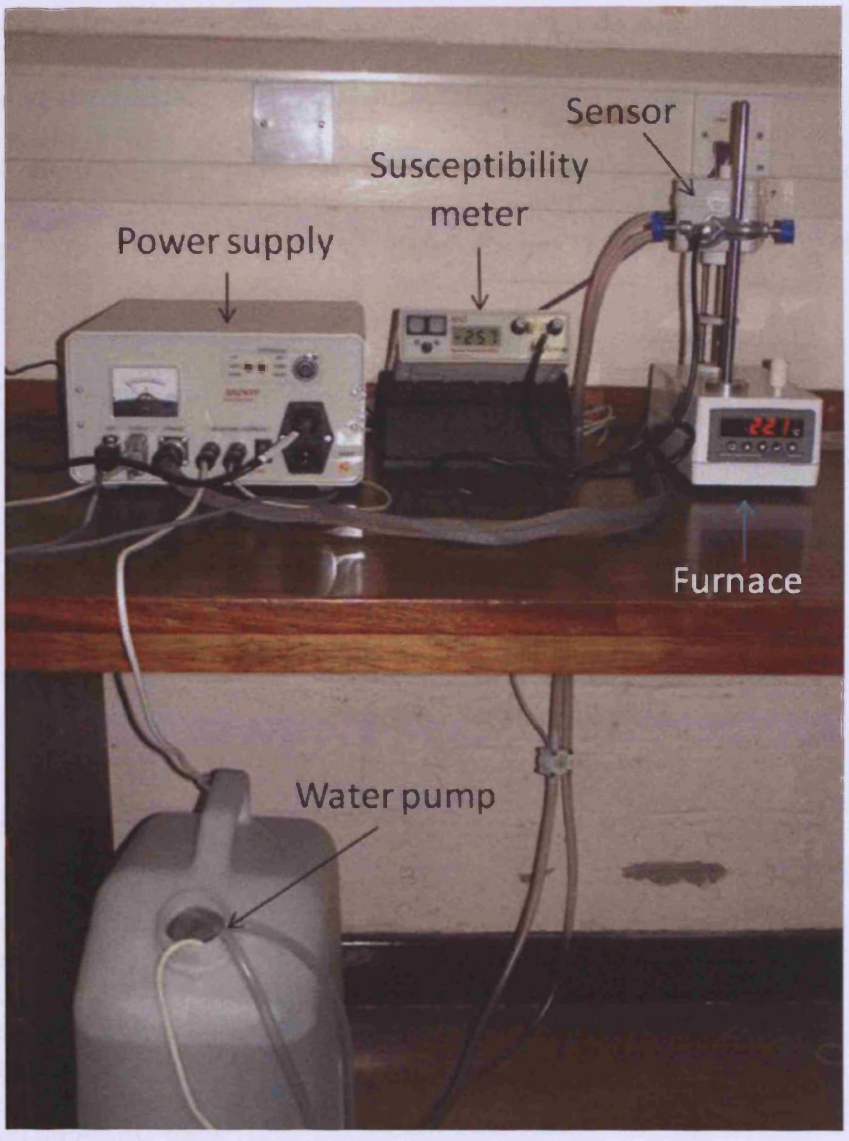

Figure 2-20. A photograph of the magnetic susceptibility meter used in this study.

The sensor consists of a very high thermal stability oscillator for which a wound inductor is the principal frequency-determining component. When the inductor contains only air, the value of μ_0 determines the frequency of oscillation. When the inductor is placed within the influence of the specimen to be measured, the value of μ determines the frequency of oscillation. The meter to which the sensor is connected digitises the μ_0 and μ dependant

frequency values with a resolution of better than one part in a million and computes the value of magnetic susceptibility.

The value of μ_0 is constant but the variable of interest is relatively small. Therefore, any thermally induced sensor drift needs to be eliminated by occasionally obtaining a new "air" value (to re-establish the μ_0 reference) by pressing the "zero" button on the MS2 meter. The μ value is obtained by pressing the "measure" button. The magnetic susceptibility value is displayed digitally and output via a serial interface.

The Curie temperatures of the samples calcined at 800 °C were taken from the extrapolation of the near-linear decreasing part of the susceptibility curves to the intercept with the abscissa. For the samples calcined at 500 °C it is difficult to determine T_c exactly as the transitions are very broad, so the estimated values $T_{c\ max}$ and $T_{c\ 1/2}$ (see Chapter 4 for details) were taken.

2.10. References

1. Avgouropoulos, G.; Ioannides, T., *Applied Catalysis A: General* **2003,** *244*, 155-167.
2. Soares, J. M. C.; Bowker, M., *Applied Catalysis A: General* **2005,** *291*, 136-144.
3. Stone, P.; Ishii, M.; Bowker, M., *Surface Science* **2003,** *537*, 179-190.
4. House, M. Selective oxidation of methanol over iron molybdate catalysts. . Cardiff University, Cardiff, 2006.
5. Edmond de Hoffmann, V. S., *Mass Spectrometry: principles and applications*. 2nd ed.; Wiley: Guildford, 2002.
6. A. Cornu, R. M., *Compilation of Mass Spectroscopic data*. Methen, London and Presses Universitaires: France, 1966.
7. Satterfield, C. N., *Heterogeneous Catalysis in Practice*. McGraw-Hill Inc: USA, 1980.
8. Redhead, P. A., *Vacuum 12*, 203-211.
9. West, A. R., *Basic Solid State Chemistry*. John Wiley & Sons: Trowbridge, 1994.
10. Nakamoto, K., *Infrared and Raman Spectra of Inorganic and Coordination Compounds*. 6th ed.; Wiley: 2009.
11. S. Amelinckx, D. v. D., J. van Landuyt, G. van Tendeloo, *Handbook of microscopy: applications in material science, solid state physics and chemistry*. Darmstadt, 1997.
12. S.J. Greeg, K. S. W. S., *Adsorption, surface science and porosity*. Academic PressInc. Ltd.: London & New York, 1967.
13. John F. Moulder, W. F. S., Peter E. Sobol, Kenneth D. Bomben, *Handbook of X-ray photoelectron spectroscopy*. Physical Electronics: 1995.

Chapter 3. Catalytic Oxidation of Methanol over Thin Layer Oxides

3.1. Introduction and literature review

3.1.1. Introduction

The oxidation of methanol to formaldehyde is an important and well-established industrial process. Adkins and Peterson discovered the high activity and selectivity of the Fe-Mo-O catalysts over eighty years ago.[1] It was postulated by many authors that the active component of Fe-Mo systems is $Fe_2(MoO_4)_3$ with a slight excess of MoO_3.[2] However, the exact nature of the active site is still controversial. As surface properties of a system play a key role in determining its catalytic performance and selectivity, investigation of model bulk Fe_2O_3 covered with monolayers of molybdenum might give us insights into the origin of activity of the Fe-Mo systems. In this Chapter structural and catalytic properties of the thin layer Mo/Fe_2O_3 systems are discussed. The second system considered is the $Mo/CoFe_2O_4$, which is closely related to Mo/Fe_2O_3. Moreover, the catalytic properties of model Zn-doped $Mo/CoFe_2O_4$ materials for magnetic experiments are discussed in Chapter 4. Thus, an understanding of the essential properties and catalytic behaviour of impregnated cobalt ferrites and component catalysts is important.

3.1.2. The structures of oxides relevant to catalysts used in the present study

3.1.2.1. Fe_2O_3

The most common structure for iron oxide is α-Fe_2O_3 modification called hematite (Figure 3-1). It belongs to R3c space group with a hexagonal crystal structure and with the lattice parameters a = 5.038 Å and c = 13.772 Å.[3] Two and six formula units are in the primitive rhombohedral and in the conventional hexagonal unit cells respectively. Hexagonal closed-packed (001) layers of oxygen atoms are present with Fe atoms filling 2/3 of the octahedral holes in between.[4] Since Fe is in trivalent state, each of the oxygens is bonded only to two iron atoms, and therefore, only two out of three available oxygen octahedrons are occupied.

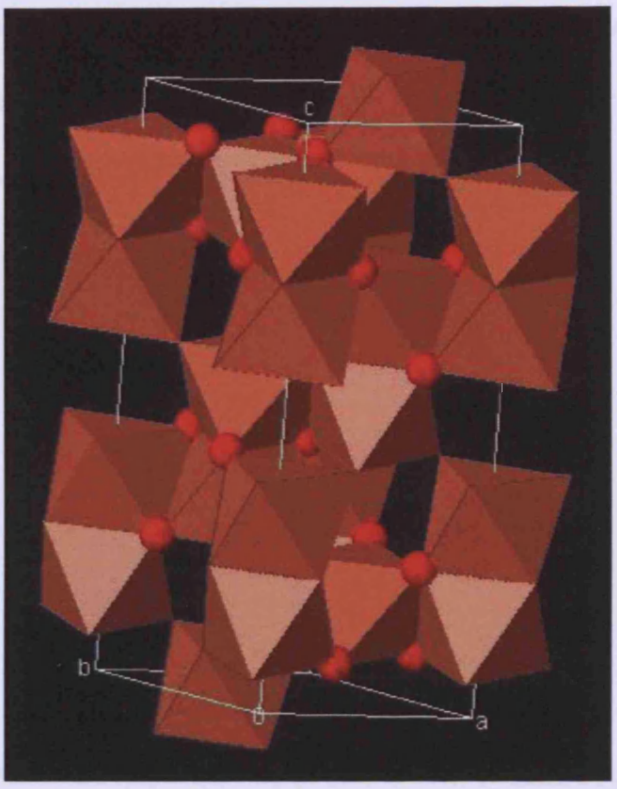

Figure 3-1. Structure of bulk α-Fe_2O_3 with Fe at the center of orange polyhedra and red balls representing oxygen.[4]

3.1.2.2. MoO_3

Molybdenum trioxide is a layered material, its layers being weakly bonded via van der Waals interactions. α-MoO_3 belongs to the space group *Qh* 16 (*bnm*), and the lattice is orthorhombic with parameters 3.962, 13.858, and 3.697 Å.[5] Each unit cell contains four MoO_3 units. The MoO_3 crystal structure is shown in Figure 3-2. It consists of bilayers parallel to the (010) plane, which are bonded through weak electrostatic interactions, with the (010) surface being the easy cleavage plane of the crystal. Each bilayer consists of two sublayers of periodically arranged distorted MoO_6 octahedra. There are three different types of oxygen in this structure: the *asymmetric bridging* oxygen is bonded with two Mo atoms by one long and one short bond, the *symmetric bridging* oxygen, which is located between the two sublayers of the bilayer and bonds to two Mo atoms of one sublayer with equal bond lengths and to one Mo

atom of the other sublayer with an elongated bond, and the univalent *terminal* oxygen connected to one Mo atom forming the shortest Mo–O bond in the system.[5]

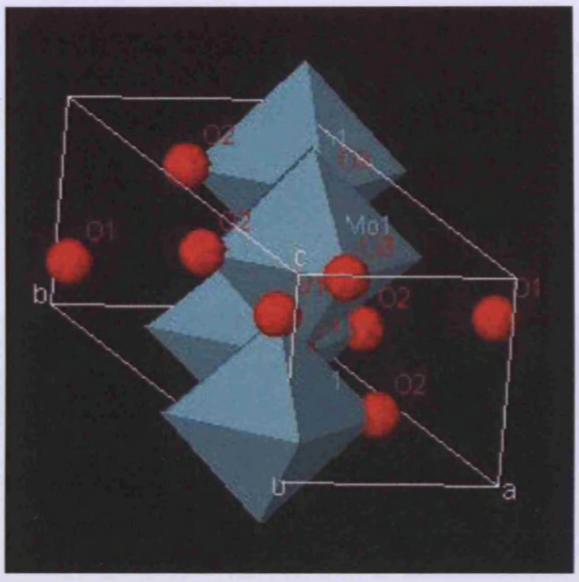

Figure 3-2. Structure of α-MoO_3 with Mo at the center of blue octahedra and red balls representing three different types of oxygen (terminal, asymmetric and symmetrical bridging) relevant to this structure.[6]

β-MoO_3 is a monoclinic form of molybdena. It belongs to P $2_1/c$ space group with lattice parameters of a= 7.122 Å, b = 5.374 Å and c = 5.565 Å.[7] The monoclinic form of MoO_3 is isostructural with ReO_3 and involves corner sharing, distorted octahedra. It can be produced by the heat treatment of freeze-dried molybdic acid.[7]

3.1.2.3. Co_3O_4

The space group of Co_3O_4 in the paramagnetic state is O^7_h-*Fd3m* and a single parameter, x = u, is required to define positions of the oxygen atoms in the 32(e) positions. The cobalt oxide structure corresponds to spinel AB_2O_4 structure. Depending on the relative sizes of the coordinating cations, the oxygen ions may shift towards A or B site cations with a systematic contraction of the A cation tetrahedron and expansion of the B cation octahedron, or vice versa. A quantitive measure of distortion from the perfect ccp arrangement is the parameter u,

which defines the relative oxygen position within the unit cell and equals 0.25 for the perfect ccp.[8] Roth *et al*[9] calculated the u value of Co_3O_4 to be 2.631 and described the structure as having normal cation distribution. Figure 3-3. Structure of Co_3O_4 with Co at the center of tethrahedra and octahedra and oxygen shown as red balls.Figure 3-3 shows Co_3O_4 structure.

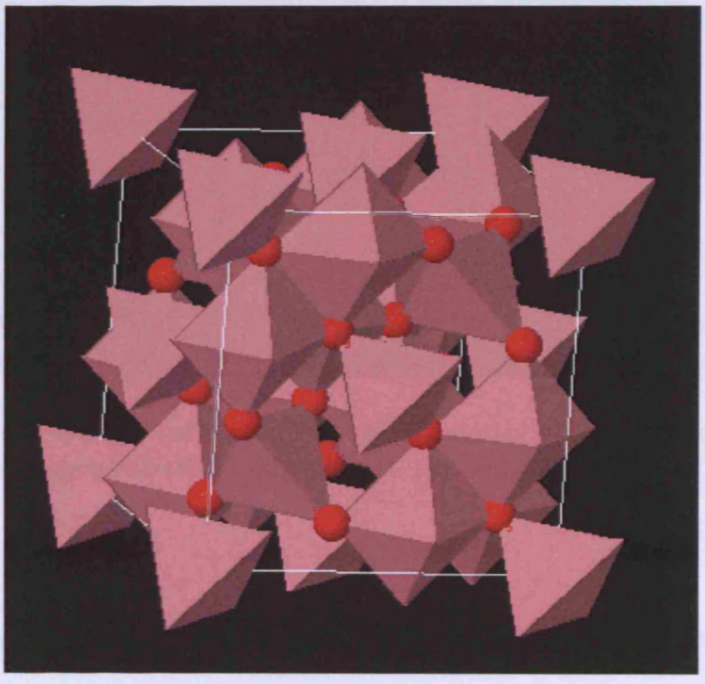

Figure 3-3. Structure of Co_3O_4 with Co at the center of tethrahedra and octahedra and oxygen shown as red balls.[8]

3.1.2.4. $Fe_2(MoO_4)_3$

There are two structural forms of $Fe_2(MoO_4)_3$ – the monoclinic, stable at room temperature, and orthorhombic, stable at temperatures above 513 °C. α-Iron molybdate exists in the monoclinic structure in the space group $P2_1$ with the lattice parameters a = 15.737 Å, b = 9.231 Å, c = 18.224 Å and β = 125.46 °.[10] The orthorhombic β- $Fe_2(MoO_4)_3$ belongs to P nca space group with lattice parameters of a = 9.236 Å, b = 12.821 Å and c = 9.108 Å.[11]

1.992 Å. The twelve molybdenum atoms are in rather distorted oxygen tetrahedra with an average Mo-O distance of 1.756 Å. Each oxygen atom links an FeO_6 octahedron with one MoO_4 tetrahedron leading to a rather open structure in which the nearest Fe-Fe distance is 5.03 Å.[12] The structure of α-iron molybdate is shown in Figure 3-4.

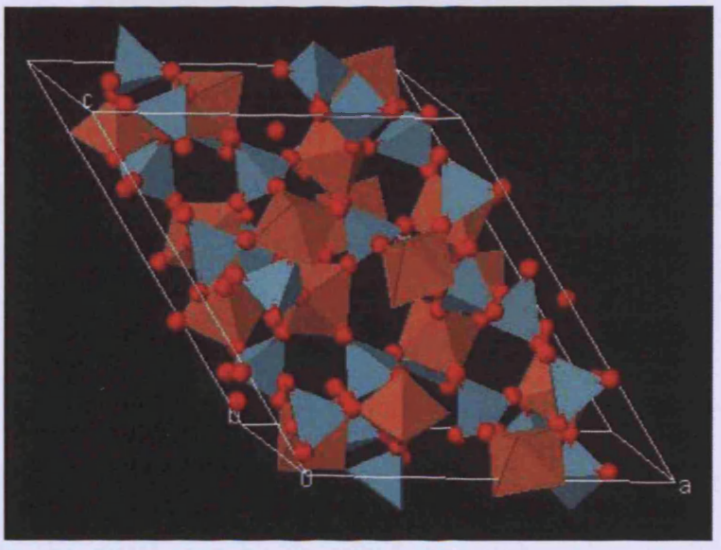

Figure 3-4. Structure of α-$Fe_2(MoO_4)_3$ with Mo at the center of the blue tethrahedra, Fe at the center of the orange octahedra and red balls representing oxygen.[12]

3.1.2.5. $CoMoO_4$

Cobalt molybdate crystallizes in the monoclinic system, space group C2/m, with 8 molecules in a cell with lattice parameters of a= 9.67 Å, b = 8.85 Å, c = 7.76 and β = 113 °.[13] The oxygen atoms are sixfold coordinated around both cations in a closed-packed arrangement of distorted octahedra, based upon NaCl-type structure (Figure 3-5). However, not all the octahedral holes are filled by cations; they only occupy edge-sharing octahedra in such a way that an infinite chains parallel to the c-axis are formed. Each chain of filled octahedra is surrounded by other chains of unfilled octahedra.

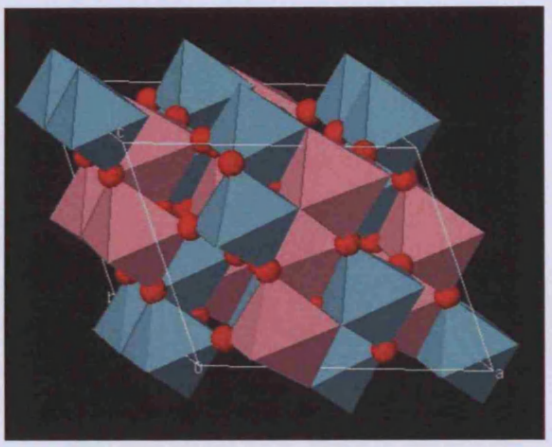

Figure 3-5. Structure of α-$CoMoO_4$ with Mo at the center of blue octahedra and Co at the center of pink octahedra and red balls representing oxygen. [13]

3.1.2.6. $CoFe_2O_4$

Cobalt ferrite has the spinel structure and its unit cell contains eight formula units and it belongs to the *Fd3m* space group (Figure 3-6). The spinel ferrite has a structure $MeFe_2O_4$, where Me refers to the metal, can be described as a cubic close-packed arrangement of oxygen atoms, with Me^{2+} and Fe^{3+} at two different crystallographic sites. These sites have tetrahedral and octahedral oxygen coordination (termed as A and B-sites, respectively), so the resulting local symmetries of both sites are different. The spinel structure contains two cation sites for metal cation occupancy. There are 8 A-sites in which the metal cations are tetrahedrally coordinated with oxygen, and 16 B-sites which possess octahedral coordination. When the A-sites are occupied by Me^{2+} cations and the B-sites are occupied by Fe^{3+} cations, the ferrite is called a normal spinel. If the A-sites are completely occupied by Fe^{3+} cations and the B-sites are randomly occupied by Me^{2+} and Fe^{3+} cations, the structure is referred to as an inverse spinel. In most spinels, the cation distribution possesses an intermediate degree of inversion where both sites contain a fraction of the Me^{2+} and Fe^{3+} cations[14]. In the $CoFe_2O_4$ spinel the Co^{2+} ions are generally reported to show a preference for the octahedral (B) sites, but they do not exclusively reside in the octahedral (B) sites, and the distribution is reported to depend on thermal treatment.[15]

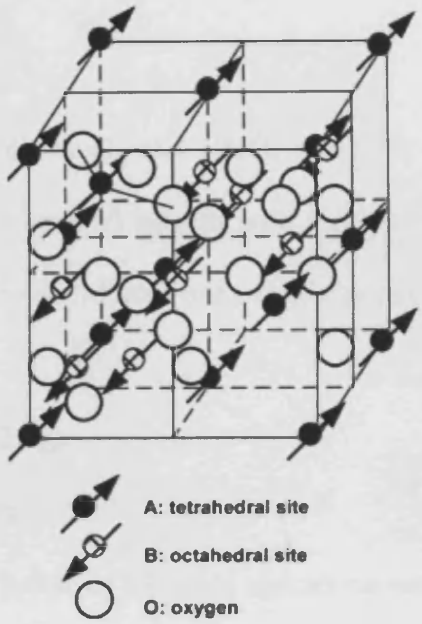

Figure 3-6. Structure of $CoFe_2O_4$.[15]

3.1.3. Single oxides. The nature of active sites.

The products formed in the methanol oxidation strongly depend on the nature of the active species of the catalyst used. Thus, molybdena is highly selective towards formaldehyde formation, whereas iron and cobalt oxides act as combustors.[16-17] The difference in the oxidation products arises from the difference in surface species which can be involved in methanol oxidation. Figure 3-7 schematically shows the structure of methoxy and formate adsorbed species. It is known that dissociative methanol adsorption on MoO_3 results in the formation of methoxy surface species,[16, 18] while on Fe_2O_3 and Co_3O_4 formates are formed.[19] Methoxy groups are generally the most abundant of the adsorbed methanol forms. Over MoO_3 methanol conversion and formaldehyde selectivity become high at 350 °C due to methoxy decomposition (reaction 3-1), however already at 400 °C CO selectivity increases. CO is formed from either methoxy species or formaldehyde via reactions 3-2 and 3-3.

$$CH_3O_{ads} + O = CH_2O + OH^- \quad (3\text{-}1)$$

$$CH_3O_{ads} + 3O = CO + 3OH^- \quad (3\text{-}2)$$

$$CH_2O + 2O = CO + 2OH^- \quad (3\text{-}3)$$

Methanol adsorption on Fe_2O_3 and Co_3O_4 results in the formation of a mixture of formate (major) and methoxy (minor) species with a prevalence towards CO_2 production.[19] Formate species might form by addition of one oxygen atom either to adsorbed methoxy or to formaldehyde species:[17]

$$CH_3O_{ads} + O_{ads} = HCOO_{ads} + 2H_{ads} \quad (3\text{-}4)$$

$$CH_2O_{ads} + O_{ads} = HCOO_{ads} + H_{ads} \quad (3\text{-}5)$$

The difference in the nature of adsorbed species on various oxides originates from the differences in the oxide structures. From Figure 3-7 one can see that methoxy groups adsorb on a single metal site in a monodentate manner with one hydrogen abstracted from methanol and adsorbed onto a neighbouring oxygen site. Formates form during adsorption of methanol onto two adjacent metal sites with the loss of two hydrogens to other surface sites (Figure 3-7). Thus, only the surfaces containing neighbouring sites in a certain proximity to each other are suitable for adsorption of formate species.

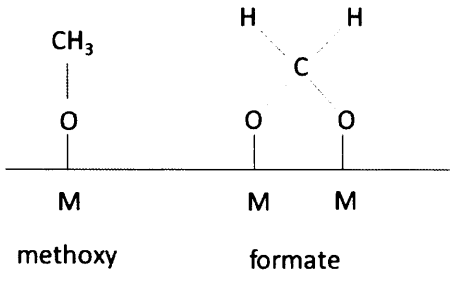

Figure 3-7. Schematic illustration of methoxy and formate species adsorbed on an oxide surface.

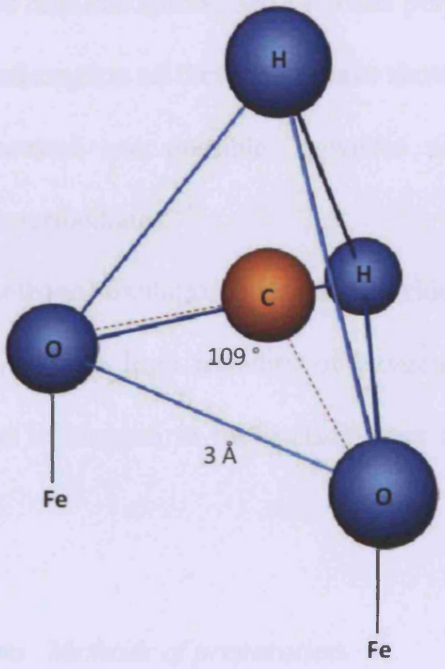

Figure 3-8. Geometry calculations of C-O bond length in formate.

The closest Fe-Fe bond in the bulk Fe_2O_3 material is ~3.0 Å.[20] If we consider the carbon atom of the formate group to be sp^3 hybridised with the bond angle of 109°, and if M-O bonds are considered to be perpendicular to the surface, than the C-O bond length could be calculated as O-O distance (3.0 Å) divided to 2·cos of half O-C-O angle (cos 54.5) and would be ~1.8 Å (Figure 3-8). As a comparison, the average length of a C-O covalent bond in organic compounds is around 1.43 Å. If similar calculations to these are carried out for molybdena with the smallest Mo-Mo distance of 3.48 Å, the C-O bond would need to be 2.1 Å. These simple calculations clarify that formation of the formate species on molybdena surface is less favourable than of the methoxy species, which do not require two-site coordination.

It has been shown that CH_3OH adsorbs in the form of methoxy- species mainly on the (100) and (010) faces of MoO_3.[21] The (010) face appears to be formed by completely coordinated molybdenum atoms with terminal oxygen atoms pointing out to the gas phase,

while formation of the (100) face requires cutting Mo-O bonds perpendicularly to the *a* axis. Theoretical studies of methanol adsorption on these faces have shown that both molecular and dissociative chemisorption processes are possible, however adsorption with hydrogen abstraction leads to more stable intermediates.[22]

Schlogl *et al*[17] studied methanol oxidation over cobalt oxides and linked formation of surface formate species on Co_3O_4 with high mobility of oxygen ions in the cobalt oxide structure as it leads to migration of oxygen to the surface layer and oxidation of methoxy species to formate (reaction 3-4).

3.1.4. Mo/Fe_2O_3 thin layer systems. Methods of preparation.

Molybdena monolayer systems on different supports (SnO_2, ZrO_2, TiO_2, *etc.*) were extensively investigated by Miki Niwa *et al.*[23-24] These authors postulated that because of the difference in properties of acid MoO_3 and base oxides, and strong interaction between these oxides when molybdena is loaded on a support, the metal oxide appears to be highly spread, forming an oxide monolayer. The structure of the monolayer oxide consists of one component covering the surface of another component metal oxide.

To prepare monolayered Mo/Fe_2O_3 systems two main techniques were used in the literature: impregnation[25-27] and mechanical mixing.[28-30] In ref 26 the 2.3% and 3% MoO_3/Fe_2O_3 catalysts were synthesized by impregnation of iron oxide support with aqueous ammonium heptamolybdate (AHM) solution followed by drying and calcination at 350 °C for four hours. The authors assumed that they obtained surface coverage close to a monolayer, corresponding to ~4.6 Mo atoms/nm^2. Yamada *et al* synthesized their monolayer MoO_3/Fe_2O_3 sample by addition of iron oxide to AHM solution with pH adjusted to 10 using NH_4OH. After excess water was evaporated the precipitate was dried and calcined at 500 °C in a stream of oxygen for three hours. Using BAT (benzaldehyde-ammonia titration) method these

authors determined the surface coverage dependence on the surface molybdenum concentration. It was shown that up to the loading 6 Mo atoms/nm^2 the surface coverage increased to 70% and then reached saturation. It was assumed that 6 Mo atoms/nm^2 is referred to one monolayer as further increase of molybdenum concentration resulted in the accumulation of molybdena on the monolayer and aggregation of the oxide. M. House from our group prepared 0.28, 0.70, 2.8 and 7.2% MoO_3/Fe_2O_3 dosed systems using incipient wetness impregnation of iron oxide by AHM. In calculating the loading it was assumed that surface of Fe_2O_3 contains 10^{19} surface sites per m^2, with a total of 5/12 of these being metal cations as it was thought a $Fe_2(MoO_4)_3$ layer may form.[25] The obtained materials were dried and calcined *in-situ* in 10% O_2/He flow at 400 °C for 30 minutes.

Dong *et al*[28-29] created MoO_3/Fe_2O_3 supported systems by heating the mixture of MoO_3 and Fe_2O_3 with different amounts of molybdena at 400 °C in air for 24 hours. They showed by XRD and XPS methods that dispersing capacity of MoO_3 on hematite is 4.8 Mo atoms/nm^2. They also showed that after calcination of MoO_3/Fe_2O_3 at 470 °C molybdena reacts with iron oxide to form bulk iron molybdate. The $Fe_2(MoO_4)_3$ formed remained at the surface, effectively encapsulating the Fe_2O_3 inside. Similar results were obtained by Huang *et al,*[30] who prepared MoO_3/Fe_2O_3 (with a molar ratio 1:1) by grinding single oxides together and calcining them at 300-600 °C. They reported thermal spreading of MoO_3 and the solid-state reaction at 400 °C with a subsequent formation of iron molybdate shell over iron oxide as the temperature was raised.

3.1.5. Mo/Fe_2O_3 thin layer systems. Activity in oxidation of methanol.

Most of the literature is focused on the activity and selectivity of an industrial iron molybdate catalyst to produce formaldehyde. Although there is no strong agreement on the composition of the most effective Fe-Mo-O catalyst, the general consideration is that the active phase is

the stoichiometric iron molybdate with an excess of Mo on the surface in order to prevent the formation of the Fe-rich phases during reaction due to loss of MoO_3.[2]

Chung *et al* studied the mechanism of methanol oxidation over MoO_3.[31] During the steady-state reaction with methanol and oxygen concentration 3.6 and 5% respectively, using 10 mg of MoO_3 and flow rate 0.0013 mol/min, they observed formation of formaldehyde, CO and water as main products and CO_2, DME and methyl formate as by-products. The rates of formaldehyde and CO production increased with the increase in temperature, while the rate of DME formation went through a maximum at around 350 °C. Using IR spectroscopy they proposed mechanisms for formaldehyde, CO, DME and other products formation. According to them, formaldehyde and CO are mainly produced on twin-type molybdenum sites from chemisorbed methoxy on terminal oxygen vacancy sites (Figure 3-9 and Figure 3-10), while bridged oxygen sites are responsible for the formation of such products as DME (Figure 3-11).

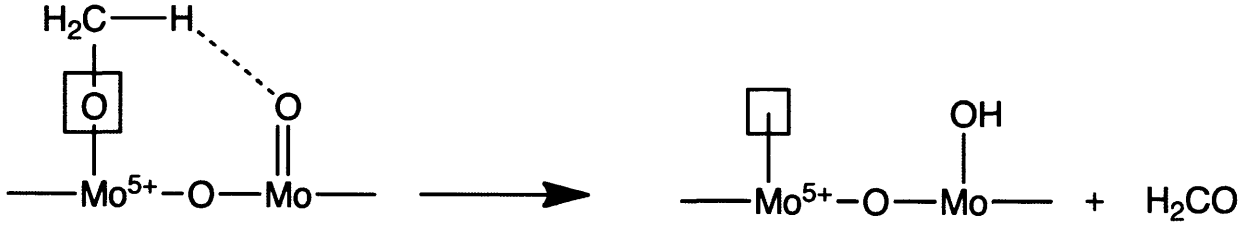

Figure 3-9. Proposed mechanism for formaldehyde formation on the MoO_3 surface.[31]

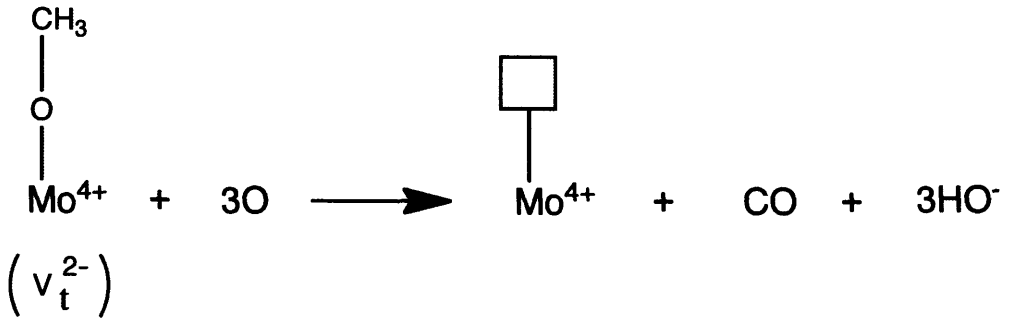

Figure 3-10. Proposed mechanism of CO formation on the MoO_3 surface.[31]

Several authors investigated the catalytic activity of MoO_3/Fe_2O_3 monolayer systems. Thus, Yamada *et al* who investigated the effect of molybdenum loading on iron oxide in methanol oxidation at 224 °C, have shown that at lower loadings (<3%) metylformate and carbon dioxide were produced as by-products; however on the 3wt% MoO_3/Fe_2O_3 formaldehyde was formed almost selectively and further increase in loading did not enhance the formation of formaldehyde, but by-products such as DME and CO_2 appeared. These authors have shown that methanol oxidation is a second order reaction with respect to Mo atom and postulated that neighbouring Mo-Mo sites catalyze simultaneously methoxy adsorption and hydrogen abstraction.[27] This mechanism is supported by other investigations and proposals.[19, 21, 31]

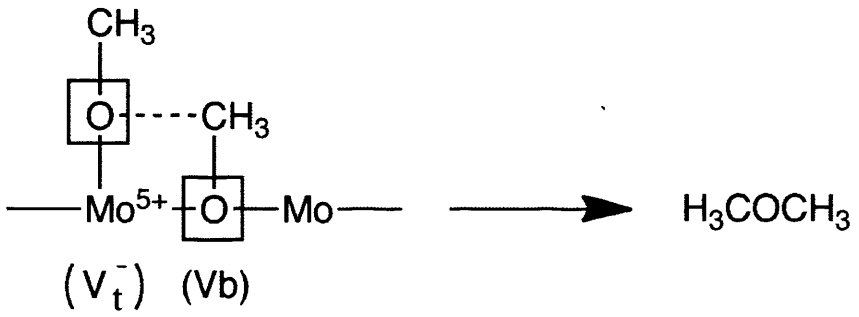

Figure 3-11. Proposed mechanism of DME formation on the MoO_3 surface.[31]

Wachs *et al*[26] investigated activity of 2.3% MoO_3/Fe_2O_3 catalyst in methanol oxidation ($CH_3OH/O_2/He$ = 6/13/81, flow rate 100 ml/min, the amount of catalyst was varied so as to keep conversion between 8 and 18 %) at 230 and 300 °C. They observed formaldehyde and DME as the only products with selectivities 80 and 20 % at 230 °C, and 95 and 5 % at 300 °C respectively. As the catalytic performance of the monolayer system was comparable to that of iron molybdate, the authors stated that the surface MoO_x monolayer, which is the dominant active redox component in bulk iron molybdate catalyst, represents the catalytic active sites.

Though it is a popular consideration in the literature that terminal Mo=O bond is responsible for the catalytic activity in the methanol oxidation, Wachs and co-authors have shown that there is no relationship between catalytic activity and Mo=O bond length or strength.[32] They underlined that the rate-determining step in methanol oxidation is the step of C-H breaking and in CH_3OH adsorption is the step of O-H bond breaking, none of which involve breaking of the Mo=O bond.

In our laboratory M. House investigated monolayer molybdenum on iron oxide catalyst.[25] He made several catalysts with loading varying from 0.24 monolayer (ML) to 7.2 monolayer of Mo on Fe_2O_3. The addition of just 0.24 ML MoO_3 onto the surface of the Fe_2O_3 catalyst had a significant impact on the reaction profile compared to pure iron oxide improving its intrinsic activity by about a factor of five. Formaldehyde selectivity was high at low conversions, with some DME formed, but CO production dominated at moderate conversion. At the highest conversions (>80 %), CO_2 production increased to ~80 % selectivity. A range of other catalysts were produced, with surface doping up to 7.2 ML of MoO_3. Surprisingly, there was relatively little change in the *general* behavior seen for the 0.24 monolayer material. The main differences were a significant reduction in the amount of CO_2 produced, an increase in the formaldehyde yield and a further increase in the activity.[25]

3.1.6. Cobalt-containing catalysts for methanol oxidation.

Recently Schlogl *et al*[17] investigated methanol oxidation over cobalt catalysts (CoO/Co_3O_4). They have shown that the reaction mechanism (partial oxidation to CH_2O or total combustion to CO_2) strongly depends on cobalt oxidation state and methanol-to-oxygen ratio. They observed formation of CoO_x ($1<x<1.33$) surface oxide under reaction conditions. At higher x total combustion was favored, whereas at lower x – partial oxidation of methanol. According

to their results Co_3O_4 catalyzes total oxidation due to high oxygen mobility leading to formate species on the surface, while CoO catalyzes methanol partial oxidation to formaldehyde.

Briand *et al*[33] studied activity of $CoMoO_4$ in methanol oxidation. They used 10 mg of the catalyst, flow rate 100 ml/min and feed gas composition $CH_3OH/O_2/He$ = 6/13/81 in order to maintain conversion less than 10%. Reaction temperature was 380 °C. Under these conditions 88.2 % selectivity towards formaldehyde was observed and 11.8 % selectivity towards DME. Several authors[34-35] reported that selectivity toward partial oxidation products over $CoMoO_4$ catalyst is related to the excess of MoO_3 present on the surface.

To understand the properties of complex supported Mo/Fe_2O_3 ($CoFe_2O_4$) systems we need to have information about all possible components, thus in Sections 3.2 and 3.3 the characterization of single and mixed two-component oxides is described.

3.2. Results and Discussion

3.2.1. Single oxides

This section presents data concerning methanol oxidation over single oxides (cobalt, iron and molybdenum) prepared in our laboratory.

Cobalt oxide Co_3O_4 is a very active combustor of methanol (Figure 3-12) with conversion reaching 50 % at around 170 °C and 100 % by 240 °C. Cobalt oxide is mainly selective towards CO_2 showing high selectivity towards CO only at low temperatures and low conversions. Already at 180 °C we observe 100 % selectivity towards carbon dioxide.

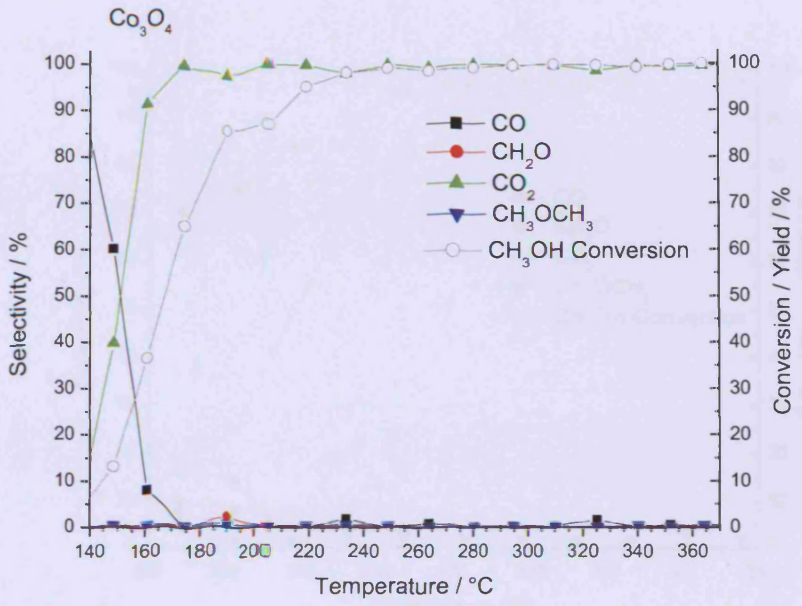

Figure 3-12. Selectivity and conversion for methanol oxidation over Co_3O_4.

The synthesized iron oxide (Figure 3-13) also burns methanol to CO_2 and water, however, as it has lower surface area than cobalt oxide (Table 3-1), it reaches 50 % conversion at a higher temperature (~ 240 °C) and 100 % by 325 °C. At low temperatures (~200 - 250 °C) iron oxide produces minor amounts of CO (<20% selectivity), formaldehyde (<10 %) and DME (<5 %). However, above 260 °C CO_2 is the dominant product with selectivity > 96 %.

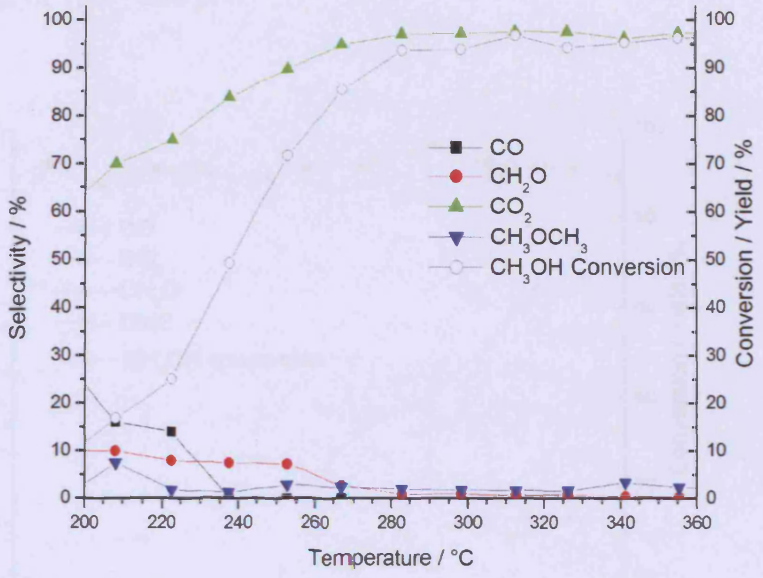

Figure 3-13. Selectivity and conversion for methanol oxidation over Fe_2O_3.

Figure 3-14 shows TPPFR results for methanol oxidation over molybdenum oxide. Both selectivity and conversion profiles are very different from iron and cobalt oxides which have shown rather high activity towards combustion. MoO_3 shows 50 % conversion only at 300 °C and only reaching 87 % at 370 °C. The difference in activity of these oxides is due to the differences in the surface (Table 3-1): molybdena has much lower surface area compared to Fe_2O_3 and Co_3O_4.

Table 3-1. BET surface area of the synthesized mixed oxides.

Sample	Surface area, m^2/g
MoO_3	< 1
Fe_2O_3	12
Co_3O_4	72
$CoFe_2O_4$	60
$Fe_2(MoO_4)_3$	7
$CoMoO_4$	25

However, excellent selectivity towards formaldehyde is observed over MoO_3: 90-96 % selectivity in the temperature range of 180 – 340 °C. At higher temperatures the CH_2O

selectivity drops and CO_2 starts to form. A minor selectivity (< 5 %) towards DME is observed in the range of 180 – 250 °C.

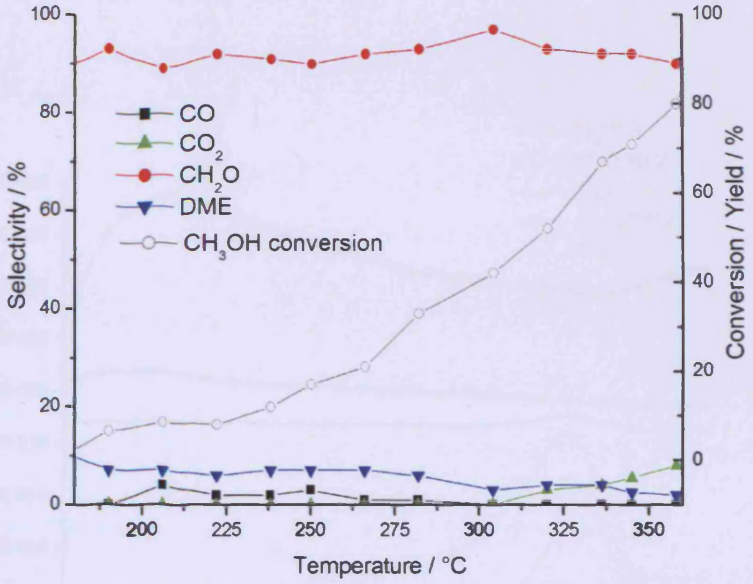

Figure 3-14. Selectivity and conversion for methanol oxidation over MoO_3.

As it was said above, the difference in catalytic behaviour of molybdena, iron and cobalt oxides is related to the nature of adsorbed intermediates on the surfaces (methoxy and formate respectively).

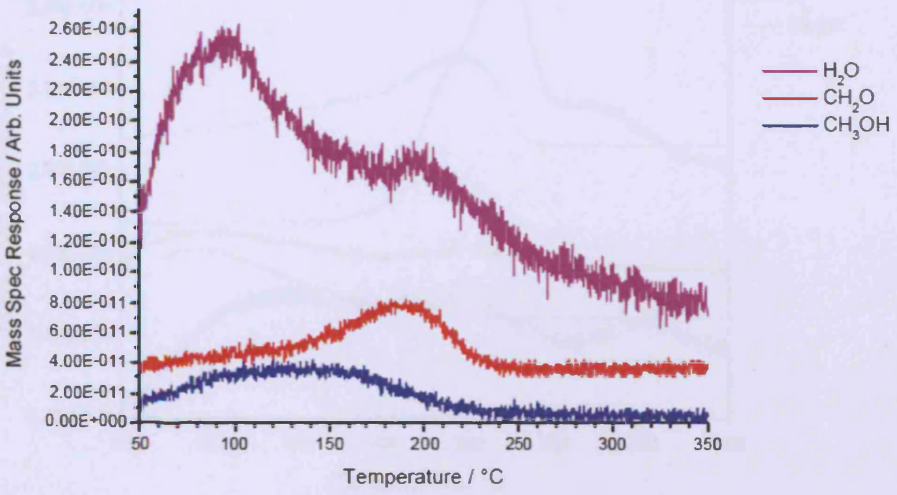

Figure 3-15. TPD of MoO_3 saturated with methanol at room temperature.

This difference in behavior is also seen in the TPD experiments (shown in Figure 3-15, Figure 3-16 and Figure 3-17), where the only carbon-containing product is formaldehyde for MoO_3, whereas the combustion product, CO_2, is major for iron and cobalt oxides.

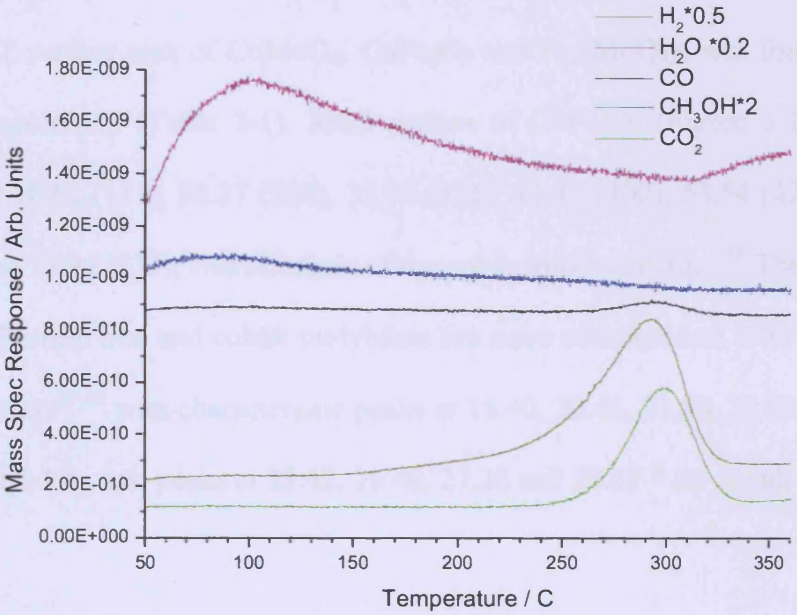

Figure 3-16. TPD of Fe_2O_3 saturated with methanol at room temperature.

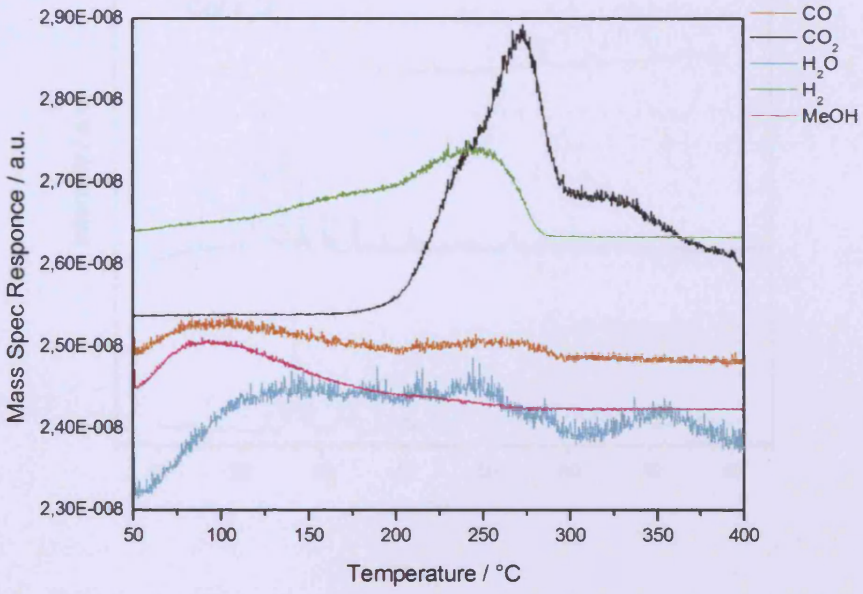

Figure 3-17. TPD of Co_3O_4 saturated with methanol at room temperature.

3.2.2. Mixed Oxides

This section contains details on methanol oxidation over mixed oxides (cobalt molybdate, cobalt ferrite and ferric molybdate) prepared in our laboratory.

3.2.2.1. Structural Characterization

The BET surface area of $CoMoO_4$, $CoFe_2O_4$ and $Fe_2(MoO_4)_3$ was found to be 25, 60 and 7 m^2/g respectively (Table 3-1). XRD pattern of $CoFe_2O_4$ (Figure 3-18) shows seven main peaks at 18.61 (111), 30.27 (220), 35.74 (311), 43.47 (400), 53.54 (422), 57.19 (511), 62.73 (440) and 73.99 (533), characteristic of the cubic spinel structure.[36] The diffraction patterns of the synthesized iron and cobalt molybdate are more complex and follow the patterns given in the literature[37-38] with characteristic peaks at 15.40, 20.48, 21.88, 23.08, 25.86 and 27.57 ° for iron molybdate, and peaks at 23.42, 26.49, 27.26 and 28.47 ° for cobalt molybdate.

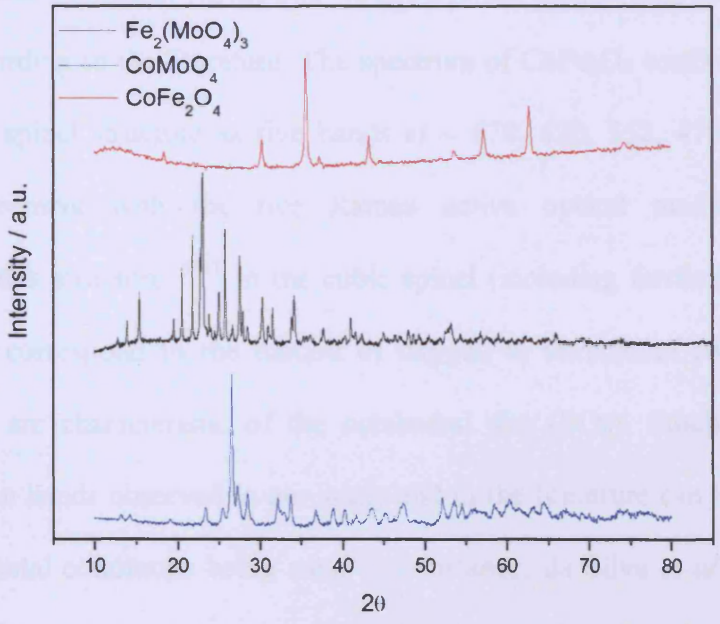

Figure 3-18. XRD patterns of $CoFe_2O_4$, $CoMoO_4$ and $Fe_2(MoO_4)_3$.

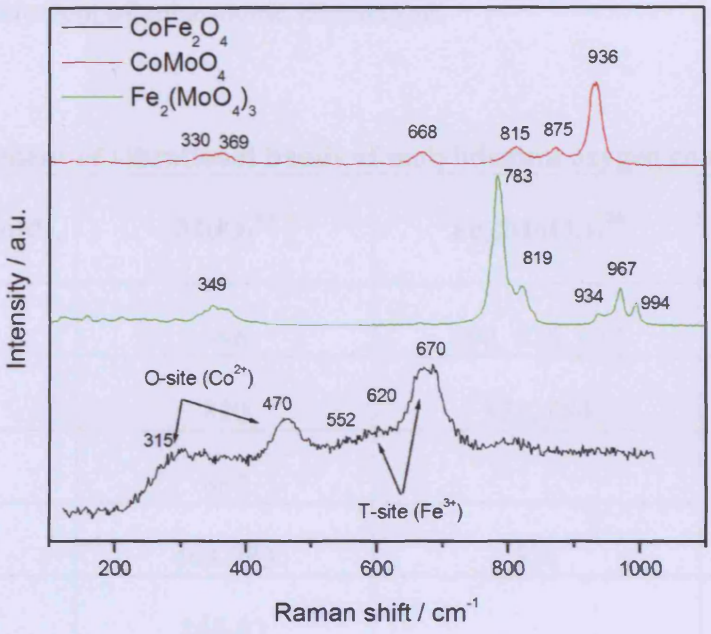

Figure 3-19. Raman spectra of $CoFe_2O_4$, $CoMoO_4$ and $Fe_2(MoO_4)_3$.

Raman spectra of cobalt ferrite and iron and cobalt molybdates are shown in Figure 3-19. Tables 3-2 and 3-3 show the Raman assignment for simple reference compounds and mixed oxides according to the literature. The spectrum of $CoFe_2O_4$ confirms the presence of the cubic inverse spinel structure as five bands at ~ 670, 620, 552, 470 and 315 cm^{-1} are observed in agreement with the five Raman active optical modes ($A_{1g}+1E_g+3T_{2g}$) characteristic for this structure.[39-41] In the cubic spinel (including ferrites) the modes above 600 cm^{-1} usually correspond to the motion of oxygen in tetrahedral AO_4, the other low-frequency modes are characteristic of the octahedral site (BO_6). Small deviations of the positions of Raman bands observed in our study and in the literature can be explained by the different experimental conditions being used. For instance, da Silva *et al*[42] observed that an increase of the laser power from 0.7 to 7 mW resulted in a shift of the Raman bands to lower

wavenumbers, which was interpreted as being due to sample heating produced by the laser light, leading to increment of anharmonic interactions.

Table 3-2. Assignment of vibrational bands of molybdenum oxygen compounds.

Compounds Vibrational bands, cm^{-1}	**MoO_3[43]**	**$Fe_2(MoO_4)_3$[26]**	**$CoMoO_4$[44]**
Mo=O stretch	996	990, 970, 937	938
Mo-O-Mo Asym. Stretch	820	821, 784	700-920
Mo-O-Mo Sym. Stretch	667		
Mo=O Bending	469-283	336	310-480
Mo-O-Mo deformation	244-83		

The spectrum of cobalt molybdate shows six bands at 936, 875, 815, 668, 369 and 330 cm^{-1} characteristic of the presence the α – $CoMoO_4$ phase.[44] The Raman spectrum of $Fe_2(MoO_4)_3$ exhibits bands at 994, 967, 934, 819, 783 and 349 cm^{-1}. Three bands at 994, 967 and 934 cm^{-1} represent symmetric stretching of the terminal Mo=O bond. Bands at 819 and 783 cm^{-1} are assigned to the asymmetric Mo-O-Mo stretching and the band at 349 cm^{-1} is related to the bending mode.[26, 45] There is no agreement in literature whether 994 and 819 cm^{-1} observed in the spectrum of iron molybdate belong to iron molybdate or to MoO_3 phase. Some authors attribute them to the surface MoO_3 species or to the octahedral MoO_6 present in the amorphous layer of iron molybdate,[46] while the others state that these bands are assigned to the iron molybdate as there is no MoO_3 characteristic band at 284 cm^{-1} in the Raman spectrum of $Fe_2(MoO_4)_3$.[26]

Table 3-3. Characteristic Raman bands for iron and cobalt oxides and cobalt ferrite.

Compound	Bands, cm^{-1}	Assignment, mode	Ref.
Co_3O_4	194 482 521 618 691	F_{2g} E_g F_{2g} F_{2g} A_{1g}	47
Fe_2O_3	225 247 293 299 412 498 613	A_{1g} E_g E_g E_g E_g A_{1g} E_g	48
$CoFe_2O_4$	311 470 575 624 695	T_{2g} T_{2g} T_{2g} E_g A_{1g}	49

3.2.2.2. Catalytic reactivity in oxidation of methanol

Figure 3-20 shows activity results of methanol oxidation over a cobalt ferrite catalyst. With conversion starting at around 120 °C and reaching 100 % by 220 °C, $CoFe_2O_4$ selectively combusts methanol to CO_2 and water. The only by-products are DME (selectivity less than 15 %) and formaldehyde (< 10 %) peaking at 180 and 200 °C respectively.

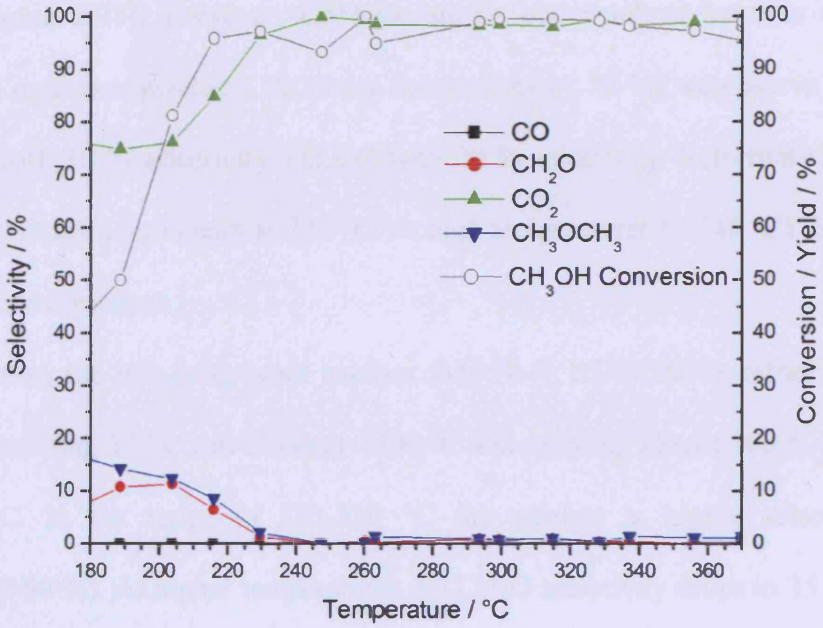

Figure 3-20. Selectivity and conversion for methanol oxidation over $CoFe_2O_4$.

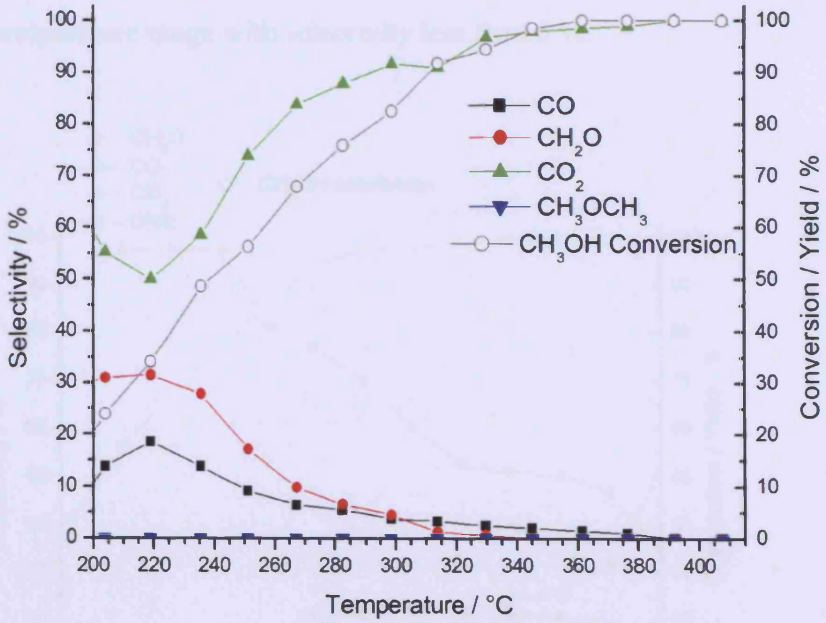

Figure 3-21. Selectivity and conversion for methanol oxidation over $CoMoO_4$.

Cobalt molybdate shows conversion attaining only 50 % at 240 °C and around 100 % at 340 °C (Figure 3-21). However, $CoMoO_4$ shows better selectivity than cobalt ferrite towards partial oxidation products. At lower conversions (< 70 %) we observe formation of formaldehyde with 30 % selectivity and CO with 20 % selectivity. Selectivity towards both products goes through a maximum at 220 °C. At high temperatures (> 340 °C) carbon dioxide is the only observed product.

In contrast, the iron molybdate catalyst (Mo:Fe = 1.5:1) shows rather high activity (Figure 3-22) reaching 50 % conversion at ~200 °C and reaching almost 100 % conversion at around 260 °C. In the range of 180-230 °C the catalyst is highly selective towards formaldehyde (>90 %). At higher temperatures the CH_2O selectivity drops to 35 % by 380 °C and the evolution of CO, CO_2 and DME begins. Carbon monoxide starts to form at 230 °C, attains maximum of selectivity ~ 25% and does not change much after. Carbon dioxide begins to be produced at 260 °C reaching 52 % selectivity at 380 °C. DME is produced across almost the whole temperature range with selectivity less than 6 %.

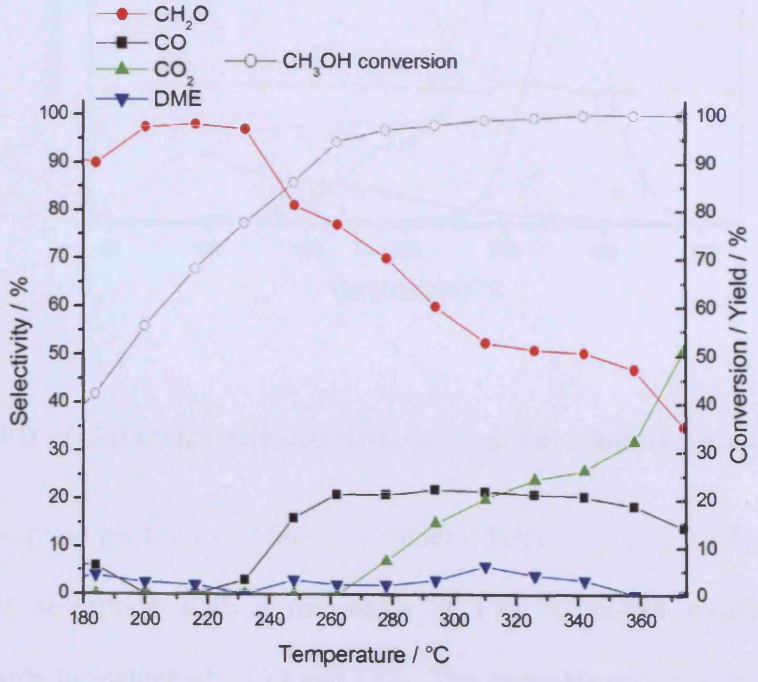

Figure 3-22. Selectivity and conversion for methanol oxidation over $Fe_2(MoO_4)_3$.

3.2.2.3. TPD

Methanol TPD experiments were used to investigate surface intermediates and to calculate energies of desorption in order to determine what energy barriers must be overcome for product formation.

Figure 3-23 shows a profile of methanol desorption for the cobalt ferrite. There is rather small but broad methanol desorption peak with a centre of desorption at 125 °C. $CoFe_2O_4$ shows no selectivity towards formaldehyde with an intense peak of CO_2 at 283 °C and a large H_2 peak at 269 °C with a shoulder at 188 °C. Water desorption is insignificant with a small peak at around 270 °C.

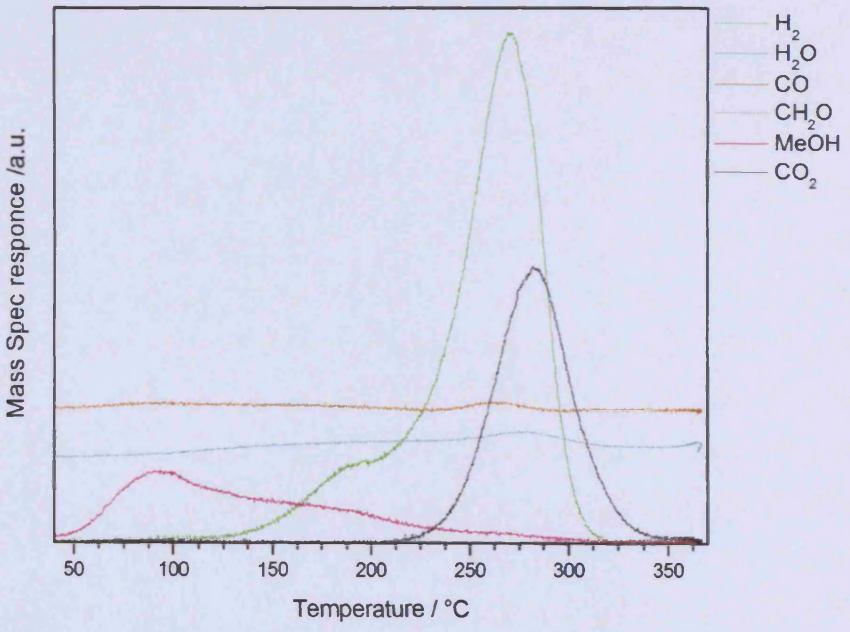

Figure 3-23. TPD of $CoFe_2O_4$ saturated with methanol at room temperature.

The desorption profile of $CoMoO_4$ is rather different (Figure 3-24). With a large and broad methanol desorption with a maximum at 110 °C cobalt molybdate also shows selectivity towards formaldehyde, CO and CO_2. The formaldehyde desorption peak is small

and occurs at 240 °C. The CO and CO_2 desorption peaks are similar in intensities and occur at 262 and 296 °C respectively. There is also hydrogen desorption with a peak at 250 °C and a shoulder at 300°C. Water desorbs in two peaks at 113 and 295 °C.

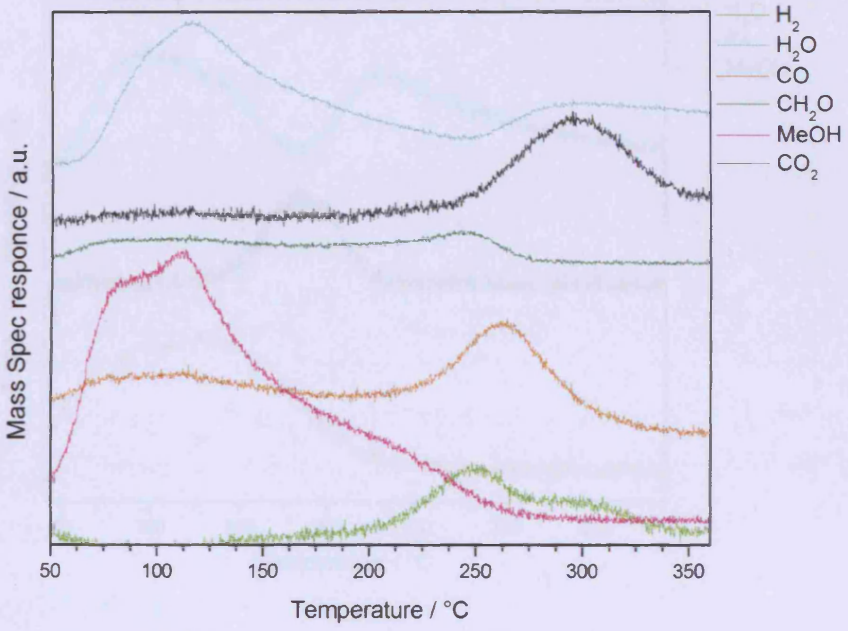

Figure 3-24. TPD of $CoMoO_4$ saturated with methanol at room temperature.

The TPD profile of iron molybdate (Mo:Fe=1.5:1) shows a broad methanol desorption centred at 120 °C (Figure 3-25). There is formaldehyde desorption peak at 184 °C. Water presents two peaks at 103 and 232 °C.

The significant difference in products observed in the TPD experiments over mixed oxides is related to different intermediates formed on the surface. We can assume that on cobalt ferrite having a spinel structure as well as Co_3O_4 methanol adsorbs as methoxy species and, due to high lattice oxygen mobility, quickly transforms to formate species (reaction 3-4) which decompose to CO_2 and H_2/H_2O.

Adsorption of methanol over cobalt and iron molybdates gives rise to methoxy species as desorption of formaldehyde is clearly observed in TPD. However, there is also production

of CO and CO_2 for $CoMoO_4$, which might be formed via two paths: production of carbon monoxide directly from methoxy species (according to reaction 3-2) or from formaldehyde re-adsorbed on the catalyst surface (reaction 3-3).

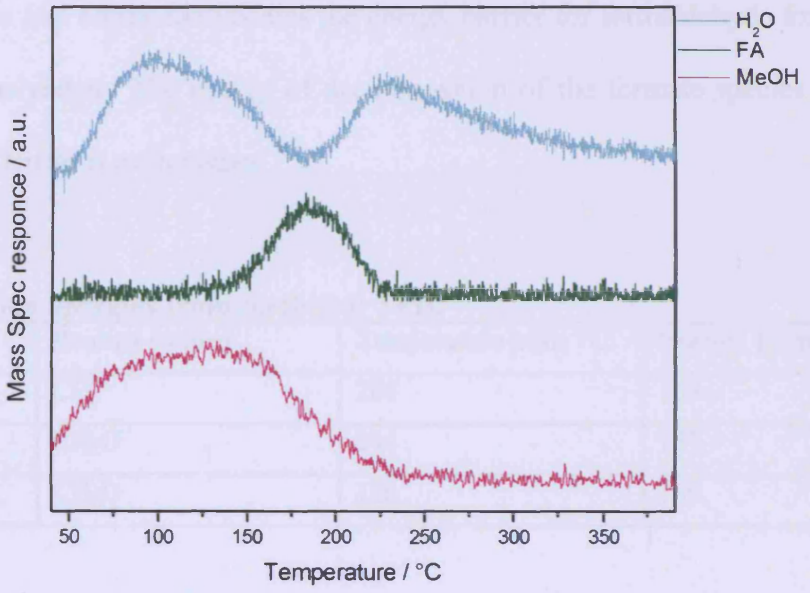

Figure 3-25. TPD of $Fe_2(MoO_4)_3$ saturated with methanol at room temperature.

It was shown previously in Bowker group[25] that low temperature water peak, observed in most of TPDs, is attributed to water introduced with a gas flow. High temperature water peak centred at around 250 °C might be the recombination of hydroxyls and hydrogen formed during dissociative adsorption of methanol[31] (see Figure 3-26).

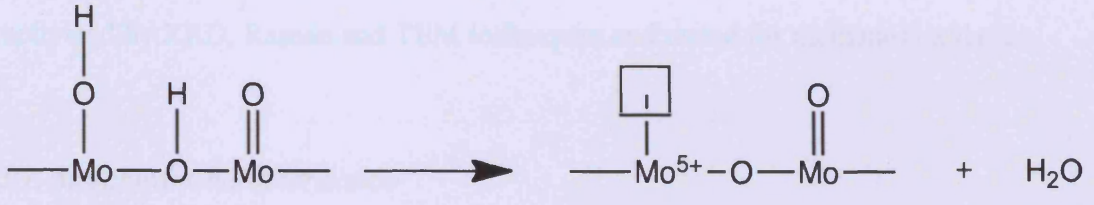

Figure 3-26. Proposed mechanism of H_2O formation on the MoO_3 surface.[31]

Table 3-4 shows the calculated values of the energy of desorption of CH_2O from iron and cobalt molybdates and CO_2 from cobalt ferrite using the Readhead equation (equation 2-4). This equation can be applied for products which do not undergo further transformation on the surface.

Between iron and cobalt molybdates the energy barrier for formaldehyde formation is higher for cobalt molybdate. The energy of decomposition of the formate species to carbon dioxide over cobalt ferrite is even higher.

Table 3-4. Desorption energies from methanol TPD.

Catalyst	Product formed	Temperature peak, °C	Energy, kJ/mol
$CoFe_2O_4$	CO_2	284	169
$CoMoO_4$	CH_2O	244	157
$Fe_2(MoO_4)_3$	CH_2O	186	139

3.2.3. Thin layer oxides Mo/Fe_2O_3

Model thin layer oxides are useful in the investigation of the interactions between their components (in our case iron oxide and molybdena) and of the reaction mechanism. In our group some work on MoO_3/Fe_2O_3 was previously carried out by M. House. He made 0.24 ML, 0.6 ML, 2.4ML and 7.2 ML samples and investigated their reactivity in methanol oxidation. Only XPS characterization of these samples has been done. In the current study monolayer samples with molybdenum loading 1 ML, 3ML, 6 ML and 8ML were synthesized, characterized by XRD, Raman and TEM techniques and tested for methanol oxidation.

3.2.3.1. Structural Characterization

Figure 3-27 presents XRD patterns of the 6 ML Mo/Fe_2O_3 sample calcined at 400 and 500 °C, the 8 ML Mo/Fe_2O_3 sample calcined at 400 °C and reference α-iron oxide. Below the loading of ~ 6 ML the only observable peaks in XRD patterns were due to haematite. However, at

higher loadings some other peaks could be discerned, though the spectra are still dominated by the hematite peaks at 2θ = 24.17, 33.3, 35.7, 40.9, 49.5, 54.2, 57.6, 62.3, 64.2, 72.0 and 75.4°.[50] Expansion of the 12-30 °θ region for the 6 ML samples and low angle experiment (the speed of accumulation 0.04 °/min) for the 8 ML sample (Figure 3-27) allowed resolution of the main molybdena peaks (12.8, 23.2, 25.5 and 27.3°)[51] for the 6 and 8 ML samples calcined at 400 °C and iron molybdate peaks at around 20, 21 and 22 °[37] for the 6 ML sample calcined at 500 °C. Though the molybdena characteristic peak at 12.8 ° is not resolved for the 6 ML sample calcined at 400 °C, the relative intensities of the peaks at 23, 25 and 27° are indicative for molybdena.[51] From these results we can conclude that iron molybdate starts to form after calcination at temperatures higher than 400 °C. This is further confirmed by Raman spectroscopy.

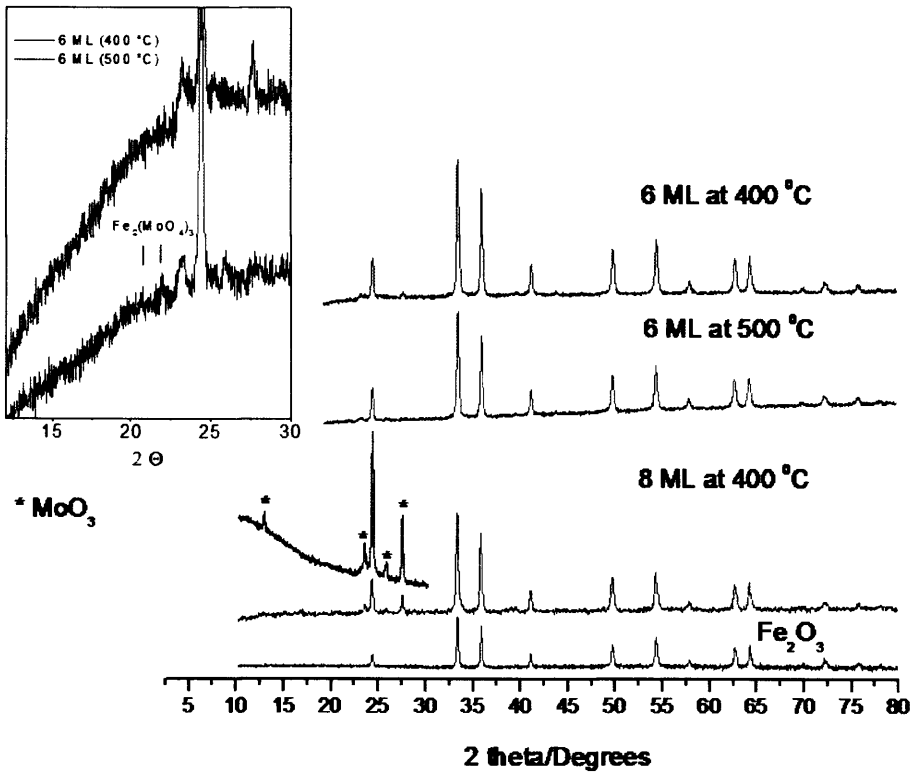

Figure 3-27. XRD patterns of 6-8 ML Mo/Fe_2O_3 with different calcination temperature. For the 6 ML Mo/Fe_2O_3 samples the 12-30 °θ region is expanded and for the 8 ML Mo/Fe_2O_3 sample a low angle experiment (in black) is shown.

The various MoO_3/Fe_2O_3 monolayer catalysts were examined by Raman spectroscopy. Figure 3-28 shows Raman spectra of reference materials *i.e.* haematite, molybdena and ferric molybdate. The main bands for haematite support are at 287, 401, 493 and 598 cm^{-1}, which are characteristic for $\alpha - Fe_2O_3$.[26] The position and assignment of bands characteristic for molybdena and iron molybdate were given in Table 3-2. Raman is not a surface-sensitive technique, and so we could not observe useful signal from the doped Mo layers on the haematite catalysts below ~ 3 ML of Mo. Figure 3-29 shows spectra from the surface of samples doped with different molybdenum loadings and calcined at 400 °C. The Raman spectrum of the 3 ML sample is essentially the same as that of iron oxide support with the only difference of a broad band appeared at around 950 cm^{-1}. This band is also observed for other samples loaded with Mo and is assigned to a two-dimensional polymeric surface molybdena species.[52] Further increase of Mo loading (to 6, 7.2ML) gives rise to bands at 817 and 990 cm^{-1} which are characteristic of Mo-O-Mo asymmetric stretching and Mo=O bond stretching in molybdena (Table 3-2). Routary *et al*[26] observed a band at 724 cm^{-1} in the Raman spectrum of 3 % MoO_3/Fe_2O_3, which was attributed to the bridging Mo-O-Fe functionality on the surface of MoO_x species. However our Raman investigations did not show the presence of such a band.

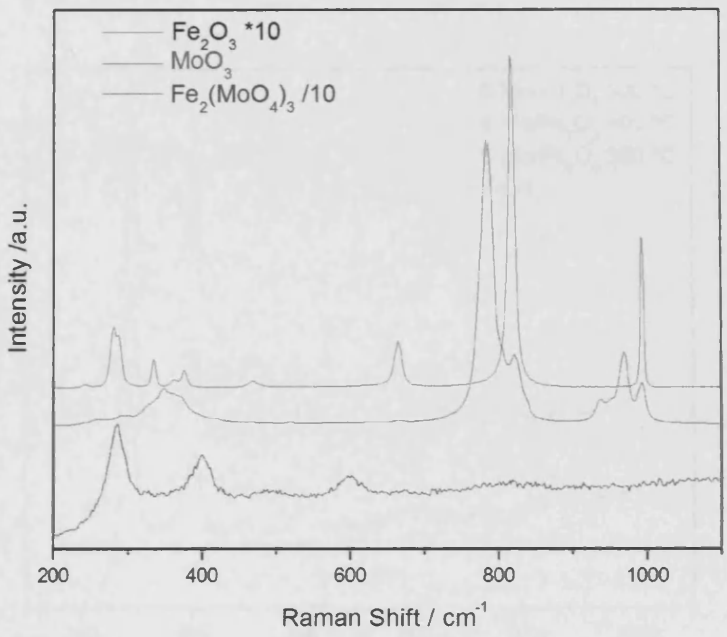

Figure 3-28. Raman spectra of reference MoO_3, Fe_2O_3 and $Fe_2(MoO_4)_3$.

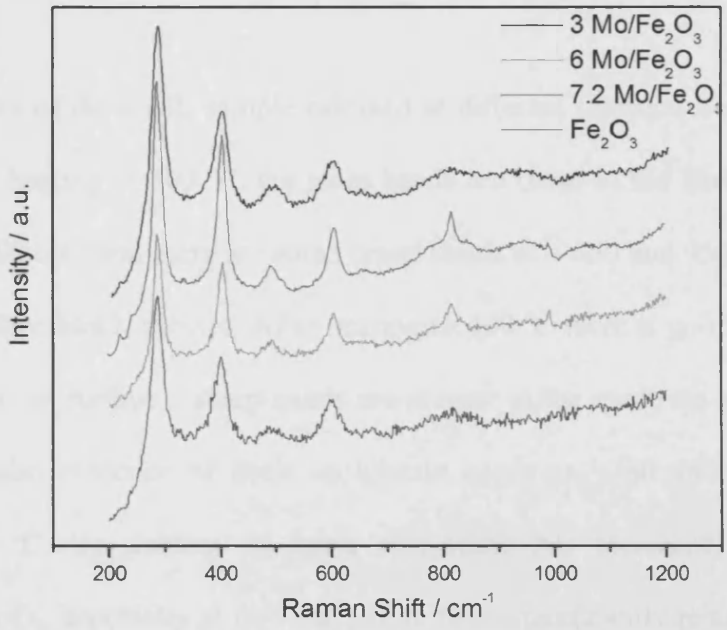

Figure 3-29. Raman spectra of the 0-7 ML Mo/Fe_2O_3 systems.

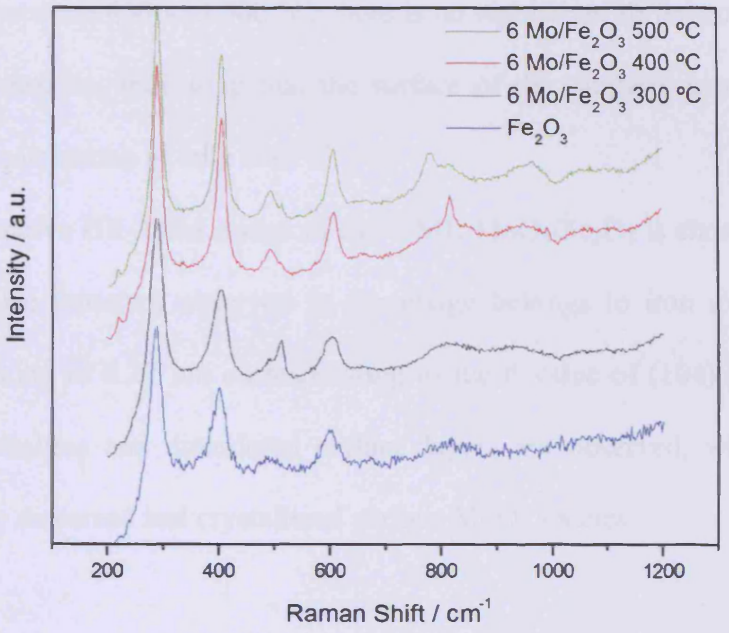

Figure 3-30. Raman spectra of the 6 ML Mo/Fe_2O_3 catalyst calcined at different temperatures (300-500 °C).

Raman spectra of the 6 ML sample calcined at different temperatures were collected (Figure 3-30). After heating to 300 °C, the main bands are those of the haematite at around 285, 400, 490 and 600 cm^{-1} and there are some broad bands at ~ 650 and 950 cm^{-1}, which are attributed to the surface MoO_x species. After heating to 400 °C there is good evidence of the presence of MoO_3 at the surface – sharp bands are present in the spectrum at ~ 817 and 993 cm^{-1}, and there is also evidence of ferric molybdate bands at ~780 and 960 cm^{-1}. After calcination to 500 °C, the content of ferric molybdate has increased, and the bands corresponding to MoO_3, especially at 817 cm^{-1}, have been significantly reduced in intensity. Since Raman is mainly a bulk technique, it is not surprising that the spectra of these samples were dominated by the iron oxide peaks, but the formation of ferric molybdate was confirmed by the bands at ~780 and 960 cm^{-1} due to the bridging and terminal Mo-O stretches

respectively. These latter bands are distinguished from those of MoO_3 itself, by being shifted by ~ 30 cm^{-1} to a lower wavenumber. However, notwithstanding that the Raman changes upon calcination between 400 and 500 °C, there is no significant difference in the reactivity between the two surfaces, indicating that the surface of the catalysts is already mainly the mixed phase after calcination at only 400 °C.

A representative HR-TEM image of the 6 ML MoO_3/Fe_2O_3 is shown in Figure 3-31. The main crystalline structure observed in the image belongs to iron oxide as the lattice fringes with a spacing of 0.27 nm corresponding to the d value of (104) plane[53-54] are seen clearly. Also, crystalline and disordered surface layers are observed, which are probably attributed to highly dispersed and crystallized surface MoO_x species.

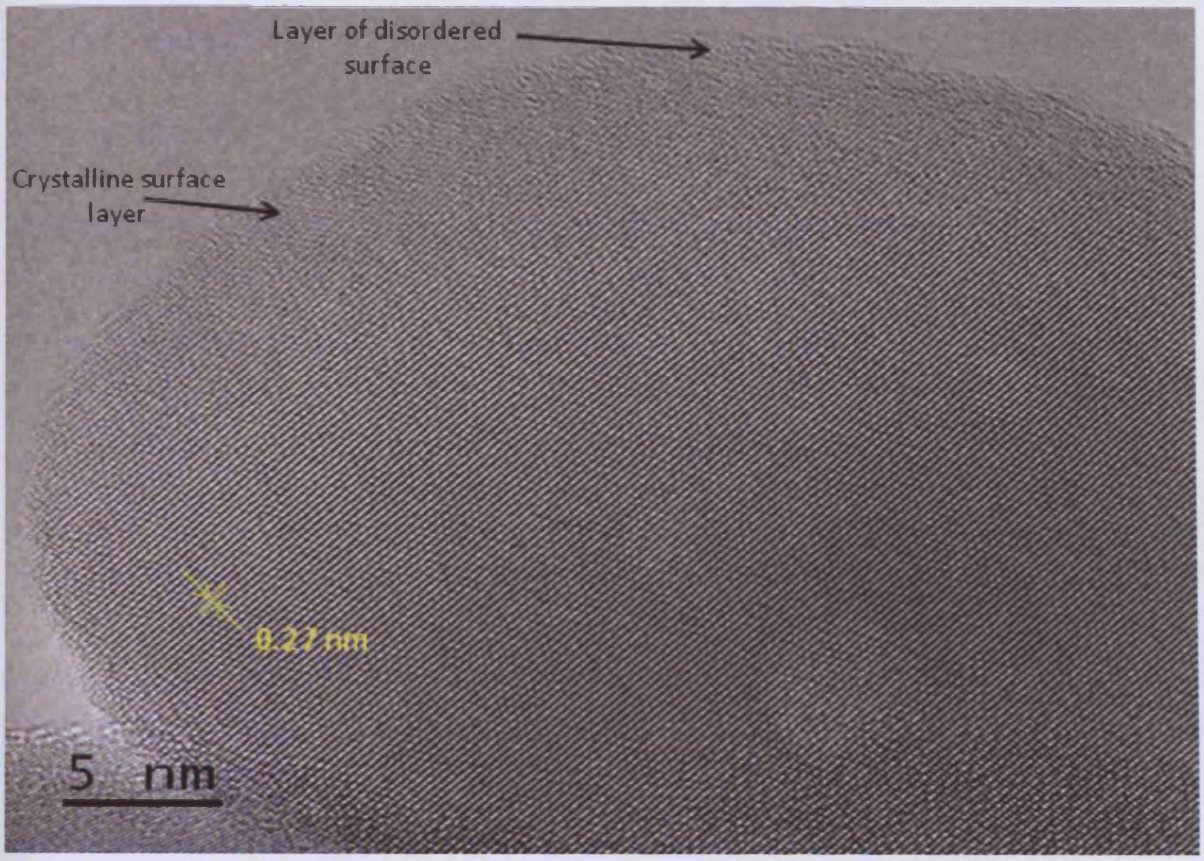

Figure 3-31. TEM image of the 6 ML Mo/Fe_2O_3 calcined at 400 °C.

3.2.3.2. Catalytic reactivity in methanol oxidation.

Doping iron oxide surface with 1 ML of molybdena (Figure 3-32) significantly affected the reaction profile compared to pure iron oxide (Figure 3-13). A 50 % conversion is observed at 230 °C and 100 % conversion – at 290 °C. For the Fe_2O_3 alone the conversion was only about 10 and 40% respectively. Thus, the intrinsic activity has improved by about a factor of five, since the surface area is about the same. Formaldehyde selectivity is high (~70%) at low conversions, with some dimethyl ether (DME) formed, but CO production begins to dominate at moderate conversion. At the highest conversions (>80 %), CO_2 production rises to ~80 % selectivity by 360 °C, but the CO_2 production overall is much less than that over iron oxide alone.

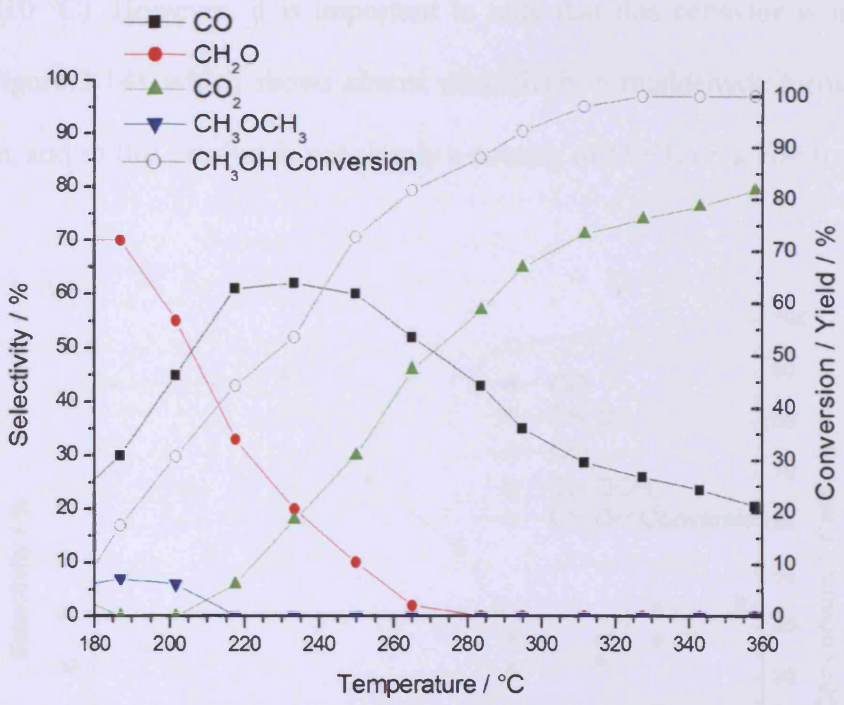

Figure 3-32. Selectivity and conversion for methanol oxidation over the 1 ML Mo/Fe_2O_3.

Figure 3-33 and Figure 3-34 show TPPFR results for the 3 ML and the 6 ML MoO_3/Fe_2O_3 samples respectively. The increase in the molybdenum loading affects selectivities of the products. Thus selectivity towards formaldehyde increases up to 85 % and 92 % at low conversion for the 3 ML and the 6 ML samples respectively compared to 70 % for the 1 ML sample. More DME is being produced (5-10 % selectivity) in the whole temperature range over these catalysts. CO production dominates over CO_2 for both the 3 and the 6 ML samples, however a little bit more CO forms over the catalyst with higher Mo content. Further loading of iron oxide with molybdenum (up to 8 monolayers) did not change reaction profile much. The main differences are a significant reduction in the amount of CO_2 produced, an increase in the formaldehyde yield and a further increase in activity ($T_{50\%\ conv}$ reduced to ~ 210 °C). However, it is important to note that this behavior is not typical of MoO_3 alone (Figure 3-14), which shows almost exclusively formaldehyde formation even at high conversion, and so this catalyst is not simply a coating of MoO_3 on a Fe_2O_3 core.

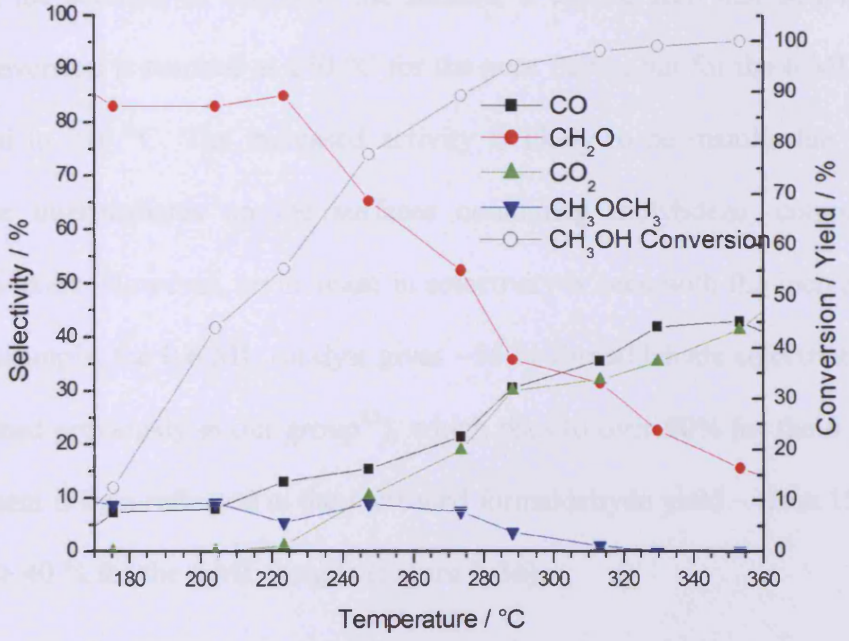

Figure 3-33. Selectivity and conversion for methanol oxidation over the 3 ML Mo/Fe_2O_3.

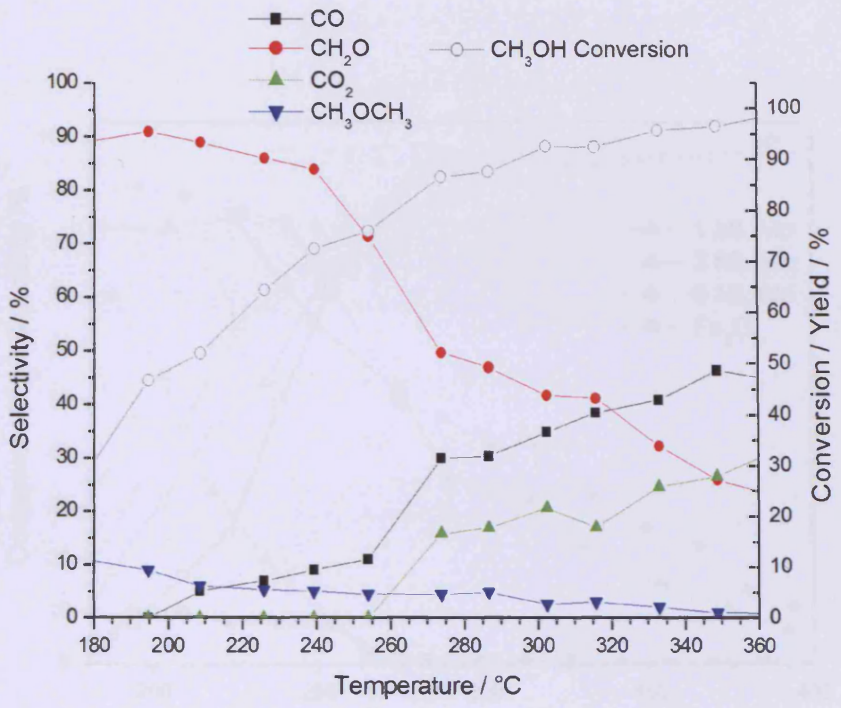

Figure 3-34. Selectivity and conversion for methanol oxidation over the 6 ML Mo/Fe_2O_3.

Figure 3-35 shows a comparison of MoO_3/Fe_2O_3 catalysts with different molybdenum loadings. With the addition of MoO_3 to the surface, it can be seen that activity increases. Thus, 50 % conversion is reached at 250 °C for the pure Fe_2O_3, but for the 6 ML catalyst the $T_{50\%}$ is reduced to 210 °C. The increased activity is likely to be mainly due to the lower stability of the intermediates on the surfaces containing molybdena, compared to one containing iron oxide. However, an increase in selectivity is seen with the increased loading, at 200 °C for example, the 0.6 ML catalyst gives ~55 % formaldehyde selectivity (according to results obtained previously in our group[25]), which rises to over 90% for the 6 ML catalyst. This improvement is then reflected in the increased formaldehyde yield – from 15 % for the 1 ML sample to > 40 % for the 6 ML sample (Figure 3-36).

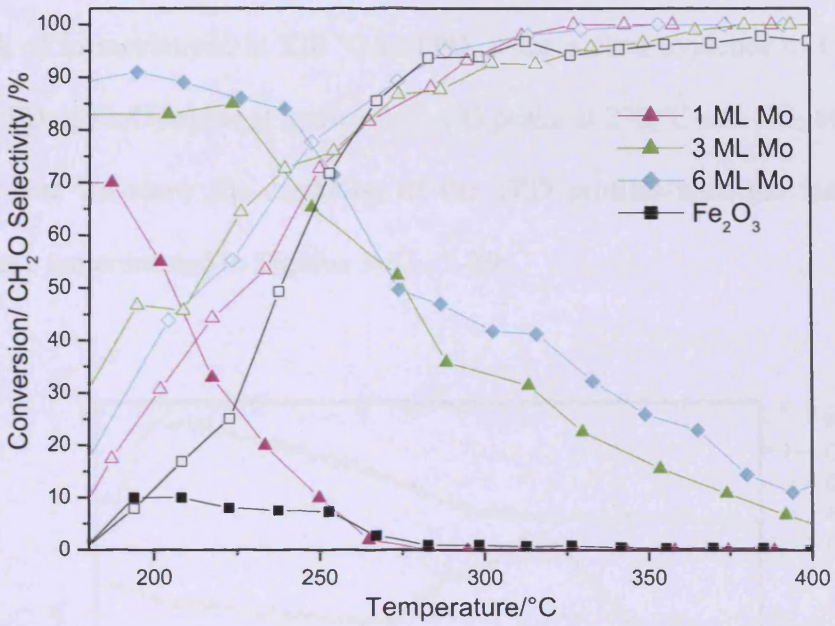

Figure 3-35. Comparison of conversion (open symbols) and formaldehyde selectivity (filled symbols) for the 0-6 ML Mo/Fe_2O_3 samples.

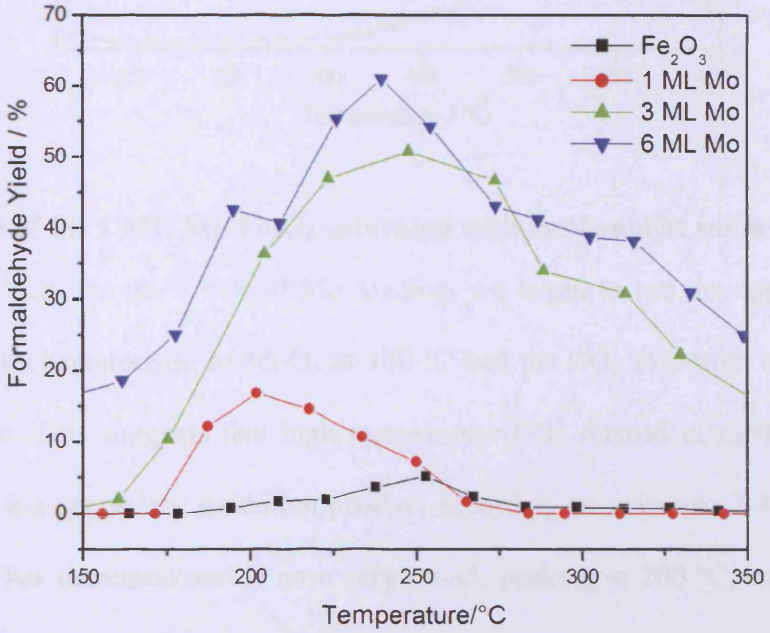

Figure 3-36. Formaldehyde yield as a function of temperature for the 0-6 ML Mo/Fe_2O_3 samples.

3.2.3.3. TPD

Figure 3-37 shows the TPD from the 1 ML Mo/Fe_2O_3 sample. Although there is quite a small desorption peak of formaldehyde at 220 °C in TPD, there is clear evidence of CO evolution, in contrast to TPD of Fe_2O_3 alone (Figure 3-16); CO peaks at 270 °C and CO_2 at 320 °C. It is important that here we show the evolution of the TPD profiles with the increase in Mo loading, and these are presented in Figures 3-37 - 3-39.

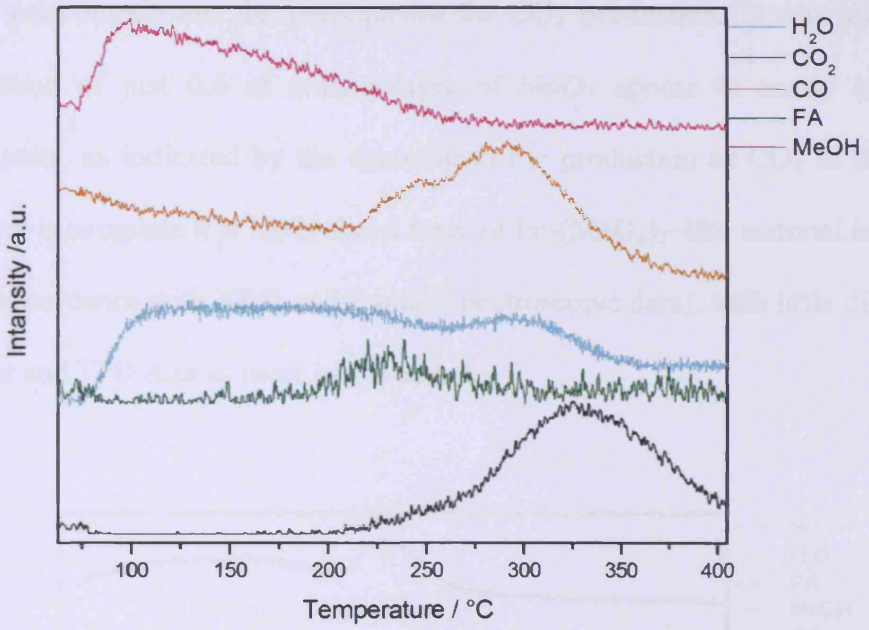

Figure 3-37. TPD of the 1 ML Mo/Fe_2O_3 saturated with methanol at room temperature.

In Figure 3-38, for the 3 ML of Mo loading, we begin to see the appearance of the formaldehyde peak characteristic of MoO_3 at 180 °C and the CO_2 evolution characteristic of iron oxide is gone. This suggests that high temperature CO_2 formed in methanol oxidation over this catalyst is a secondary oxidation product according to reactions 3-4 and 3-5. Also, the CO evolution has increased and is now very broad, peaking at 200 °C, but with a higher temperature tail up to ~300 °C.

The TPD profile of the 6 ML sample is very similar to that of the 3 ML sample. It appears that at low loadings, the isolated molybdenum sites produce high temperature (~270 °C) CO as a primary product and the presence of uncovered Fe_2O_3 is revealed by CO_2 production. With further addition of molybdenum the surface becomes increasingly covered with Mo (Figure 3-39), with the likely formation of neighboring molybdena pair sites, which we suggest are necessary for formaldehyde production, following the proposals of [21-22] and from the previous work in our lab.[55-57] At that point it appears that there are no remaining neighboring iron pairs which are the prerequisite for CO_2 production. It was shown by House[25] that addition of just 0.6 of a monolayer of MoO_3 appear to nearly eliminate neighboring iron pairs, as indicated by the decrease in the production of CO_2 in the TPD. Once the monolayer is complete it is likely that a layer of $Fe_2(MoO_4)_3$–like material is formed at the surface (in accordance with XRD and Raman spectroscopic data), with little difference observed in reactor and TPD data as more Mo is added.

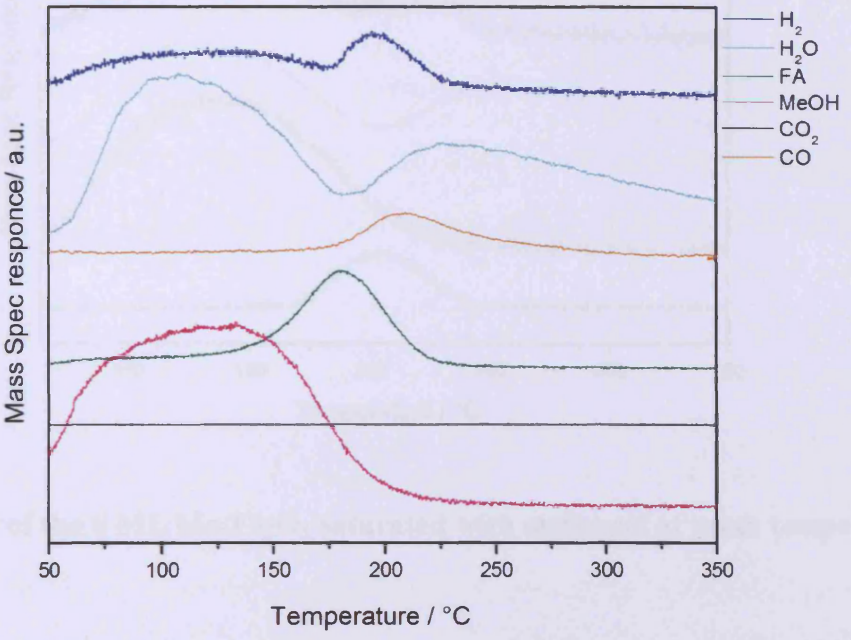

Figure 3-38. TPD of the 3 ML Mo/Fe_2O_3 saturated with methanol at room temperature.

If we turn to the nature of CO evolution, there is a significant change of the temperature of the peak with increasing loading of Mo. At low loading (1 ML) the peak is close to the iron oxide formate, and appears at 270 °C, while at loadings of 3 ML and above it is fixed at 200 °C, close to the formaldehyde evolution temperature. At the intermediate coverage of 3 ML the peak is broad, probably due to the presence of both states. The fact that the temperature of CO production from the catalyst made of 3 ML of Mo and over, being close to that seen for the formaldehyde peak, suggests that this in some way is associated with Mo. It may be that these two distinct CO states may be associated with the isolated Mo (the high temperature state) and mixed Fe-Mo (the low temperature state) sites, as discussed below.

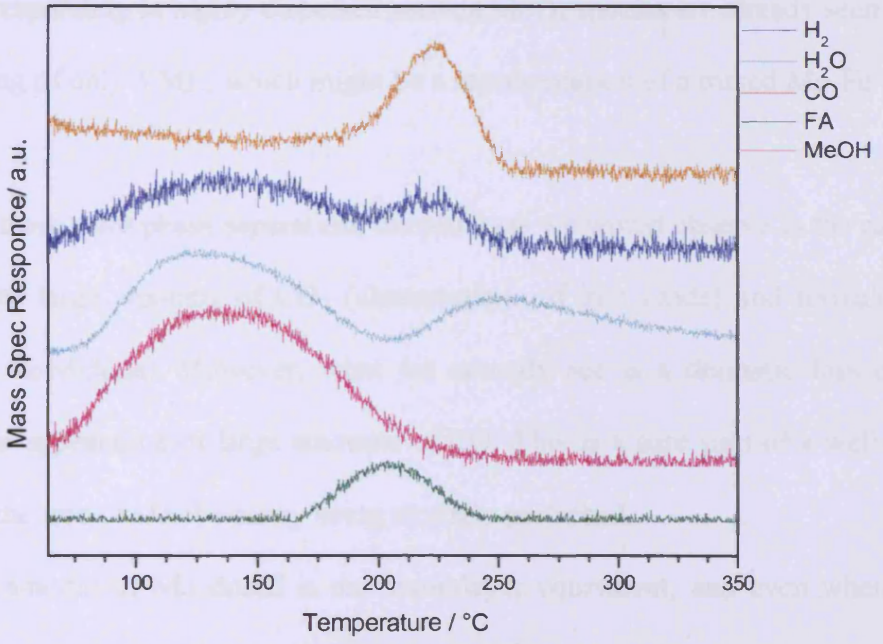

Figure 3-39. TPD of the 6 ML Mo/Fe_2O_3 saturated with methanol at room temperature.

From the data collected within this work and by previous investigations it is apparent that the most important requirement for the formaldehyde production is the presence of

surface molybdenum oxide. Production of CO_2 and H_2 is observed in TPD from the pure Fe_2O_3 surface, due to methanol reacting with the catalyst surface via a formate surface intermediate.[16, 56-57] Addition of only small amounts of molybdenum, either by impregnation as used here, or by co-precipitation reported before,[57] results in a significant reduction in CO_2 yield and an increase in partial oxidation products, due to stabilization of surface methoxy species. Only low levels of Mo are required to have dramatic effects on reactivity, because Mo preferentially segregates to the surface of the sample, producing a ferric molybdate coating of the iron oxide core. This is evidenced by XRD and Raman spectroscopy for the sample calcined at 400 °C, where bands (Mo-O-Mo vibrations and Mo=O terminal vibrations) associated with MoO_3 (octahedral Mo), along with those for $Fe_2(MoO_4)_3$ (tetrahedral molybdenum) are observed even for catalysts with a Mo loading of 6 ML. Also the broad Raman bands corresponding to highly dispersed surface MoO_x species are already seen for the sample with loading of only 3 ML, which might be a representation of a mixed Mo-Fe surface layer.

Finally, if there were phase separation, the products we would observe in the catalysis and TPD would be large amounts of CO_2 (characteristic of iron oxide) and formaldehyde (characteristic of molybdena). However, what we actually see is a dramatic loss of CO_2 production and the appearance of large amounts of CO. This is a sure sign of a well mixed surface layer and the iron oxide chemistry being strongly perturbed.

When the amount of Mo dosed is one monolayer equivalent, and even when much more is dosed, the catalysts produce large amounts of CO, and have a relatively low yield of formaldehyde (~ 50 % maximum), unlike a real catalyst (>1.5:1 Mo:Fe, yield ~90%)[16, 56-57] or molybdena itself (~100% yield at ~90% conversion, the maximum conversion measured).[16, 56-57] This is because the surface layer formed, although it is enriched in Mo, is not pure Mo, but is a mixed layer, probably an exposed surface of ferric molybdate, with both cations

present in the surface layer. This is a recipe for CO production, due to the presence of significant amounts of isolated sites of Fe and Mo. It is only surfaces which are completely Mo-covered which produce high selectivity to formaldehyde, as was shown earlier.[16, 57] It appears that dosing in the way we have, that is impregnation plus annealing, does not produce a complete layer of molybdenum oxide. This situation would only be reached if we could dose enough Mo into our iron oxide catalysts to saturate it, by completing formation of ferric molybdate throughout the bulk, at which point excess Mo could form a very selective monolayer.

Thus, we believe that in the case of the impregnated catalyst we never achieve a complete layer of Mo oxide. Explanation for this is illustrated in Figure 3-40 below, and relates closely to the work of Huang *et al.*[30] We propose that a low doping of Mo, followed by calcination to 500 °C, leads to a thin surface layer of ferric molybdate, adhering to a core of iron oxide. Increasing the Mo dosed increases the thickness of the molybdate layer. Eventually the bulk would saturate and finally, if even more Mo could be doped then a very selective material with a monolayer of Mo on the surface would be formed.

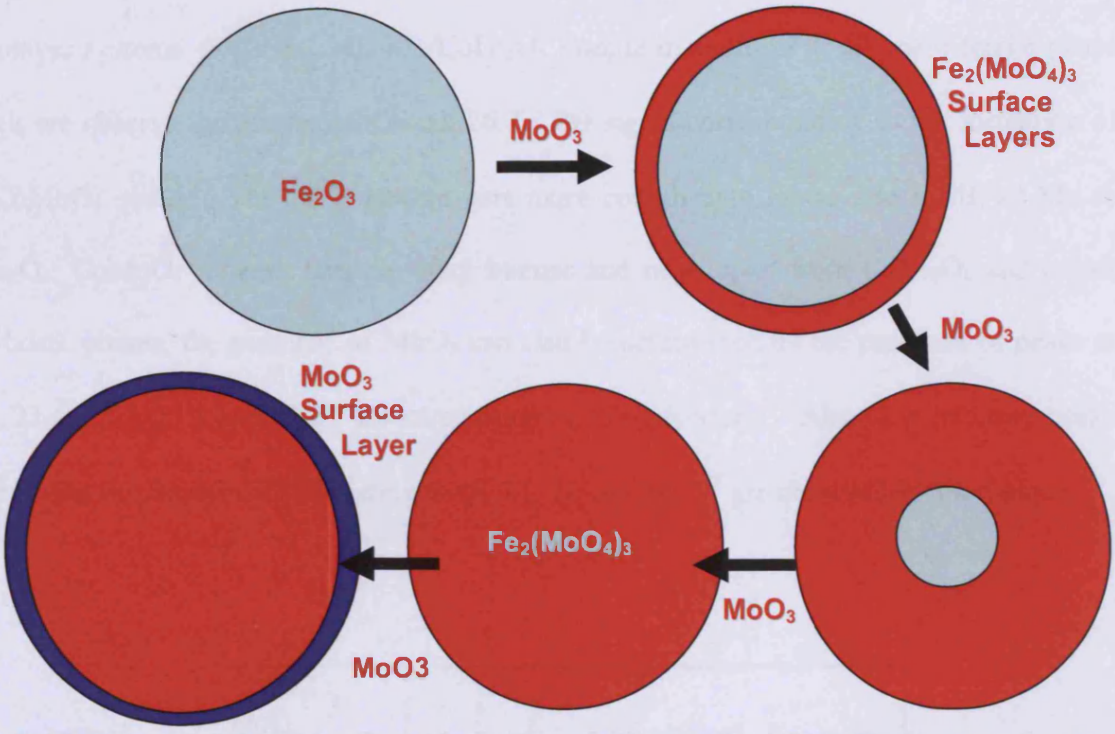

Figure 3-40. A suggested mechanism of phase evolution in the MoO_3/Fe_2O_3 monolayer system with the increase of Mo loading on the surface of Fe_2O_3.

This model is very close to the proposal of Huang *et al,*[30] who made Fe-Mo catalysts by simply grinding iron and molybdenum oxides together, followed by calcination at different temperatures. They propose that MoO_3 begins to disperse over the surface of iron oxide at ~400 °C, leading to a mixed surface of ferric molybdate and molybdena. Further heating to 500 °C reduces the amount of MoO_3 and is proposed to result in a ferric molybdate shell on a core of Fe_2O_3.

3.2.4. Thin layer oxide $Mo/CoFe_2O_4$

This part of the chapter is dedicated to structural and catalytic characterization of cobalt ferrite based thin layer systems.

3.2.4.1. Structural Characterization

Figure 3-41 presents XRD patterns of pure and impregnated with molybdenum cobalt ferrite calcined at 500 °C. These systems are more complicated than two component Mo-Fe

monolayer systems. For the 2 ML $Mo/CoFe_2O_4$ sample in addition to the main ferrite phase signals we observe the presence of small 26.7 ° 2Θ signal corresponding to the formation of the $CoMoO_4$ phase.[38] The XRD pattern gets more complicated as we add 6 ML of Mo to $CoFe_2O_4$: $CoMoO_4$ reflexes become more intense and now, apart from $CoFe_2O_4$ and cobalt molybdate phases, the presence of MoO_3 can also be determined by the presence of peaks at 12.8, 23.4, 25.7, 27.3 and 39.2 ° 2Θ corresponding to molybdena.[51] Also, low intensity peaks attributed to iron molybdate formation at 19, 21, 22 and 34 °,[37] are observed in this sample.

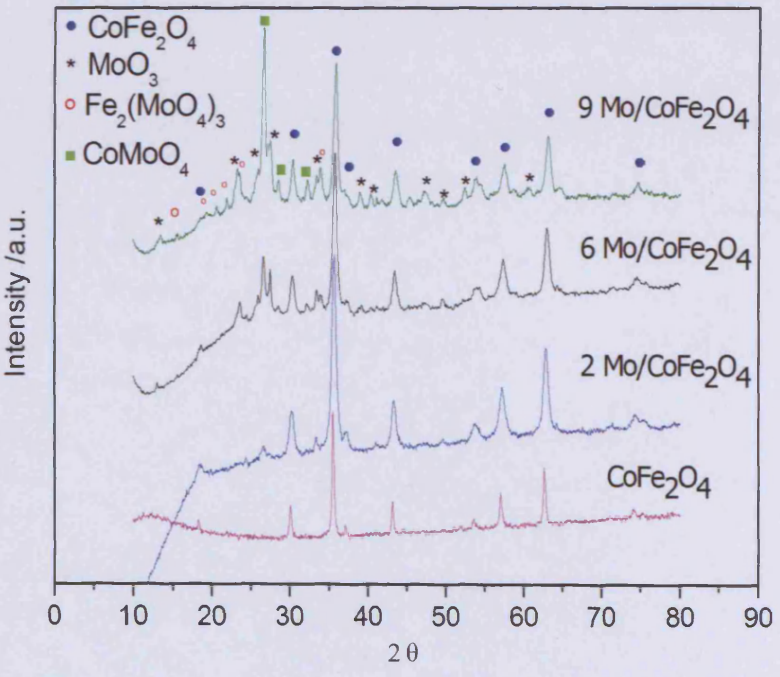

Figure 3-41. XRD patterns of 2-9 ML $Mo/CoFe_2O_4$ samples.

The subsequent increase of the molybdenum loading to 9 monolayers results in a significant increase of the relative intensities of $CoMoO_4$, $Fe_2(MoO_4)_3$ and MoO_3 phases (Figure 3-41). Impregnation of cobalt ferrite with molybdenum decreases the surface area

from 60 to 10 m^2/g and increases the particle size from 7 nm for the pure $CoFe_2O_4$ to 13 nm for the 9 monolayer Mo cobalt ferrite sample (Table 3-5).

Table 3-5. Surface area and particle size of $Mo/CoFe_2O_4$ based catalysts.

Sample	BET surface area, m^2/g	d, nm
$CoFe_2O_4$	60.2	7.0
2 Mo/ CF	42.7	7.1
6 Mo/CF	13.7	12.6
9 Mo/CF	9.6	13.0

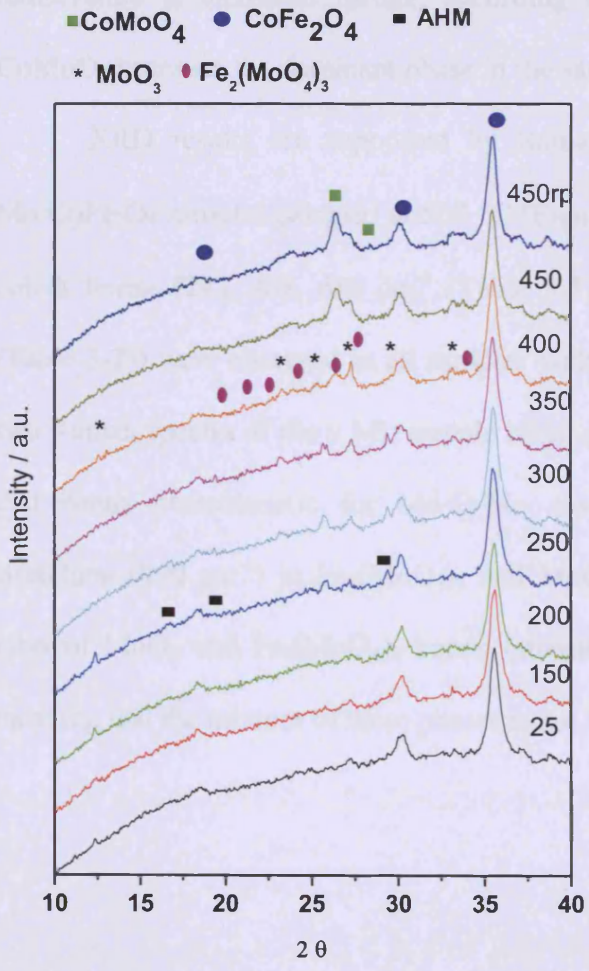

Figure 3-42. *In-situ* XRD of the 6 ML $Mo/CoFe_2O_4$ in 10% O_2/He flow with the temperature increased from 25 to 450 °C.

To investigate the evolution of phase composition of the 6 ML $Mo/CoFe_2O_4$ sample at different temperatures, *in-situ* XRD was measured in 10% O_2/He flow (Figure 3-42). In the temperature range of 25 – 300 °C the only observable phases, apart from cobalt ferrite, were molybdena and un-decomposed ammonium heptamolybdate (which was used in sample preparation) with characteristic peaks at 13, 23, 25 and 27 ° for MoO_3[51] and at 16, 19 and 29 ° for un-decomposed AHM.[58] At 400 °C we observe the evolution of iron and cobalt molybdates as peaks characteristic for these phases appear (Figure 3-42).[37-38] As the temperature is increased further, according to the observed intensities of XRD signals, $CoMoO_4$ becomes the dominant phase in the sample.

XRD results are supported by Raman spectroscopy studies for the impregnated $Mo/CoFe_2O_4$ samples calcined at 500 °C (Figure 3-43) as the Raman bands characteristic for cobalt ferrite (293, 468, 686 cm^{-1} (Table 3-3)) and cobalt molybdate (816, 875, 936 cm^{-1} (Table 3-2)) were observed in all samples with different loadings of Mo. Figure 3-43 shows two Raman spectra of the 9 ML sample taken in different spots of the sample. It can be seen that bands characteristic for Mo-O-Mo asymmetric stretching (785 cm^{-1}) and Mo=O stretching (990 cm^{-1}) in $Fe_2(MoO_4)_3$ and MoO_3 characteristic bands appear. However, the ratio of MoO_3 and $Fe_2(MoO_4)_3$ bands intensities vary for the two different sample spots, meaning that the mixture of these phases is not homogeneous.

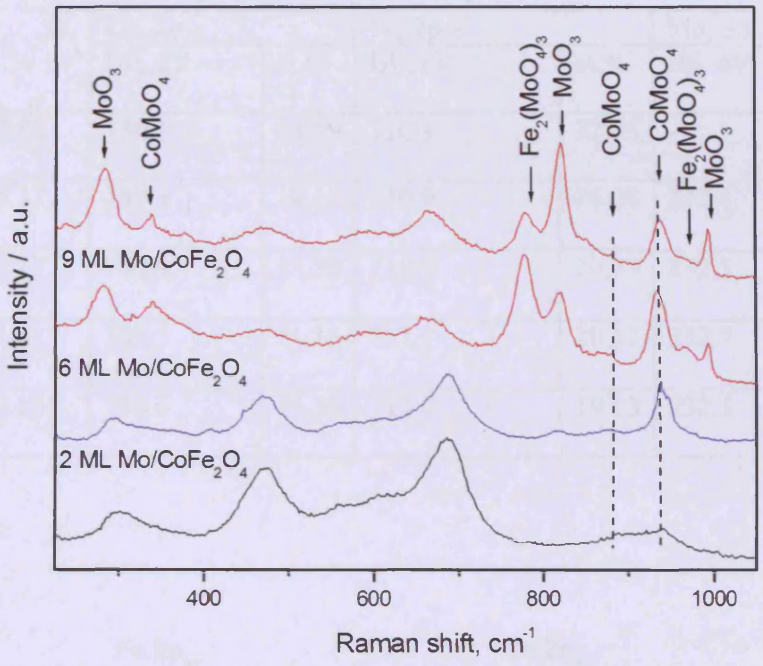

Figure 3-43. Raman spectra of the 2-9 Mo/$CoFe_2O_4$ samples.

In order to investigate the surface composition of the Mo/$CoFe_2O_4$ systems, XPS studies were performed. Table 3-6 shows the observed binding energies and the calculated surface atomic percentage of Mo, Co, Fe and O ions. All samples have iron present in the +3 oxidation state and molybdenum present in the +6 state. Cobalt is in +2 oxidation state, however, for the 6 ML Mo/$CoFe_2O_4$ sample it seems to posses two oxidation states as, apart from the main peak at 780 eV characterizing +2 oxidation state, we observe a peak at 783 eV characteristic for Co^{+3} [59] (Figure 3-44).

Table 3-6. XPS data of $Mo/CoFe_2O_4$ monolayer catalysts.

Sample	O, 1s, at.%	Co, $2p_{3/2}$		Fe, $2p_{3/2}$		Mo, $3d_{5/2}$	
		BE, eV	at.%	BE, eV	at.%	BE, eV	at.%
$CoFe_2O_4$	52.86	780.1	14.59	710.8	32.55	-	-
$2Mo/CoFe_2O_4$ (500°C)	55.37	780.3	14.11	710.9	26.08	232.4	4.45
$6Mo/CoFe_2O_4$ (500°C)	57.77	780.4	13.56	710.9	20.73	232.5	7.94
$6Mo/CoFe_2O_4$ (120°C)	62.31	780.5	11.13	711.1	20.12	232.7	6.44
$6Mo/CoFe_2O_4$ post reactor	59.17	780.6	14.10	711.0	19.13	232.5	7.59

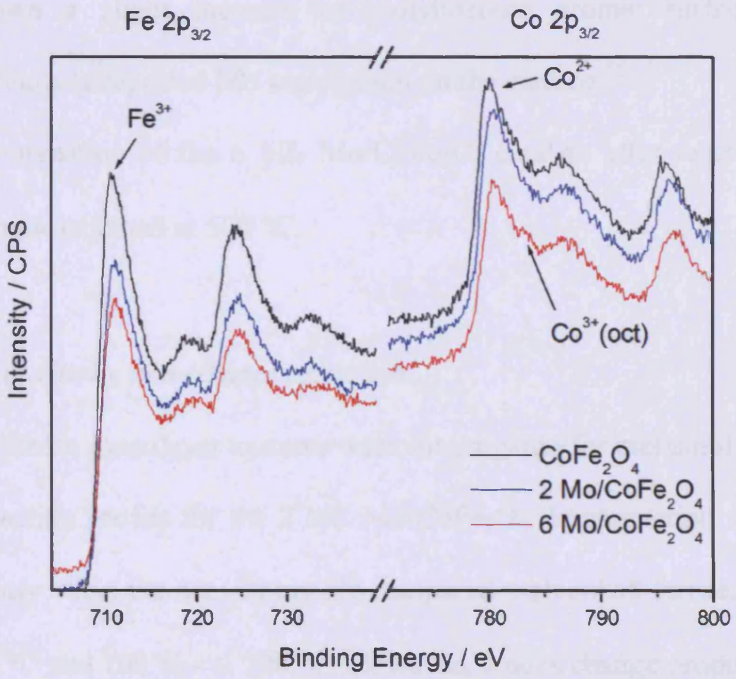

Figure 3-44. Fe 2p and Co 2p XPS spectra of cobalt ferrite and Mo loaded cobalt ferrite.

Speaking of surface composition, one can see that integration of XPS peaks for Co and Fe for the $CoFe_2O_4$ sample gave the iron-to-cobalt ratio of 2.2(±0.3):1 at the surface, which is very close to the stoichiometric composition. Impregnation of cobalt ferrite with 2

monolayers of molybdenum results in a decrease of the Fe/Co ratio to 1.53. This can be easily explained considering XRD results, which show preferential formation of the $CoMoO_4$ phase as molybdenum is loaded onto the surface of cobalt ferrite. We believe that cobalt molybdate forms complete layers over $CoFe_2O_4$, hence we see an increased signal of Co in the XPS spectra. The total thickness of 2 monolayers is less than the depth of XPS analysis (~10nm), therefore we still observe a significant contribution of Fe and Co XPS signals from the cobalt ferrite phase and Co/Mo surface ration is 3/1 instead of 1/1 as in $CoMoO_4$. XPS data for the 6 monolayers sample further confirms this as the surface percentage of Co almost does not change, while Fe percentage decreases and Mo percentage increases (Table 3-6).

Investigation of the effect of calcination on surface composition of the 6 $Mo/CoFe_2O_4$ sample have shown a slight increase of molybdenum atomic surface concentration, confirming the previously reported Mo segregation on the surface.[55]

Surface composition of the 6 ML $Mo/CoFe_2O_4$ catalyst after reaction is almost the same as for the sample calcined at 500 °C.

3.2.4.2. Catalytic reactivity in methanol oxidation

The Mo on cobalt ferrite monolayer systems were investigated for methanol oxidation. Figure 3-45 shows the reaction profile for the 2 ML $Mo/CoFe_2O_4$. Impregnation with molybdenum does not significantly affect the activity profile compared with cobalt ferrite: 50 % conversion is observed at 190 °C and 100 % - at 220 °C. However, it does change product distribution as, apart from CO_2 being selectively produced at low conversions, carbon monoxide starts to form at 210 °C and attains 50 % selectivity by 275 °C. Also, minor amounts of formaldehyde (with <5 % selectivity) and DME (with <3 % selectivity) are observed in the range of 180-280 °C.

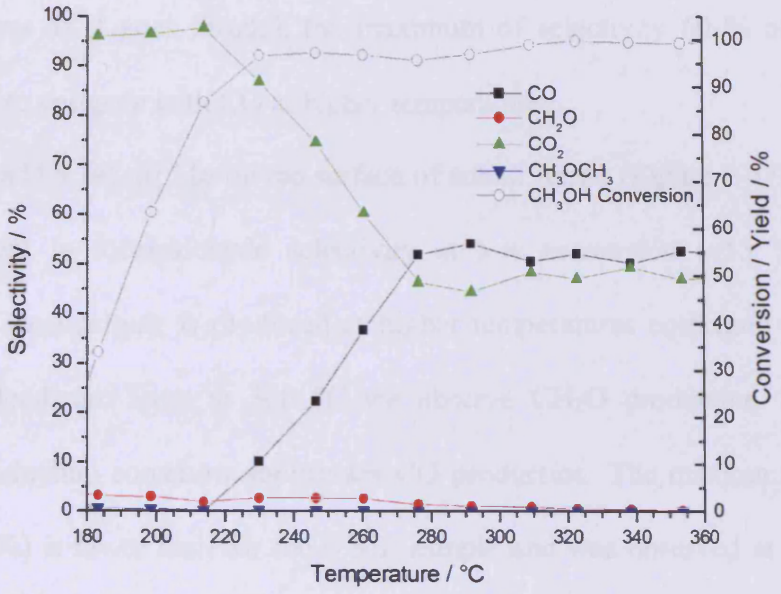

Figure 3-45. Selectivity and conversion for methanol oxidation over the 2 ML $Mo/CoFe_2O_4$ catalyst.

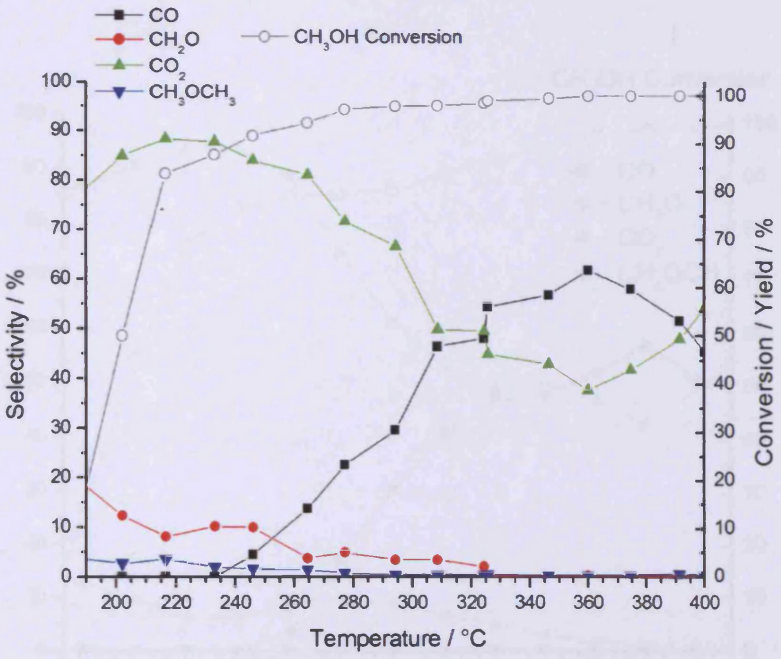

Figure 3-46. Selectivity and conversion for methanol oxidation over the 6 ML $Mo/CoFe_2O_4$ catalyst.

The increase of molybdenum loading to the 6 ML further changes the reaction profile (Figure 3-46) as formaldehyde production rises at low conversions up to 20 % selectivity. The

selectivity towards DME attains 3-5 % at low conversion. CO is produced more selectively at higher temperatures as it goes through the maximum of selectivity 60 % at 360 °C. CO_2 production seems to compete with CO at higher temperatures.

When we add 9 ML of Mo on the surface of cobalt ferrite (Figure 3-47) we do not see much improvement in formaldehyde selectivity at low conversion (~15 % at 210 °C). However, more formaldehyde is produced at higher temperatures compared to the samples with lower Mo loadings. Even at 360 °C we observe CH_2O production. This enhanced formaldehyde production somehow suppresses CO production. The maximum of selectivity towards CO (55 %) is lower than for the 6 ML sample and was observed at 370 °C. Minor amount of DME was also formed over this sample. Again, we observe significant CO_2 formation over the whole temperature range.

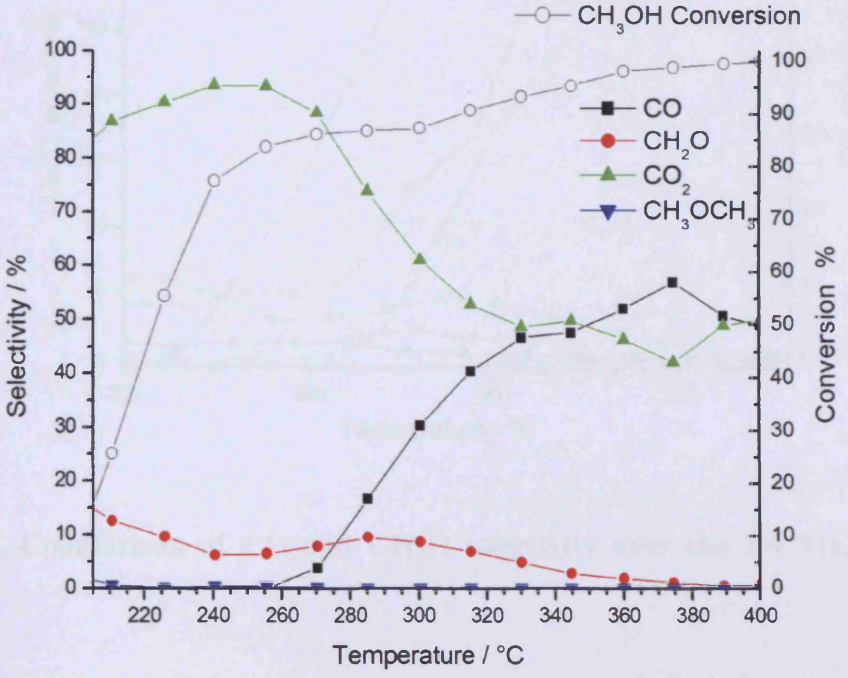

Figure 3-47. Selectivity and conversion for methanol oxidation over the 9 ML $Mo/CoFe_2O_4$ catalyst.

Figure 3-48 shows a comparison of CO and formaldehyde selectivity over cobalt ferrite samples with different molybdenum loading. From there we can clearly see that CO production shifts to higher temperatures with higher Mo loading and formaldehyde production increases. Formaldehyde formation at lower temperatures is probably due to the presence of minor amounts of molybdena and iron molybdate in the catalyst, as it is evident from XRD and Raman data that iron molybdate content increases with higher Mo loading as so does the formaldehyde selectivity.

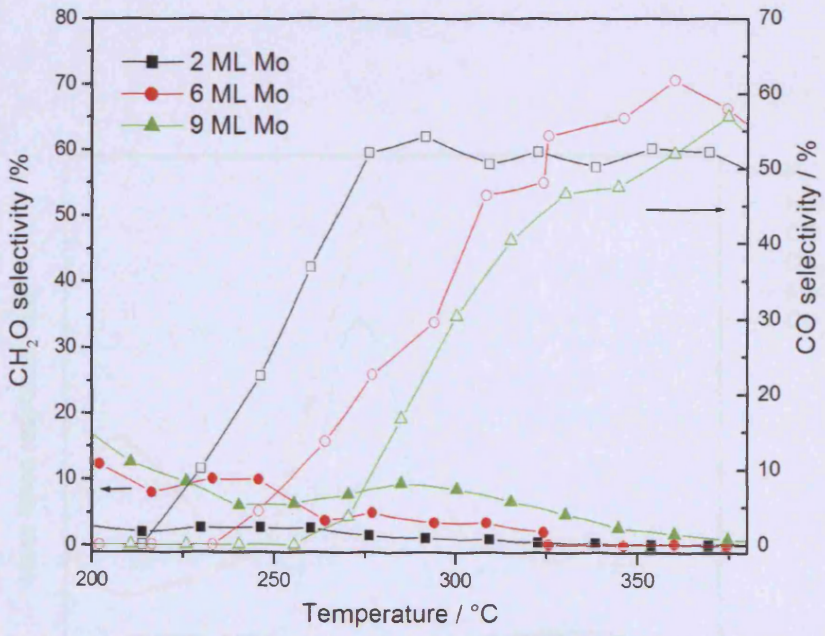

Figure 3-48. Comparison of CO and CH_2O selectivity over the 2-9 ML Mo/$CoFe_2O_4$ samples.

3.2.4.3. TPD

Figures 3-49- 3-51 show TPD data for the Mo/$CoFe_2O_4$ systems. Qualitatively TPD profiles for all molybdenum loadings are the same as broad desorption of methanol centred at around 100 °C and desorption of hydrogen, water, CO, formaldehyde and CO_2 is observed. For all

samples CO desorption at around 200 °C is dominant; formaldehyde desorbs in a small peak at 160 °C and only traces of CO_2 are observed at ~280 °C. The fact that we observe only traces of CO_2 in TPD, although a lot of it forms during the reaction, says that carbon dioxide formed in methanol oxidation is a secondary oxidation product. If it would have been produced from the cobalt ferrite or cobalt molybdate surface, we would have seen a significant peak of CO_2 in the TPD, as carbon dioxide is a dominant peak in the TPD of pure $CoFe_2O_4$ (Figure 3-23) and it is rather significant in the TPD of $CoMoO_4$ (Figure 3-24). Still, the presence of small CO_2 desorption peak might be the evidence of the presence of minor amounts of $CoFe_2O_4$ or $CoMoO_4$ on the surface of the catalyst.

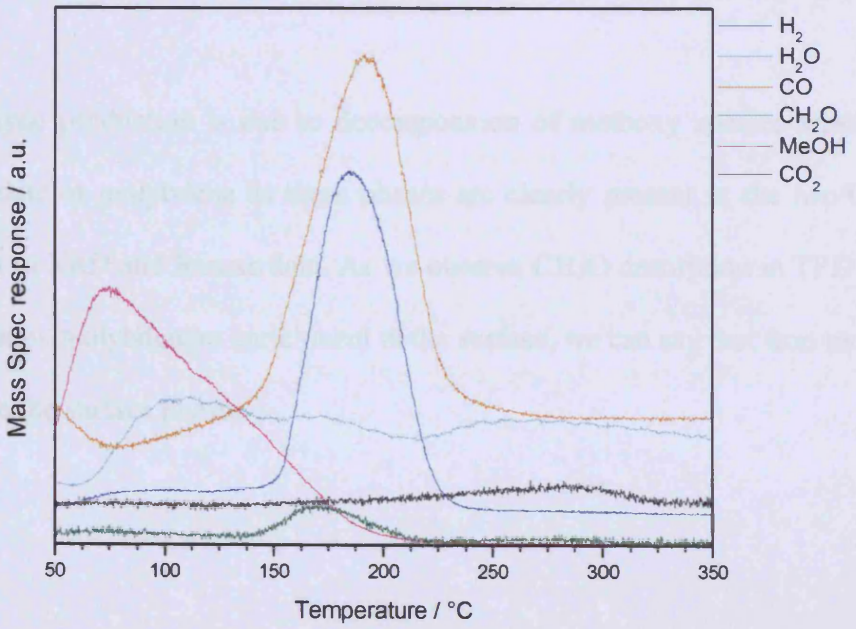

Figure 3-49. TPD of the 2 ML $Mo/CoFe_2O_4$ saturated with methanol at room temperature.

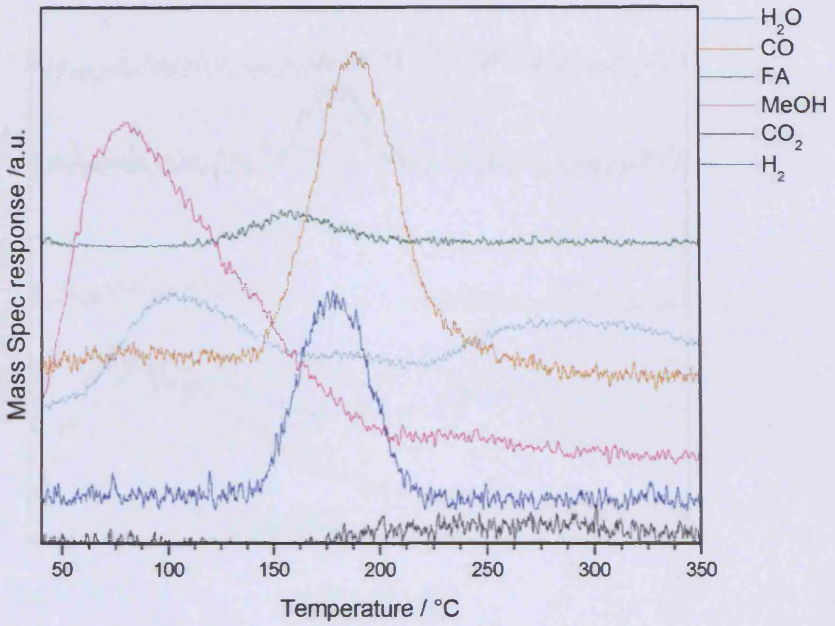

Figure 3-50. TPD of the 6 ML $Mo/CoFe_2O_4$ saturated with methanol at room temperature.

Formaldehyde production is due to decomposition of methoxy species adsorbed on either iron molybdate or molybdena as these phases are clearly present in the $Mo/CoFe_2O_4$ samples according to XRD and Raman data. As we observe CH_2O desorption in TPD profiles and as XPS data show molybdenum enrichment at the surface, we can say that iron molybdate and molybdena are the surface phases.

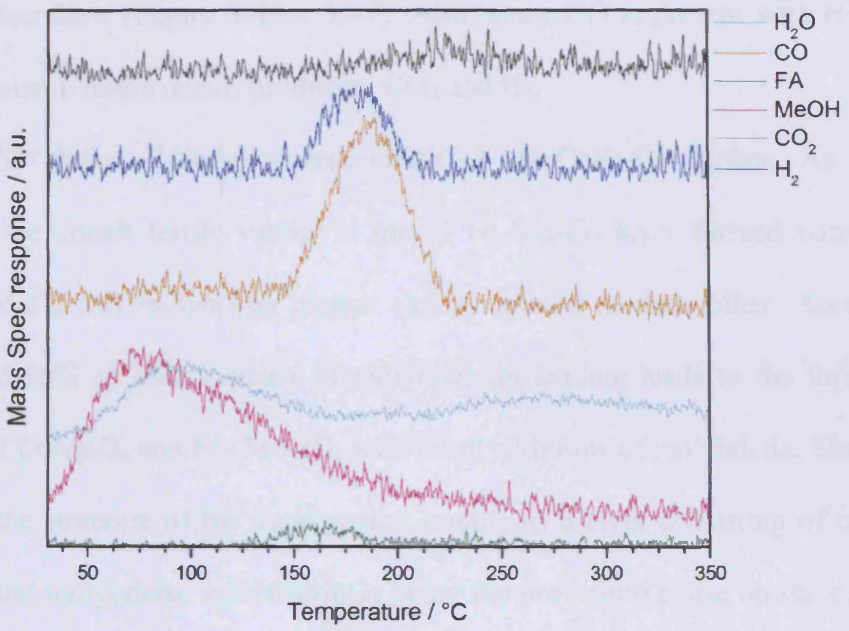

Figure 3-51. TPD of the 9 ML $Mo/CoFe_2O_4$ saturated with methanol at room temperature.

CO desorption in TPD profiles coincide with the beginning of CO formation during TPR and, analogous to the Mo/iron oxide systems discussed above, the position of CO desorption peak is close to formaldehyde desorption, which points to the Mo related origin of the species producing carbon monoxide. It is most probable that, as in case with the Fe-Mo mixed surface, in cobalt ferrite based samples we also have mixed surface with Fe-Mo and Co-Mo neighboring sites, responsible for the production of high temperature CO in the TPPFR experiments.

Thus, methanol adsorbs as methoxy species on the mixed oxide surface and part of it desorbs as formaldehyde and another part desorbs as CO. The fact that we observe CO_2 at low temperatures in TPPFR experiments might be explained as follows. At low oxygen concentrations (low conversion) the primary produced CO is readily oxidized to CO_2 by the surface cobalt ferrite or cobalt molybdate species. As oxygen conversion becomes higher, CO

cannot be fully oxidized and it appears as a high temperature product in TPPFR profile, while CO_2 production decreases (Figure 3-45 – 3-47). Also, since CO is present with H_2O, some water-gas-shift reaction might occur, producing CO_2 and H_2.

Figure 3-52 shows a model representation of $Mo/CoFe_2O_4$ surface. As we dope molybdenum on the cobalt ferrite surface a mixed Fe-Mo-Co layer formed consisting of $Fe_2(MoO_4)_3$, $CoMoO_4$ and molybdena phases closely related to each other. According to XRD, Raman and XPS an data increase of molybdenum loading leads to the formation of bigger amounts of $CoMoO_4$ and $Fe_2(MoO_4)_3$ with small additions of molybdena. Simplifying, we can describe the structure of the impregnated sample as a layer consisting of cobalt and iron molybdates and molybdena, with $CoMoO_4$ being the prevailing phase on the core cobalt ferrite. The fact that we do not see significant CO_2 formation during the TPD experiment over the impregnated samples, though there is carbon dioxide desorption from bulk cobalt molybdate (Figure 3-24), can potentially be the result of the modification of the electronic state of cobalt molybdate by iron species from the neighbouring iron containing phases (cobalt ferrite, iron molybdate). We suggest that the neighbouring Fe-Mo and Co-Mo pairs are responsible for high temperature CO production and Mo-Mo pairs of built-up molybdena – for the little formaldehyde production.

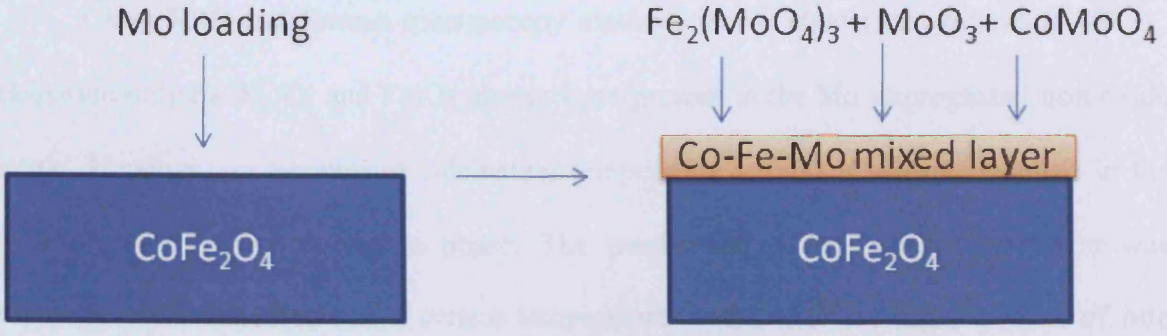

Figure 3-52. Scheme of the suggested core – shell structure of the impregnated $Mo/CoFe_2O_4$ system.

3.3. Conclusions

In the work described above we have shown the difference in reactivity of the single and mixed iron, cobalt and molybdenum oxides. While Fe_2O_3 and Co_3O_4 exhibit combustion properties, burning methanol to CO_2 and water via the formation of formate intermediates on the surface, molybdena shows an excellent selectivity to formaldehyde as methoxy species are being formed on its surface. When it comes to the mixed oxides, $CoFe_2O_4$ is very active in combustion of methanol; cobalt molybdate produces a mixture of partial oxidation products (CO, CH_2O) and CO_2 and iron molybdate (with Mo:Fe = 1.5:1) is highly selective towards formaldehyde at lower temperatures (180-220 °C), however it produces CO and CO_2 in the high temperature region as the secondary oxidation products.

When molybdenum is doped into the surface of iron oxide it drastically affects the catalytic properties in methanol oxidation. Even at the loading of one monolayer the evolution of formaldehyde and CO production is observed (at 210 °C 50 % and 47 % selectivity respectively) suppressing CO_2 formation from the Fe_2O_3 surface. A further increase of the molybdenum loading promoted formaldehyde production. However, stable 100 % selectivity towards CH_2O has never been reached, as large amounts of CO are always produced over these catalysts.

Using XRD and Raman spectroscopy methods it was shown that following 400 °C calcination only the MoO_3 and Fe_2O_3 phases were present in the Mo impregnated iron oxide sample. However, an increase of calcination temperature to 500 °C clearly resulted in the formation of the iron molybdate phase. The mechanism of the surface evolution was proposed, which stated that at a certain temperature, at low Mo loadings, a layer of iron molybdate is formed. A mixed surface layer appears to be formed and thus Fe-Mo pairs are suggested to be responsible for CO production during methanol oxidation.

A more complicated situation exists when Mo is loaded on the surface of cobalt ferrite. It was shown that when the loading of molybdenum on the cobalt ferrite surface is increased, some evolution of formaldehyde at the high temperature range is observed. And as more Mo is added to the surface, more CH_2O is formed. CO production starts at around 210 °C and it shifts to higher temperature as more Mo is loaded to the cobalt ferrite. Large amounts of CO_2 are produced in the low temperature range over these samples.

Structural (XRD, Raman and XPS) investigations of the $Mo/CoFe_2O_4$ systems have shown the preferential formation of $CoMoO_4$ phase as the molybdenum is loaded to the surface. Small amounts of iron molybdate and molybdena alone were also detected. Thus, we proposed that a mixed layer of cobalt molybdate, iron molybdate and molybdena is formed over cobalt ferrite. This mixed layer produces CO in the whole temperature range, however at lower temperatures and low oxygen conversion this CO is oxidized to CO_2 by highly reactive traces of pure cobalt ferrite or cobalt molybdate present on the surface. As the conversion increases, CO appears as the main product. Formaldehyde is believed to be produced on the Mo-Mo species of molybdena or iron molybdate present in the samples.

3.4. References

1. Adkins, H.; Peterson, W. R., *Journal of the American Chemical Society* **1931,** *53*, 1512-1520.
2. Soares, A. P. V.; Portela, M. F.; Kiennemann, A., *Catalysis Reviews: Science and Engineering* **2005,** *47*, 125 - 174.
3. Blake, R. L.; Hessevick, R. E.; Zoltai, T.; Finger, L. W., *Am. Mineral.* **1966,** *51*, 123-9.
4. Catti, M.; Valerio, G.; Dovesi, R., *Phys. Rev. B: Condens. Matter* **1995,** *51*, 7441-50.
5. Remediakis, I. N.; Kaxiras, E.; Chen, M.; Friend, C. M., *J. Chem. Phys.* **2003,** *118*, 6046-6051.
6. Kihlborg, L., *Arkiv foer Kemi* **1963,** *21*, 357.
7. Parise, J. B.; McCarron, E. M., III; Von, D. R.; Goldstone, J. A., *J. Solid State Chem.* **1991,** *93*, 193-201.
8. Liu, X.; Prewitt, C. T., *Phys. Chem. Miner.* **1990,** *17*, 168-72.
9. Roth, W. L., *Journal of Physics and Chemistry of Solids* **1964,** *25*, 1-10.
10. Massarotti, V.; Flor, G.; Marini, A., *J. Appl. Crystallogr.* **1981,** *14*, 64-5.

11. Koenig, U.; Morgenstern, T.; Foersterling, G., *Mater. Sci. Forum* **1993,** *133-136*, 687-92.
12. Rapposch, M. H.; Anderson, J. B.; Kostiner, E., *Inorg. Chem.* **1980,** *19*, 3531-9.
13. Smith, G. W.; Ibers, J. A., *Acta Crystallogr.* **1965,** *19*, 269-75.
14. Mathew, D. S.; Juang, R.-S., *Chemical Engineering Journal* **2007,** *129*, 51-65.
15. Lee, S. J.; Lo, C. C. H.; Matlage, P. N.; Song, S. H.; Melikhov, Y.; Snyder, J. E.; Jiles, D. C., *Journal of Applied Physics* **2007,** *102*, 073910.
16. Bowker, M.; Holroyd, R.; Elliott, A.; Morrall, P.; Alouche, A.; Entwistle, C.; Toerncrona, A., *Catalysis Letters* **2002,** *83*, 165-176.
17. Zafeiratos, S.; Dintzer, T.; Teschner, D.; Blume, R.; Hävecker, M.; Knop-Gericke, A.; Schlögl, R., *Journal of Catalysis* **2010,** *269*, 309-317.
18. Chowdhry, U.; Ferretti, A.; Firment, L. E.; Machiels, C. J.; Ohuchi, F.; Sleight, A. W.; Staley, R. H., *Applications of Surface Science* **1984,** *19*, 360-372.
19. Busca, G., *Catalysis Today* **1996,** *27*, 457-496.
20. Maslen, E. N.; Streltsov, V. A.; Streltsova, N. R.; Ishizawa, N., *Acta Crystallographica Section B* **1994,** *50*, 435-441.
21. Tatibouët, J. M., *Applied Catalysis A: General* **1997,** *148*, 213-252.
22. Rahmouni, A.; Barbier, C., *Journal of Molecular Structure: THEOCHEM* **1995,** *330*, 359-364.
23. Niwa, M.; Habuta, Y.; Okumura, K.; Katada, N., *Catalysis Today* **2003,** *87*, 213-218.
24. Niwa, M.; Igarashi, J.-y., *Catalysis Today* **1999,** *52*, 71-81.
25. House, M. Selective Oxidation of Methanol over Iron Molybdate Catalysts.
26. Routray, K.; Zhou, W.; Kiely, C. J.; Grünert, W.; Wachs, I. E., *Journal of Catalysis* **2010,** *275*, 84-98.
27. Yamada, H.; Niwa, M.; Murakami, Y., *Applied Catalysis A: General* **1993,** *96*, 113-123.
28. Dong, L.; Chen, K.; Chen, Y., *Journal of Solid State Chemistry* **1997,** *129*, 30-36.
29. Fei, X., *Chinese Science Bulletin* **2000,** *45*, 214-219.
30. Huang, Y.; Cong, L.; Yu, J.; Eloy, P.; Ruiz, P., *Journal of Molecular Catalysis A: Chemical* **2009,** *302*, 48-53.
31. Chung, J. S.; Miranda, R.; Bennett, C. O., *Journal of Catalysis* **1988,** *114*, 398-410.
32. Routray, K.; Briand, L. E.; Wachs, I. E., *Journal of Catalysis* **2008,** *256*, 145-153.
33. Briand, L. E.; Hirt, A. M.; Wachs, I. E., *Journal of Catalysis* **2001,** *202*, 268-278.
34. Grzybowska, B.; Haber, J.; Janas, J., *Journal of Catalysis* **1977,** *49*, 150-163.
35. Ozkan, U.; Schrader, G. L., *Applied Catalysis* **1986,** *23*, 327-338.
36. Rajendran, M.; Pullar, R. C.; Bhattacharya, A. K.; Das, D.; Chintalapudi, S. N.; Majumdar, C. K., *Journal of Magnetism and Magnetic Materials* **2001,** *232*, 71-83.
37. JCPDS, 31-642.
38. JCPDS, 21-868.
39. Ballarini, N.; Cavani, F.; Passeri, S.; Pesaresi, L.; Lee, A. F.; Wilson, K., *Applied Catalysis A: General* **2009,** *366*, 184-192.
40. Melo, T. F. O.; da Silva, S. W.; Soler, M. A. G.; Lima, E. C. D.; Morais, P. C., *Surface Science* **2006,** *600*, 3642-3645.
41. Qu, Y.; Yang, H.; Yang, N.; Fan, Y.; Zhu, H.; Zou, G., *Materials Letters* **2006,** *60*, 3548-3552.
42. da Silva, S. W.; Melo, T. F. O.; Soler, M. A. G.; Lima, E. C. D.; da Silva, M. F.; Morais, P. C., *Magnetics, IEEE Transactions on* **2003,** *39*, 2645-2647.
43. Mestl, G.; Srinivasan, T. K. K., *Catalysis Reviews: Science and Engineering* **1998,** *40*, 451 - 570.

44. Saleem, S. S., *Infrared Physics* **1987,** *27*, 309-315.
45. Tian, H.; Wachs, I. E.; Briand, L. E., *The Journal of Physical Chemistry B* **2005,** *109*, 23491-23499.
46. Bowker, M.; Holroyd, R.; House, M.; Bracey, R.; Bamroongwongdee, C.; Shannon, M.; Carley, A., *Top. Catal.* **2008,** *48*, 158-165.
47. V G Hadjiev, M. N. I. a. I. V. V., *Journal of Physics C: Solid State Physics* **1988,** *21*, L199-L201.
48. de Faria, D. L. A.; Venâncio Silva, S.; de Oliveira, M. T., *Journal of Raman Spectroscopy* **1997,** *28*, 873-878.
49. Chandramohan, P.; Srinivasan, M. P.; Velmurugan, S.; Narasimhan, S. V., *Journal of Solid State Chemistry* **2011,** *184*, 89-96.
50. JCPDS, 11-053.
51. JCPDS, 10-706.
52. Matsuoka, Y.; Niwa, M.; Murakami, Y., *The Journal of Physical Chemistry* **1990,** *94*, 1477-1482.
53. Min, Y.; Zheng, F.; Zhao, Y.; Chen, Y., *Solid State Sciences* **2011,** *13*, 976-980.
54. Xu, Y.; Yang, S.; Zhang, G.; Sun, Y.; Gao, D.; Sun, Y., *Materials Letters* **2011,** *65*, 1911-1914.
55. House, M.; Shannon, M.; Bowker, M., *Catalysis Letters* **2008,** *122*, 210-213.
56. House, M. P.; Carley, A. F.; Bowker, M., *Journal of Catalysis* **2007,** *252*, 88-96.
57. House, M. P.; Carley, A. F.; Echeverria-Valda, R.; Bowker, M., *The Journal of Physical Chemistry C* **2008,** *112*, 4333-4341.
58. Wienold, J.; Jentoft, Rolf E.; Ressler, T., *European Journal of Inorganic Chemistry* **2003,** *2003*, 1058-1071.
59. Zhou, Z.; Zhang, Y.; Wang, Z.; Wei, W.; Tang, W.; Shi, J.; Xiong, R., *Applied Surface Science* **2008,** *254*, 6972-6975.

Chapter 4. Catalytic Oxidation and Magnetocatalysis

4.1. Introduction

This chapter is devoted to the investigation of magnetic properties of ferrimagnetic $Zn_xCo_{1-x}Fe_2O_4$ based samples, e.g. their susceptibility and the Curie temperature (T_c) and of the effect of the Curie transition on the catalytic activity in methanol oxidation reaction.

In terms of magnetism materials are classified by their response to an externally applied magnetic field. Descriptions of orientations of the magnetic moments in a material help to identify different forms of magnetism observed in nature. Five basic types of magnetism can be described: diamagnetism, paramagnetism, ferromagnetism, antiferromagnetism and ferrimagnetism.

Materials that possess *ferromagnetism* have aligned atomic magnetic moments of equal magnitude and their crystalline structure allows for direct coupling interactions between the moments, which may strongly enhance the flux density. Furthermore, the aligned moments in ferromagnetic materials can confer a spontaneous magnetization in the absence of an applied magnetic field. Materials that retain permanent magnetization in the absence of an applied field are known as hard magnets. Materials having atomic magnetic moments of equal magnitude that are arranged in an antiparallel fashion display *antiferromagnetism*. *Ferrimagnetism* is a property exhibited by materials whose atoms or ions tend to assume an ordered but non-parallel arrangement in a zero applied field below a certain characteristic temperature known as the Neel temperature. In the usual case, within a magnetic domain, a substantial net magnetization results from the antiparallel alignment of neighboring non-equivalent sublattices.[1-2]

In the XXth century a number of researches have been investigating the relation between magnetism and catalysis. The founder of studies of magnetic effects in catalysis was Hedvall[3] who postulated that transition from the ferromagnetic to paramagnetic state involves a change in the state of those electrons which may determine the catalytic activity of a substance. For

the decomposition of nitrous oxide and carbon monoxide with nickel or copper-nickel alloy as catalysts, and for the hydrogenation of unsaturated oils with copper-nickel and cobalt-palladium alloys as catalysts, he showed that the reaction yield was increased simultaneously with the loss of ferromagnetism of the catalyst. Thus, the activation energy of decomposition of formic acid by a Co-Pd alloy was increased by about 30% at the transition to the paramagnetic state of the catalyst and it was concluded that a state of higher electronic order in a catalyst might yield an energetically stronger catalytic action.

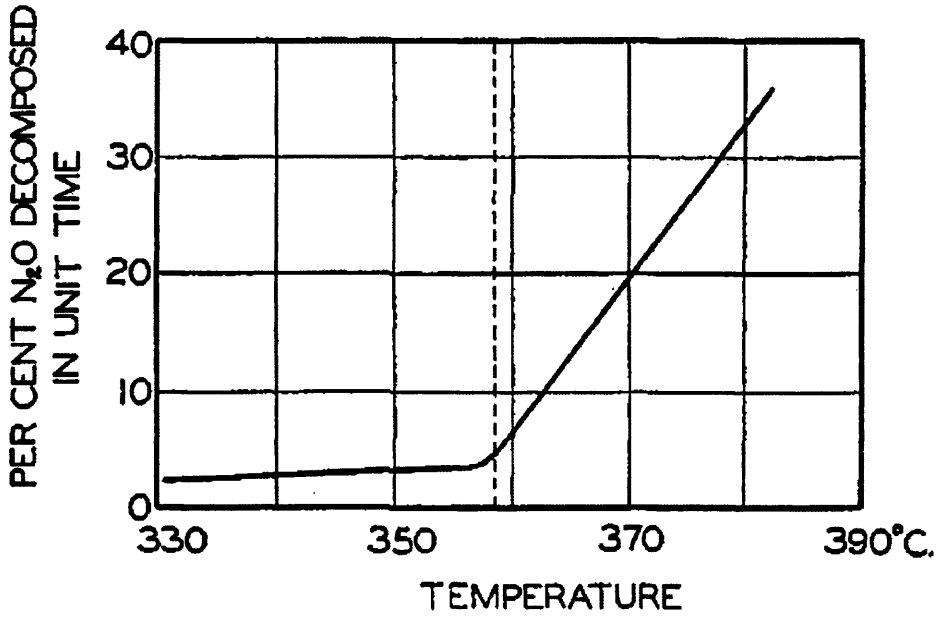

Figure 4-1. Catalytic activity of nickel near the Curie point. Adapted from ref 4.

Later on different authors tried to reproduce the Hedvall effect, although obtaining rather controversial results. Forestier and Lille[5] confirmed the existence of some kind of change in catalytic activity at the Curie point for the acetic acid over variety of ferrites. But, the changes took the form of an acceleration of catalytic activity at the Curie point, followed by a decrease of activity above the Curie point.

Olmer was unable to observe the Hedvall effect for the catalytic decomposition of carbon monoxide over Fe, Co, Ni, and the compounds CMn_3, BMn, SbMn, all of which ferromagnetic.[6] Further criticism of the Hedvall effect was given by Spingler and Reinhard. In

experiments closely paralleling those of Hedvall they observed no discontinuity for the decomposition of carbon monoxide over nickel.[7]

Morris and Selwood[4] studied benzene hydrogenation over nickel-activated copper. In their experiments they observed that the loss of ferromagnetism occurs in linear relationship to the loss of catalytic activity. Leilmezs studied the magneto-catalytic effect in the hydrogenation of ethylene over nickel catalyst with and without external magnetic field. The Hedvall effect II (activation energy slope discontinuity) was present in experiments without a magnetic field,[8] while the presence of magnetic field resulted in a set of decaying aperiodic oscillations in the conversion rate of the reacting system superimposed on the change in the reaction rate. Below Curie point of the catalyst, the applied magnetic field generally decreased the rate of ethylene hydrogenation but increased the reaction rate above Curie point of the catalyst.[9] Sales and Mehta reported the decrease of activation energy of oxidation of nickel[10] and of nickel carbonylation[11] respectively in the vicinity of the Curie point. However, despite all these studies, no clarity was achieved, and the effect of magnetism on catalysis and especially on selectivity remains an open topic.

In our work we chose spinel structured cobalt ferrites as well-known magnetic systems. Magnetically, spinel ferrites display ferrimagnetic ordering. The magnetic moments of cations in the A and B-sites are aligned parallel with respect to one another. Between the A and B-sites the arrangement is antiparallel and as there are twice as many B-sites as A-sites, there is a net moment of spins yielding ferrimagnetic ordering within the crystal. The choice of metal cation and the distribution of ions between the A and B-sites, therefore, offer a tunable magnetic system.[1]

Recently the synthesis and magnetic structure characterization of spinel nanoferrites have been investigated with much interest and a lot of attention has been focused on the preparation and characterization of superparamagnetic metal oxide nanoparticles.[1, 12-23] There

is a significant body of literature on the cobalt ferrite synthesis including such techniques as the microemulsion method,[1, 24] the combustion method,[16, 19] the polyol method[21] and a combination of nonhydrolytic process and a seed-mediated growth.[22] The big advantage of using these methods is a more precise control of particle shape and size. Thus, Song *et al*[22] synthesized $CoFe_2O_4$ spherical nanocrystals with a mean diameter of 5 nm using coordination compounds of Fe and Co acetylacetonate as precursors in nonhydrolytic process. Such 5 nm crystals were used as seeds to grow 8 or 9 nm spherical nanocrystals in solution of precursors. Baldi *et al*[21] carried out polyol synthesis to produce $CoFe_2O_4$ nanoparticles with an average particle diameter ranging from 5.5 to 6.72 nm.

However, the most frequently used method remains co-precipitation,[13-15, 17-18] partly due to its simplicity. Iron and cobalt nitrates or chlorides are usually used as precursors and Na_2CO_3, NaOH and NH_4OH are used as precipitation agents. For example, Manova *et al*[13] synthesized 27 nm $CoFe_2O_4$ particles via precipitation of 0.5M cobalt and iron nitrate solutions with 1M Na_2CO_3; Maaz *et al*[17] used 0.4 M and 0.2 M iron and cobalt chloride solutions respectively for the precipitation with 3M NaOH to obtain $CoFe_2O_4$ particles in the range of 16-24 nm. Many of the co-precipitation synthesis parameters, such as precursor's concentrations, pH and temperature of precipitation, calcination temperature, could be varied. Thus, the surfactants (polyethylene glycol and oleic acid respectively) were added to the precursor solution to investigate the effect on particles size.[14, 17] It was shown that in both cases the addition of a surfactant allows to decrease cobalt ferrite particle size approximately two times. Kumar *et al*[25] investigated the effect of the calcination temperature. The samples prepared by co-precipitation method were calcined at 100, 300, 500, 700 and 900 °C. The $CoFe_2O_4$ particle size (as was determined by XRD and TEM methods) varied from 4-10 nm for the samples calcined at 100 °C to 100 nm for samples calcined at 900 °C. Magnetic characterization of these samples had shown the absence of saturation and coercivity in B-H

curve of the sample annealed at 100 °C, which indicates the superparamagnetic nature of the particles which relax back their spins by rotation upon removal of an applied magnetic field so as to give a zero net magnetic moment. Superparamagnetism (SP) occurs when material is composed of very small particles (4-12 nm). Also, it was shown that coercivity goes from 0, for the 100 °C calcined samples, through the maximum for the 700 °C calcined sample. This was explained on the basics of the domain structure and particle size: the initial increase in coercivity is due to the increase in particle size from SP size (4-12 nm) to single domain size (35-40 nm), which then decreases on further annealing due to the formation of multi-domains (growth) after single-domain size limit of the $CoFe_2O_4$ nano-particles.

Calcination of cobalt ferrite precipitated particles from 100 to 900 °C resulted in the particle sizes from 5 to 100 nm.

Comparison of different cobalt ferrite preparation methods was performed by Bhame *et al.*[26] The $CoFe_2O_4$ particles were synthesized be co-precipitation, citrate and combustion methods and resulted particles sizes were 12, 15 and 45 nm respectively.

Several attempts were done to produce substituted cobalt ferrites.[18, 20, 27-28] In the cubic system of ferrimagnetic spinels, the magnetic order is mainly due to a super exchange interaction mechanism occurring between the metal ions in the A and B sublattices. The substitution of nonmagnetic ion such as Zn, which has a preferential A site occupancy results in a reduction of the exchange interaction between A and B sites. Hence, by varying the degree of cation substitution, it is possible to vary magnetic properties of the fine particles.[18]

It was shown that varying x in $Co_{1-x}Zn_xFe_2O_4$ systems synthesized by co-precipitation method from 0.1 to 0.5 results in a decrease in particle sizes from 11.7 to 8.9.[27-28] In the $CoFe_{2-x}Al_xO_4$ systems obtained via a sol-gel method, varying x from 0 to 0.5 shows the change in particle size from 18 to 23nm.[20]

Paulsen *et al*[29] synthesized a series of manganese-dopes cobalt ferrite samples with compositions of $CoFe_{2-x}Mn_xO_4$ (where x ranges from 0 to 0.8) via a standard powder ceramic technique. The measured T_c of these samples was shown to decrease approximately linearly from 520 to 250 °C with an increased manganese content.

Lee *et al*[30] prepared $CoFe_{2-x}Cr_xO_4$ (where x ranges from 0 to 0.8) using the same synthetic method. In this case T_c dropped from 520 to 150 °C with an increase in Cr content.

4.2. Results and Discussion

4.2.1. Magnetic properties – engineering the Curie temperature

All ferromagnets when heated to a sufficiently high temperature become paramagnetic. The transition temperature from ferromagnetic to paramagnetic behaviour is called the Curie temperature (T_c). At this temperature the permeability of the material drops suddenly and both coercivity and remanence become zero.[31]

There are a number of methods to measure the T_c of a material. They are: Vibrating Sample Magnetometer (VSM), where the magnetic moment is measured as a function of temperature and T_c is determined from the linear extrapolation of the curve of magnetic moment versus temperature from the region of maximum slope down to the temperature axis;[29] Magnetic Balance, where the induced magnetic moment of a specimen during heating-cooling processes is detected as a change in an amplitude of electric current measured by a feedback coil; Kappa Bridge Magnetic susceptibility Meter, and Magnetic Property Measurement System.

Within this work we synthesized Zn-doped cobalt ferrite materials with a lower T_c compared to that of pure cobalt ferrite, to use in catalytic investigations of methanol oxidation at 250 – 400 °C.

4.2.1.1. Sample preparation

In order to obtain a single-phase sample of cobalt ferrite and Zn-doped cobalt ferrite we tested several preparation methods, including the combustion method and co-precipitation with different agents (ammonia, sodium carbonate). Details of the preparation methods are given in Chapter 2.

Phase composition of the prepared catalysts was studied by XRD. Figure 4-2 presents XRD patterns of $CoFe_2O_4$ samples prepared by different methods. For the sample prepared by the urea-nitrate combustion method phase separation is observed as, besides the main cobalt ferrite phase, characterized by the presence of seven main peaks at 18.6 (111), 30.3 (220), 35.7 (311), 43.5 (400), 53.5 (422), 57.2 (511), 62.7 (440) and 73.9 °(533)[32], reflections characteristic of Fe_2O_3 (24.2, 33.3, 35.7, 49.9, 54.2, 57.6 and 64.2 °)[33] and Co_3O_4 (18.9, 31.3, 44.8 and 59.4 °)[34] are present. Co-precipitation with ammonia also leads to phase separation and formation of both $CoFe_2O_4$ and Fe_2O_3 phases (Figure 4-2). Only co-precipitation of nitrates with Na_2CO_3 results in the formation of a single-phase cobalt ferrite sample.

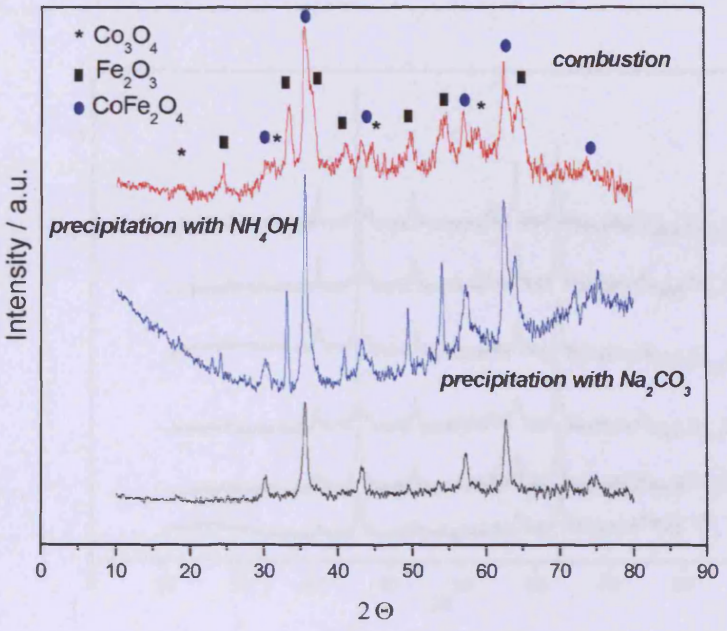

Figure 4-2. Influence of preparation methods on the phase composition of the cobalt ferrite samples.

As co-precipitation method with sodium carbonate appear to be the best way to obtain single-phase cobalt ferrite, we used this method to synthesize all Zn-doped $Zn_xCo_{1-x}Fe_2O_4$ samples, later denoted as Zn_xCF, where x=0 to 0.5 (see details in Chapter 2).

4.2.1.2. Structural characterization

Different characterization techniques (XRD, Raman, BET, XPS, TEM) were used to obtain information about the cobalt ferrite-based samples, their structure, morphology, phase composition, chemical state and changes occurring after the samples were exposed to methanol oxidation reaction environment.

(a) XRD

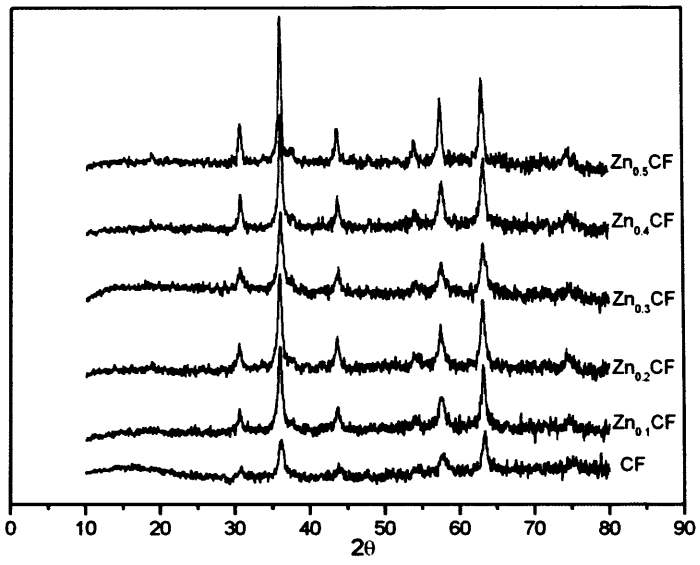

Figure 4-3. XRD of the cobalt ferrite and Zn-substituted $Zn_xCo_{1-x}Fe_2O_4$ (x=0-0.5) cobalt ferrites calcined at 500 °C.

Figure 4-3 and Figure 4-4 show XRD patterns of $Zn_xCo_{1-x}Fe_2O_4$ (x=0-0.5) samples synthesized by the co-precipitation method and calcined at 500 °C and 800 °C respectively. As mentioned above the cubic spinel structure is characterized by the presence of the main characteristic peaks at 18.61° (111), 30.27° (220), 35.74° (311), 43.47° (400), 53.5° (422), 57.19° (511), 62.73° (440) and 73.99° (533).[32] Analysis of the XRD patterns of all the samples confirmed the formation of the cubic spinel structure, as the main characteristic peaks were observed. Furthermore, it is apparent that zinc substitution does not affect the original spinel crystal structure. For the samples calcined at 500 °C the XRD peaks are rather broad, while for the samples calcined at 800°C we observe much sharper peaks and hence intense diffraction features. This indicates growth of particles with the increase in the calcination temperature. The particle sizes (D_{aveXR}) were calculated from the Debye-Scherrer equation (equation 2-7), using the full-width at half-maximum (FWHM) value of the respective

indexed reflections (Table 4-1). For the $Zn_xCo_{1-x}Fe_2O_4$ samples calcined at 500 °C the average particle size is 20.4 nm (standard deviation, S.D., of 2.0 nm.), but a significant increase in particle size occurs with the samples calcined at 800 °C (average 29.3 nm, S.D. 1.0 nm). Within experimental error (0.6 – 1.1 nm), the average crystallite size does not appear to change very much with the Zn substitution level.

Thus, the increase of calcination temperature from 500 °C to 800 °C results in particle growth by *ca.* 50 %.

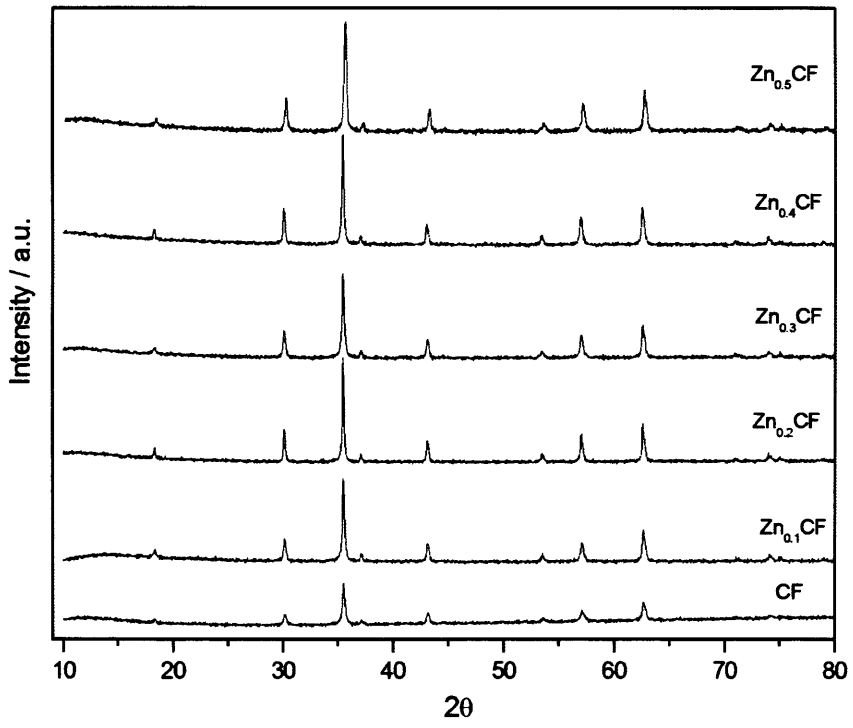

Figure 4-4. XRD of the cobalt ferrite and Zn-substituted $Zn_xCo_{1-x}Fe_2O_4$ (x=0-0.5) cobalt ferrites calcined at 800 °C.

There are some shifts in peaks positions in the XRD and the calculated lattice constant a_0 (using *d* value and respective *hkl* (311) parameters) was found to increase from 8.298 Å to 8.307 Å for the samples calcined at 500 °C and from 8.382 Å to 8.405 Å for the samples calcined 800 °C with increasing Zn substitution from 0 to 0.5 (Table 4-1, and Figure 4-5). The

increase of the lattice parameter is due to the difference in Zn^{2+} (0.74 Å) and Co^{2+} (0.72 Å) ionic radii.[35-36] The relationship between Zn doping and lattice parameter is nearly linear and, according to Vegard's law,[37] this implies the formation of homogeneous $Zn_xCo_{1-x}Fe_2O_4$ solid solutions. The difference in lattice parameter for the samples with identical composition, but different calcination temperature, points at different crystallization state of these samples. Thus, the samples calcined at 500 °C have a higher level of disorder in the lattice.

Table 4-1. The structural characterization data for the Zn_xCF samples.

Sample	S_{BET} (m^2/g)		Average crystallite size (D_{aveXR}) (nm)		Lattice parameter(a_0) (A)	
	500°C	800°C	500°C	800°C	500°C	800°C
CF	46.1	16.7	17.5	31.5	8.298	8.382
$Zn_{0.1}CF$	41.0	12.0	22.2	28.1	8.301	8.387
$Zn_{0.2}CF$	39.7	6.7	21.1	28.6	8.302	8.393
$Zn_{0.3}CF$	49.0	13.8	17.2	28.1	8.303	8.394
$Zn_{0.4}CF$	46.1	11.4	22.9	29.8	8.305	8.401
$Zn_{0.5}CF$	46.5	5.0	21.7	29.5	8.307	8.405

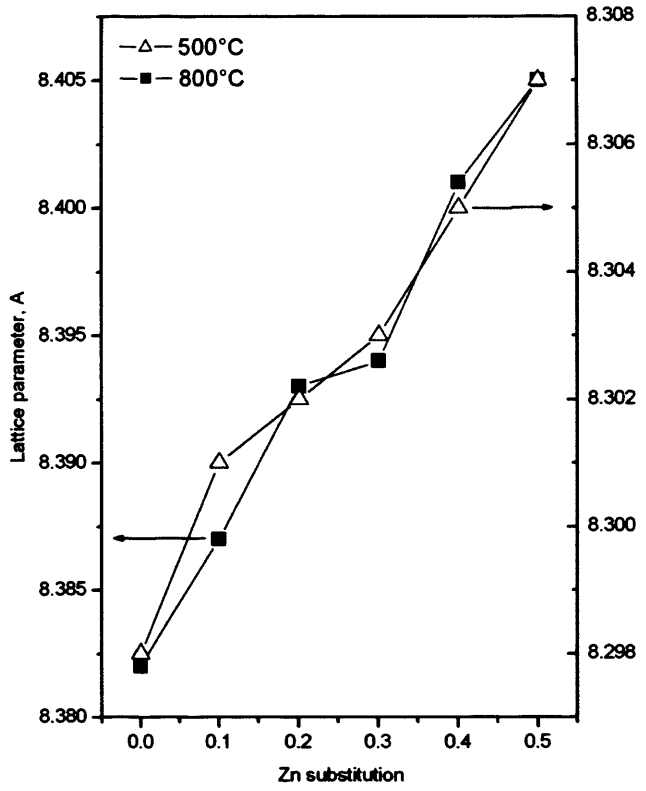

Figure 4-5. The dependence of lattice parameter value on sample composition.

In-situ XRD of the $Zn_{0.5}CF$ sample impregnated with six monolayers of molybdenum was recorded in order to investigate the evolution of a catalyst phase composition with an increased temperature. The sample was heated up to 450 °C in 10 % O_2/He flow (20 ml/min) and starting from 150 °C the XRD pattern was recorded every 50 °C. At 450 °C two repeat patterns were recorded to see if there are any structural changes in the sample with time. The sample was initially impregnated with ammonium heptamolybdate (AHM) and dried at 120 °C. Figure 4-6 shows the evolution of diffraction patterns during heating of the impregnated sample in oxygen/helium ambient.

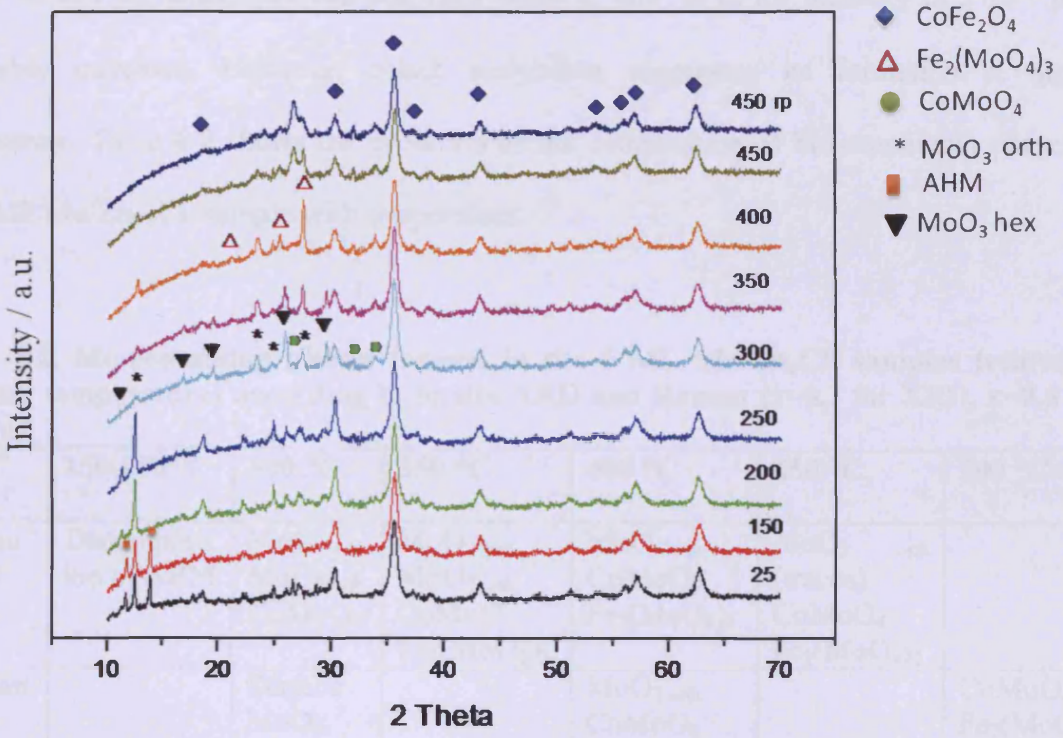

Figure 4-6. In situ XRD over the 6 Mo/$Zn_{0.3}$CF sample dried at 120 °C.

Interpretation of the data obtained is rather difficult because of the many phases with overlapping signals are expected to be formed in this experiment. Indeed, in every pattern we see reflections attributed to $CoFe_2O_4$.[32] Moreover up to 250 °C XRD patterns change due to the process of AHM[38] decomposition. Starting from 300 °C, the formation of a mixture of hexagonal MoO_3[39] and orthorhombic α-MoO_3[40] is observed showing characteristic reflections at 16.9, 19.5, 25.7, 29.4 ° and at 12.6, 23.3, 25.0, 27.3, 38.9 ° respectively. The cobalt molybdate also starts to form at 300 °C as low intensity characteristic peaks at 26.6, 34.0 and 32.1 ° are observed.[41] At 400 °C the formation of iron molybdate is observed.[42] During the heating process the intensities, and hence ratio of formed phases changes. Thus, hexagonal MoO_3 stops to form after 350 °C, which is in accordance with Wienold[38] who investigated AHM decomposition. The concentration of $CoMoO_4$ goes from minor at 300 °C to major at

450 °C. Formation of iron molybdate starts to compete with formation of orthorhombic MoO_3 at 350 °C and the latter becomes dominant phase at 400 °C as the intensity of 27.7 ° peak noticeably increases. However, cobalt molybdate suppresses its formation at higher temperature. Table 4-2 shows the evolution of the composition of Mo-containing phases in the 6 ML $Mo/Zn_{0.3}CF$ sample with temperature.

Table 4-2. Mo-containing phases formed in the 6 ML Mo/Zn_xCF samples treated at different temperatures according to in-situ XRD and Raman (x=0.3 for XRD, x=0.5 for Raman).

T, °C	150-250 °C	300 °C	350 °C	400 °C	450 °C	500 °C
In-situ XRD	Decomposition of AHM	$MoO_{3\ hex}$ $MoO_{3\ orth}$ $CoMoO_4$	$MoO_{3\ hex}$ $MoO_{3\ orth}$ $CoMoO_4$ $Fe_2(MoO_4)_3$	$MoO_{3\ orth}$ $CoMoO_4$ $Fe_2(MoO_4)_3$	$MoO_{3\ orth}$ (traces) $CoMoO_4$ $Fe_2(MoO_4)_3$	
Raman		Surface MoO_x $MoO_{3\ orth}$		$MoO_{3\ orth}$ $CoMoO_4$ $Fe_2(MoO_4)_3$		$CoMoO_4$ $Fe_2(MoO_4)_3$

(b) BET

BET surface area of Zn cobalt ferrites confirmed XRD results on sintering and particle growth (Table 4-1): for the samples calcined at 500 °C it is 45±3 m^2/g but after calcination to 800 °C it decreases to 11±3 m^2/g. There is a discrepancy here between the relatively small increase in particle size and the large decrease in surface area, since the two are approximately related by the relationship $SA = 3/\rho r$, where SA is the specific surface area (in m^2/g), ρ is the material density and r is the average particle radius. It is approximate because this assumes spherical particles. Nonetheless, clearly the surface area decreases by much more than ~ 50 %, it is closer to a factor of four difference. This is likely to be because, although the particles fuse together during sintering, there may still be phase boundaries (multiple twinning) within the sintered particles. This would then appear as if they were still separate particles in XRD, but

would result in a much greater loss in surface area. Impregnation of Zn-substituted cobalt ferrites with molybdenum did not affect the surface area values much.

(c) Raman Spectroscopy

Figure 4-7 shows Raman spectra of the $Zn_xCo_{1-x}Fe_2O_4$ (x=0-0.5) samples calcined at 500 °C. For all of the samples three major broad bands are seen at ~315, 470 and ~ 670 cm^{-1}. There is also some evidence of two other less intense bands at ~ 552 and 620 cm^{-1}. The detailed assignment of the cobalt ferrite Raman bands was given in Chapter 3. There are clearly some changes with Zn incorporation: some general broadening of the peaks and a noticeable increase in intensity of the 620 cm^{-1} band (Figure 4-7). This change in the 620 and 670 cm^{-1} band intensity is likely to be attributed to Co substitution by Zn and consequent change in M-O bond, as those bands correspond to symmetric stretching of oxygen atom with respect to metal ion in a tetrahedral void.[43] As in spinel ferrite, the distribution of divalent and trivalent cations can change due to migration of metal ions from tetrahedral (A) to octahedral (B) sites and vice versa. Changes in Raman spectra also might be due to a high degree of cation disorder induced by Zn^{2+} ion incorporation and/or a particle size effect.[44-45]

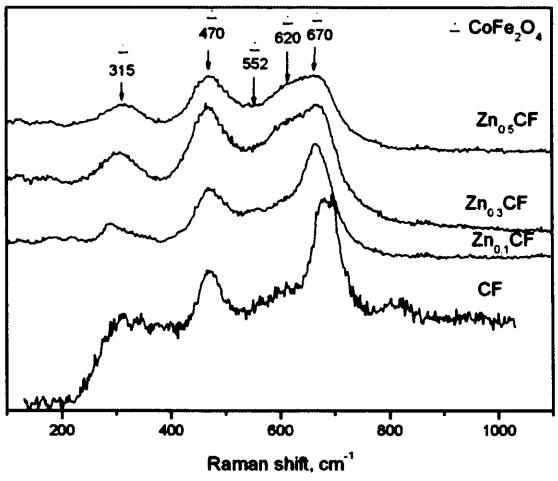

Figure 4-7. Raman spectra of cobalt ferrite and Zn-substituted cobalt ferrites.

Figure 4-8 shows the Raman spectra of the 6 $Mo/Zn_{0.5}CF$ sample calcined at different temperatures. These results match with XRD data and the sequence of phase composition changes with a temperature increase is the same: spinel (120 °C) – spinel + MoO_3 (300 °C) – spinel + MoO_3 + $Fe_2(MoO_4)_3$ (400 °C) – spinel + $Fe_2(MoO_4)_3$ + $CoMoO_4$ (500 °C) (bands were assigned according to Table 3-2 and Table 3-3). The sample after reaction (AR) shows very sharp and intensive MoO_3 characteristic bands with small admixture of iron molybdate. The other additional information obtained from Raman is that for the samples dried at 120 and calcined at 300 °C additional broad bands at ~870 and 950 cm^{-1} are seen (Figure 4-8). These bands were assigned to a two-dimensional polymeric surface molybdena species.[46-47]

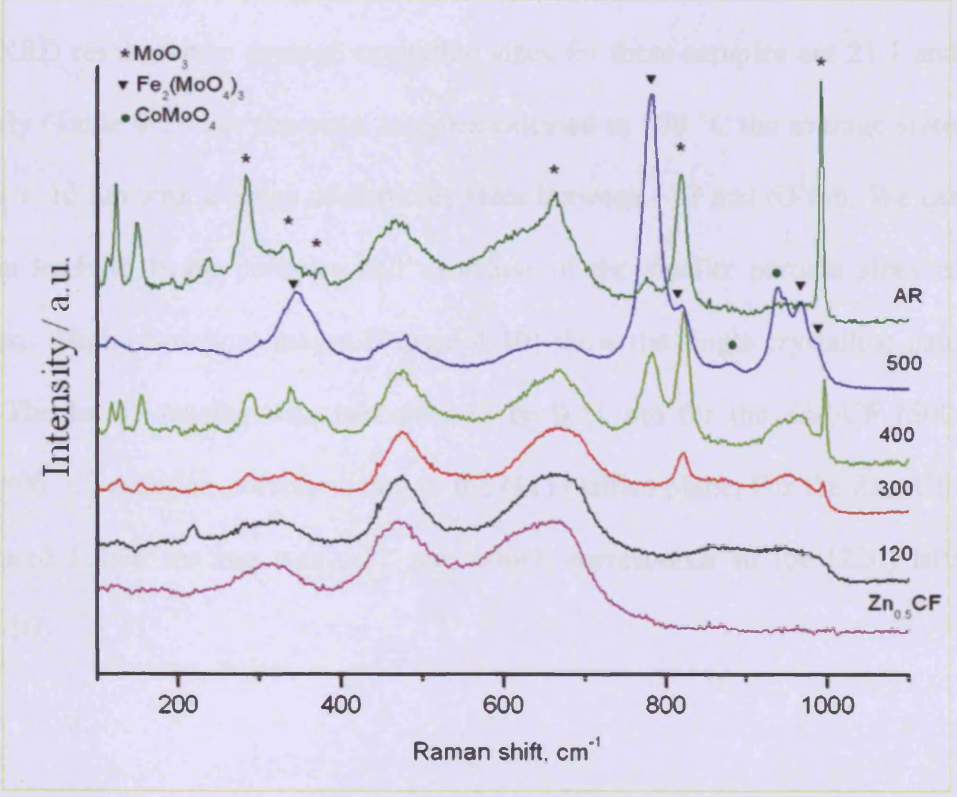

Figure 4-8. Raman spectra of the $Zn_{0.5}CF$, the impregnated 6 $Mo/Zn_{0.5}CF$ calcined at different temperatures and the sample after reaction (AR).

(d) High resolution TEM

HR-TEM micrographs of the $Zn_{0.2}CF$ sample (calcined at 500 and 800 °C) are given in Figure 4-9. The high magnification image reveals that particles are generally rounded in shape, with some evidence of crystallite faceting.

With increasing calcination temperature from 500 to 800 °C particles become larger. According to the images, the nanoparticles are agglomerated masses of individual particles. From the analysis of several images the average sizes of particles for the two samples were determined and they are listed in Table 4-1. For the $Zn_{0.2}CF$ and $Zn_{0.5}CF$ samples calcined at 500 °C the average sizes are similar at ~ 20 nm, with a mean deviation of ~7 nm, and with particles ranging in size from some very small ones (~2 nm) up to 38 nm. This is in agreement with the XRD result, where average crystallite sizes for these samples are 21.1 and 21.7 nm respectively (Table 4-1). For the same samples calcined at 800 °C the average sizes are 49 ± 13 and 32 ± 10 nm with a range of particles sizes between ~17 and 63 nm. We can see that calcination leads to larger particles and to a loss of the smaller particle sizes end of the distribution. High-resolution images (Figure 4-10) show the single-crystalline nature of the samples. The lattice spacing was measured to be 0.51 nm for the $Zn_{0.2}CF$ (500 °C) and $Zn_{0.5}CF$ (800 °C) samples, corresponding to the (111) lattice plane. For the $Zn_{0.5}CF$ (500 °C) the measured lattice spacing was 0.31 nm, which corresponds to the (220) lattice plane (Figure 4-10).

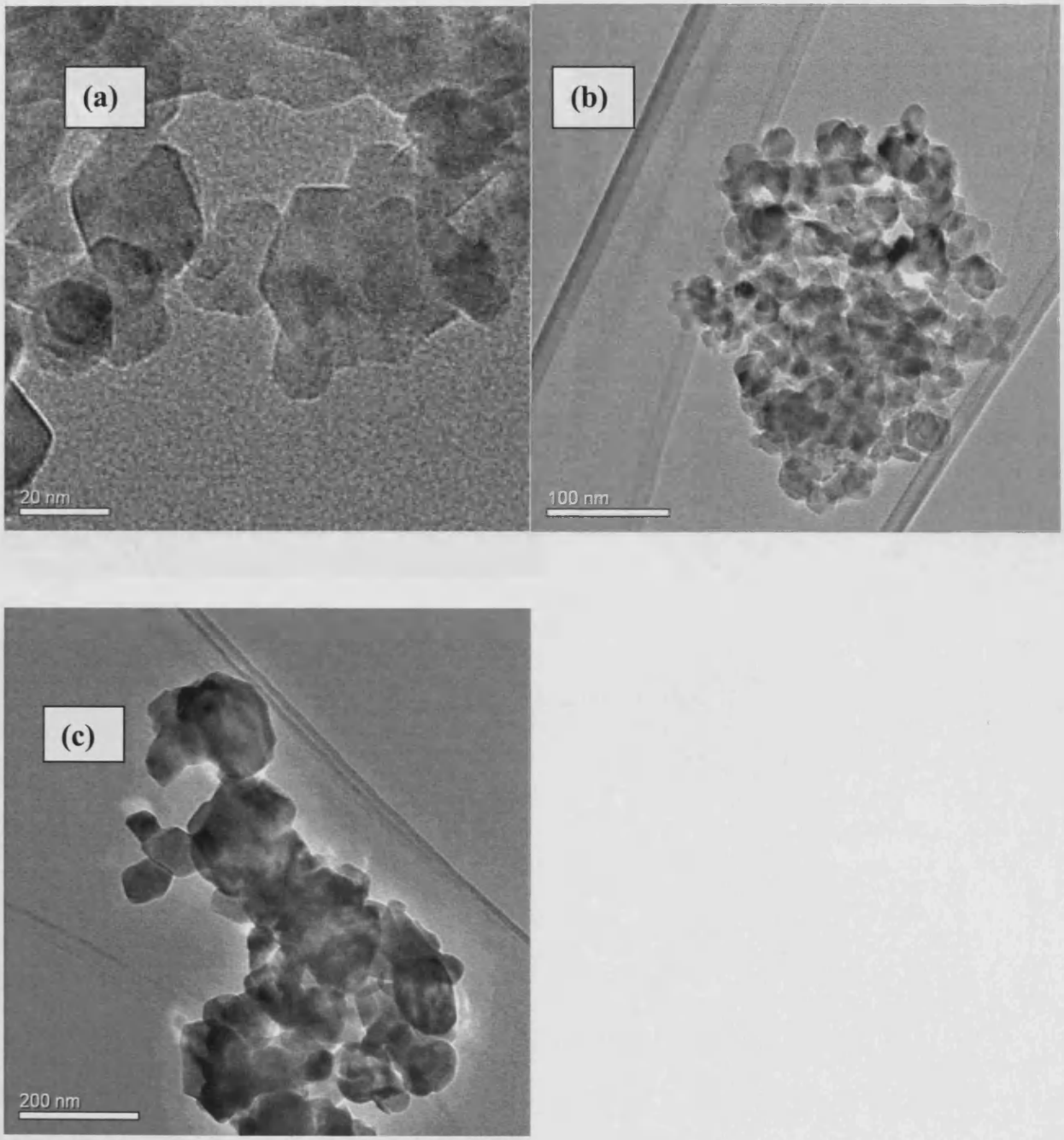

Figure 4-9. TEM of the cobalt ferrites a) $Zn_{0.2}CF$ (500 °C), b) $Zn_{0.2}CF$ (500 °C), c) $Zn_{0.2}CF$ (800 °C).

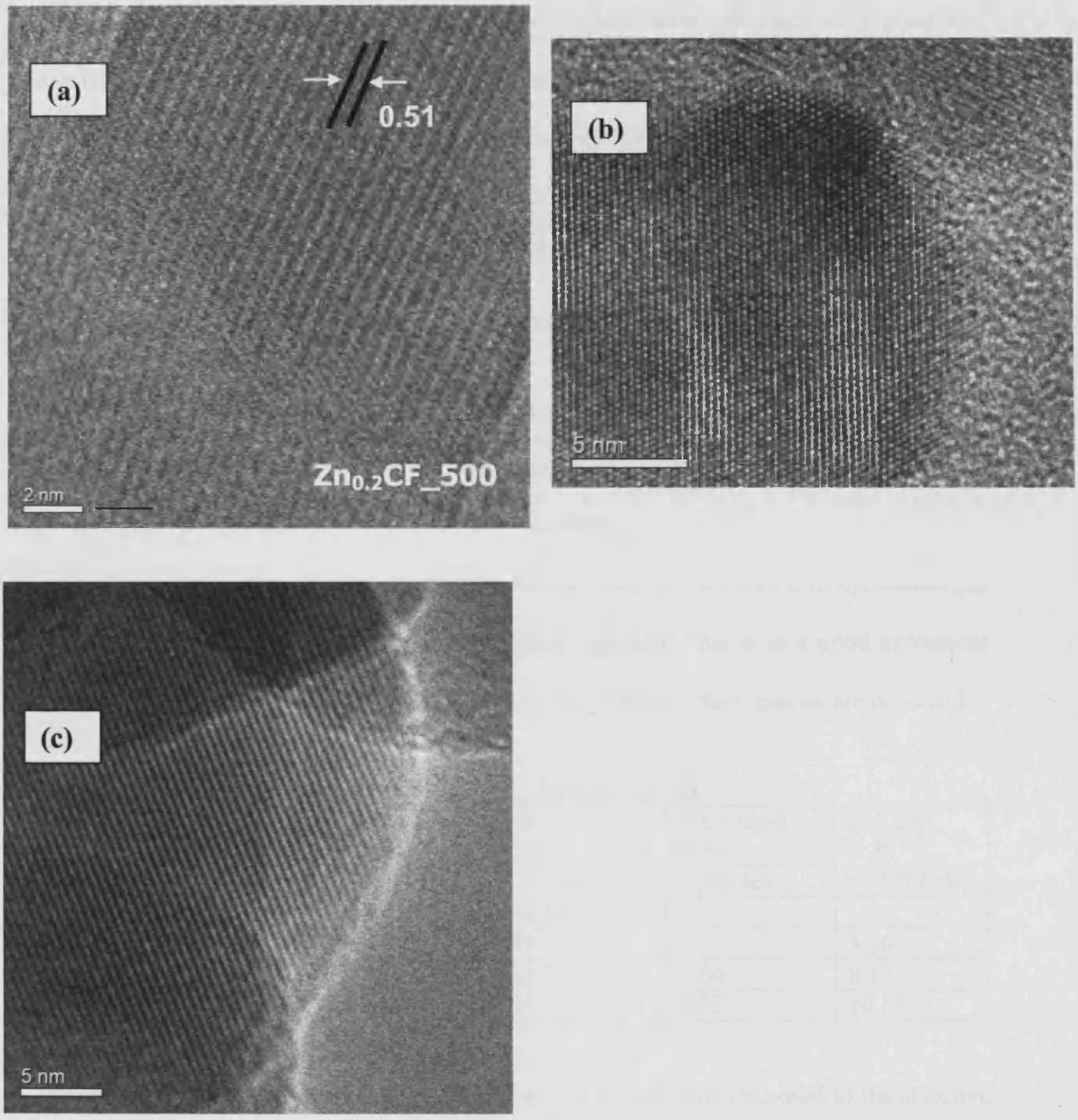

Figure 4-10. HRTEM images of a) $Zn_{0.2}CF$ (500 °C), b) $Zn_{0.5}CF$ (500 °C), c) $Zn_{0.5}CF$ (800 °C).

(e) XPS

In order to investigate catalyst surface composition and chemical states of the catalyst components XPS studies were done. It showed that in all catalysts iron is present in the +3 oxidation state, cobalt in +2 state, zinc in +2 state and molybdenum in + 6 state (Table 4-3).[48] Table 4-3 shows details of XPS measurements for the catalysts studied. It can be observed that for the pure $CoFe_2O_4$ sample integration of XPS peaks for Co and Fe gave an iron-to-cobalt ratio of 2.2 (±0.3):1 at the surface, which is very close to the stoichiometric composition. In the $Zn_{0.5}CF$ sample we observe an opposite situation: Co/Zn (2.16) and Fe/Zn (5.96) ratios are higher than it should be stoichiometrically. This fact could be explained by migration of Zn into the bulk cobalt ferrite spinel structure.

After impregnation of cobalt ferrite (Zn-doped cobalt ferrite) with a molybdenum (up to 6 monolayers) catalyst surface becomes enriched with Mo. This is in a good agreement with Raman spectroscopy, where bands assigned to molybdena surface species are observed.

Table 4-3. Surface composition of the $CoFe_2O_4$ -based catalysts.

Sample	Co ($2p_{3/2}$) at.%	Fe ($2p_{3/2}$) at.%	Mo ($3d_{5/2}$) at.%	Zn (2p) at.%
Position	~779.7eV	~711.4eV	~233.4eV	~1021.0eV
$CoFe_2O_4$	14.59	32.55	-	-
$Zn_{0.5}Co_{0.5}Fe_2O_4$	10.72	29.60	-	4.96
6 Mo/$Zn_{0.5}Co_{0.5}Fe_2O_4$	7.94	21.26	3.66	8.13
6 Mo/$Zn_{0.5}Co_{0.5}Fe_2O_4$ AR	9.85	16.88	4.52	10.58

For the 6 Mo/$CoFe_2O_4$ and the 6 Mo/$Zn_{0.5}Co_{0.5}Fe_2O_4$ catalysts exposed to the selective oxidation of methanol, the surfaces become enriched with Co and Mo (Table 4-3), which is in agreement with XRD and Raman data showing the formation of cobalt ferrite and iron molybdate phases.

4.2.1.3. Magnetic Susceptibility Measurements

(a) Effect of Zn-doping

The alternating current (AC), susceptibility (χ_{AC} (T)) and the Curie temperature (T_c) of the $Zn_xCo_{1-x}Fe_2O_4$ (x=0-0.5) samples were measured in the temperature range from 35 to 550 °C. Figure 4-11 shows the temperature dependence of the normalized susceptibility χ_{AC} (T)/ χ_{AC} (RT) for the $Zn_xCo_{1-x}Fe_2O_4$ (x=0-0.5) samples calcined at 500 °C. All these materials display ferrimagnetic order and become paramagnetic when heated to a sufficiently high temperature. It can be observed (Figure 4-11) that for all the samples calcined at 500 °C the T_c transition is very broad, which we consider to be due to the significant inhomogeneity in the particle sizes, as shown in TEM images (Figure 4-9, Figure 4-10), including very small particles (evidenced by the broad XRD peaks). It is likely that Curie temperature varies strongly with particles size, especially at small sizes, hence the broadness of the susceptibility curves. At the lower temperatures the susceptibility value rises with heating. According to some studies[49-50] the susceptibility is inversely proportional to the coercive force (H_c). Therefore, the increase in χ_{AC} (T) implies a decrease in H_c. The existence of the coercive force indicates that the samples contain spin clusters of different sizes.[1]

Table 4-4. Curie temperature dependence on Zn substitution and calcination temperature.

Sample	T_c (°C)				Average particle size (TEM)	
	500°C, $T_{c\,max}$	500°C, $T_{c\,1/2}$	800°C, $T_{c\,max}$	800°C, T_c *	500°C	800°C
CF	359	438	460	494		
$Zn_{0.1}CF$	319	394	398	419		
$Zn_{0.2}CF$	274	340	344	363	20.0	49.3
$Zn_{0.3}CF$	208	275	262	296		
$Zn_{0.4}CF$	171	223	200	228		
$Zn_{0.5}CF$	133	181	157	176	17.2	31.9

* - extrapolation of the near-linear decreasing part of the susceptibility curves to the intercept with the abscissa.

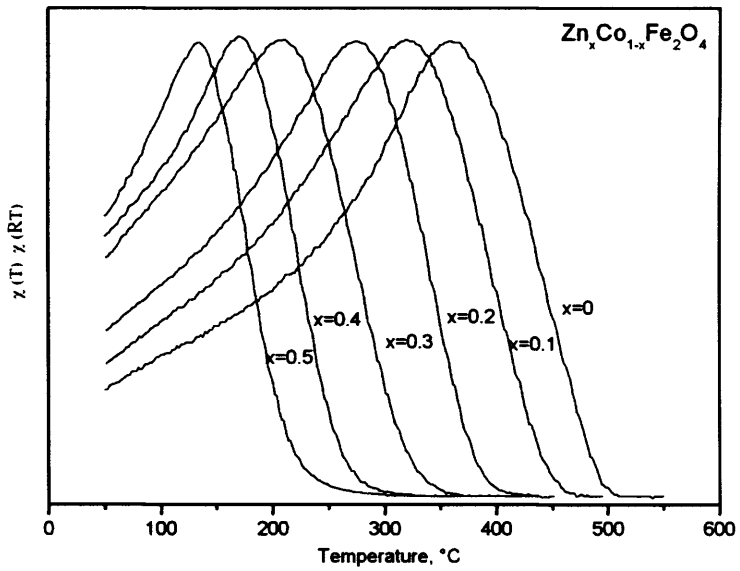

Figure 4-11. Magnetic susceptibility dependence on temperature for the ferrites calcined at 500 °C.

For the samples calcined at 500 °C it is difficult to determine T_c exactly as the transitions are very broad, but the estimated values ($T_{c\,max}$, taken from the point of maximum susceptibility and $T_{c\,½}$, from the point at which the susceptibility is ½ of the maximum value)

are given in Table 4-4. However, it is clear that with an increasing Zn substitution the position of the T_c transition shifts significantly to lower temperatures. Pure $CoFe_2O_4$ becomes fully non-magnetic at ~440 °C but doping of cobalt ferrite with zinc (up to 0.5 mol %) results in a shift of this point down to 181 °C for the $Zn_{0.5}CF$ sample (Figure 4-11). This shift of Curie transition is explained by the substitution of non-magnetic zinc. In the cubic system of ferrimagnetic spinels, the magnetic ordering is mainly due to a super exchange interaction mechanism occurring between the metal ions in the two oppositely magnetized sublattices A (tetrahedral) and B (octahedral), each of which is ferrimagnetically ordered. According to the Neel model,[51] the A-B interaction is the most dominant in ferrites, therefore T_c of a ferrite is determined from the overall strength of A-B interaction.[18, 20] The substitution of a non-magnetic ion, such as Zn, which has a preference for A site occupancy, results in the reduction of the exchange interaction between the A and B sites. The magnetization of the tetrahedral lattice will be smaller than in the case of the pure cobalt ferrite, and since Fe^{3+} ions have the largest moment, the saturation magnetization of a mixed ferrite at the absolute zero point would be expected to increase with rising zinc content.[18, 27-28] Hence, by varying the degree of zinc substitution, it is possible to vary the magnetic properties of the fine particles.

(b) Effect of calcination temperature

The influence of the calcination temperature and particle size on susceptibility curves and on T_c was investigated by calcining the $Zn_{0.4}CF$ sample for 1 h at 600, 700 and 800 °C (Figure 4-12). It is apparent that with the increase in calcination temperature the Curie transition becomes sharper and better defined. For the samples calcined at 500 and 800 °C we can define the $T_{c\,max}$ as 171 and 200 °C respectively. The increase in the temperature of the start of the Curie transition can be explained either by the differences in the particle size distributions or by possible partial evaporation of zinc at the higher temperatures. We assume that the

change in sharpness of the transition is due to the increased particle size homogeneity (see TEM, Figure 4-9): for the samples calcined at high temperature, the size distribution is not as broad as for the samples calcined at 500 °C and, in particular, there is a loss of particles in the small size end of the range (narrowed XRD peaks). At high calcination temperatures the sample sinters and the surface area decreases markedly. Figure 4-13 shows the dependence of the $T_{c\,max}$ and S_{BET} on temperature. For the sample calcined at 800 °C the T_c transition is sharp and occurs at 200 °C, at the same time the surface area is still significant for such ferrites (9 m^2/g).

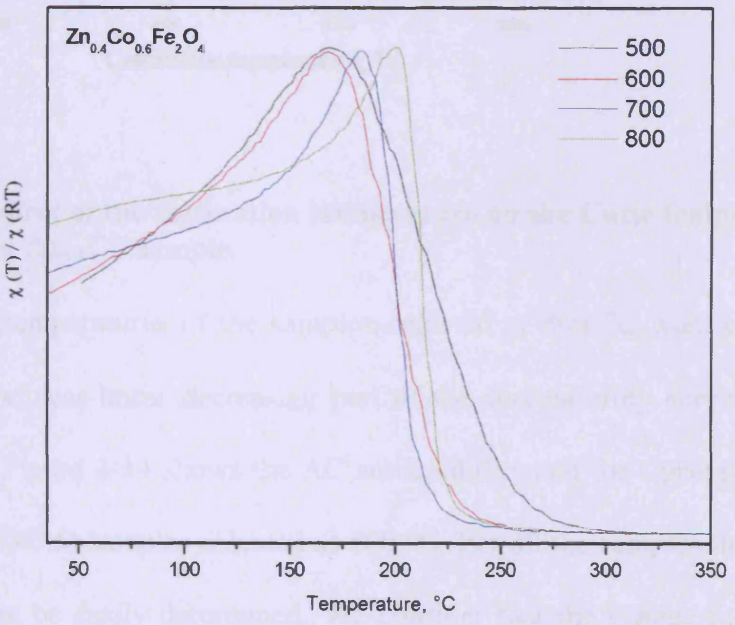

Figure 4-12. The effect of calcination temperature on the susceptibility-temperature curves for the $Zn_{0.4}$CF sample.

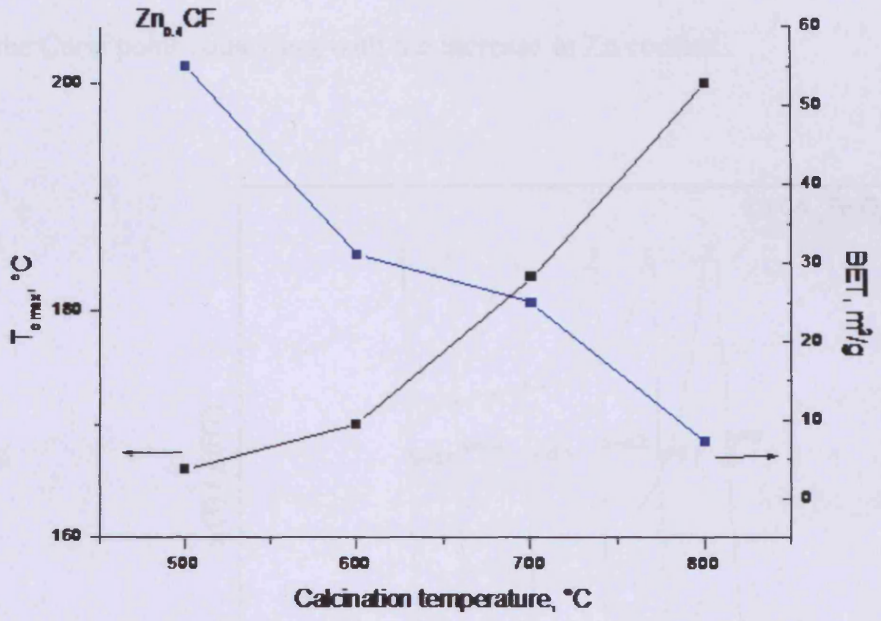

Figure 4-13.The effect of the calcination temperature on the Curie temperature and the surface area of the $Zn_{0.4}CF$ sample.

The Curie temperatures of the samples calcined at 800 °C were obtained from the extrapolation of the near-linear decreasing part of the susceptibility curves to the intercept with the abscissa. Figure 4-14 shows the AC susceptibility and the Curie temperature of the $Zn_xCo_{1-x}Fe_2O_4$ (x=0-0.5) samples calcined at 800 °C. For all the samples the Curie transition is sharp and T_c can be easily determined. We consider that the change in the T_c transition nature is due to the improved particle homogeneity. The Curie point of the non-substituted cobalt ferrite, 494 °C, decreases to 176 °C for the $Zn_{0.5}CF$ substituted sample (Table 4-4, Figure 4-14). It is evident that substituting Zn for Co in the cobalt ferrite decreases the T_c by as much as 300 °C.

Arulmurugan *et al*[27-28] have shown that the position of T_c for Zn-substituted cobalt ferrites depends on the magnetic field strength for the same materials ($Zn_{0.5}Co_{0.5}Fe_2O_4$) investigated; at 1 kOe and 5 kOe field the T_c values were 125 and 267 °C respectively. As we

investigated our samples at very weak magnetic field (1 Oe), we cannot compare our values with their results directly, however, they also observed a significant decrease in the position of the Curie point coinciding with the increase in Zn content.

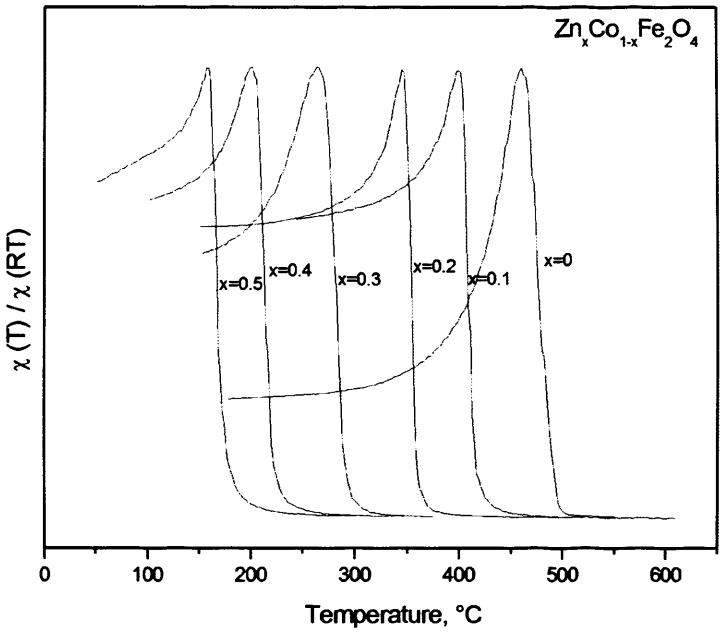

Figure 4-14. The effect of Zn substitution upon the temperature dependence of the susceptibility of the cobalt ferrites calcined at 800 °C.

(c) Effect of molybdenum loading

To see whether magnetic susceptibility changes with impregnation of Zn-doped cobalt ferrites with molybdenum we measured susceptibility curves of samples before and after impregnation. Figure 4-15 shows results for $Zn_{0.4}CF$ sample, pure and impregnated with 6 monolayers of molybdenum. There is almost no change in susceptibility curve, as it should be since molybdenum is a non-magnetic element.

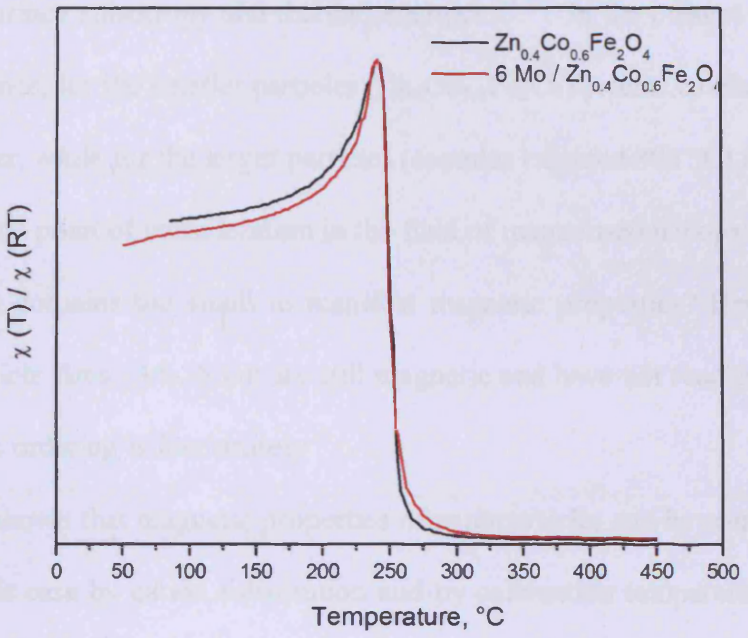

Figure 4-15. Comparison of susceptibilities of the pure $Zn_{0.4}Co_{0.4}Fe_2O_4$ and the 6 ML Mo/ $Zn_{0.4}Co_{0.4}Fe_2O_4$ sample.

It is clear that in these data we have two separate effects which contribute significantly to decreasing the value of T_c, that is, nanoparticle size and Zn substitution. As the nanoparticles become smaller in size, so the T_c also diminishes significantly (Figure 4-13).

Particle size is very important in magnetism, at least when particles are below ~20 nm as at this critical size the transition from ferromagnetic to super-paramagnetic behaviour occurs. In the super-paramagnetic state of the material, although the particle itself is a single-domain ferromagnet, the ability of an individual magnetic "dot" to store magnetic orientation information is lost when its dimension is below a certain threshold. Consequently, the magnetic moments within a particle flip rapidly in unison, exhibiting the super-paramagnetic relation phenomenon.[1] Maaz *et al*[17] investigated correlation between the coercivity and mean particle diameter of $CoFe_2O_4$ nanoparticles. It was shown that H_c increases with a decrease of particle sizes below ~ 45 nm, reaching a maximum at 28 nm (critical size) and then diminishing again. They postulated that this effect could be firstly due to the crossover from

single domain to multi-domain behaviour with increasing size. Secondly, it can arise from a combination of surface anisotropy and thermal energies.[17, 52] In the present work we observe the same effect since, for the smaller particles ($Zn_xCo_{1-x}Fe_2O_4$ systems calcined at 500 °C) the coercivity is higher, while for the larger particles (samples calcined 800 °C) it is lower (Figure 4-12). An important point of consideration in the field of magnetised nanoparticles is - at what size are magnetic domains too small to manifest magnetic properties? Here $Zn_xCo_{1-x}Fe_2O_4$ samples with particle sizes ~15-25 nm are still magnetic and have not reached the critical size at which magnetic ordering is lost entirely.

We have shown that magnetic properties of nanoparticles can be controlled by careful preparation, in this case by cation substitution and by calcination temperature control. When particle size becomes too small it is difficult to achieve homogeneous distributions of particle by the co-precipitation method. Hence, a range of the Curie temperatures for different sized particles gives rise to a broad distribution of magnetic susceptibility with temperature.

4.2.2. Catalytic reactivity

4.2.2.1. Cobalt ferrites and Zn-doped Cobalt Ferrites

This section contains data on methanol oxidation TPPFR for pure and Zn-doped cobalt ferrites calcined at different temperatures. The methanol oxidation reaction was chosen as a model reaction to study whether there is any relationship between magnetic properties of materials and catalysis.

(a) Effect of different calcination temperatures

The main objective of this chapter was to investigate if there is any influence of the Curie transition of ferrites on the activity or selectivity in methanol oxidation reaction. As it was said above, the $Zn_xCo_{1-x}Fe_2O_4$ (x=0-0.5) samples were calcined at 500 and 800 °C in order to

obtain sharp Curie transition. Figure 3-20 and Figure 4-16 show methanol TPPFR over the cobalt ferrite calcined at 500 and 800 °C respectively.

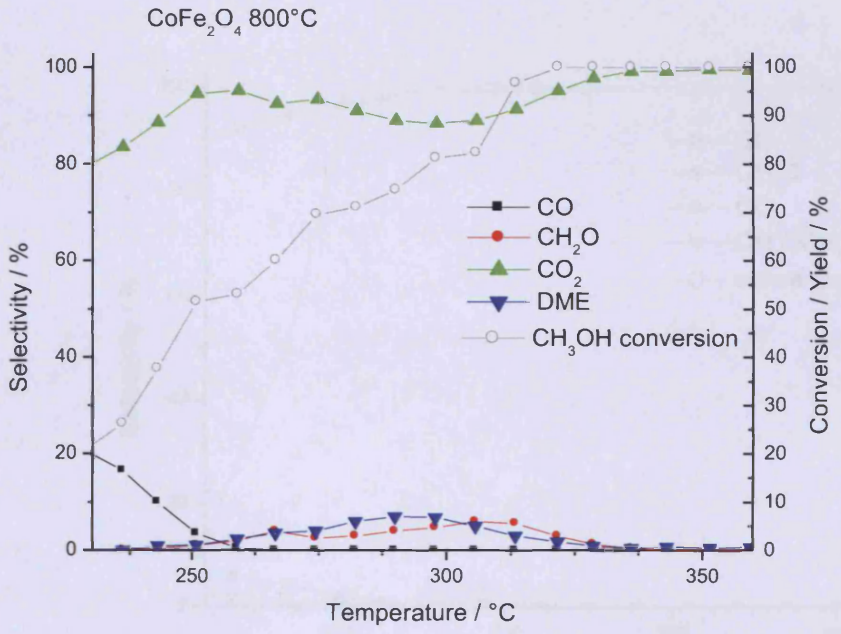

Figure 4-16. Selectivity and conversion for methanol oxidation over $CoFe_2O_4$ calcined at 800 °C.

Cobalt ferrite combusts methanol mainly to carbon dioxide and water. Catalytic activity of cobalt ferrite calcined at 500 °C was described in Chapter 3. For the cobalt ferrite calcined at 800 °C we observe a significant decrease in activity as surface area drops from 46 to 17 m^2/g (Table 4-1). Thus, methanol conversion reaches 50 % only at 260 °C and 100 % at 310 °C. Selectivities distribution is the same as for the 500 °C calcined sample: CO forms at low conversions, traces of CH_2O and DME are observed at around 300 and 290 °C and again the main product is CO_2.

Cobalt ferrite has a Curie temperature of 494 °C which is too high for methanol oxidation as our reaction runs only up to 400 °C and we needed a sample which would have a Curie transition at the point when conversion has already started, but has not reached 100 %. Thus, to compare the influence of calcination temperature and to see if there is any effect of

ferromagnetic transition we picked the $Zn_{0.35}Co_{0.65}Fe_2O_4$ sample with T_c = 256 °C. Figure 4-17 and Figure 4-18 show results on oxidation of methanol over the $Zn_{0.35}CF$ samples calcined at 500 and 800 °C respectively.

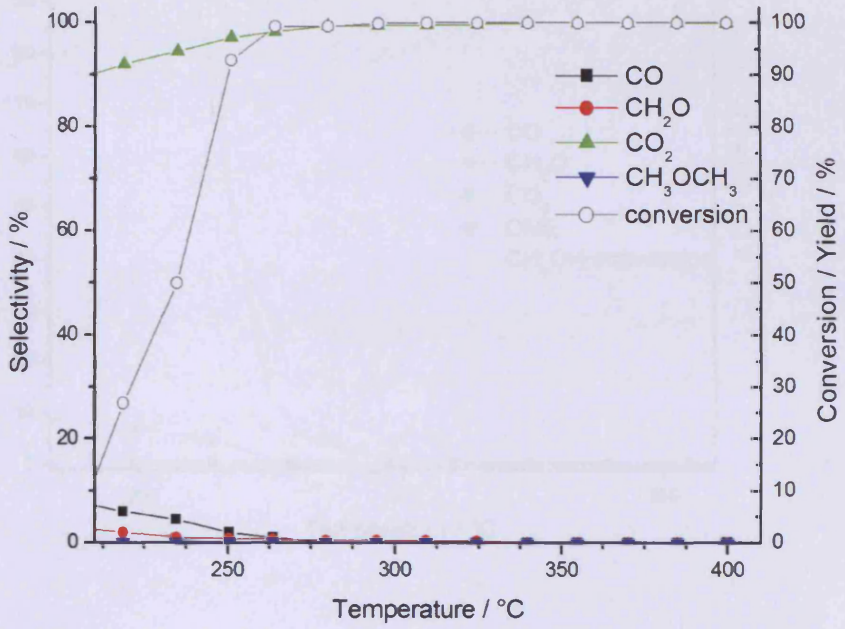

Figure 4-17. Selectivity and conversion for methanol oxidation over the $Zn_{0.35}CF$ calcined at 500 °C.

Zn-doped cobalt ferrites also turned to be methanol combustors. $Zn_{0.35}CF$ shows 50 % conversion at 240 °C and 100 % at 260 °C with almost 100% selectivity towards CO_2. A minor formation of CO and formaldehyde is observed at low conversions. No formation of DME was detected over this sample. So far we can say that addition of Zn to cobalt ferrite does not result in formation of new products, but somehow decreases activity as conversion decreases. In terms of magnetic investigation, we can say that nothing unusual happens in the range of the Curie temperature, which is presumably because of the very broad Curie transition for the 500 °C calcined samples giving no chance to observe any sharp changes either in activity or in selectivity. Selwood *et al*[4] postulated that they could see an effect of the

Curie transition only when this transition occurred rather sharply. Thus, we will not show any other results for the $Zn_xCo_{1-x}Fe_2O_4$ samples calcined at 500 °C as all of them are rather similar.

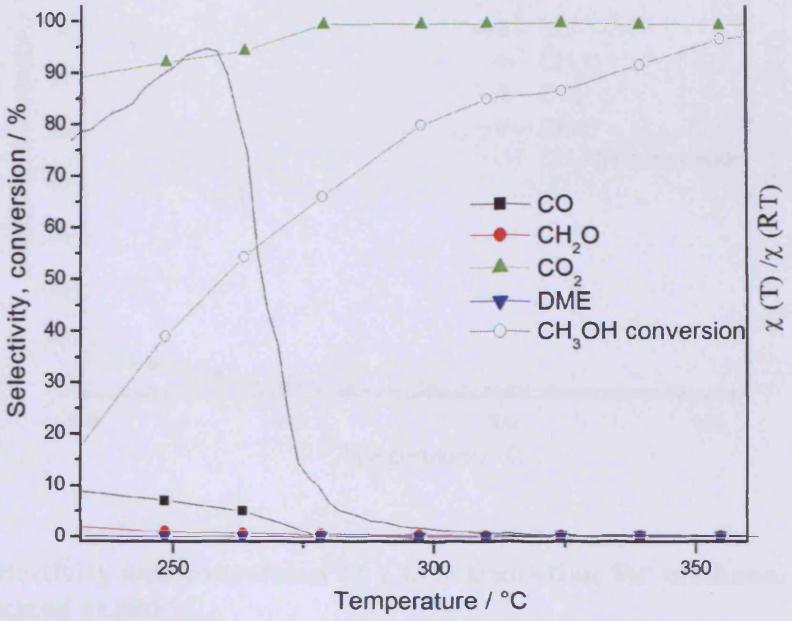

Figure 4-18. Selectivity and conversion vs Curie transition for methanol oxidation over the $Zn_{0.35}$CF calcined at 800 °C.

Figure 4-18 shows conversion and selectivity for methanol oxidation over the $Zn_{0.35}$CF sample calcined at 800 °C compared with the susceptibility curve. After calcination of $Zn_{0.35}$CF at 800 °C the surface area drops from 57 to 15 m^2/g, so does the conversion which now attains 50 % at 265 °C and does not reach 100 % even at 360 °C. In terms of selectivity, this sample is again selective to CO and CH_2O at low conversion and almost 100 % selective towards CO_2 after conversion reached 60 % value. The Curie transition for this sample is sharp and occurs at 256 °C. However, we do not see any related changes in conversion or selectivity in the Curie temperature range.

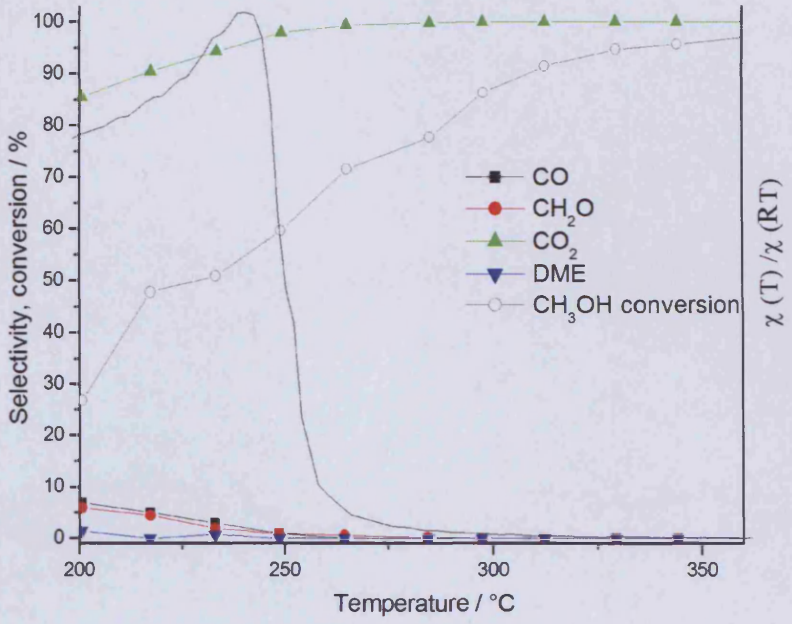

Figure 4-19. Selectivity and conversion vs Curie transition for methanol oxidation over the $Zn_{0.4}$CF calcined at 800 °C.

Another experiment with $Zn_{0.4}$CF sample calcined at 800 °C is shown in Figure 4-19. With almost the same conversion and selectivity profiles as for the $Zn_{0.35}$CF sample, the $Zn_{0.4}$CF sample produces a minor amount of DME (<3%). The Curie temperature for this sample occurred at 245 °C, and again we do not see any changes in conversion or selectivity towards carbon-containing products either before the T_c transition or after.

(b) Different rate of heating

To obtain more information about the reaction in the range of the Curie transition we ran experiments with a slower rate of temperature ramp and also isothermal experiments in the range of the T_c.

In the standard TPPFR experiment temperature is ramped with the speed of 8 °C/min and one injection per every 2 minutes (16 °C) is made. For comparison you can see in Figure 4-20 and Figure 4-21 methanol oxidation over $Zn_{0.2}$CF sample calcined at 800°C in the range

of the Curie transition with a temperature ramp of 8°C/min and 1°C/min respectively. Methanol was injected every 2 minutes in both experiments. Comparing the results of these two experiments we can see that in both cases conversion is increasing over the whole temperature range reaching ~ 100% only at 360°C, CO_2 is the major carbon-containing product in the range of Curie transition and starting from 250 °C selectivity towards carbon dioxide is ~95%. Going through the Curie temperature range we do not see any sharp changes either in conversion or in selectivity even when the speed of experiment is reduced 8 times.

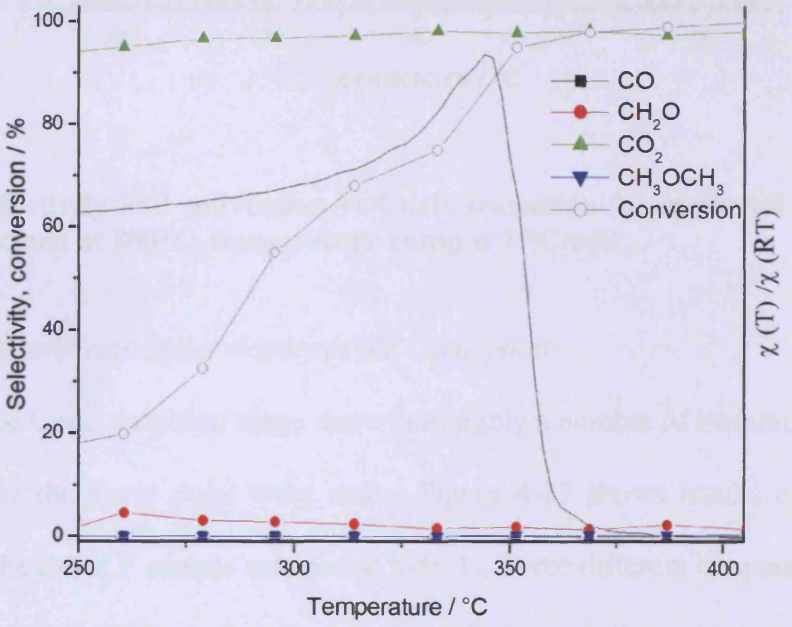

Figure 4-20. Selectivity and conversion vs Curie transition for methanol oxidation over the $Zn_{0.2}CF$ calcined at 800 °C, temperature ramp is 8 °C/min.

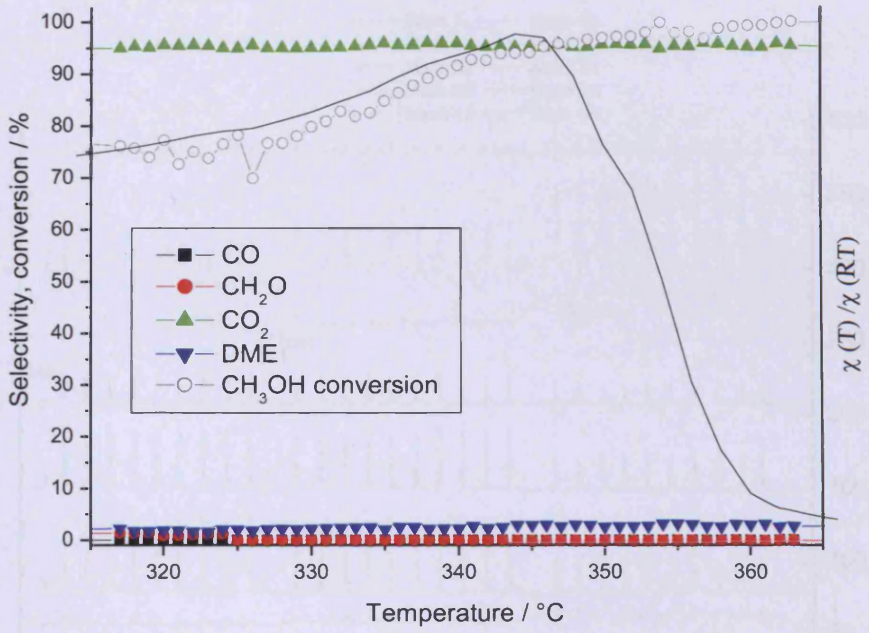

Figure 4-21. Selectivity and conversion vs Curie transition for methanol oxidation over the $Zn_{0.2}CF$ calcined at 800°C, temperature ramp is 1 °C/min.

(c) Isothermal experiments in the vicinity of the Curie point

To investigate the Curie transition range more thoroughly a number of isothermal experiments in the vicinity of the Curie point were made. Figure 4-22 shows results of an isothermal experiment for the $Zn_{0.4}CF$ sample calcined at 800 °C. Three different temperatures around T_c (245 °C) were taken: 240 °C – before T_c, 260 °C – after the transition starts and 280 °C – after transition ends. Due to methanol conversion the intensities of masses 31, 30, 29 and 28 (cracking masses of methanol) drop as temperature increases. On the contrary mass 44 (CO_2), mass 18 (water) and mass 2 (hydrogen) increase showing the occurrence of the combustion reaction. However, for every temperature all masses show very consistent behaviour – peaks have very similar intensity and no sharp changes in any mass, indicating unusual catalyst behaviour, are observed.

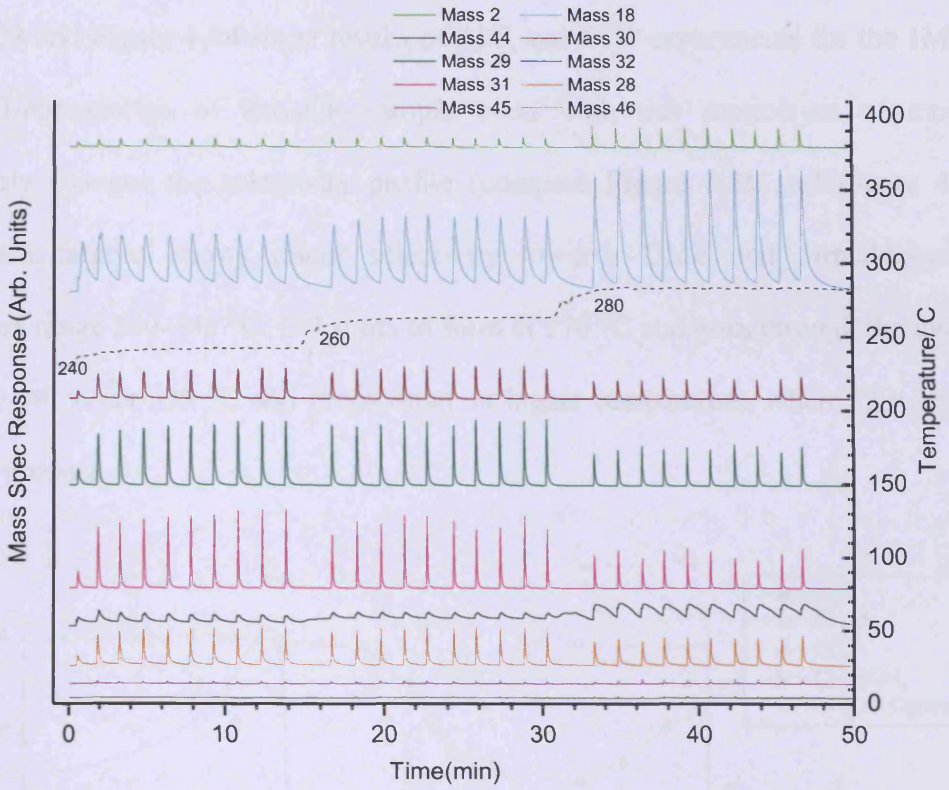

Figure 4-22. Isothermal methanol injections over the $Zn_{0.4}CF$ sample calcined at 800 °C.

4.2.2.2. Impregnated samples. Effect of Molybdenum loading.

We were mainly interested in the effect the Curie transition may have on the selectivity of catalytic reactions. For this purpose we needed a model reaction with several products. As our Zn-doped cobalt ferrite samples act as combustors of methanol to CO_2 and water, we impregnated them with different amounts of molybdenum to increase selectivity towards partial oxidation products (CO, formaldehyde). In this section results of TPPFR, TPD and isothermal experiments for 1-6 monolayers of $Mo/Zn_{0.4}CF$ (800 °C) are presented and discussed.

(a) One monolayer sample

Figure 4-23 and Figure 4-24 show results of TPR and TPD experiments for the $1Mo/Zn_{0.4}CF$ catalyst. Impregnation of $Zn_{0.4}CF$ sample even with one monolayer of molybdenum significantly changes the selectivity profile (compare Figure 4-19 and Figure 4-23). The impregnated catalyst shows minor selectivity towards DME and formaldehyde in the temperature range 240-340 °C. CO starts to form at 270 °C and goes through the maximum of selectivity (40 %) at 335 °C and drops down at higher temperature, where CO_2 becomes the dominant product.

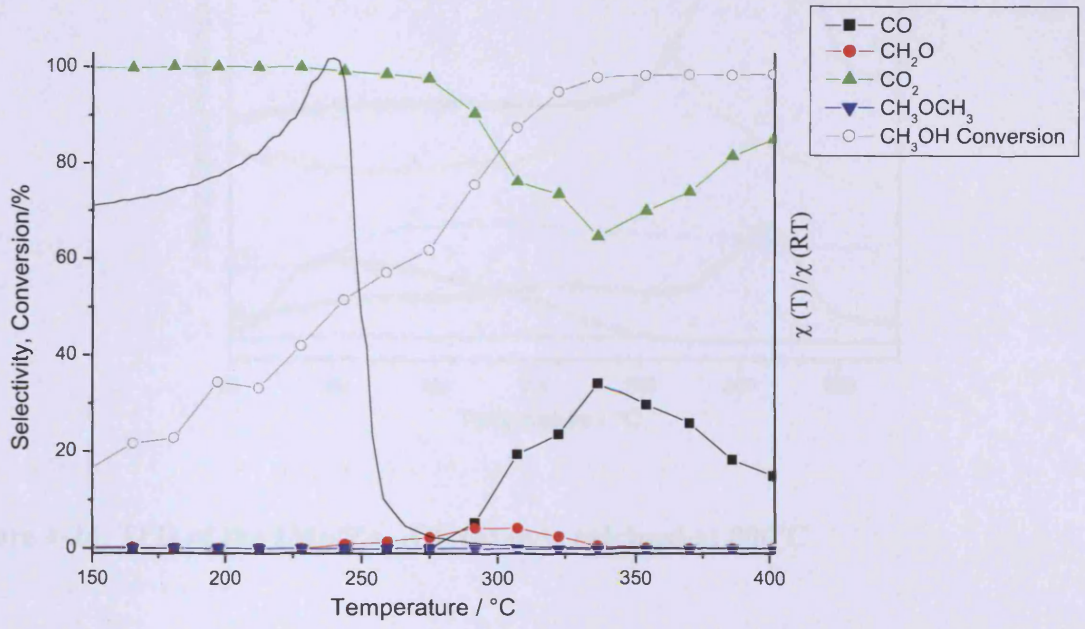

Figure 4-23. Selectivity and conversion for methanol oxidation over the $1Mo/Zn_{0.4}CF$ catalyst calcined at 800°C.

These results are in good agreement with TPD experiments (Figure 4-24) showing desorption of CO peaking at ~250 °C and CO_2 desorption at 325 °C. There are two peaks of hydrogen desorption at 215 and 320 °C. There is also a broad methanol desorption peak centred at around 115 °C. Analogous to the $Mo/CoFe_2O_4$ catalysts discussed in Chapter 3, here the production of significant amounts of CO is due to formation of mixed Co-Mo-Fe

layer on the surface of Zn-doped cobalt ferrite. CO_2 might be produced via two pathways: as a product of secondary oxidation of CO and directly from the formate species on the uncovered Zn cobalt ferrite surface. The presence of CO_2 peak in the TPD profile indicates that the monolayer of Mo is not homogeneous for this sample and some of the ferrite phase is exposed to the surface.

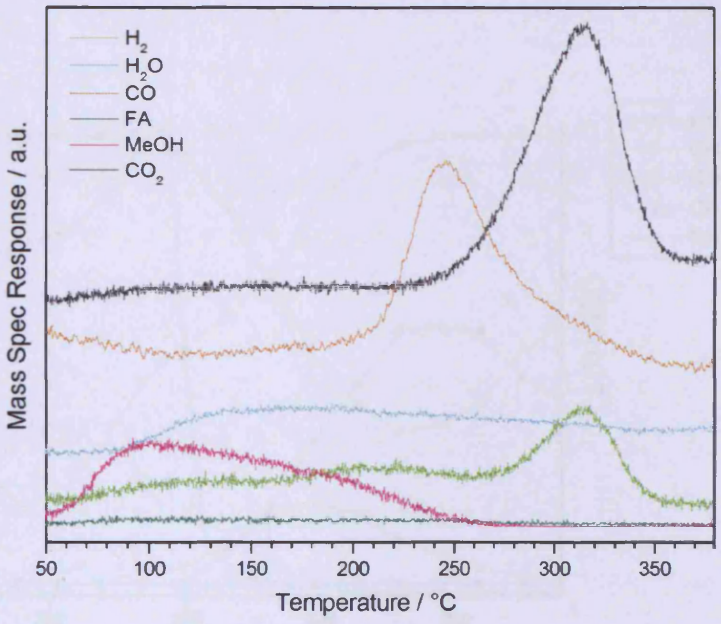

Figure 4-24. TPD of the 1Mo/$Zn_{0.4}$CF catalyst calcined at 800°C.

(b) Three monolayers sample

When impregnated with three monolayers of molybdenum $Zn_{0.4}$CF starts to produce more selective oxidation products. Thus, selectivity towards formaldehyde increases up to 18 % at 300 °C and selectivity towards CO increases significantly in the range of 300-400 °C reaching a maximum value 55 % at 330 °C. Methanol conversion is complete at only around 340 °C (Figure 4-25). These changes in selectivity are due to formation of the Mo-containing phases (cobalt molybdate, iron molybdate, molybdena) on the surface of the catalyst.

These results are supported by TPD experiments (Figure 4-26) showing desorption of selective oxidation products. There is a formaldehyde desorption peak at 215 °C. Carbon monoxide shows intense desorption maximum at 230 °C, which coincides with the only hydrogen desorption peak. CO_2 desorbs at around 315 °C and the intensity of its peak decreases significantly compared to the 1 monolayer sample indicating that less ferrite phase is exposed on the surface of the catalyst. There is also methanol desorption maximum centred at 130 °C.

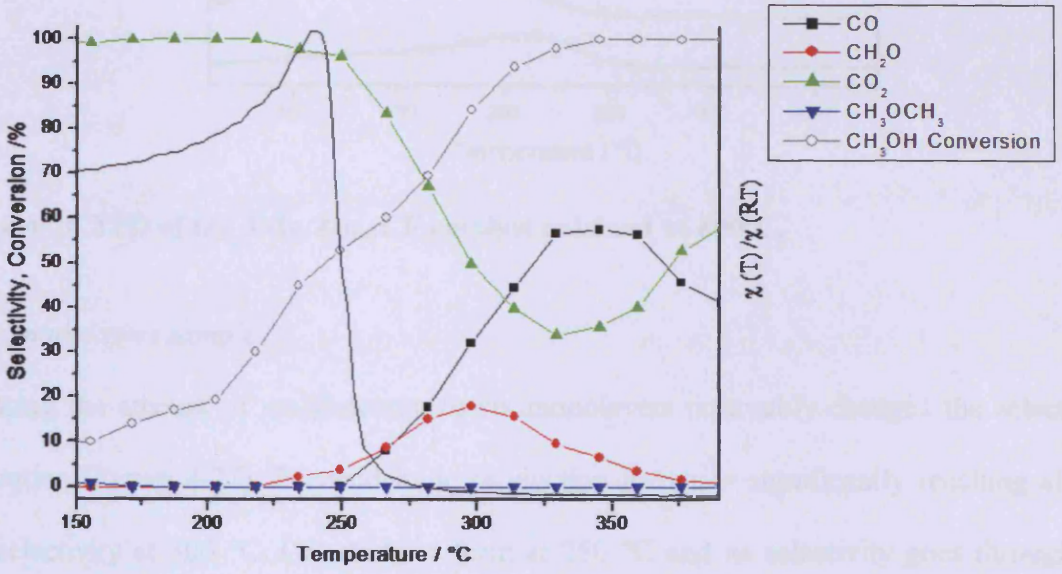

Figure 4-25. Selectivity and conversion for methanol oxidation over the 3Mo/$Zn_{0.4}$CF catalyst calcined at 800°C.

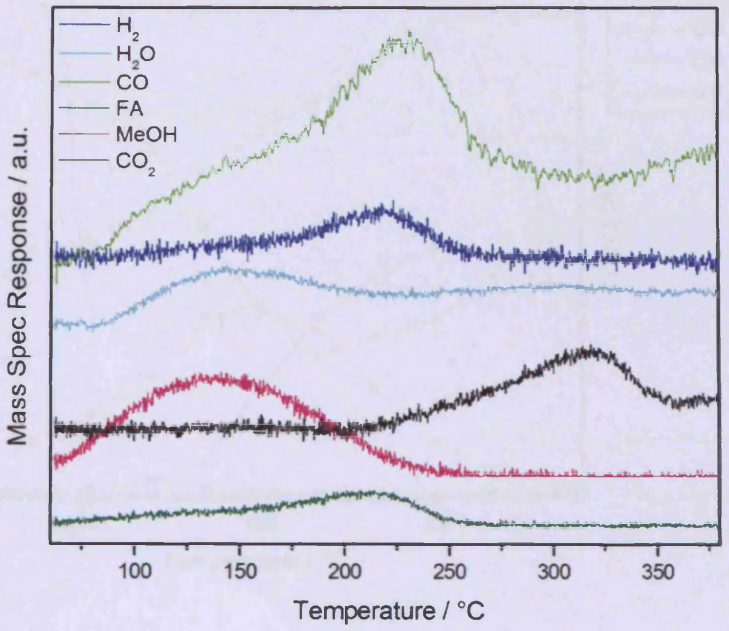

Figure 4-26.TPD of the 3Mo/$Zn_{0.4}$CF catalyst calcined at 800°C.

(c) Six monolayers sample

Increasing the amount of molybdenum to six monolayers noticeably changes the selectivity distribution (Figure 4-27). Formaldehyde production increases significantly reaching almost 40% selectivity at 300 °C. CO starts to form at 250 °C and its selectivity goes through the maximum at 350 °C (50 %). DME is present as a minor product over the whole temperature range (selectivity ~5-7 %). Selectivity towards CO_2 is high at low conversion, goes through the minimum at ~315 °C and then increases again.

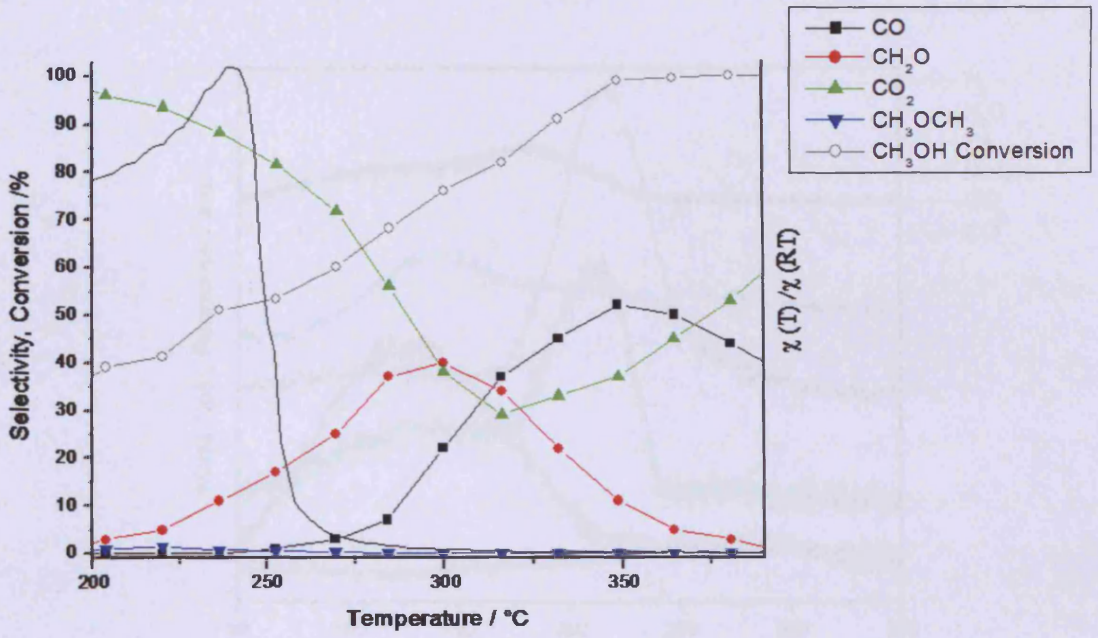

Figure 4-27. Selectivity and conversion for methanol oxidation over the 6 Mo/$Zn_{0.4}$CF catalyst calcined at 800 °C.

The TPD profile of the 6 Mo/$Zn_{0.4}$CF catalyst (Figure 4-28) is rather similar to that of the 3 Mo/$Zn_{0.4}$CF sample showing a large desorption of CO centred at 220 °C. Hydrogen desorbs simultaneously with CO in a broad peak. CO_2 presents a small desorption peak at higher temperature. There are methanol and formaldehyde desorption peaks centred at 130 °C and 180 °C respectively. Small CO_2 desorption peak is observed at ~ 275 °C.

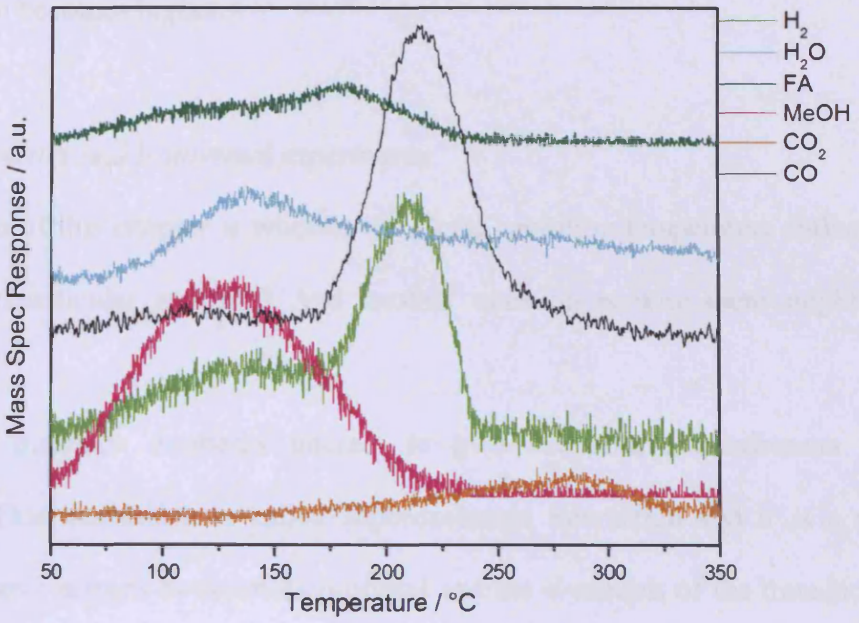

Figure 4-28. TPD of the 6 Mo/$Zn_{0.4}$CF catalyst calcined at 800 °C.

From the results obtained it is clear that dosing of molybdenum on the Zn-substituted cobalt ferrite leads to a significant reduction in CO_2 production and the increase in the partial oxidation products. We presume that in the un-doped zinc cobalt ferrites, due to the basic nature of the surface sites composed of Zn, Co and Fe[53] cations, dissociative methanol adsorption leads to the formate groups being formed and, consequently, to CO_2 production. Even small amount of doping of molybdenum onto the zinc cobalt ferrite surface results in formation of mixed Co-Mo-Fe surface layer, which, according to XRD and Raman data, consists of cobalt molybdate, iron molybdate and molybdena. This mixed layer appears to be important for the stabilization of surface methoxy species and direction reaction to the partial oxidation products (primarily CO). Presumably, on this type of surface sites methanol forms methoxy groups as intermediates (-O-CH_3-) and yields formaldehyde. The latter can be quickly decomposed into H_2 and CO.[54-55] The high level of production of CO_2 at low oxygen conversion observed in TPPFR experiments is attributed to the fast secondary oxidation of

CO on the highly active surface zinc cobalt ferrite. This CO_2 concentration drops as the oxygen conversion becomes higher.

(d) Magnetic properties and isothermal experiments

The main question of this chapter is whether the Curie transition temperature influences the selectivity of our particular reaction? And another question is why there might be any influence?

In oxides magnetic moments interact to give cooperative phenomena such as ferromagnetism. This interaction is called superexchange interaction and it is a result of exchange of oxygen electrons between its *p*-orbital and the *d*-orbitals of the transition metal. Figure 4-29 presents a schematic picture of the superexchange interaction. When *p* orbital of oxygen is in its ground state (two electrons), the electrons must be of opposite spin. When an electron is exchanged or shared by the overlapping orbitals between two sites, the spin is conserved as the electron hops from the *p*-like to the *d*-like orbital. The result is that the two T ions must have opposite spin directions. At its root, the superexchange interaction is a consequence of the different symmetry of the *p* and *d* states. Notice that one of the three *p* orbitals represents two electron states (spin-up and spin-down) whose spatial wavefunctions have 360 ° (single-fold) rotational symmetry. One of the five *d* orbitals represents two states that have 180 ° rotational symmetry. Thus, a *p* state has spinup and spindown concentrated in lobes 180 ° apart while a *d* state has opposite spin concentrations every 90 ° rotation about the ion. These symmetry considerations, plus the fact that electron hopping conserves spin orientation, produce the antiferromagnetic spin coupling between nearest neighbor transition metal ions.

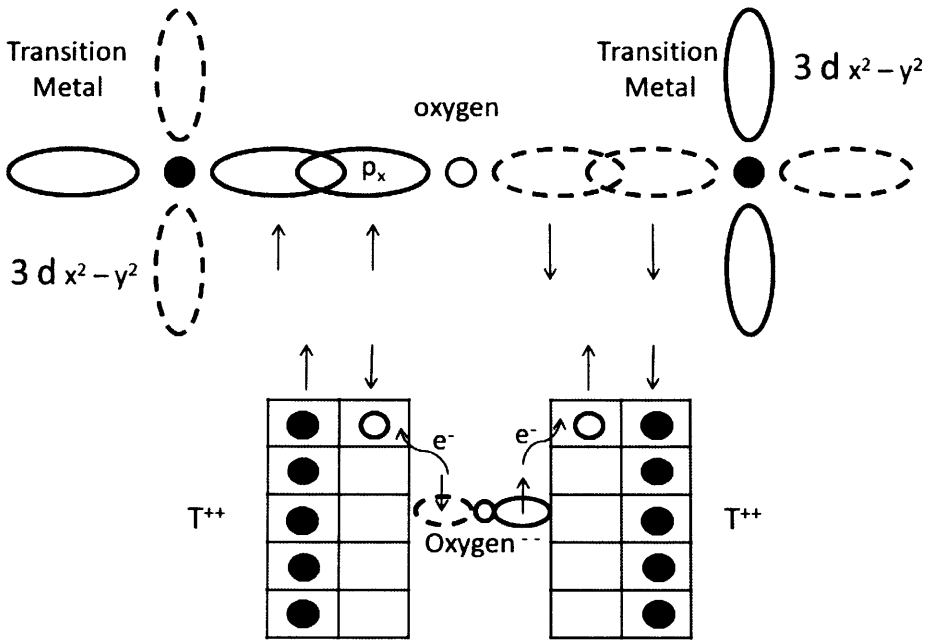

Figure 4-29. Schematic of *p* and *d* orbital important to the superexchange interaction. Adapted from ref 31.

Thus, the magnetic exchange interactions between 3*d* cations in ionic solids are antiferromagnetic superexchange couplings. The exchange is mediated by an intervening anion *p* orbital and is therefore strongest in structures for which the three ions are collinear. In the spinel structure, the A-O-B bond angle is 125 ° (Figure 3-6), the B-O-B angle is 90 ° and there are no A-O-A bonds. Hence, the strongest superexchange interaction is the 125 ° antiferromagnetic A-B coupling. B sites exhibit a weak 90 ° antiferromagnetic coupling among themselves. These interactions are most economically accommodated if all A moments are parallel to each other and antiparallel to all B moments.[2, 31]

As it was said above the Curie transition is a second-order phase transition changing the state of electrons so that the system can no longer maintain a spontaneous magnetization. Often these *d* electrons are responsible for determining the activity and selectivity of a material; that is why the Curie transition might be expected to affect them.

As we do not have information about the size of this possible effect and as we cover our magnetic material (cobalt ferrite) with non-magnetic ammonium heptamolybdate, we took several samples with different molybdenum coverage (1-6 monolayers). In the ordinary TPPFR experiments over Mo impregnated samples (Figure 4-23, Figure 4-25 and Figure 4-27) we did not observed any unusual changes of selectivity in the vicinity of the T_c. Of course selectivities of products change with the increase in temperature, however this smooth and even change rather relates to the Arrhenius dependence of kinetic constants. To prove that we did not miss anything in our research, we ran several isothermal experiments in the vicinity of the Curie point. Figure 4-30 and Figure 4-31 show raw results of the isothermal pulse flow reaction experiments (IPFR) for the 1 Mo/$Zn_{0.4}$CF and the 6 Mo/ $Zn_{0.4}$CF catalysts. The Curie temperature for these is 245 °C and continuous methanol injections were done at constant temperatures within the range of 240-260 °C. The difference between the 1 monolayer and the 6 monolayer samples is that for the former CO_2 is the main product (mass 44), whereas for the latter much less CO_2 is observed and CO (mass 28) and formaldehyde (mass 30) start to be dominant products. However, going through the Curie transition, we see that all monitored masses show even and stable signals at all monitored temperatures and no magnetic effect can be seen.

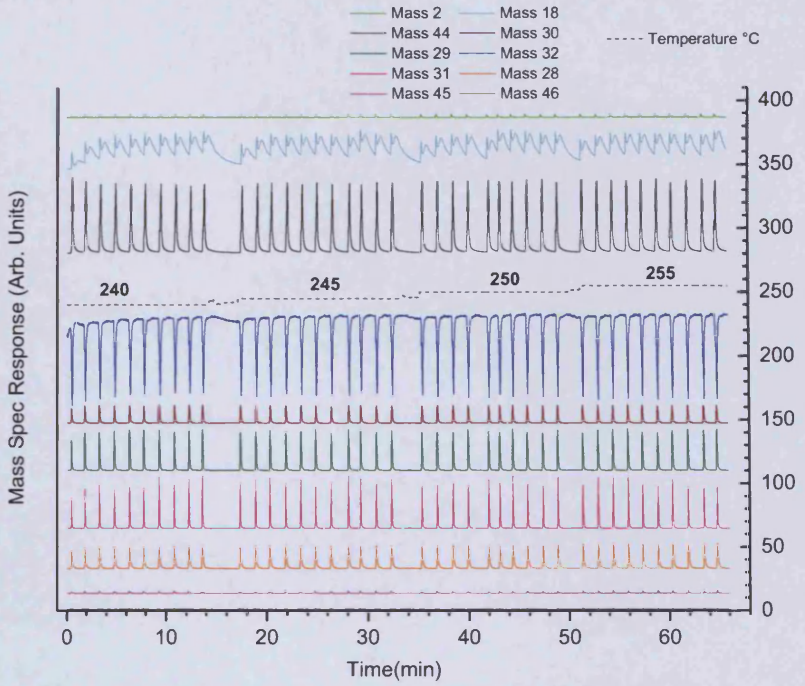

Figure 4-30. Raw data of IPFR of methanol over the 1 Mo/$Zn_{0.4}$CF catalyst.

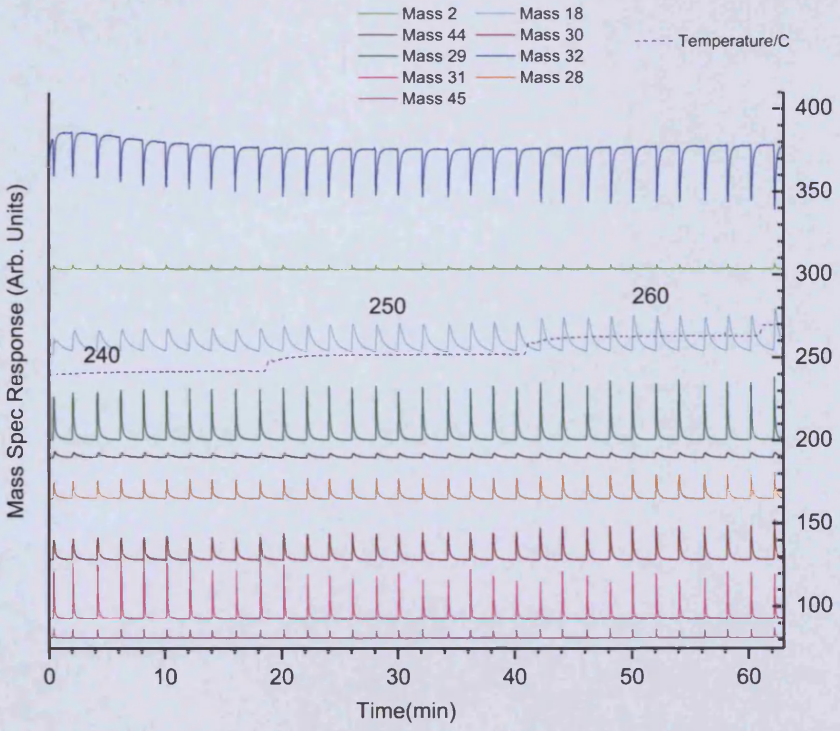

Figure 4-31. Raw data of a IPFR of methanol over the 6 Mo/$Zn_{0.4}$CF catalyst.

4.2.2.3. Experiments in the presence of a magnetic field

Several authors in the past have reported that they observed the effect of the Curie transition on catalysis only in the presence of a magnetic field.[4] For our research we made a special magnetic set-up in order to run methanol oxidation reaction upon an externally applied magnetic field (see details in Chapter 2).

(a) Isothermal experiment in the vicinity of the T_c

Figures 4-32-4-35 show results of isothermal experiments for the $Zn_{0.35}CF$ sample with T_c=256 °C upon the application of a switchable external magnetic field (magnetic field strength $2 \cdot 10^{-3}$ T).

Several temperatures around the Curie point were monitored (260, 270, 280 and 290 °C). The magnetic field was turned on and off by switching on and off the power supply. We might have expected changes in the intensities of mass signals and consequently in selectivity, however isothermal experiments have shown almost no difference in the signals for any particular mass with magnetic field turned on and off. Insignificant deviations of signal intensities for some injections might be attributed to the fluctuation of temperature generated by the wrapped cord itself, rather than to the effect of Curie transition.

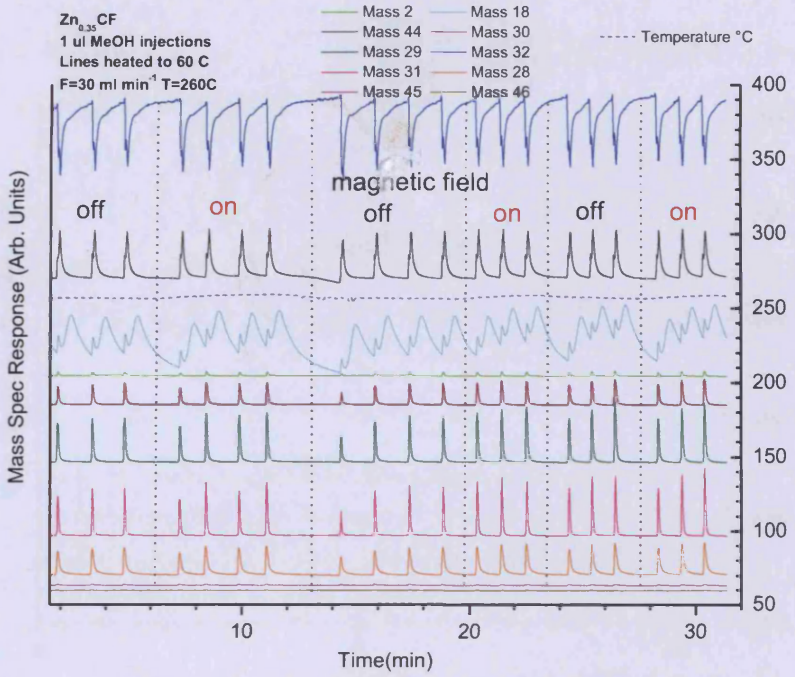

Figure 4-32. Isothermal methanol oxidation at 260 °C over the $Zn_{0.35}CF$ with magnetic field switched on and off.

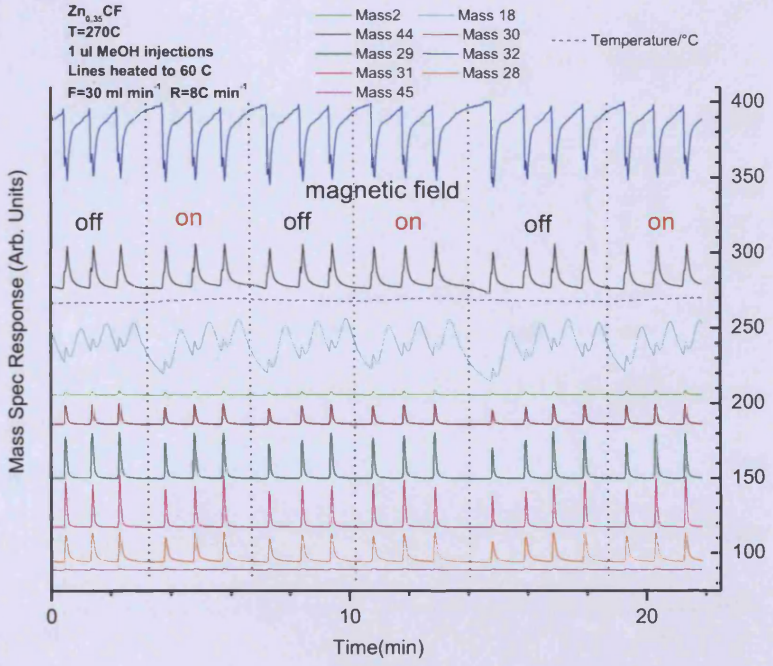

Figure 4-33. Isothermal methanol oxidation at 270 °C over the $Zn_{0.35}CF$ with magnetic field switched on and off.

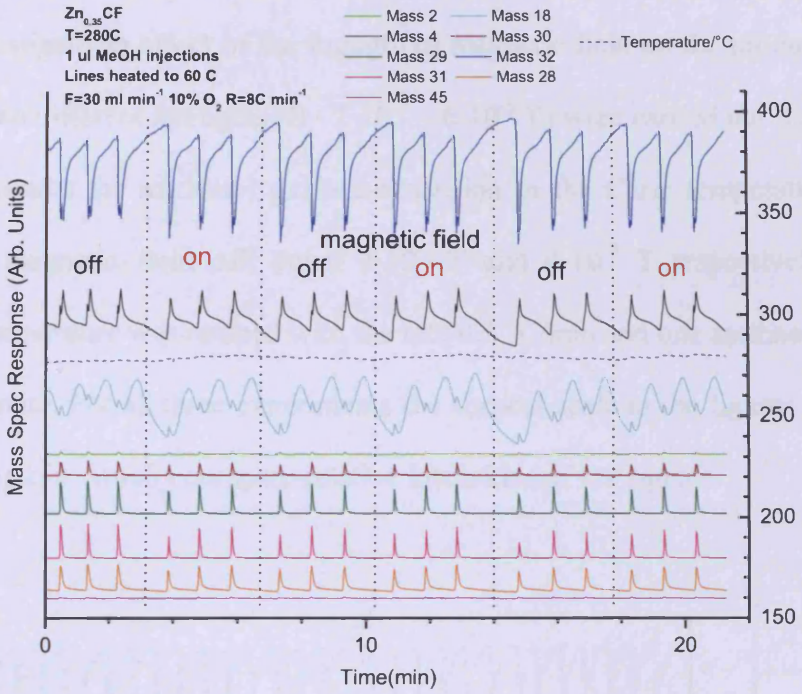

Figure 4-34. Isothermal methanol oxidation at 280 °C over the $Zn_{0.35}CF$ with magnetic field switched on and off.

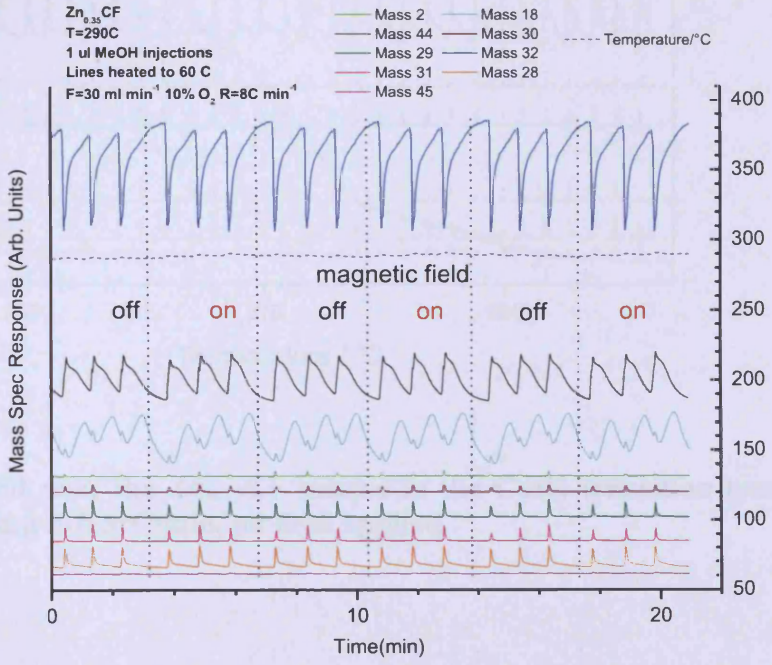

Figure 4-35. Isothermal methanol oxidation at 290 °C over the $Zn_{0.35}CF$ with magnetic field switched on and off.

(b) Different strength of magnetic field

In order to investigate an effect of the strength of magnetic field on the products distribution, experiments with different strengths (B= $2 \cdot 10^{-3}$ – $6 \cdot 10^{-3}$ T) were carried out. Figures 4-36 – 4-38 show raw results for methanol oxidation reaction in the Curie temperature range (250-285 °C) with magnetic field off, equal $2 \cdot 10^{-3}$ T and $4 \cdot 10^{-3}$ T respectively. In all these experiments temperature was ramped with the rate 0.5 °C/min and one methanol injection was made every minute. For all three experiments the vertical scale in the figures is the same and consequently we can visually compare relative intensities of the signals.

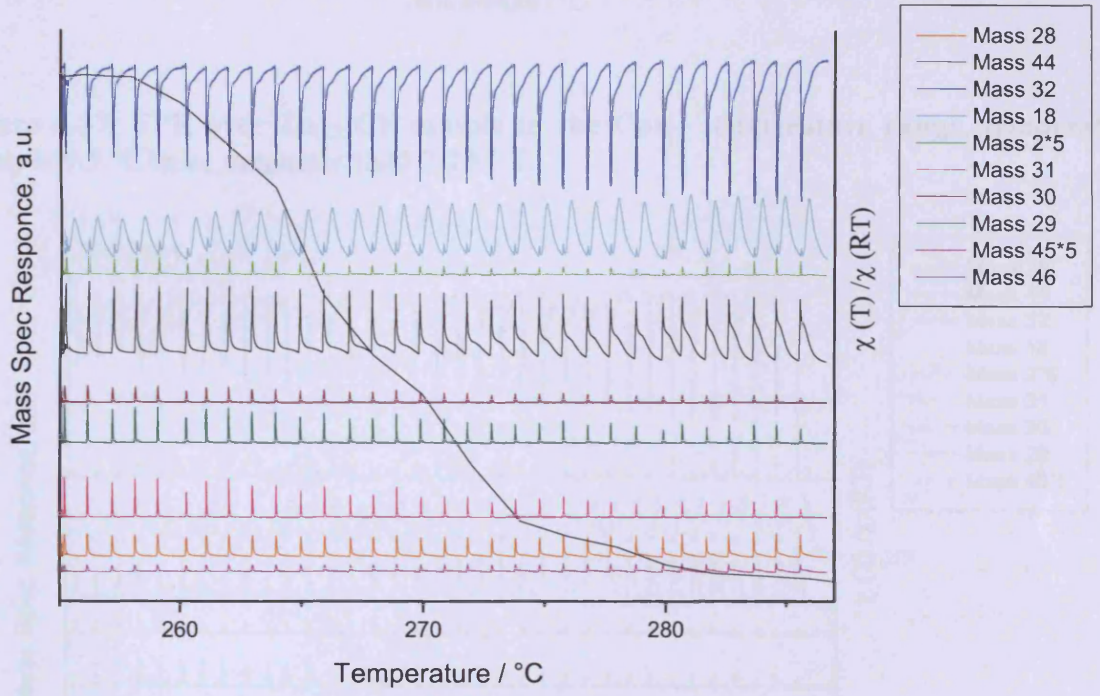

Figure 4-36. TPR over the $Zn_{0.35}CF$ sample in the Curie transition temperature range, temperature ramp is 0.5°C/min, no field applied.

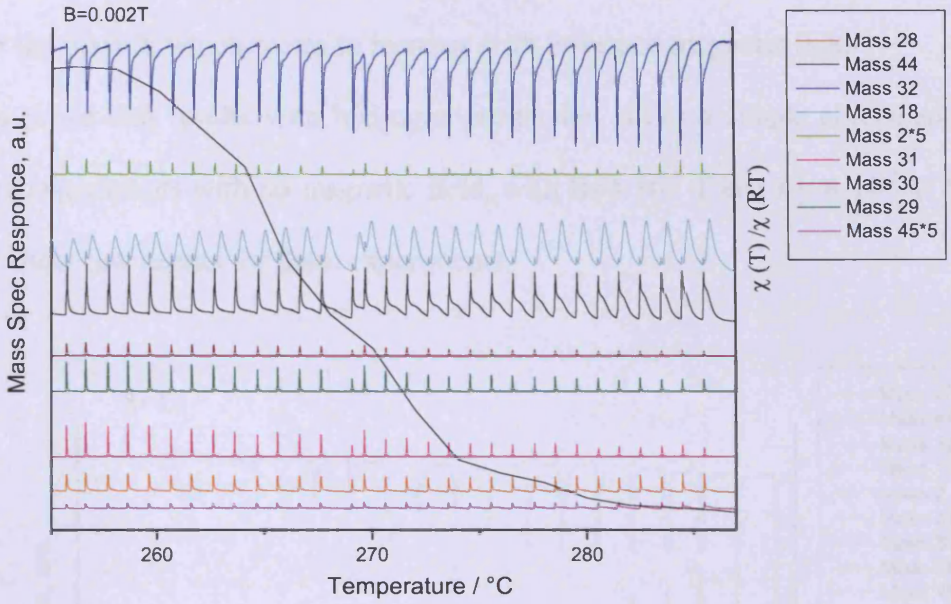

Figure 4-37. TPR over $Zn_{0.35}CF$ sample in the Curie temperature range, temperature ramp is 0.5 °C/min, magnetic field $2 \cdot 10^{-3}$ T.

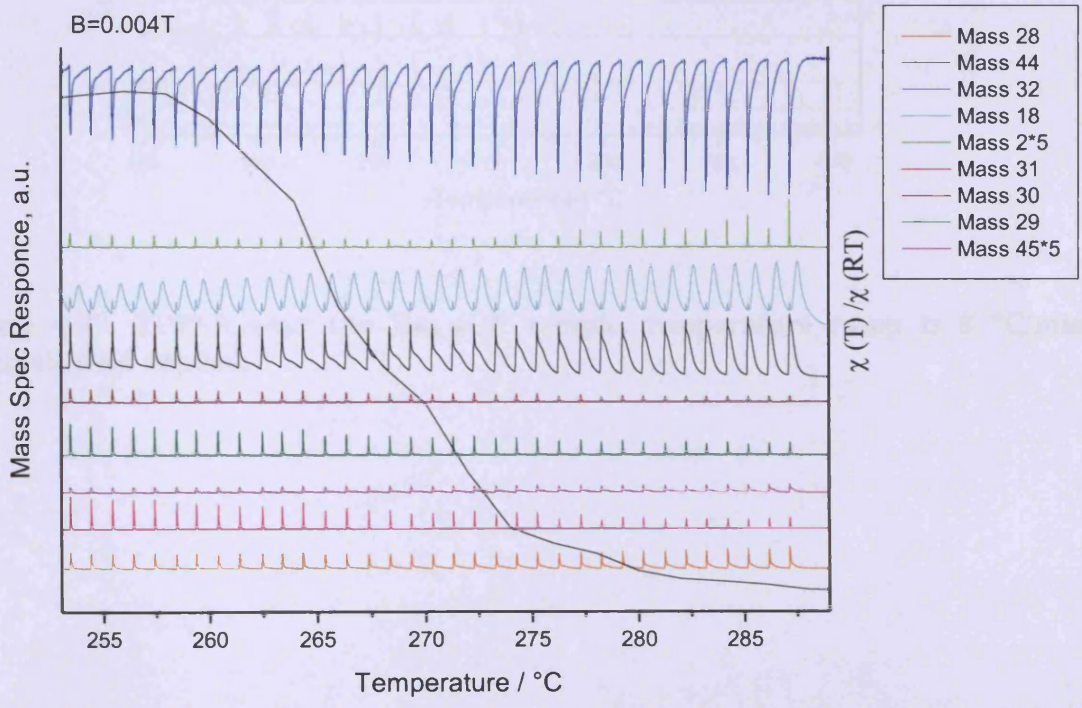

Figure 4-38. TPR over the $Zn_{0.35}CF$ sample in the Curie temperature range, temperature ramp is 0.5 °C/min, magnetic field $4 \cdot 10^{-3}$ T.

All these three experiments show rather smooth and unchangeable masses signals, except for the mass 2, which seems to increase with increased magnetic field.

To prove that results with hydrogen production is not a simple coincidence we ran three more experiments with no magnetic field, with $B=4\cdot10^{-3}$ T and $B= 6\cdot10^{-3}$ T. Figures 4-39 – 4-41 show raw results for these experiments.

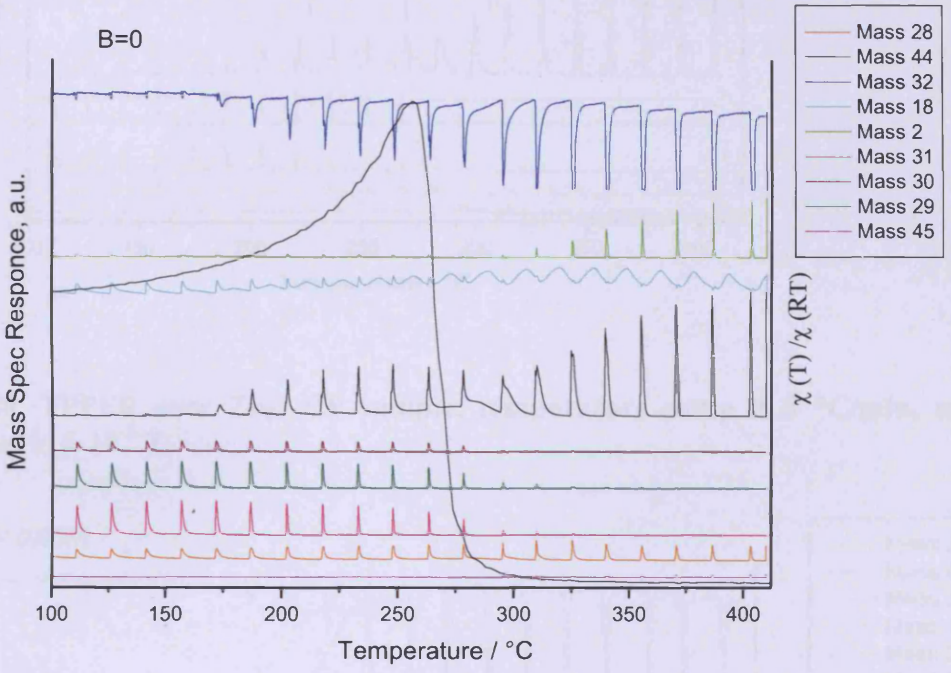

Figure 4-39. TPPFR over the $Zn_{0.35}CF$ sample, temperature ramp is 8 °C/min, no magnetic field applied.

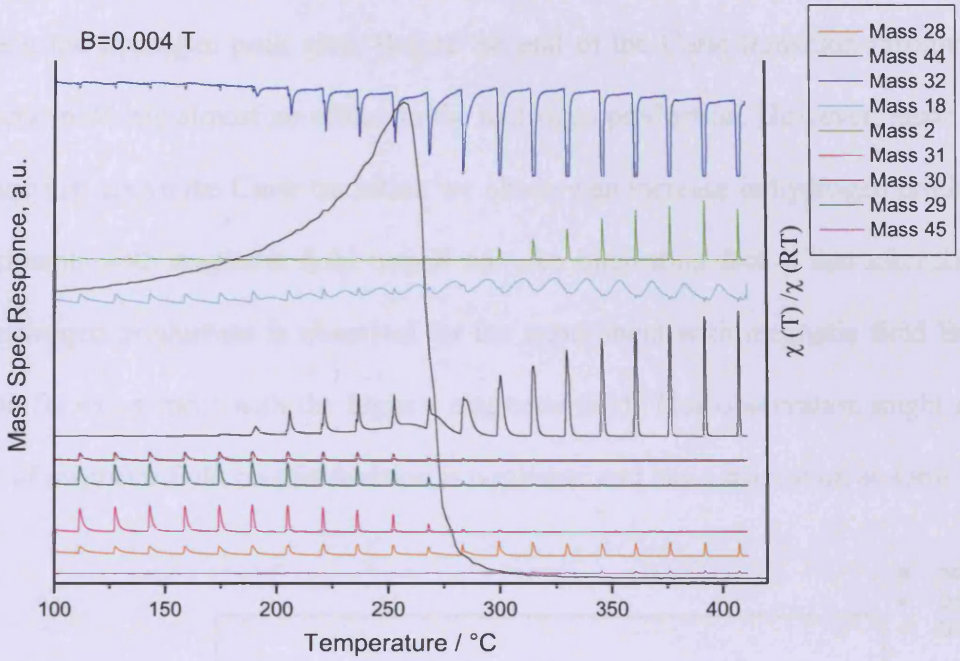

Figure 4-40. TPPFR over $Zn_{0.35}CF$ sample, temperature ramp is 8 °C/min, magnetic field applied is $4 \cdot 10^{-3}$ T.

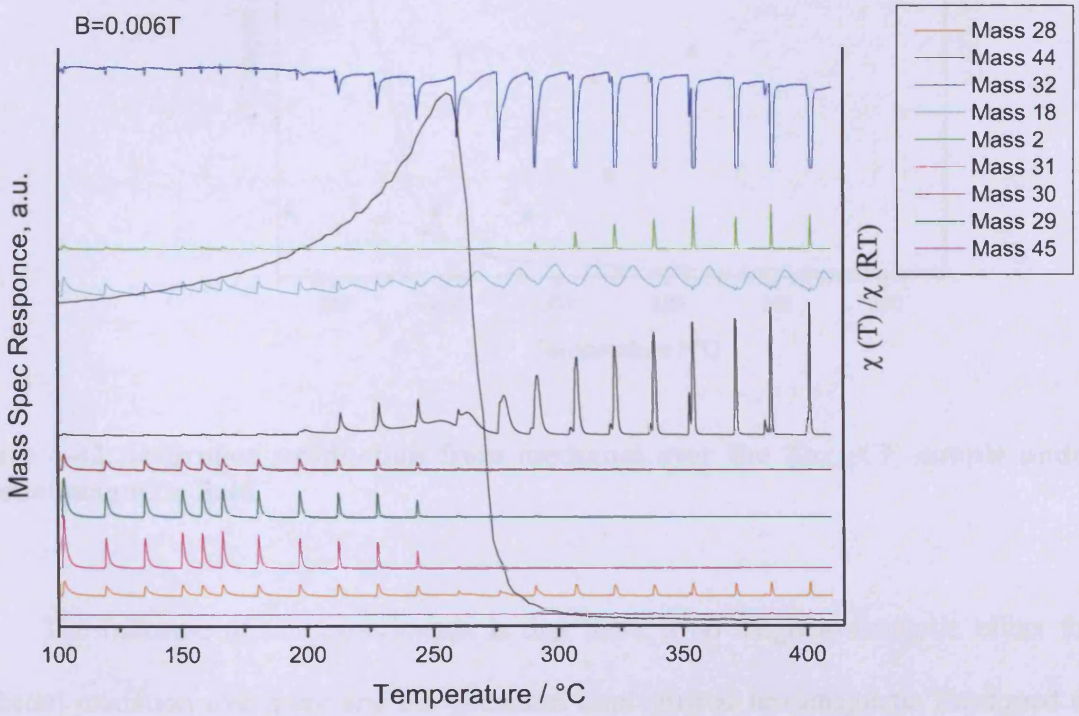

Figure 4-41. TPPFR over the $Zn_{0.35}CF$ sample, temperature ramp is 8 °C/min, magnetic field applied is $6 \cdot 10^{-3}$ T.

Figure 4-42 shows the calculated hydrogen integrals and the standard deviation of determining the hydrogen peak area. Before the end of the Curie transition (around 280 °C) the magnetic field has almost no effect on the hydrogen production. However, again at higher temperature just above the Curie transition we observe an increase in hydrogen production for the experiments with magnetic field turned on. An interesting fact is that after 280 °C the highest hydrogen production is observed for the experiment with magnetic field B=0.004 T rather than for experiment with the highest magnetic field. This observation might mean that the effect of magnetic field on this reaction is nonlinear and has a maximum at some point.

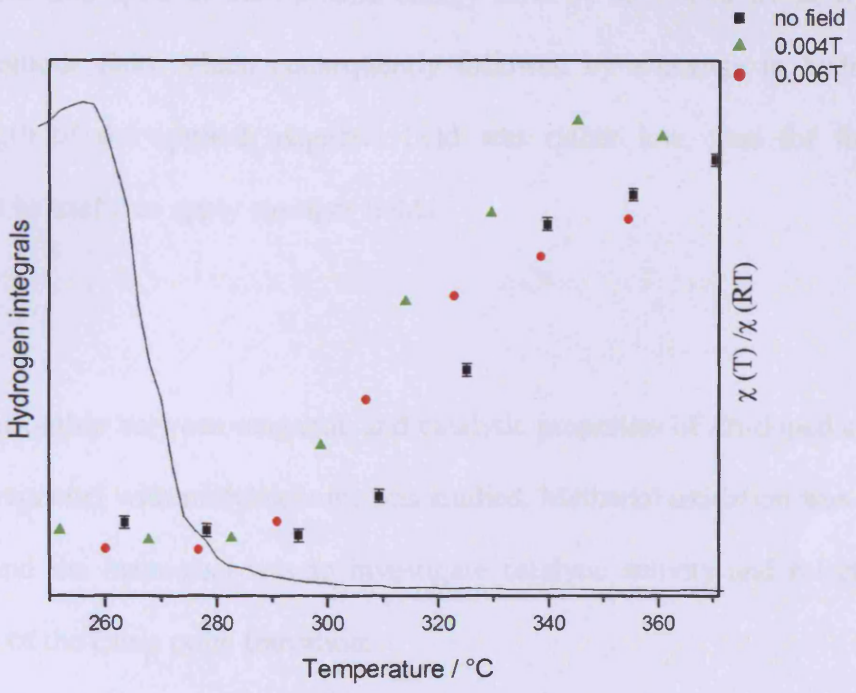

Figure 4-42. Hydrogen production from methanol over the $Zn_{0.35}CF$ sample under an external magnetic field.

The outcome of our experiments is that there is no magneto-catalytic effect for the methanol oxidation over pure and molybdenum impregnated ferromagnetic Zn-doped cobalt ferrites within the range of the Curie point region. This can be explained by too broad Curie transition region (around 10-20 °C), which does not allow to see sharp changes in both

catalyst state and selectivity. A further point which may significantly affect magnetic properties of the surface and consequently catalysis is that disordered or spin glass type (dead) layer forms at the surface of cobalt ferrite nanoparticles due to the broken symmetries and exchange bonds, as was shown earlier.[55-56] Considering the samples impregnated with molybdenum, we cannot see magneto-catalytic effect probably because its magnitude is not big enough.

When we applied magnetic field to pure $Zn_{0.35}CF$ system we observed an increase in hydrogen production. This might be attributed to the amplification of the effect of sudden disorientation of the electron spins at the 3*d*-band energy level of the cobalt ferrite by the externally applied magnetic field, which consequently followed by a change in hydrogen formation. The strength of the applied magnetic field was rather low, thus for further investigations it would be useful to apply stronger fields.

4.2.3. Conclusions

In this chapter the relationship between magnetic and catalytic properties of Zn-doped cobalt ferrites, pure and impregnated with molybdenum, was studied. Methanol oxidation was used as a model reaction and the main goal was to investigate catalytic activity and selectivity changes in the vicinity of the Curie point transition.

To obtain a single-phase sample with a Curie temperature in a range of the methanol oxidation (250-400 °C) Zn-doped cobalt ferrites $Zn_xCo_{1-x}Fe_2O_4$ with x=0-0.5 were synthesized via a co-precipitation method. It was shown that zinc, substituting cobalt in cobalt ferrite, decreases T_c. Also, as we needed a rather sharp and fast Curie transition for our experiments, the influence of the calcination temperature on the nature of the Curie transition was studied. It was shown that the increase of calcination temperature from 500 to 800 °C results in a much sharper and narrow Curie transition. These changes in the magnetic

properties of the samples are related to better lattice ordering at higher temperatures and to the difference of the particle size distribution for the samples calcined at 500 and 800 °C as it was shown by TEM method. The single-phase nature of the synthesized $Zn_xCo_{1-x}Fe_2O_4$ systems was confirmed by XRD and Raman data. All the Zn-doped cobalt ferrites are combustors of methanol and produce CO_2 as the main carbon-containing product.

Characterization of the Mo impregnated $Zn_xCo_{1-x}Fe_2O_4$ samples by XRD and Raman revealed the formation of $CoMoO_4$, $Fe_2(MoO_4)_3$ and MoO_3 phases on the Zn-doped cobalt ferrite. It was shown that the ratio of these phases depends on the sample calcination temperature. The catalytic activity profiles of Mo/ $Zn_xCo_{1-x}Fe_2O_4$ are similar to the Mo/ $CoFe_2O_4$ systems discussed in the Chapter 3: as molybdenum is doped on the surface, the mixed surface Co-Mo-Fe layer forms and produce partial oxidation products (CO and formaldehyde).

To investigate catalytic behaviour in the vicinity of the Curie point for the pure and the Mo impregnated $Zn_xCo_{1-x}Fe_2O_4$ standard TPPFR experiments with different temperature ramp and isothermal experiments at the temperatures around Curie point were carried out. Unfortunately, no effect of the Curie transition on either activity or selectivity was detected.

Application of the external magnetic field during methanol oxidation over the $Zn_{0.35}Co_{0.65}Fe_2O_4$ sample had an effect on the hydrogen concentration formed during experiment. Thus, after the Curie transition was complete, the hydrogen production in the experiment with applied magnetic field at 0.004 T was higher than hydrogen production in the experiment with no magnetic field on, significantly above the experimental error. However, this interesting result needs further confirmation and additional experiments to be done.

4.3. References

1. Mathew, D. S.; Juang, R.-S., *Chemical Engineering Journal* **2007,** *129*, 51-65.

2. O'Handley, R., *Modern Magnetic Materials: principles and applications*. Wiley: New York, **2000.**
3. Cohn, G.; Hedvall, J. A., *The Journal of Physical Chemistry* **1942,** *46*, 841-847.
4. Selwood, P. W., *Chemical Reviews* **1946,** *38*, 41-82.
5. Forestier, L., *Comp. Rend.* **1937,** *204*, 1254.
6. Olmer, *Journal of Physical chemistry* **1942,** *46*, 405-414.
7. Spingler, *Z. physik. Chem.* **1942,** *A190*, 331.
8. Lielmezs, J.; Morgan, J. P., *Chemical Engineering Science* **1967,** *22*, 781-791.
9. Lielmezs, J.; Aleman, H., *Thermochimica Acta* **1990,** *161*, 267-277.
10. Sales, B. C.; Maple, M. B., *Physical Review Letters* **1977,** *39*, 1636.
11. Mehta, R. S.; Dresselhaus, M. S.; Dresselhaus, G.; Zeiger, H. J., *Physical Review Letters* **1979,** *43*, 970.
12. Müller, R.; Schüppel, W., *Journal of Magnetism and Magnetic Materials* **1996,** *155*, 110-112.
13. Manova, E.; Tsoncheva, T.; Estournès, C.; Paneva, D.; Tenchev, K.; Mitov, I.; Petrov, L., *Applied Catalysis A: General* **2006,** *300*, 170-180.
14. Chen, Z.; Gao, L., *Materials Science and Engineering: B* **2007,** *141*, 82-86.
15. Mirzaei, A. A.; Habibpour, R.; Kashi, E., *Applied Catalysis A: General* **2005,** *296*, 222-231.
16. Yan, C. H.; Xu, Z. G.; Cheng, F. X.; Wang, Z. M.; Sun, L. D.; Liao, C. S.; Jia, J. T., *Solid State Communications* **1999,** *111*, 287-291.
17. Maaz, K.; Mumtaz, A.; Hasanain, S. K.; Ceylan, A., *Journal of Magnetism and Magnetic Materials* **2007,** *308*, 289-295.
18. Vaidyanathan, G.; Sendhilnathan, S.; Arulmurugan, R., *Journal of Magnetism and Magnetic Materials* **2007,** *313*, 293-299.
19. Rajendran, M.; Pullar, R. C.; Bhattacharya, A. K.; Das, D.; Chintalapudi, S. N.; Majumdar, C. K., *Journal of Magnetism and Magnetic Materials* **2001,** *232*, 71-83.
20. Gul, I. H.; Maqsood, A., *Journal of Alloys and Compounds* **2008,** *465*, 227-231.
21. Baldi, G.; Bonacchi, D.; Innocenti, C.; Lorenzi, G.; Sangregorio, C., *Journal of Magnetism and Magnetic Materials* **2007,** *311*, 10-16.
22. Song, Q.; Zhang, Z. J., *Journal of the American Chemical Society* **2004,** *126*, 6164-6168.
23. Virden, A.; Wells, S.; O'Grady, K., *Journal of Magnetism and Magnetic Materials* **2007,** *316*, e768-e771.
24. Lin, X.-M.; Samia, A. C. S., *Journal of Magnetism and Magnetic Materials* **2006,** *305*, 100-109.
25. Kumar, D.; Gupta, A., *J. Magn. Magn. Mater.* **2007,** *308*, 318-324.
26. Bhame, S. D.; Joy, P. A., *Sensors and Actuators A: Physical* **2007,** *137*, 256-261.
27. Arulmurugan, R.; Vaidyanathan, G.; Sendhilnathan, S.; Jeyadevan, B., *Physica B: Condensed Matter* **2005,** *363*, 225-231.
28. Arulmurugan, R.; Vaidyanathan, G.; Sendhilnathan, S.; Jeyadevan, B., *Journal of Magnetism and Magnetic Materials* **2006,** *303*, 131-137.
29. Paulsen, J. A.; Ring, A. P.; Lo, C. C. H.; Snyder, J. E.; Jiles, D. C., *Journal of Applied Physics* **2005,** *97*, 044502.
30. Lee, S. J.; Lo, C. C. H.; Matlage, P. N.; Song, S. H.; Melikhov, Y.; Snyder, J. E.; Jiles, D. C., *Journal of Applied Physics* **2007,** *102*, 073910.
31. Jiles, D., *Introduction to magnetism and magnetic materials*. 2nd ed.; Chapman&Hall: London, **1998**.
32. JCPDS, 11-121.
33. JCPDS, 11-053.

34. JCPDS, 42-1467.
35. Akther Hossain, A. K. M.; Tabata, H.; Kawai, T., *Journal of Magnetism and Magnetic Materials* **2008,** *320*, 1157-1162.
36. Gözüak, F.; Köseoglu, Y.; Baykal, A.; Kavas, H., *Journal of Magnetism and Magnetic Materials* **2009,** *321*, 2170-2177.
37. West, A. R., *Solid State Chemistry*. Wiley: Chichester, New York, **1988**.
38. Wienold, J.; Jentoft, R. E.; Ressler, T., *ChemInform* **2003,** *34*, no-no.
39. JCPDS, 62-163.
40. JCPDS, 35-659.
41. JCPDS, 21-868.
42. JCPDS, 35-183.
43. Chandramohan, P.; Srinivasan, M. P.; Velmurugan, S.; Narasimhan, S. V., *Journal of Solid State Chemistry* **2011,** *184*, 89-96.
44. Ayyappan, S., Mahadevan, S., Chandramohan, P., Srinivasan, M.P., John Philip, Baldev, R. , *Journal Physical Chemistry C* **2010,** *114*, 6334.
45. Tahar, L. B.; Smiri, L. S.; Artus, M.; Joudrier, A. L.; Herbst, F.; Vaulay, M. J.; Ammar, S.; Fiévet, F., *Materials Research Bulletin* **2007,** *42*, 1888-1896.
46. H. Jeziorowski, H. K., *J Phys Chem* **1979,** *83*.
47. Y. Matsuoka, M. N., Y. Murakami, *J Phys Chem* **1990,** *94*, 1477-1482.
48. House, M. Selective oxidation of methanol over iron molybdate catalysts. Cardiff University, Cardiff, 2006.
49. Dunlop, D. J., Ozdemir, O., Enkin, R. , *J. Phys. Earth planet interiors* **1987,** *49*, 181.
50. Alone, S. T., Jadhav, K.M. , *Pramana* **2008,** *70*, 173.
51. McCurrie, R. A., *Ferromagnetic materials – Structure and Properties*. 1994.
52. Kodama, R. H., *Journal of Magnetism and Magnetic Materials* **1999,** *200*, 359-372.
53. Briand, L. E.; Hirt, A. M.; Wachs, I. E., *Journal of Catalysis* **2001,** *202*, 268-278.
54. César, D. V.; Robertson, R. F.; Resende, N. S., *Catalysis Today 133-135*, 136-141.
55. Espinosa, L. A.; Lago, R. M.; Peña, M. A.; Fierro, J. L. G., *Topics in Catalysis* **2003,** *22*, 245-251.
56. Maaz, K.; Usman, M.; Karim, S.; Mumtaz, A.; Hasanain, S. K.; Bertino, M. F., *J. Appl. Phys.* **2009,** *105*, 113917/1-113917/5.

Chapter 5. Conclusions

5.1. Conclusions

The main aim of the present thesis was to investigate methanol oxidation over mixed oxide catalysts. Two MoO_3/Fe_2O_3 and $MoO_3/Co(Zn)Fe_2O_4$ different systems were studied and the work was divided into two results chapter: Chapter 3 dealing with structural and catalytic characterization of thin layer MoO_3/Fe_2O_3 and $MoO_3/CoFe_2O_4$ systems and Chapter 4 considering the influence of magnetic properties of pure and Mo doped Zn-substituted cobalt ferrites on the oxidation of methanol.

Study of model MoO_3/Fe_2O_3 catalyst is important because it gives an insight into the catalytic properties of industrial iron molybdate catalysts. Single iron oxide produces CO_2 and water in the methanol oxidation due to stabilization of formate intermediates on its surface, while MoO_3 is highly selective to formaldehyde due to formation of methoxy species. When molybdenum is doped on the surface of iron oxide it drastically changes the selectivity profile: CO_2 production decreases and partial oxidation products, CO and formaldehyde, become dominant. Already, when 3 monolayers of molybdenum is doped on the Fe_2O_3, carbon dioxide desorption is not seen in the TPD profile of this sample. CO and formaldehyde are produced from the Fe-Mo and Mo-Mo neighbouring sites of the surface iron molybdate layer, which forms on the top of iron oxide during the impregnation and calcination process.

The phase composition of MoO_3/Fe_2O_3 depends on the calcination temperature. Thus, according to XRD and Raman data, during the calcination from 300 °C to 500 °C, the phase composition goes from a mixture of MoO_3 and Fe_2O_3 to mixture of $Fe_2(MoO_4)_3$ and Fe_2O_3 indicating the formation of an iron molybdate layer. As the molybdenum loading is increased the thickness of this layer also increases. However, at any Mo loading used within this work, the core iron oxide never was fully converted into iron molybdate and no molybdena surface

layer was formed over the iron molybdate. Therefore these catalysts produce mainly CO as a partial oxidation product.

When molybdenum is doped on the surface of $CoFe_2O_4$, it also significantly changes its catalytic activity in methanol oxidation. Cobalt ferrite, like iron oxide, combusts methanol to CO_2 and water. With increasing Mo loading on the surface of cobalt ferrite, more CO and formaldehyde start to form. However, the major CO production appears only at high temperature, whereas at lower temperature a lot of CO_2 is observed. This carbon dioxide is a secondary oxidation product as almost no CO_2 was detected in the TPD profiles of these samples. Spectroscopy data and TPD results combining together revealed the formation of mixed Co-Mo-Fe layer consisting of $CoMoO_4$, $Fe_2(MoO_4)_3$ and MoO_3 phases when Mo is loaded on the cobalt ferrite. Thus, analogous to Mo/Fe_2O_3 system, the neighbouring Co-Mo, Fe-Mo and Mo-Mo sites of this layer are assumed to be responsible for the production of CO and formaldehyde respectively. The methoxy species are stabilized on this mixed layer producing mainly CO, which at low temperature and low oxygen conversion is easily converted to carbon dioxide by the traces of either cobalt ferrite or cobalt molybdate presented on the catalyst surface.

To establish whether there is relationship between catalytic activity and selectivity and magnetic properties of materials, the catalytic behaviour of pure and Mo impregnated $Zn_xCo_{1-x}Fe_2O_4$ systems in the vicinity of the Curie point was studied using methanol oxidation as a model reaction. Varying Zn content and calcination temperature it is possible to change the Curie temperature of the material and the nature of Curie transition. Thus, an increase of the Zn content leads to the shift of T_c to lower temperatures and increase of calcination temperature from 500 °C to 800 °C leads to formation of better ordered spinel structure and consequently to the sharper Curie transition.

The influence of the Curie transition on the catalytic behaviour of the $Zn_{0.4}Co_{0.6}Fe_2O_4$ sample, pure and impregnated with molybdenum, with the T_c~250 (the point when methanol conversion is ~ 50 %) was studied in standard TPPFR experiments and isothermal experiments in the vicinity of the T_c. However, all of these experiments showed a negative result. The possible explanation for this is the formation of disordered or spin glass type (dead) layer at the surface of cobalt ferrite nanoparticles due to the broken symmetries and exchange bonds at the surface, which may significantly affect the magnetic properties of the surface and consequently catalysis which takes place there. As for samples impregnated with molybdenum, the magneto-catalytic effect probably cannot be seen simply because its magnitude is not big enough.

Application of external magnetic field (0.004 T) during methanol oxidation over $Zn_{0.35}Co_{0.65}Fe_2O_4$ sample resulted in enhanced hydrogen production at the temperatures when magnetic transition is finished compared to hydrogen production in experiment with no magnetic field on. This magnetic effect might be due to amplification of the effect of sudden disorientation of the electron spins at the 3d-band energy level of the cobalt ferrite by the externally applied magnetic field, which consequently followed by a change in hydrogen formation. Still these experiments need further proof and more experimental work.

5.2. Future work

For thin layer oxide systems, to make the composition of the mixed surface layer clear, would be very useful to do further characterization of the surface using combination of powerful surface science techniques such as HRTEM to obtain images of the surface and HAADF-STEM and EELS to probe the distribution of Mo, Fe, Co and O across the phases observed in the images.

In-situ Raman spectroscopy investigations of both Mo/Fe_2O_3 and $Mo/CoFe_2O_4$ systems might give more clear information about the active surface sites participating in formation of CO and formaldehyde in methanol oxidation, for instance, it could give an answer to the question whether Mo=O is responsible for the selectivity towards formaldehyde or not.

The scientific field of correlation between magnetism and catalysis is rather unexplored and the experiments which were made within this work are only preliminary. As we observed some magnetic effect when running catalytic reaction in the presence of a magnetic field, it would be useful to run this type of experiments over samples with different Curie point in order to prove this effect. In our experiments, we used magnetic fields with quite low strength, therefore, in future investigation of the influence of magnetic field strength on the catalytic activity and selectivity would be interesting.

Another important experiment for this research is methanol oxidation over Mo doped zinc cobalt ferrite in the presence of a magnetic field. The product distribution over this catalyst is broader than that for un-doped sample and probably it will be easier to detect the change in selectivity after the T_c, if there is a change.

Within our work we used only methanol oxidation as a model reaction for magnetic experiments. However, it would be very interesting to try magnetic experiments with oxidation of some other compounds as well.